A Joint Analysis of T2K Beam Neutrino and

Super-Kamiokande Sub-GeV Atmospheric Neutrino Data

A Dissertation presented

by

Xiaoyue Li

to

The Graduate School

in Partial Fulfillment of the

Requirements

for the Degree of

Doctor of Philosophy

in

Physics

Stony Brook University

July 2018

Stony Brook University

The Graduate School

Xiaoyue Li

We, the dissertation committee for the above candidate for the

Doctor of Philosophy degree, hereby recommend

acceptance of this dissertation

Chang Kee Jung – Dissertation Advisor
Department of Physics and Astronomy, Stony Brook University

Clark McGrew – Chairperson of Defense
Department of Physics and Astronomy, Stony Brook University

Michael Wilking
Department of Physics and Astronomy, Stony Brook University

Robert Shrock
Department of Physics and Astronomy, Stony Brook University

Georgia Karagiorgi
Department of Physics, Columbia University

This dissertation is accepted by the Graduate School

Charles Taber
Dean of the Graduate School

Abstract of the Dissertation

A Joint Analysis of T2K Beam Neutrino and Super-Kamiokande Sub-GeV Atmospheric Neutrino Data

by

Xiaoyue Li

Neutrino oscillation is a phenomenon in which neutrinos produced from charged current weak interactions can change flavor as they propagate. The mixing between the three flavor eigenstates and mass eigenstates can be measured through neutrino oscillations as the oscillation probabilities depend on the mixing angles and neutrino mass squared differences.

T2K is a long baseline neutrino experiment, in which a nearly pure muon neutrino or muon antineutrino beam is produced at J-PARC on the east coast of Japan and travels 295 km through the Earth's crust towards the far detector, Super-Kamiokande (Super-K), a 50 kiloton water Cherenkov detector, in the west of Japan. The neutrino fluxes in the absence of oscillation are measured by the near detectors 280 meters away from the target, and again with oscillation effects at Super-K. Aside from the beam neutrino from J-PARC, it also measures neutrino oscillations independently through the neutrinos produced in the Earth atmosphere.

This thesis presents the first analysis in which both the T2K beam neutrino data and the sub-GeV atmospheric neutrino data at Super-K are used in a unified framework to measure neutrino oscillation parameters. The beam neutrino samples are selected for optimal sensitivity to $\sin^2\theta_{23}$ and δ_{CP}. A Bayesian analysis using a Markov Chain Monte Carlo method is performed. Using T2K Run 1-8 data which amounts to 14.7×10^{20} POT in neutrino-mode and 7.6×10^{20} protons on target (POT) in antineutrino-mode, and 2519 days of Super-K data, the oscillation parameters are measured to be $\sin^2\theta_{23} = 0.528^{+0.032}_{-0.028}$, $|\Delta m^2_{32}| = 2.46^{+0.084}_{-0.060}(10^{-3}\text{eV}^2)$, $\sin^2\theta_{13} = 0.0270^{+0.0065}_{-0.0047}$; and the 90% credible interval of δ_{CP} is $[-\pi, -0.18]\&[2.33, \pi]$. When the data is also combined with the constraint on $\sin^2 2\theta_{13} = 0.857 \pm 0.046$ from reactor neutrino experiments, the oscillation parameters are measured to be $\sin^2\theta_{23} = 0.543^{+0.026}_{-0.023}$, $|\Delta m^2_{32}| = 2.49^{+0.042}_{-0.090}(10^{-3}\text{eV}^2)$, $\sin^2\theta_{13} = 0.0223^{+0.0012}_{-0.0013}$; the 90% credible interval of δ_{CP} is $[-\pi, -0.628]$, and the CP-conserving value $\delta_{CP} = 0$ is excluded at 2σ.

To my mother

Contents

List of Figures

List of Tables

Preface

This thesis contains the work that I performed within the T2K and Super-Kamiokande (SK) collaborations, as well as the work by the past and present members from both collaborations; the former would not have been possible without the latter. The experimental apparatus described in Chapter 3, the event simulation and reconstruction software described in Chapter 4 as well as the data reduction procedure in section 5.1 are the work product of many past and present collaborators not including me; they are included in this thesis in order to paint a more complete picture. My contributions are listed below.

I performed the T2K event selection optimization study described in section 5.2. The original analysis framework was developed by Megan Friend (KEK) and Motoyasu Ikeda (ICRR), upon which I made various modifications; I also developed the additional algorithms needed for the optimization. The fiTQun event reconstruction algorithm for SK (described in section 4.2) on which the event selection is based was developed by Michael Wilking (formerly TRIUMF, now Stony Brook U.), Shimpei Tobayama (U. of British Columbia), Patrick de Perio (formerly U. of Toronto, now Columbia U.), Andrew Missert (CU Boulder), Hiro Tanaka (formerly U. of British Columbia, now SLAC), Sophie Berkman (U. of British Columbia), Akira Konaka (TRIUMF), Eric Zimmerman (CU Boulder) and Miao Jiang (Kyoto U.).

The T2K beam neutrino and SK atmospheric neutrino joint analysis in Chapter 6 was performed by me. The Markov Chain Monte Carlo (MCMC) algorithm used by this Bayesian analysis as well as the the basis of the software were provided by the analysis framework of T2K named MaCh3. The SK atmospheric neutrino flux systematic uncertainty treatment was inherited from existing SK analysis framework, and part of the input was provided by Roger Wendell (Kyoto U.) and Miao Jiang (Kyoto U.); the improved (computation speed-wise) SK atmospheric neutrino oscillation probability calculation algorithm was developed by Shimpei Tobayama. The T2K beam flux and cross section systematic uncertainty input was provided by the "BANFF" working group at T2K. I introduced the new method to unify

the implementation of the cross section systematic uncertainties used in this analysis. The treatment of the SK detector systematic uncertainties was also developed by me, inspired by the SK fiducial volume expansion study by Andrew Missert. The Hybrid-π^0 study used in the joint analysis was performed by Miao Jiang. The SK atmospheric neutrino MC was generated by Cristóvão Vilela (Stony Brook U.). This is the first truly simultaneous analysis of T2K and SK data in both collaborations. Although only the sub-GeV SK atmospheric neutrino data was used, this analysis will form the basis on which a complete joint analysis will be conducted including the multi-GeV, partially contained and upward-going muon samples from SK.

The work which I did in T2K but not presented in this thesis includes: (1) the upgrade and maintenance of the T2K data quality and data reduction online monitor; (2) extensive studies of T2K data quality and data/MC comparisons after each T2K run period. The latter work is presented in the following T2K technical notes: TN-218, TN-284 and TN-317.

Aside from T2K and SK, I have participated in the development of a novel event reconstruction algorithm for DUNE single-phase detectors named Wire-Cell (`https://www.phy.bnl.gov/wire-cell/`), which was pioneered by Xin Qian (BNL), Brett Viren (BNL) and Chao Zhang (BNL). My work on Wire-Cell involved the implementation of a parametrizable detector wire geometry and improvements in the signal simulation within Wire-Cell. In addition, I co-authored the following paper: *Data Unfolding with Wiener-SVD Method*, JINST, 12, P10002 (2017), which introduces a new data unfolding technique.

Acknowledgements

I am truly grateful for all the amazing people I have met in this long journey. First and foremost I would like to thank my advisor Chang Kee Jung, for his patience and support, for giving me enough freedom to choose the topics that interested me, and for all the sage advice he has given me. And not to mention all the BBQ, "fun" facts and anecdotes, and the wine and cheese at group meetings (shhh).

My work has also benefited immensely from Michael Wilking, Roger Wendell, Xin Qian, Clark McGrew, Prof. Robert Shrock, Chao Zhang and Brett Viren. Mike has been the driving force in making me think critically about my analyses and physics in general, and he is always delightful to have a conversation with on just about anything (although it can be frustrating when I can hardly ever win an argument against him). Roger is the convener that everyone wishes to have – he is both knowledgable and pragmatic, and more importantly, always willing to go out of his way to help. Both Mike and Roger have been instrumental in making the joint analysis happen, and their friendship has made the work much more enjoyable. Clark has been my go-to person for the trickiest questions and he never fails to offer an answer or suggestion. And I learned so many programming tricks from Chao and Brett. Xin is my mentor when it comes to physics in liquid argon TPCs. He not only shared his deep knowledge, but also showed me the kind of creativity and work ethic that I can only dream to have. Discussions with Prof. Shrock are always enlightening, and his enthusiasm about physics is infectious.

I would like to thank all my friends from Stony Brook: I may grimace a little when I think back about Long Island, but you will always put a smile on my face. My days at Stony Brook started in the office with Karin Gilje, Joshua Hignight, Jay Hyun Jo, James Imber, and Jeanine Adam, who made me feel welcome in the new country and new environment. Karin is like a big sister I never had, and Joshua, despite being a Duck Dynasty lookalike, is also kind and a lot of fun to hang out with. Being properly English, James has had to teach

me all the good English words for every bad one I would learn from Karin and Joshua. It was James and Joshua who guided me through the first two years on the T2K and SK related work and endured all my unsophisticated questions; James has also given me tremendous help and shared his wisdom on work throughout his career in T2K and SK. In spite of his misguided love for the Yankees, Jay is an otherwise intelligent person who is always delightful to talk to. Jeanine is ever so generous and also the reason why I initially committed the contemptible offense in New York of eating pizza with knife and fork. I would also like to thank all the current NNGroup members, especially Gabriel Santucci, Zoya Vallari and Cristóvão Vilela. Gabriel is unfailingly kind and always a good company, especially during the World Cup. Zoya is my feminist ally who is always ready to rail against the patriarchy together, which has become a common theme since 2016. Cris never says no to a heated discussion about physics or politics, or a sixth beer in a row. I also thank Tatiana Konstantinova for being such a good friend and always embracing me every time I would emerge again after a long trip.

I thank the members of the T2K-SK group who have endured my increasingly lengthy talks over the years and provided me with useful feedback, especially Kimihiro Okumura-san, Yoshinari Hayato-san, Shoei Nakayama-san, Hiro Tanaka, Sophie Berkman, Andrew Missert, Shimpei Tobayama, Miao Jiang, Christophe Bronner and Ryosuke Akutsu. It has been illuminating and fun working with them. I thank the members of the MaCh3 group with whom I worked: Clarence Wret, Patrick Dunne, Asher Kaboth, Elder Pinzon and Artur Sztuc. They have generously helped me understand the MCMC technique and the nitty-gritty details of the framework. I also thank Lluís Martí Magro and Kai Martens for the many memorable outings around Toyama accompanied by good conversations.

T2K and SK are ultimately the results of team work, and it has been such an honor to be part of it. Although I can't thank everyone whose path has crossed with mine, your hard work and academic rigor have been truly inspiring, and your kindness has made the time I spent in Japan some of my most treasured memories.

Last but not least, I'd like to thank my mom for her tireless support over the years and for her trust in me. My being thousands of miles away has not been easy on her, but she still gave me the freedom to define my own path. I hope I can be a better daughter in the next phase of my life. I'd also like to thank James for his love and extraordinary patience, for getting me through the darkest times, and for keeping me sane with everything that's going on. I look forward to sharing the next journey with you.

Chapter 1

Introduction

Neutrinos are neutral, fermionic elementary particles that interact only through the weak force and the gravitational force. It has been established by numerous experiments that there are three known neutrino flavors: ν_e, ν_μ and ν_τ, in correspondence with the three charged leptons. The Homestake experiment (1968), the Super-Kamiokande (Super-K) experiment (1998) and the SNO experiment (2001) showed that neutrinos produced in the atmosphere and in the Sun can change flavors – a phenomenon known as neutrino oscillation. It remains the only phenomenon observed in laboratories beyond the Standard Model of particle physics.

Neutrino oscillation occurs because neutrinos are not massless as the Standard Model originally prescribed, and the mixing matrix connecting the mass eigenstates and the flavor eigenstates is not identity. The mixing matrix can be described by three Euler angles θ_{12}, θ_{13}, θ_{23}, and the CP-violating phase δ_{CP} (two additional CP-violating phases if neutrinos are Majorana particles). Measuring these oscillation parameters precisely is of great importance for our understanding of the Standard Model and beyond; most notably, a non-zero δ_{CP} may help explain the very existence of the universe we see today – why there is more matter than anti-matter.

Many past and present experiments have made measurements of the oscillation parameters through the observation of neutrino oscillations, Super-K and T2K amongst them. After six years of data taking, T2K has made the most precise measurement on $\sin^2\theta_{23}$ and $|\Delta m^2_{32}|$ [1]. Due to the relatively large value of $\sin^2\theta_{13}$, T2K has the potential of probing the CP-violating phase by running the beam in a neutrino-dominated mode as well as an antineutrino-dominated mode. T2K is the first experiment to reject the CP-conserving values

$\delta_{CP} = 0, \pi$ at 2σ [2]. To further improve the measurement of δ_{CP}, it is desirable to combine the data from T2K and Super-K atmospheric neutrinos, as well as the NOνA experiment. This thesis presents the first simultaneous fit to the T2K beam neutrino data and the Super-K atmospheric neutrino data in which the data sets from both experiments are treated on an equal footing.

Chapter 2 gives a brief discussion of the theoretical and experimental development of our understanding of neutrinos. The phenomenology of neutrino oscillations in vacuum and in matter will be introduced, followed by experiments which have made measurements of the neutrino oscillation parameters.

Chapter 3 describes the experimental apparatus of the T2K and Super-K experiments, while Chapter 4 focuses on the software used by both experiments, including the simulation of the expected neutrino events observed in SK as well as the reconstruction of neutrino events by the signal recorded in the SK detector.

The first part of Chapter 5 describes the process in which the Super-K atmospheric neutrino and T2K beam neutrino data are extracted from the backgrounds. The second half describes the T2K event selection optimization study, in which the rejection of the π^+ background in the ν_μ and $\bar{\nu}_\mu$ samples are optimized based on the measurement precision of $\sin^2\theta_{23}$, and the rejection of the π^0 background in the ν_e and $\bar{\nu}_e$ samples are optimized based on the sensitivity to δ_{CP}.

Chapter 6 describes the joint analysis, which uses 2519 days of SK-IV atmospheric neutrino data and T2K data (Runs 1-8) amounting to 14.7×10^{20} POT in neutrino-mode and 7.6×10^{20} POT in antineutrino-mode. Three CCQE-like samples of Super-K atmospheric neutrinos and four CCQE-like samples of T2K are used to extract the oscillation parameters. The statistical method, analysis strategy, pre-fit data/MC comparisons, sensitivity improvements, as well as the data fit results will be shown in Chapter 6. The last chapter gives a brief summary and a discussion of the future prospect of this analysis.

Chapter 2

A brief summary of neutrino physics

Neutrinos pose some of the most intriguing questions in particle physics. The fact that neutrinos have mass has proven the Standard Model of particle interactions incomplete; the study of certain aspects of neutrinos, such as the leptonic CP violation, or whether neutrinos are their own antiparticles, will advance our understanding of the universe. Neutrinos are neutral particles that interact with matter so weakly that the neutrinos coming from the Sun almost always traverse the Earth without interacting. This makes neutrino experiments a challenging endeavor.

This chapter will first walk through briefly the properties of neutrinos in the Standard Model and how each of them is confirmed or discovered experimentally. The focus will then be turned to the phenomenon known as neutrino oscillation, which is the focus of this thesis. The phenomenology of neutrino oscillations in vacuum and in matter will be discussed, followed by a review of neutrino oscillation experiments. The final part of this chapter will be a brief discussion of the unresolved questions about neutrinos. Much of the discussion in this chapter is inspired by the book on neutrino physics by Giunti and Kim [3].

2.1 Neutrinos in the Standard Model

The Standard Model of particle physics is a theory that describes (1) the nature of the three fundamental forces in nature, namely the strong, weak, and electromagnetic forces (with the only exception being the gravitational force), and (2) the elementary particles that participate in these three types of interactions. Figure 2.1 shows the Standard Model particles and their

properties.

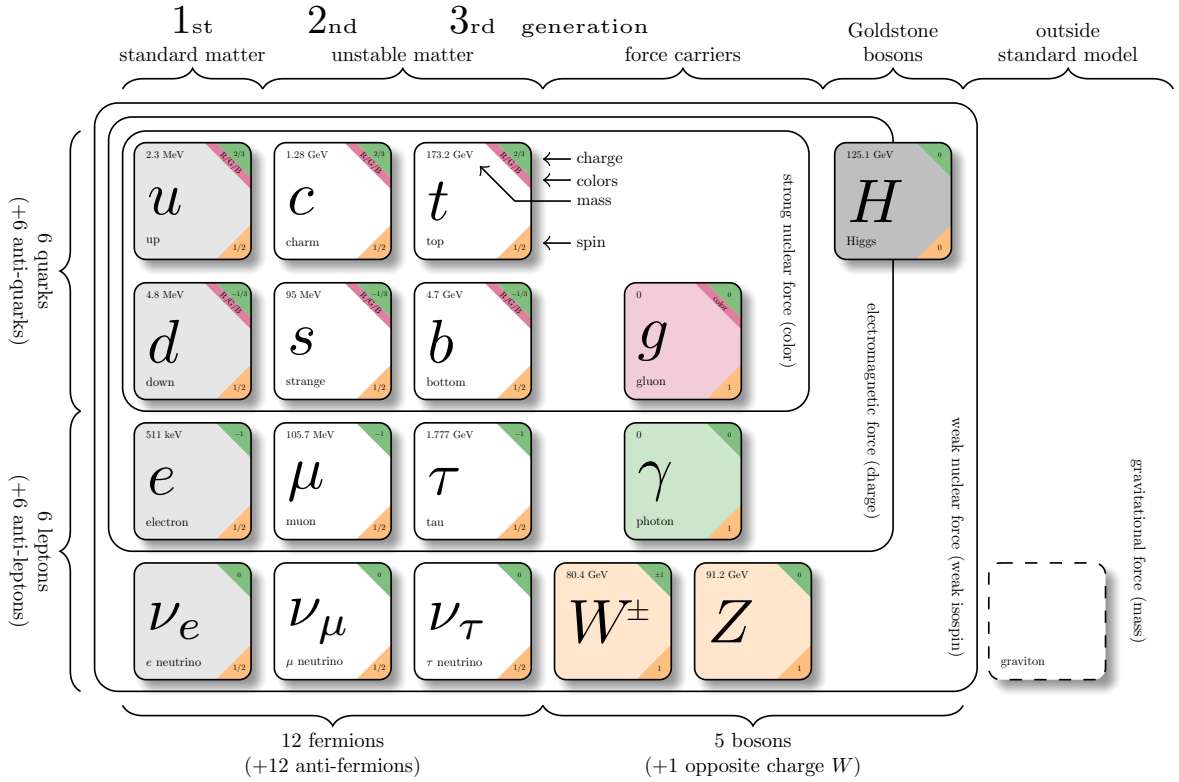

Figure 2.1: The Standard Model of particle physics [4].

There are two families of fermions – quarks and leptons, each having three generations. Quarks have fractional charge of $+2/3$ (u, c, t) or $-1/3$ (d, s, b). Aside from electric charge and spin, quarks also carry a "color" charge and participate in strong interactions. There are three charged leptons: e^-, μ^- and τ^-, and three corresponding neutral leptons ν_e, ν_μ and ν_τ. Both the charged and neutral leptons can participate in weak interactions, and only the charged leptons can directly participate in electromagnetic interactions as neutrinos do not carry electric charge. The three generation of quarks and leptons have mass in ascending order in magnitude. In the original Standard Model, neutrinos are massless – a prediction which has been disproven by the observation of neutrino oscillations (more discussion in section 2.2).

The three fundamental forces are mediated by the spin-1 gauge bosons: gluons (strong force), photon (electromagnetic force) and the $W^\pm/Z$ bosons (weak force). In the language of modern quantum field theory, the Standard Model Lagrangian is invariant under local $SU(3)\times SU(2)_L\times U(1)$ transformations and Lorentz transformations. The strong interactions

between quark-gluon and gluon-gluon are invariant under $SU(3)$, therefore the gauge bosons – gluons are massless. The electromagnetic and weak interactions are governed by the $SU(2)_L \times U(1)$ symmetry. Unlike gluons, the $W^{\pm}$ and Z bosons are massive. This is due to the gauge fields coupling to the Higgs field, and the spontaneous breaking of gauge symmetry gives rise to the $W^{\pm}$ and Z mass as well as the mass of the fermions. The Standard Model does not predict the mass of the fermions, weak interaction bosons or the mass of the Higgs; their masses have been determined through experiments over the years.

The Standard Model has withstood the tests by decades of experiments, which all culminated in the discovery of the Higgs boson in 2012. In fact, that neutrinos have mass is the only laboratory-observed phenomenon not predicted by the Standard Model. What also puzzles physicists is the smallness of the neutrino mass, even when compared to the lightest charged fermion. The remainder of this chapter will focus on the theory and experimental tests of neutrinos.

2.1.1 Neutrino interactions in the Standard Model

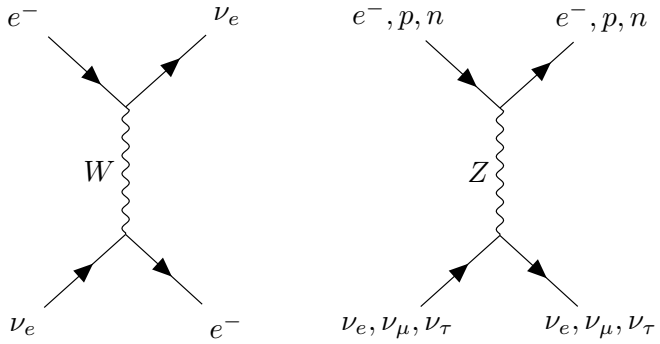

Figure 2.2: The Feynman diagrams of neutrino charged current (left) and neutral current (right) interactions with electrons. Time is to the right in the case of neutrino scattering in matter.

According to the Standard Model, neutrinos are neutral, left-handed fermions. Neutrinos can participate in two types of weak interactions: charged current (CC) interaction mediated by a $W^{\pm}$ boson, and neutral current (NC) interaction mediated by a Z boson. Figure 2.2 shows an example of the Feynman diagrams of neutrino CC and NC interactions. Similar diagrams can be made for neutrino-quark interactions as well. Each generation of leptons also carry a unique lepton number, e.g. the lepton of number of $e^-(e^+)$ and $\nu_e(\bar{\nu}_e)$ is $L_e =$

$1(-1), L_\mu = 0, L_\tau = 0$. Both the CC and NC neutrino interactions must conserve each lepton number L_e, L_μ, L_τ.

2.1.2 Path to understanding neutrinos

The experimental discovery of neutrinos and the measurement of their properties have not come easily. Neutrinos were first postulated by W. Pauli in 1930 to provide an explanation of the observed continuous electron energy spectrum in the beta-decay process. However, due to its extremely small interaction cross section, it was not until the 1950s when F. Reines and C. Cowan devised a way [5] to detect neutrinos via inverse beta-decay:

$$\bar{\nu}_e + p \rightarrow e^+ + n \tag{2.1}$$

The experiment was conducted at the Savannah River Plant next to a nuclear reactor which was the source of $\bar{\nu}_e$. A sandwich configuration of water tank and liquid scintillator was used. The positron from the CC interaction would produce a scintillation signal by slowing down and annihilating with an electron, which is detected by photomultiplier tubes. They also added neutron absorbing material $CdCl_2$, which can absorb a neutron and emit a delayed photon separated from the the prompt scintillation signal by a few microseconds, thus giving them a better identification of the $\bar{\nu}_e$ interactions. This was the first confirmation of the existence of neutrinos.

In the 1950s, a series of discoveries led to the understanding of parity violation and subsequently the $V - A$ structure of the weak interaction. In this theory, all neutrinos are left-handed and all antineutrinos are right-handed. In 1958, M. Goldhaber et.al. [6] first proved that electron neutrinos are indeed left-handed particles. They used the following electron capture process:

$$^{152}\mathrm{Eu} + e^- \rightarrow {}^{152}\mathrm{Sm}^* + \nu_e \rightarrow {}^{152}\mathrm{Sm} + \nu_e + \gamma\ (960\ \mathrm{keV}) \tag{2.2}$$

Because of the momentum conservation laws, the ν_e and the de-excitation γ always have the same helicity. Therefore, one could infer the neutrino helicity by measuring the circular polarization of the γ. The excited state of $^{152}\mathrm{Sm}^*$ has a life-time of $3 \pm 1 \times 10^{-14}$ sec, which means the γ emission happens before the nucleus comes to a rest, therefore allowing the γ to gain momentum at the same direction as the $^{152}\mathrm{Sm}^*$ recoil. This allows the γ to pass through a magnet in either the up or down direction, and then be resonantly scattered from a Sm_2O_3

scatterer. By measuring the photon count with up and down magnet configurations, they found that the result was consistent with ν_e being 100% left-handed [1].

In the original $V - A$ theory, the leptons and their associated neutrinos are assigned a lepton number $L = 1$ while the anti particles have $L = -1$; and this lepton number should be conserved in weak interactions. This would allow the reaction $\mu \to e+\gamma$ to occur; however, the experimental limits were orders of magnitude smaller than what the original theory predicted. This led to the conclusion that different generation of leptons should have different lepton numbers, automatically making $\mu \to e + \gamma$ forbidden. B. Pontecorvo [7] suggested that if one could show that the ν_μ produced in $\pi^+ \to \mu^+ + \nu_\mu$ cannot induce a e^-, then ν_μ and ν_e must be different particles. In 1962, L. Lederman et al. [8] used the Alternating Gradient Synchrotron (AGS) at Brookhaven National Laboratory (BNL) to generate a 15 GeV proton beam, which is then collided with a beryllium target to produce pions. A 13.5 m steel wall was used to absorb the remaining protons as well as the pions which have not decayed, only letting neutrinos pass through. A 10-ton spark chamber was situated downstream of the beam to detect the leptons produced from neutrino CC interactions. They found that all the observed signal events were muons and not electrons, and thusly concluded that ν_μ and ν_e are indeed different particles. The significance of this experiment also lies in the fact that it provided the foundation for the neutrino beam used in modern long baseline experiments, which will be discussed in Chapter 3.

The discovery of τ lepton in 1975 [9] strongly suggested that a third generation neutrino, ν_τ, must also exist. However, the detection of ν_τ through CC interactions was no easy task because the τ lepton has a mean lifetime of $\sim 2.9 \times 10^{-13}$ sec and decays hadronically $> 60\%$ of the time. In 2000, the DONUT experiment was the first to establish the existence of ν_τ [10]. They used a 800 GeV proton beam from the Fermilab Tevatron interacting in a meter long tungsten beam dump to generate hadrons. The emulsion detector was situated 36 m downstream from the beam dump, and was shielded by magnets, concrete, iron and lead to reduce the other products from the proton interactions. The primary source of ν_τ is from the decay of $D_s^\pm$ into $\tau^\pm$ and $\overset{(-)}{\nu}_\tau$ and the subsequent $\tau^\pm$ decays with $\overset{(-)}{\nu}_\tau$. They identified 4 τ decay events with no other lepton at the decay vertex, against a total background estimate of 0.34 ± 0.05 events.

Following the discoveries of the b quark (1977) [11] and t quark (1995) [12] [13], all building blocks of the Standard Model (except for the Higgs) are completed with three generations

[1] In retrospect, the Goldhaber experiment should not be considered conclusive evidence that all neutrinos are left-handed. Experiments have been done since to probe the $V + A$ component of the weak interaction and no evidence of its existence has been found so far.

of quarks and leptons. The natural question then was whether there are more generations to come. This question was answered in 1989 by the MARK-II experiment at SLC and the LEP experiments at CERN using the invisible decay of the Z boson ($Z \to \nu\bar{\nu}$) [14] [15] [16]. Figure 2.3 shows latest constraint on the number of light neutrino species through a combined analysis of LEP data, which is found to be 2.9840 ± 0.0082.

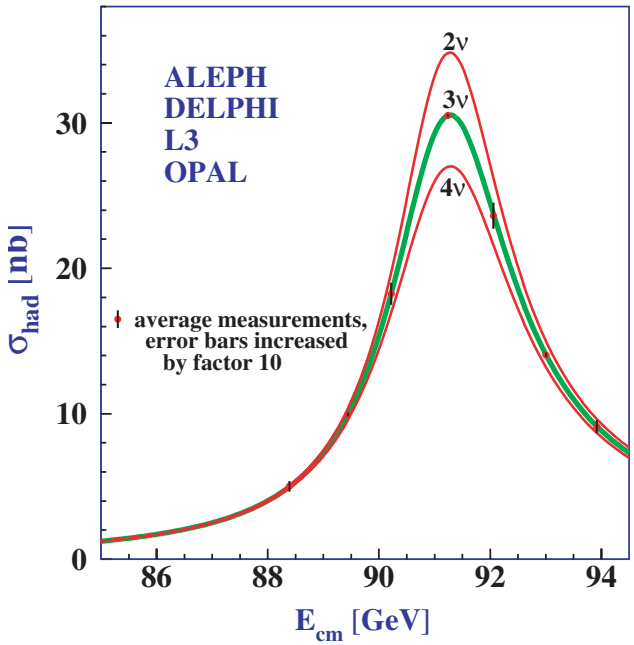

Figure 2.3: Measurements of the hadron production cross section around the Z resonance. The curves show the predicted cross section for two, three and four neutrino species with SM couplings and negligible mass. Figure is taken from the reference [17].

2.2 Neutrino oscillations

As mentioned in the previous section, in the original Standard Model ν_e, ν_μ and ν_τ are massless, left-handed, neutral fermions that only interact weakly. However, it was later found through a phenomenon called neutrino oscillation that neutrinos have non-zero mass. This section will discuss the phenomenology of neutrino oscillations.

2.2.1 Three-flavor neutrino mixing

Consider a neutrino of flavor α and momentum $\vec{p}$ created in a charged current weak interaction. It is described by the flavor eigenstate

$$|\nu_\alpha\rangle = \sum_k U^*_{\alpha k}|\nu_k\rangle \quad (\alpha = e, \mu, \tau) \tag{2.3}$$

where $|\nu_k\rangle$ are the mass eigenstates, and $U^*_{\alpha k}$ describes the mixing between the flavor eigenstates and the mass eigenstates. Note that the summation in Eq. 2.3 is not restricted to three: more than three mass eigenstates are allowed provided that the additional neutrinos are sterile neutrinos which do not participate in any Standard Model interactions. If sterile neutrinos exist, and they mix with the active neutrinos, their existence can be inferred from the disappearance of active neutrinos.

Assuming there are no sterile neutrinos, the unitary matrix U can be parameterized by three mixing angles $\theta_{12}, \theta_{13}, \theta_{23}$, one Dirac phase δ_{CP} and two Majorana phases α_{21}, α_{31}:

$$\begin{aligned} U &= \begin{pmatrix} U_{e1} & U_{e2} & U_{e3} \\ U_{\mu 1} & U_{\mu 2} & U_{\mu 3} \\ U_{\tau 1} & U_{\tau 2} & U_{\tau 3} \end{pmatrix} \\ &= \begin{pmatrix} 1 & 0 & 0 \\ 0 & c_{23} & s_{23} \\ 0 & -s_{23} & c_{23} \end{pmatrix} \begin{pmatrix} c_{13} & 0 & s_{13}e^{-i\delta_{CP}} \\ 0 & 1 & 0 \\ -s_{13}e^{-i\delta_{CP}} & 0 & c_{13} \end{pmatrix} \begin{pmatrix} c_{12} & s_{12} & 0 \\ -s_{12} & c_{12} & 0 \\ 0 & 0 & 1 \end{pmatrix} \begin{pmatrix} 1 & 0 & 0 \\ 0 & e^{-i\frac{\alpha_{21}}{2}} & 0 \\ 0 & 0 & e^{-i\frac{\alpha_{31}}{2}} \end{pmatrix} \end{aligned} \tag{2.4}$$

where $c_{ij} = \cos\theta_{ij}$, $s_{ij} = \sin\theta_{ij}$. Note that the last diagonal matrix would only exist if neutrinos are Majorana fermions, and not if they are Dirac fermions. The three mixing angles can and have been measured by various neutrino experiments which will be discussed in section 2.3. The mixing matrix is also called the PMNS matrix in honor of Pontecorvo, Maki, Nakagawa and Sakata. Pontecorvo first predicted neutrino oscillation, and Maki-Nakagawa-Sakata first introduced the mixing matrix in the two-generation scenario.

2.2.2 Neutrino oscillations in vacuum

The neutrinos observed experimentally are typically produced in the flavor eigenstates, but they propagate in the mass eigenstates:

$$|\nu_k(t)\rangle = e^{-iE_k t}|\nu_k\rangle \tag{2.5}$$

where E_k is the energy. The flavor eigenstate in Eq. 2.3 then propagates as

$$|\nu_\alpha(t)\rangle = \sum_k U^*_{\alpha k} e^{-iE_k t}|\nu_k\rangle \tag{2.6}$$

Because U is a unitary matrix, the mass eigenstates can be written as a superposition of the flavor eigenstates:

$$|\nu_k\rangle = \sum_\alpha U_{\alpha k}|\nu_\alpha\rangle \tag{2.7}$$

Substituting Eq. 2.7 into Eq. 2.6

$$|\nu_\alpha(t)\rangle = \sum_\beta \left(\sum_k U^*_{\alpha k} e^{-iE_k t} U_{\beta k} \right) |\nu_\beta\rangle \tag{2.8}$$

After the neutrino travels for $t > 0$, the probability of it transitioning into a flavor state $|\nu_\beta\rangle$ is given by

$$P^{\nu_\alpha \to \nu_\beta}(t) = |\langle \nu_\beta | \nu_\alpha(t)\rangle|^2 = \sum_{k,j} U^*_{\alpha k} U_{\beta k} U_{\alpha j} U^*_{\beta j} e^{-i(E_k - E_j)t} \tag{2.9}$$

Unless the mixing matrix U is diagonal (i.e. no mixing between mass eigenstates and flavor eigenstates) or the neutrino masses are degenerate, $P^{\nu_\alpha \to \nu_\beta}(t)$ can change as a function of time. For ultra-relativistic neutrinos (as is the case in neutrino oscillation measurements), the approximation below can be made:

$$E_k = \sqrt{\vec{p}^2 + m_k^2} \simeq E + \frac{m_k^2}{2E} \tag{2.10}$$

The neutrino travel time t is usually unknown in oscillation experiments; however, one can make the approximation $L = ct$ for ultra-relativistic neutrinos, where L is the distance the neutrino travels from its production to its detection and $c = 1$ is the speed of light. Therefore, the oscillation probability can be written as a function of the neutrino energy E

and propagation length L

$$P^{\nu_\alpha \to \nu_\beta}(E, L) = \sum_{k,j} U^*_{\alpha k} U_{\beta k} U_{\alpha j} U^*_{\beta j} e^{-i\frac{\Delta m^2_{kj} L}{2E}} \tag{2.11}$$

where $\Delta m^2_{kj} = m^2_k - m^2_j$. It can be seen from Eq. 2.11 that the Majorana phase parameters in Eq. 2.3 does not appear in the oscillation probability, i.e. neutrino oscillation measurements cannot measure the Majorana phase of the mixing matrix. However, the three rotational angles $\theta_{12}, \theta_{13}, \theta_{23}$ and the mass squared difference Δm^2_{ij} can be measured through neutrino oscillations if at least one $\Delta m^2_{ij} \neq 0$.

For antineutrinos, because the flavor eigenstates and mass eigenstates are related by

$$|\bar{\nu}_\alpha\rangle = \sum_k U_{\alpha k} |\bar{\nu}_k\rangle \tag{2.12}$$

Following the same derivation as neutrinos, the antineutrino oscillation probability is

$$P^{\bar{\nu}_\alpha \to \bar{\nu}_\beta}(E, L) = \sum_{k,j} U_{\alpha k} U^*_{\beta k} U^*_{\alpha j} U_{\beta j} e^{-i\frac{\Delta m^2_{kj} L}{2E}} \tag{2.13}$$

It is instructive to re-write Eq. 2.11 and Eq. 2.13 as follows:

$$\begin{aligned} P^{\nu_\alpha \to \nu_\beta}(E, L) = \delta_{\alpha\beta} &- 4 \sum_{k>j} \mathfrak{Re}\left[U^*_{\alpha k} U_{\beta k} U_{\alpha j} U^*_{\beta j}\right] \sin^2\left(\frac{\Delta m^2_{kj} L}{4E}\right) \\ &+ 2 \sum_{k>j} \mathfrak{Im}\left[U^*_{\alpha k} U_{\beta k} U_{\alpha j} U^*_{\beta j}\right] \sin\left(\frac{\Delta m^2_{kj} L}{2E}\right) \end{aligned} \tag{2.14}$$

$$\begin{aligned} P^{\bar{\nu}_\alpha \to \bar{\nu}_\beta}(E, L) = \delta_{\alpha\beta} &- 4 \sum_{k>j} \mathfrak{Re}\left[U^*_{\alpha k} U_{\beta k} U_{\alpha j} U^*_{\beta j}\right] \sin^2\left(\frac{\Delta m^2_{kj} L}{4E}\right) \\ &- 2 \sum_{k>j} \mathfrak{Im}\left[U^*_{\alpha k} U_{\beta k} U_{\alpha j} U^*_{\beta j}\right] \sin\left(\frac{\Delta m^2_{kj} L}{2E}\right) \end{aligned} \tag{2.15}$$

Eq. 2.14 and Eq. 2.15 are only different in the sign of the third term. If $\beta = \alpha$, the survival probabilities $P^{\nu_\alpha \to \nu_\alpha}(E, L) = P^{\bar{\nu}_\alpha \to \bar{\nu}_\alpha}(E, L)$. For $\beta \neq \alpha$, the transition probabilities $P^{\nu_\alpha \to \nu_\beta}(E, L) \neq P^{\bar{\nu}_\alpha \to \bar{\nu}_\beta}(E, L)$, unless the third terms in Eq. 2.14 and Eq. 2.15 are zero. It indicates that a potential CP asymmetry can be measured via the transition probabilities of neutrino appearance (but not neutrino disappearance) [2].

[2]This phenomenological treatment of neutrino oscillations would only apply if the energy and momentum of the particles produced from the neutrino interactions are not measured to such precision that the emitted

2.2.3 Neutrino oscillations in matter

When active neutrinos propagate through matter, the oscillation probabilities can be modified due to the forward elastic weak CC and NC scatterings of (anti)electron neutrinos (similar to the light refraction in a medium). Figure 2.2 shows the Feynman diagrams of the forward elastic scattering processes. Assume the matter has a constant density, the charged current interaction shown on the left gives rise to a potential in the effective CC Hamiltonian

$$V_{CC} = \sqrt{2} G_F N_e \tag{2.16}$$

where G_F is the Fermi constant, and N_e is the electron density. The effective potential for anti neutrinos would take a negative sign of Eq. 2.16. The potentials are very small in regular matter because

$$\sqrt{2} G_F \simeq 7.63 \times 10^{-14} \frac{\text{eV cm}^3}{N_A} \tag{2.17}$$

where N_A is the Avogadro's number. The neutral current forward elastic scattering processes also gives rise to a potential; however, it will not be discussed here because it does not modify the oscillation probabilities as NC interactions do not distinguish flavors.

To understand how the matter density modifies the oscillation probabilities, consider the following total Hamiltonian in matter

$$\mathcal{H} = \mathcal{H}_0 + \mathcal{H}_I \tag{2.18}$$

where $\mathcal{H}_0$ is the vacuum Hamiltonian and $\mathcal{H}_I$ is the matter potential Hamiltonian:

$$\mathcal{H}_0 |\nu_k\rangle = E_k |\nu_k\rangle, \qquad \mathcal{H}_I |\nu_\alpha\rangle = V_\alpha |\nu_\alpha\rangle \tag{2.19}$$

In the three-neutrino framework, $\mathcal{H}_I = \text{diag}\,(V_{CC}, 0, 0)$.

Although it is rather complicated to obtain the three-flavor neutrino oscillation probabilities in matter, it is both straightforward and instructive to look at the case of two-flavor neutrino mixing. Consider two flavors ν_e, ν_μ, and two mass eigenstates ν_1, ν_2. The evolution

massive neutrino can be determined through energy and momentum conservation laws. A more rigorous way is to treat neutrino fields as wave packets which are localized at production, and propagate between production and detection with a group velocity close to the speed of light [3].

of the neutrino fields is described by the following Schroedinger equation [3]:

$$i\frac{\mathrm{d}}{\mathrm{d}t}\begin{pmatrix}\nu_e\\ \nu_\mu\end{pmatrix} = \left(\frac{\Delta m^2}{4E}\right)\begin{pmatrix}-\cos 2\theta + \frac{4EV_{CC}}{\Delta m^2} & \sin 2\theta\\ \sin 2\theta & \cos 2\theta\end{pmatrix}\begin{pmatrix}\nu_e\\ \nu_\mu\end{pmatrix} \tag{2.20}$$

One can revise Eq. 2.20 by subtracting a diagonal matrix without changing the physics:

$$i\frac{\mathrm{d}}{\mathrm{d}t}\begin{pmatrix}\nu_e\\ \nu_\mu\end{pmatrix} = \left(\frac{\Delta m^2}{4E}\right)\begin{pmatrix}-\cos 2\theta + A & \sin 2\theta\\ \sin 2\theta & \cos 2\theta - A\end{pmatrix}\begin{pmatrix}\nu_e\\ \nu_\mu\end{pmatrix} \tag{2.21}$$

where $A = \frac{2\sqrt{2}G_F N_e E}{\Delta m^2}$. Define the following effective parameters θ_M and Δm^2_M:

$$\sin 2\theta_M = \frac{\sin 2\theta}{\sqrt{\sin^2 2\theta + (\cos 2\theta - A)^2}} \tag{2.22}$$

$$\Delta m^2_M = \Delta m^2\sqrt{\sin^2 2\theta + (\cos 2\theta - A)^2} \tag{2.23}$$

Eq. 2.21 can be re-diagonalized as

$$i\frac{\mathrm{d}}{\mathrm{d}t}\begin{pmatrix}\nu_e\\ \nu_\mu\end{pmatrix} = \left(\frac{\Delta m^2_M}{4E}\right)\begin{pmatrix}-\cos 2\theta_M & \sin 2\theta_M\\ \sin 2\theta_M & \cos 2\theta_M\end{pmatrix}\begin{pmatrix}\nu_e\\ \nu_\mu\end{pmatrix} \tag{2.24}$$

This is similar to the case without the matter potential with effective mixing angle θ_M and mass splitting Δm^2_M. Therefore, the oscillation probability follows

$$P^{\nu_e\to\nu_\mu}(L,E) = \sin^2 2\theta_M \sin^2\left(\frac{\Delta m^2_M L}{4E}\right) \tag{2.25}$$

One interesting consequence from Eq. 2.25 is that oscillation enhancement can happen when $A = \cos 2\theta$, even when the mixing angle θ is very small (in which case the oscillation effects are small in vacuum). It also follows that long baseline or high matter density is required in order to observe the matter effect. Furthermore, Eqs. 2.22 and 2.23 indicate that $P^{\nu_e\to\nu_\mu} \neq P^{\bar{\nu}_e\to\bar{\nu}_\mu}$ in matter, even if the mixing matrix is real. For anti neutrinos, $A = -\frac{2\sqrt{2}G_F N_e E}{\Delta m^2}$, in which case the matter resonance can only happen if $\Delta m^2 < 0$. In other words, depending on

[3] It follows from

$$U^\dagger \mathcal{H}_0 U = \begin{pmatrix}E + \frac{m_1^2+m_2^2}{4E} & 0\\ 0 & E + \frac{m_1^2+m_2^2}{4E}\end{pmatrix} + \left(\frac{\Delta m^2}{4E}\right)\begin{pmatrix}-\cos 2\theta & \sin 2\theta\\ \sin 2\theta & \cos 2\theta\end{pmatrix}$$

where $\Delta m^2 = m_2^2 - m_1^2$. The diagonal term in $U^\dagger \mathcal{H}_0 U$ does not contribute to oscillation and can be ignored in the calculation.

the mass hierarchy, the matter effect resonance can only happen to either neutrino or anti neutrino, but not to both. The matter effect is also called the MSW effect in honor of Mikheev, Smirnov and Wolfenstein who first theorized it.

2.3 Experimental measurements of neutrino oscillations

The mixing angles – $\theta_{12}, \theta_{13}, \theta_{23}$, the Dirac phase δ_{CP}, and the neutrino masses are fundamental parameters in the Standard Model which have to be measured experimentally. Neutrino oscillation experiments are sensitive to the PMNS matrix (except for the Majorana phases) as well as Δm^2_{21} and Δm^2_{32}. Table 2.1 shows the latest limits on these parameters measured by various experiments. Normal hierarchy (NH) refers to the case where $m_3 > m_2 > m_1$, and inverted hierarchy (IH) $m_2 > m_1 > m_3$.

$\sin^2\theta_{12}$	0.307 ± 0.013
$\sin^2\theta_{13}$	$(2.10 \pm 0.11) \times 10^{-2}$
$\sin^2\theta_{23}$	0.51 ± 0.04 (Normal hierarchy)
	0.50 ± 0.04 (Inverted hierarchy)
Δm^2_{21}	$(7.53 \pm 0.18) \times 10^{-5}$ eV^2
$\lvert\Delta m^2_{32}\rvert$	$(2.45 \pm 0.05) \times 10^{-3}$ eV^2 (Normal hierarchy)
	$(2.52 \pm 0.05) \times 10^{-3}$ eV^2 (Inverted hierarchy)

Table 2.1: Current measurements of neutrino mixing angles and mass squared difference, taken from [18].

Because $|\Delta m^2_{32}| >> \Delta m^2_{21}$ and neutrino oscillation probabilities depend on $\Delta m^2_{ij} L/E$ ($\approx 1.27 \times \frac{\Delta m^2}{\mathrm{eV}^2} \frac{L}{\mathrm{km}} \frac{\mathrm{GeV}}{E}$) as shown by Eq. 2.14, experiments can use neutrinos with different energy and different distances from the source such that the desired oscillation parameters can be measured through the leading oscillation effect.

For example, a typical long baseline reactor neutrino experiment has neutrino energy $E_{\bar{\nu}_e} \sim 1$ MeV and $L \sim 1$ km, resulting in the following leading-term oscillation probability

$$P(\bar{\nu}_e \to \bar{\nu}_e) \simeq 1 - \sin^2 2\theta_{13} \sin^2 \frac{\Delta m^2_{ee} L}{4E} \tag{2.26}$$

where Δm^2_{ee} ($\simeq \cos^2_{12} |\Delta m^2_{31}| + \sin^2\theta_{12} |\Delta m^2_{32}|$) is used as an effective parameter as $|\Delta m^2_{31}|$ and $|\Delta m^2_{32}|$ are indistinguishable at this baseline. Therefore, such an experiment is ideal for the measurement of θ_{13} and Δm^2_{ee}. If such a reactor neutrino experiment is conducted tens

of kilometers away from the source, then the leading term becomes

$$P(\bar{\nu}_e \to \bar{\nu}_e) \simeq 1 - \cos^2\theta_{13}\sin^2 2\theta_{12}\sin^2\frac{\Delta m^2_{21}L}{4E} \tag{2.27}$$

in which case θ_{12} and $|\Delta m^2_{21}|$ can be measured. The same experiment can also be conducted ~ 10 meters away from the reactor to make it a sterile neutrino search experiment, as the observation of a disappearance signal requires the mass splitting to be $\Delta m^2 \gtrsim 0.1$ eV^2.

There are many ways in which neutrino oscillation experiments can be classified. This section opts to categorize experiments by their neutrino sources, which determines the neutrino energy and therefore the neutrino detection technology. For man-made neutrino sources, i.e. accelerator neutrinos and reactor neutrinos, we also have a choice of the baseline and therefore the physics that can be probed. Only one or two experiments in each category will be discussed; however, it must be noted that there are many past and present experiments in each category.

2.3.1 Solar neutrinos

Nuclear reactions in the Sun produce neutrinos with energy $E_\nu \sim 1$ eV. In spite of the high density in the solar core, the neutrinos can mostly pass through due to the extremely small cross section, making solar neutrinos a powerful tool to study the solar core and star evolution. Figure 2.4 shows the *pp* chain (left) and the CNO cycle (right) of the solar thermonuclear reactions which power the Sun. Both processes release energy and produce ν_e. Figure 2.5 shows the energy spectra of the solar ν_e flux from the *pp* and CNO chains as predicted by the standard solar model described in [19].

The so-called "solar neutrino problem", i.e. a deficit in the measured solar neutrino flux relative to the standard solar model prediction, was first observed by the Homestake experiment in 1968 [20] and confirmed by the Kamiokande experiment [21] in the late 1980s, and later the GALLEX/GNO [22] and SAGE [23] experiments in the 1990s. The Super-Kamiokande experiment (1998) [24] and SNO experiment (2001) [25] and confirmed that what was thought to be an error in the theory of thermonuclear energy generation in stars was actually a manifestation of neutrino oscillations.

The Sudbury Neutrino Observatory (SNO) is a spherical (6 m in radius) Cherenkov detector loaded with 1 kiloton of heavy water instrumented with 9,456 20-cm photomultiplier

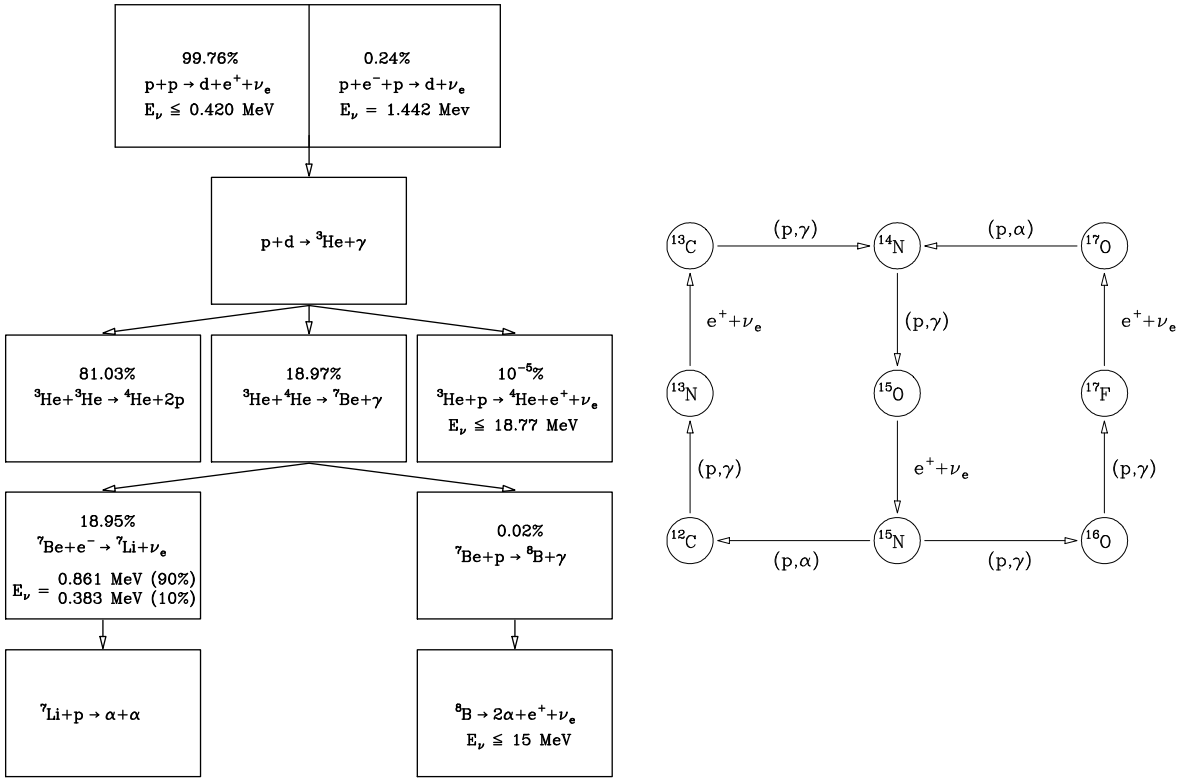

Figure 2.4: The *pp* chain (left) and the CNO cycle (right) of the solar thermonuclear reactions. The processes which produce ν_e are indicated. Figures are taken from [19].

tubes (PMTs) [26]. It detects solar neutrinos through the following reactions

$$\begin{aligned} \text{CC}: &\quad \nu_e + d \to p + p + e^- \\ \text{NC}: &\quad \nu_\alpha + d \to p + n + \nu_\alpha,\ \alpha = e, \mu, \tau \\ \text{ES}: &\quad \nu_\alpha + e^- \to \nu_\alpha + e^-,\ \alpha = e, \mu, \tau \end{aligned} \tag{2.28}$$

The CC interaction can only happen to ν_e, but the NC and elastic scattering (ES) can happen to all three flavors. The first results from the D_2O phase confirmed the previously observed solar ν_e deficit. It observed $1967.7^{+61.9}_{-60.9}$ CC events, $263.6^{+26.4}_{-25.6}$ ES events and $576^{+49.5}_{-48.9}$ NC events, which correspond to the following measured fluxes of ^{8}B ν_e (in unit of 10^6 cm^{-2}s^{-1}):

$$\begin{aligned} \Phi_{CC} &= 1.776^{+0.06}_{-0.05}(\text{stat.})^{+0.09}_{-0.09}(\text{syst.}) \\ \Phi_{ES} &= 2.39^{+0.24}_{-0.23}(\text{stat.})^{+0.12}_{-0.12}(\text{syst.}) \\ \Phi_{NC} &= 5.09^{+0.44}_{-0.43}(\text{stat.})^{+0.46}_{-0.43}(\text{syst.}) \end{aligned} \tag{2.29}$$

One can translate the fluxes measured through CC/NC/ES processes into electron (ϕ_e) and

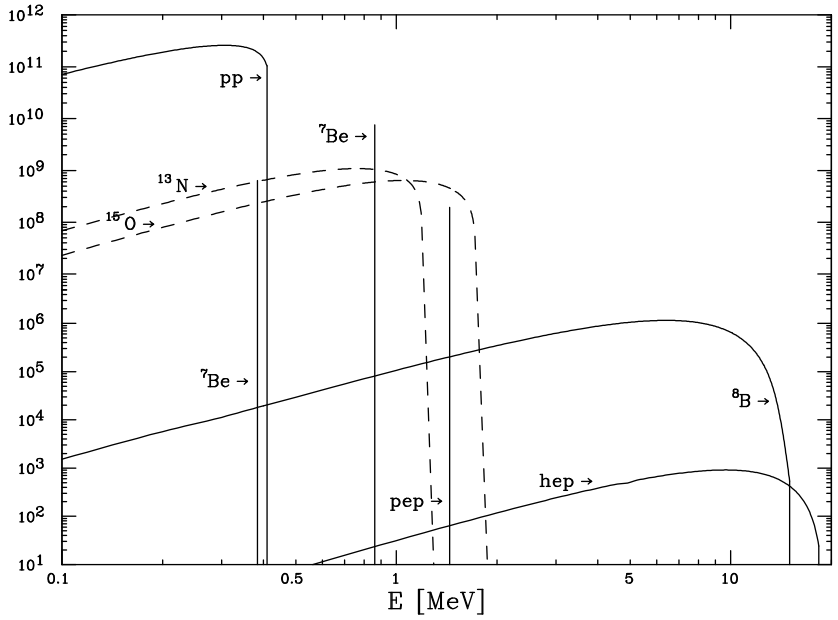

Figure 2.5: The predicted solar neutrino flux from the *pp* and CNO chains. Figure is taken from [19]. The unit fo flux is $\mathrm{cm}^{-2}\mathrm{s}^{-1}\mathrm{MeV}^{-1}$ for the continuous spectra and $\mathrm{cm}^{-2}\mathrm{s}^{-1}$ for the discrete lines.

non-electron ($\phi_{\mu\tau}$) components:

$$\begin{aligned} \phi_e &= 1.776^{+0.06}_{-0.05}(\text{stat.})^{+0.09}_{-0.09}(\text{syst.}) \\ \phi_{\mu\tau} &= 3.41^{+0.45}_{-0.45}(\text{stat.})^{+0.48}_{-0.45}(\text{syst.}) \end{aligned} \tag{2.30}$$

The $\phi_{\mu\tau}$ is 5.3σ above zero, which is direct evidence of the solar neutrino flavor change. Figure 2.6 shows $\phi_{\mu\tau}$ v.s. ϕ_e from CC, NC and ES measurements compared with the standard solar model (SSM) prediction. The three bands intercept with one another, and agree with the the SSM prediction. This is the first evidence that the SSM is correct, and that the observation is consistent with neutrino flavor transformation.

As the ν_e produced in the solar core propagate through the Sun, two processes can affect the probability of observing ν_e and ν_μ at the surface of the Sun – neutrino oscillation and the MSW effect (described in section 2.2.3). The derivation of $P(\nu_e \to \nu_e)$ of solar neutrinos is complicated as the solar mass density is not a constant; thus the derivation will be not given here (a brief review can be found in [3]). Figure 2.7 shows the solar ν_e survival probability at Earth distance as a function of neutrino energy assuming $\sin^2\theta_{12} = 0.308$ and $\Delta m^2_{21} = 7.54 \times 10^{-}5$ eV^2 [18]. The MSW effect dominates at high energy; at low energy, the

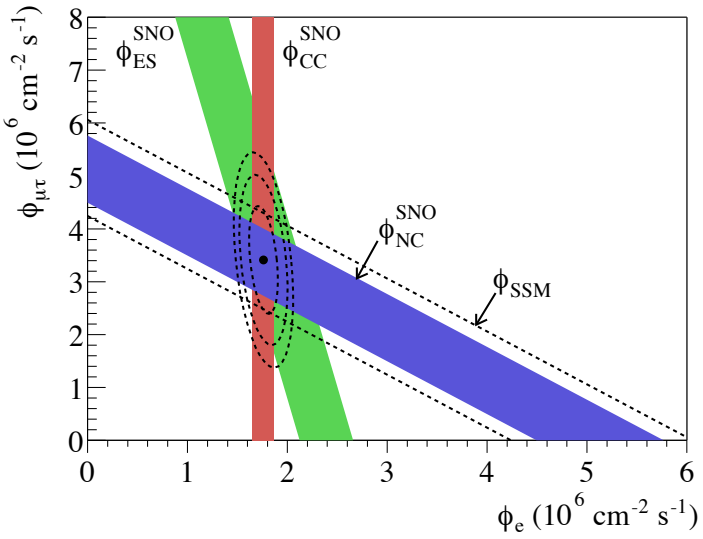

Figure 2.6: The $\nu_\mu + \nu_\tau$ flux v.s. ν_e flux from CC, NC and ES measurements compared with standard solar model prediction (dashed lines) [27]. The width of the bands represents the 1σ error. Figure is taken from [25]

MSW effect gives way to (averaged) vacuum oscillation.

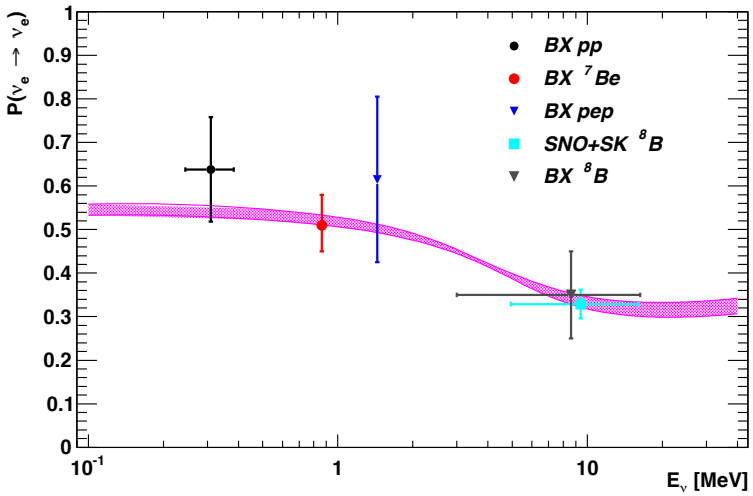

Figure 2.7: Electron neutrino survival probability as a function of neutrino energy according to the MSW-LMA (large mixing angle) model (figure is taken from [18]). The low-energy region (< 1 MeV) of the curve corresponds to *pp* and ^{7}Be neutrinos, and the high-energy region ^{8}B neutrinos, assuming $\sin^2\theta_{12} = 0.308, \Delta m^2_{21} = 7.54 \times 10^{-}5\text{eV}^2$. The width of the curve indicates the $\pm 1\sigma$ errors from uncertainties in the oscillation parameters [28]. BX stands for the Borexino experiment.

2.3.2 Atmospheric neutrinos

The primary cosmic rays – mostly protons, also He, and other heavier nuclei – strike the nuclei in the Earth atmosphere as they enter and produce hadronic showers. The hadrons (mostly $\pi^{\pm}$, also $K^{\pm}$ etc.) then undergo the following decays:

$$\begin{aligned} \pi^+ &\to \mu^+ + \nu_\mu,\ \mu^+ \to e^+ + \nu_e + \bar{\nu}_\mu \\ \pi^- &\to \mu^- + \bar{\nu}_\mu,\ \mu^- \to e^- + \bar{\nu}_e + \nu_\mu \end{aligned} \tag{2.31}$$

Therefore, in the absence of neutrino oscillation, the flux ratio $(f^{\nu_e} + f^{\bar{\nu}_e})/(f^{\nu_\mu} + f^{\bar{\nu}_\mu})$ should be $\sim 1/2$ at low energy ($E_\nu \lesssim 1$ GeV), and decreases as the energy goes up as the high energy muons can reach the ground before decaying. The neutrino energy can range from tens of MeV to a few TeV. However, as observed by the Super-K in 1998, the aforementioned flux ratio does not hold, and that there is an up-down asymmetry in observed $\nu_\mu, \bar{\nu}_\mu$ events, as shown by Figure 2.8. The Super-K detector technology and its neutrino detection will be discussed in detail in section 3.2.

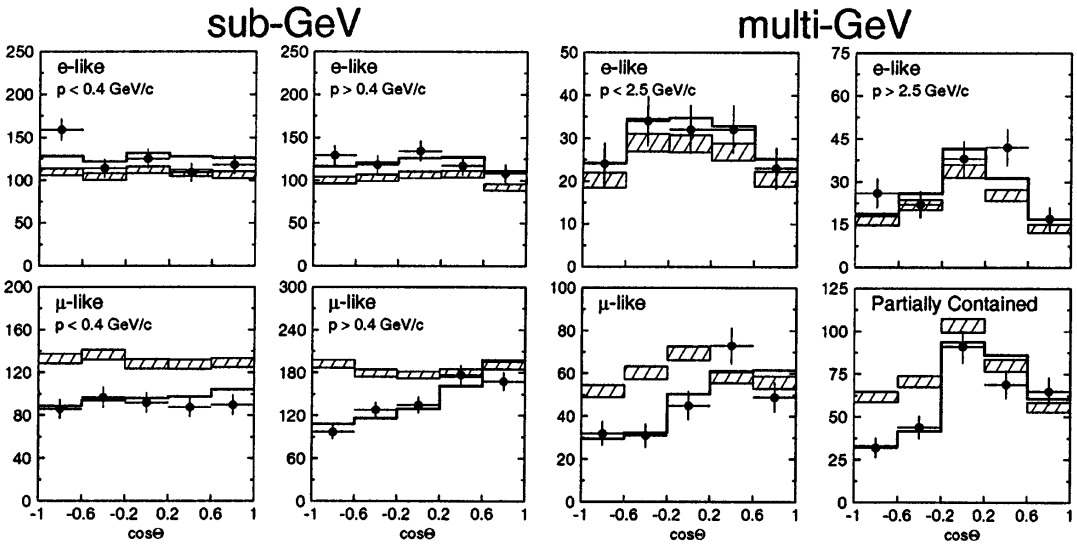

Figure 2.8: Super-Kamiokande atmospheric neutrino zenith angle distributions of μ-like and e-like events for the sub-GeV and multi-GeV data sets. $\cos\theta$ is the zenith angle in the detector frame. $\cos\theta > 0$ for upward-going events, and $\cos\theta < 0$ for downward-going events. The hatched region shows the expectation in the absence of neutrino oscillation. The bold line is the best-fit with $\nu_\mu \leftrightarrow \nu_\tau$ oscillation. Figure is taken from [29] (1998).

This can be explained by the neutrino oscillation process $\nu_\mu \leftrightarrow \nu_\tau$, the leading term of

which is

$$P(\nu_\mu \to \nu_\mu) \simeq 1 - \sin^2 2\theta_{23} \sin^2 \frac{\Delta m^2_{32} L}{4E} \tag{2.32}$$

In Figure 2.8, $\cos\theta > 0$ for upward-going events, and $\cos\theta < 0$ for downward-going events; the μ-like and e-like events can be considered as a good proxy of the ν_μ and ν_e events, respectively. The downward-going neutrinos typically travel $\sim$ 10 km before reaching the detector; however, the upward-going neutrinos traverse the Earth and have a baseline of $\sim 10^4$ km. This renders a higher disappearance probability for the $\nu_\mu, \bar{\nu}_\mu$ coming from below the detector, hence the deficit in event rate with $\cos\theta < 0$. The up-down asymmetry is defined as $A = (U-D)/(U+D)$ where U is the number of events with $-1 < \cos\theta < -0.2$ and D is the number of events with $0.2 < \cos\theta < 1$. It was found that $A = 0.65 \pm 0.05(\text{stat.}) \pm 0.08(\text{syst.})$ for μ-like events – 6.8σ from zero (in 1998). The atmospheric neutrino disappearance observed by Super-K is the first direct evidence that neutrinos have non-zero mass – a prerequisite for neutrino oscillations.

Atmospheric neutrinos have been used to measure oscillation parameters Δm^2_{32}, $\sin^2\theta_{23}$, and δ_{CP} [30]; they also provide the possibility of probing mass hierarchy. Recall from Eq. 2.25, that the resonant enhancement of $\nu_e \leftrightarrow \nu_\mu$ or $\bar{\nu}_e \leftrightarrow \bar{\nu}_\mu$ oscillation can happen when the resonance condition is met, depending on the mass hierarchy. For atmospheric neutrinos, the matter effect resonance can happen for upward going neutrinos with energy between $2 \sim 10$ GeV. Figure 2.9 shows the neutrino/antineutrino appearance probabilities at Super-K. If the mass hierarchy is normal, then the resonant enhancement in oscillation probability can only be seen in the $\nu_e \leftrightarrow \nu_\mu$ channel but not the $\bar{\nu}_e \leftrightarrow \bar{\nu}_\mu$ channel; and vice versa. This can provide an additional handle on the mass hierarchy – an excess of upward-going ν_e events with $2 \lesssim E \lesssim 10$ GeV would hint at normal hierarchy; on the other hand, an excess of upward-going $\bar{\nu}_e$ events with $2 \lesssim E \lesssim 10$ GeV would be a signature of inverted hierarchy. Figure 2.10 shows the up/down asymmetry for the multi-GeV ν_e and $\bar{\nu}_e$ samples at SK, and the difference between normal and inverted hierarchy. The multi-GeV ν_e and $\bar{\nu}_e$ samples at Super-K are statistically limited, and only a weak preference for the normal hierarchy is obtained from an analysis of Super-K data [30].

2.3.3 Accelerator neutrinos

The same process that produces atmospheric neutrino can be used to produce neutrinos in a controllable way. A typical accelerator based neutrino beam is produced by bombarding high energy protons onto a carbon or beryllium target, which produces hadrons; the hadrons

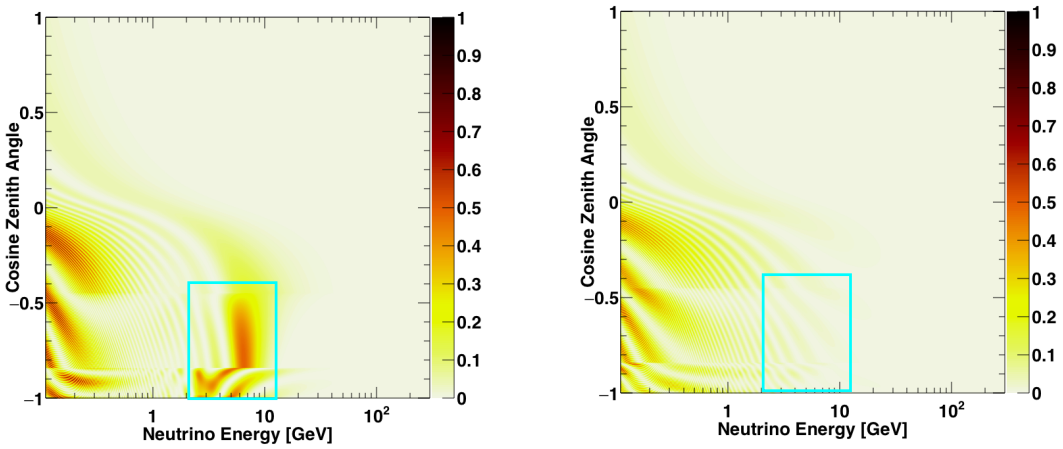

Figure 2.9: The atmospheric neutrino $P(\nu_\mu \to \nu_e)$ (left) and $P(\bar{\nu}_\mu \to \bar{\nu}_e)$ (right) oscillation probabilities as a function of neutrino energy and cosine zenith angle at Super-K, assuming $\Delta m^2_{32} = 2.5 \times 10^-3$ eV^2, $\sin^2\theta_{23} = 0.5$, $\sin^2\theta_{13} = 0.0219$ and $\delta_{CP} = 0$. Cyan boxes are the matter effect resonance region. Figure is taken from [30].

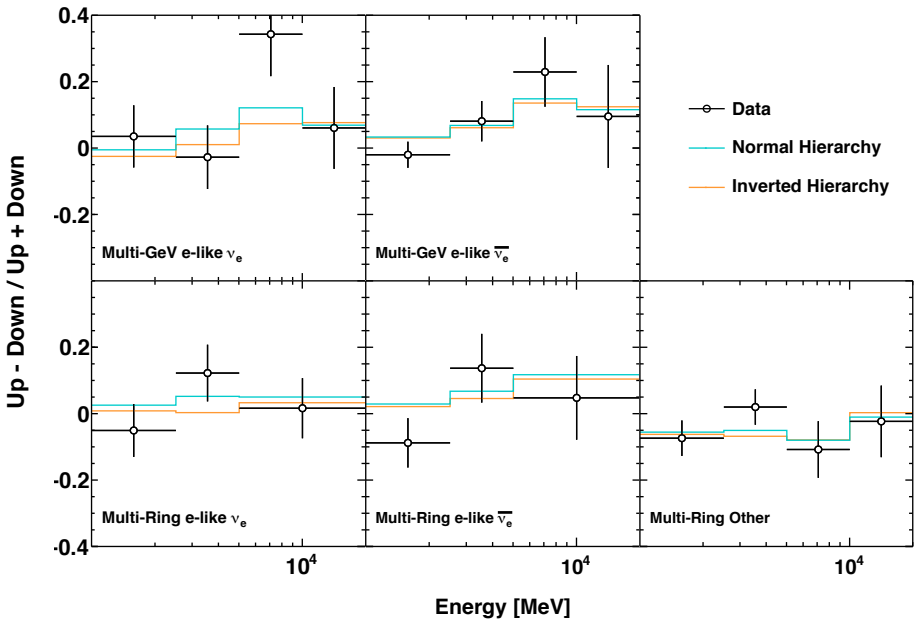

Figure 2.10: Upward- ($\cos\theta < -0.4$) to downward-going ($\cos\theta > 0.4$) asymmetry as a function of energy. The best fit from the normal hierarchy hypothesis is shown in cyan, and inverted hierarchy hypothesis shown in orange. The ν_e and $\bar{\nu}_e$ samples are separated statistically. Figure is taken from reference [30].

then decay into predominantly muon and anti muon neutrinos. A contemporary neutrino beam also comes with a series of magnetic horns just downstream of the target, which focuses

either positively or negatively charged hadrons to select predominantly muon neutrinos or muon antineutrinos. A beam dump is needed before the neutrino detector to absorb the surviving protons and hadrons. Typical neutrino beams have a neutrino energy of ~ 1 GeV, and can be tuned by the proton beam energy and the angle at which the neutrino detector is placed with respect to the beam center.

Short baseline accelerator neutrino experiments such as MicroBooNE [31] has a detector, or a series of detectors ~ 1 km away from the beam target to probe sterile neutrinos with $\Delta m^2 \gtrsim 0.1$ eV^2. A typical long baseline accelerator neutrino experiment such as T2K and NOνA has a near detector a few hundred meters away from the target and a far detector which is placed hundreds of kilometers away from the target. The neutrino fluxes are measured once at the near detector before they oscillate, and then again at the far detector. The oscillation effect can be inferred by comparing the near and far detector spectra:

$$N_{\nu_\alpha}^{far}(E) = \sum_\beta \Phi_\beta^{near}(E) \cdot P(\nu_\beta \to \nu_\alpha) \cdot \sigma_{\nu_\alpha}(E) \cdot \eta_{\nu_\alpha}(E) \tag{2.33}$$

where $N_{\nu_\alpha}^{far}(E)$ is the measured ν_α event energy spectrum at the far detector, $\Phi_\beta^{near}(E)$ is the ν_β energy spectrum at the near detector, $\sigma_{\nu_\alpha}(E)$ is the ν_α interaction cross section, $\eta_{\nu_\alpha}(E)$ is the far detector efficiency and $P(\nu_\beta \to \nu_\alpha)$ is the oscillation probability. The experimental setup of T2K will be discussed in section 3.1.

Long baseline experiments are capable of probing a large number of different aspects of neutrino oscillations, including the observation of neutrino appearances, mass hierarchy and δ_{CP}, which are not easily accessible by other types of oscillation experiments. T2K was the first experiment to observe ν_e appearance from a ν_μ beam [32], and the first to reject the CP-conserving values $\delta_{CP} = 0, \pi$ at 2σ confidence level [2]. T2K has also made the most precise measurement on $\sin^2\theta_{23}$ and Δm^2_{32} [1]. Mass hierarchy is not the strong suit of T2K as its peak energy is ~ 0.6 GeV and the baseline is 295 km. The NOνA experiment [33], with its higher energy and longer baseline, has a better sensitivity to the mass hierarchy. The future long baseline experiment DUNE and Hyper-Kamkamiokande will be able to determine the mass hierarchy and whether there is CP-violation in the lepton section for a large phase space of true δ_{CP} [34].

2.3.4 Reactor neutrinos

Reactor neutrino experiments utilize the thermonuclear reactions in nuclear reactors as the source of $\bar{\nu}_e$. The $\bar{\nu}_e$ can be detected though inverse beta-decay in the detectors. Reactor experiments have been used to successfully measure Δm^2_{21} (very long baseline: KamLAND [35]) and θ_{13} (long baseline: Daya Bay [36], RENO [37], Double CHOOZ [38], etc.).

In 2012, the Daya Bay experiment was the first to definitively measure reactor $\bar{\nu}_e$ disappearance and therefore a non-zero θ_{13}; its latest measurement of $\sin^2 2\theta_{13}$ is still the most precise in the world [39]. It uses the Daya Bay nuclear power complex with 8 identical detector modules, three of which are $\sim 1500 - 1900$ m away from the reactors (far detector), and the rest have baselines of $\sim 350 - 550$ m (near detector). The oscillation probability $P(\bar{\nu}_e \to \bar{\nu}_e)$ can be obtained by comparing the near and far detector spectra. The detector modules are filled with liquid scintillator and instrumented with PMTs. They are submerged in 10m deep water pools (also instrumented with PMTs) to shield the neutrino detectors from natural radiations and veto cosmic muons. The e^+ from the inverse beta-decay generates a prompt scintillation signal, which enables a calorimetric reconstruction of the neutrino energy: $E_{prompt} = T_{e^+} + 2m_e$, where m_e is the electron mass, and T_{e^+} is the kinetic energy of the positron. The $2m_e$ in the equation follows from positron annihilation. And based on the inverse beta-decay kinematics, the initial $\bar{\nu}_e$ energy can be accurately reconstructed as $E_{\bar{\nu}_e} \simeq E_{prompt} + 0.8$ MeV. The neutron from the inverse beta-decay thermalizes in the detector, and is captured on a scintillator nucleus on a time scale of ~ 100 μs. The excited nucleus then immediately emits one or more γ's, which also get detected. This prompt-delayed signature can efficiently distinguish the reactor neutrino interaction signal from backgrounds.

The KamLAND experiment [35] is located in the same cavern as the Kamiokande experiment. It consists of a transparent balloon filled with 1 kton ultra-pure scintillator, which is held inside a spherical tank filled with buffer oil and instrumented with 1,879 PMTs on the inner wall; the tank is inside of a 3.2-kton cylindrical water Cherenkov outer detector. The neutrino energy reconstruction method is similar to that used by the Daya Bay experiment. The KamLAND detector is surrounded by 55 nuclear power units at varying distances (the flux weighted average distance is ~ 180 km). This enables the observation of the oscillation effects due to Δm^2_{21}. Figure 2.11 shows the KamLAND L/E spectrum and Δm^2_{21}-θ_{12} results overlaid with results from solar neutrino measurement. The oscillation effects can be clearly seen; the dip at $L/E \sim 50$km/MeV indicates that $|\Delta m^2_{21}| \sim 10^{-4}$ eV^2. Historically the KamLAND measurement of $|\Delta m^2_{21}|$ proved that the MSW-LMA (Large Mixing Angle) solution to the solar neutrino problem is correct.

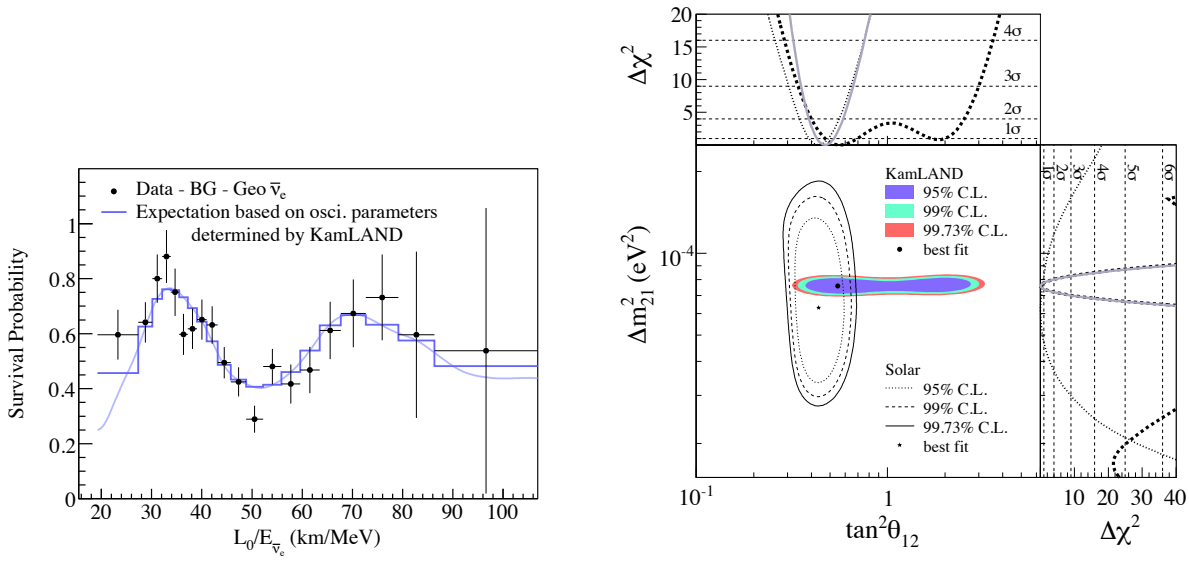

Figure 2.11: KamLAND results. Left: ratio of the background and geo-neutrino-subtracted $\bar{\nu}_e$ spectrum to the expectation for no-oscillation as a function of L/E. Right: allowed region for neutrino oscillation parameters from KamLAND and solar neutrino experiments; the side panels show the $\Delta\chi^2$ of KamLAND (dashed), solar (dotted) and them combined (solid) constraint on the parameters individually. Figures are taken from [35]

2.4 Unanswered questions about neutrinos

Despite the progress made in the past few decades, such things as the exact neutrino masses and their Dirac/Majorana nature, are still unknown. This chapter will give a brief discussion on some of the unanswered questions about neutrinos and their experimental prospect.

2.4.1 Neutrino mixing and mass hierarchy

The neutrino mixing angles in the PMNS framework are fundamental parameters in the Standard Model that should be measured. In addition, the existence of CP-violation in the lepton sector could provide an answer to the matter-antimatter asymmetry in the universe [40]. The next generation neutrino experiment such as the Deep Underground Neutrino Experiment (DUNE) [34], the Hyper-Kamiokande (HK, Hyper-K) experiment [41], and the Jiangmen Underground Neutrino Observatory (JUNO) [42] will have the potential of determining the mass hierarchy (DUNE, HK and JUNO) and leptonic CP-violation (DUNE and HK), and also improving the measurement precision of the other oscillation parameters.

Before the next-generation neutrino experiments start data taking, improvements can also be made by combining the data sets from existing experiments. Different types of oscillation experiments are complimentary to one another. For example, θ_{13} is measured most precisely by reactor experiments, whereas Δm^2_{ij} are measured most precisely by long baseline accelerator and very long baseline reactor experiments. Even for experiments sensitive to the same parameters, they generally measure the same oscillations with different baseline and energy, with which different systematic errors are often associated. Therefore, combining the existing data sets could potentially improve the measurement precision as all parameters often contribute to oscillations in a convoluted way within a given experiment. One of such combined analyses is presented in the reference [43]; Figure 2.12 shows their combined fit results of δ_{CP} [4]. One may notice that a reactors+LBL combined analysis does not necessarily improve the constraint on δ_{CP} compared to reactors+T2K. This is because the constraint on δ_{CP} is mainly driven by T2K, which favors maximal CP-violation; even if the true $\delta_{CP} = 270°$, the data sets from the other experiments do not necessarily favor the same δ_{CP} value due to statistical fluctuation; thus, the combined fit can yield a weaker constraint. Nevertheless, combined analyses represent at the moment the best chance in measuring δ_{CP} and mass hierarchy.

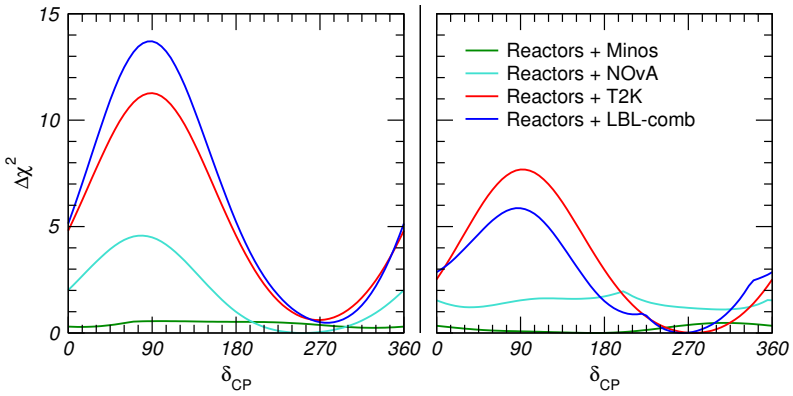

Figure 2.12: Global fit result on δ_{CP} in [43]. Left figure is for inverted hierarchy and right figure is for normal hierarchy. Long baseline (LBL) experiments T2K, NOνA and MINOS are shown separately from the LBL-reactors combined fit results. The $\Delta\chi^2$ of each experiment is defined with respect to the global minimum of the two mass hierarchies.

[4]This combined analysis does not accurately take into account the correlations between each experiment due to cross-sections and detector effects. It serves a different purpose than the combined analysis presented in this thesis.

2.4.2 Neutrino mass

As previously discussed, neutrino oscillation experiments are only sensitive to the mass squared differences Δm^2_{ij}, but not the absolute values m_i. The mass of neutrino has been measured in both model-independent and model-dependent approaches, by beta-decay experiments and cosmological measurements respectively [5]. Using the Cosmic Microwave Background data collected by the Planck experiment and assuming the existence of three light massive neutrinos and the Λ CDM model, the Planck collaboration reported that the limits on the sum of neutrino masses are $\sum_j m_j < (0.340 - 0.715)$ eV at 95% C.L. [44].

The best model-independent limit on electron neutrino (effective) mass comes from measuring the end-point of the electron momentum spectrum (i.e. the kinematical difference from the massless neutrino scenario) in the tritium beta-decay process:

$$^3\mathrm{H} \rightarrow {}^3\mathrm{He} + e^- + \bar{\nu}_e \tag{2.34}$$

which has a Q-value of 18.574 keV. Due to the neutrino mixing, the effective electron neutrino mass it can measure is

$$m^2_\beta = \sum_k |U_{ek}|^2 m^2_k \tag{2.35}$$

where U_{ek} are the PMNS matrix elements. In the standard three-flavor paradigm,

$$m^2_\beta = m^2_1 \cos^2\theta_{12}\cos^2\theta_{13} + m^2_2 \sin^2\theta_{12}\cos^2\theta_{13} + m^2_3 \sin^2\theta_{13} \tag{2.36}$$

The Troitsk experiment [45] has provided the most stringent limit on m_β [6]:

$$m_\beta < 2.05 \text{ eV, at 95\% C.L.} \tag{2.37}$$

In the future, the successor of the experiments at Mainz [46] and Troitsk – the KATRIN experiment [47] will reach the sensitivity of $m_\beta \sim 0.20$ eV.

[5] Pion and tau decays, as well as supernova neutrino measurements also provided limits on neutrino mass, but their upper limits are much higher than the constraints from tritium beta-decay measurements or cosmological data.

[6] The smallness of neutrino mass has made physicists ponder whether neutrinos gain mass through the same Higgs mechanism as other charged fermions. In fact, many believe that the small neutrino masses are the remnant of physics beyond the Standard Model. The most celebrated theories are based on the *see-saw* mechanism (a brief discussion can be found in section 6.4.6 of [3]), which also stipulates the existence of Majorana neutrinos.

2.4.3 Nature of neutrinos

In 1937, E. Majorana pointed out that there could exist particles whereby a particle is the same of its charge conjugate, which implies the equality of a particle and its antiparticle. Among all the known Standard Model fermions, only neutrinos can be Majorana particles due to their neutral electric charge. The only practical way of probing the Majorana nature of neutrinos is via the neutrinoless double beta-decay ($2\beta_{0\nu}$-decay) process:

$$\begin{aligned} \mathcal{N} &\to \mathcal{N}(A, Z+2) + 2e^- \quad (2\beta^-_{0\nu}) \\ \mathcal{N} &\to \mathcal{N}(A, Z-2) + 2e^+ \quad (2\beta^+_{0\nu}) \end{aligned} \tag{2.38}$$

$2\beta_{0\nu}$-decay breaks the lepton number conservation by two units and therefore is forbidden in the Standard Model; however, it can happen if neutrinos are Majorana particles as shown by the Feynman diagram in Figure 2.13. In the case of Majorana neutrinos, the process is allowed because $\nu_e = \bar{\nu}_e$ and $m_{\nu_e} \neq 0$, which means the upper vertex can emit a $\bar{\nu}_e$ with negative helicity with a relative amplitude of m_{ν_e}/E_{ν_e} which is then absorbed by the lower vertex.

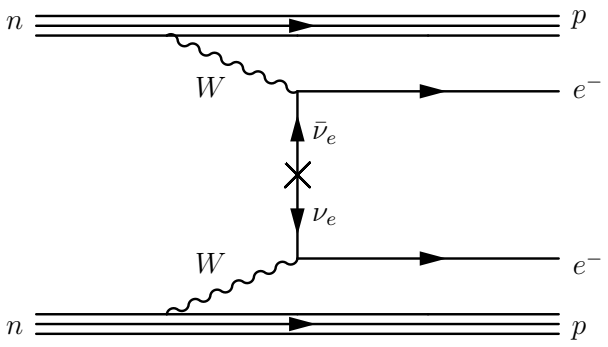

Figure 2.13: The Feynman diagram of $2\beta_{0\nu}$-decay. It is forbidden if neutrinos are Dirac particles but allowed if they are Majorana particles ($\nu_e = \bar{\nu}_e$).

Should $2\beta_{0\nu}$-decay be discovered, the measurement of its decay lifetime can also provide information on the Majorana CP-violating phase and the neutrino mass scale [7]. In the

[7] $2\beta_{0\nu}$-decay can be used to infer neutrino mass only if neutrinos are Majorana particles.

three-flavor paradigm, the effective Majorana mass in $2\beta_{0\nu}$-decay is

$$\begin{aligned} m_{2\beta} &= \sum_{k=1}^{3} U_{ek}^2 m_k \\ &= |U_{e1}|^2 m_1 + e^{i\alpha_{21}} |U_{e2}|^2 m_2 + e^{i(\alpha_{31}-2\delta)} |U_{e3}|^2 m_3 \end{aligned} \tag{2.39}$$

where α_{21} and α_{31} are the Majorana phases in Eq. 2.4. $m_{2\beta}$ not only depends on the mass terms m_i, but also the mixing angles and the CP-violating phases. Currently the most stringent constraint on $m_{2\beta}$ is claimed by the KamLAND-zen experiment at $T_{1/2}^{0\nu}(^{136}\text{Xe}) > 1.07 \times 10^{26}$y at 90% CL, which implies that the effective Majorana mass $m_{2\beta} \lesssim 0.061 \sim 0.165$ eV, with the uncertainty largely coming from the nuclear matrix element calculations [48]; other leading $2\beta_{0\nu}$-decay experiments include GERDA [49] and EXO [50].

Chapter 3

The T2K experiment and the Super-Kamiokande experiment

This chapter will describe the configurations of the T2K beam-line, the near detectors and the far detector, Super-K. The content of this chapter follows from [51], [52] and [53], in which more detailed information of the experimental apparatus can be found.

The T2K (Tokai-to-Kamioka) experiment [54] is a long baseline neutrino oscillation experiment located in Japan. It was designed for the precision measurement of neutrino oscillation parameters ($\delta(\Delta m^2_{32}) \sim 10^{-4}$ eV^2, $\delta(\sin^2 2\theta_{32}) \sim 0.01$), and to observe electron neutrino appearance from a muon neutrino beam if $\sin^2 2\theta_{13} > 0.008$ [1]. The intense neutrino beam also enables the study of neutrino interactions from CCQE and resonant pion production to deep inelastic scattering. With the many successes of reactor experiments came the realization that θ_{13} is relatively large, making the measurement of leptonic CP-violation possible. In fact, by running the neutrino beam in both ν_μ-dominated mode and $\bar{\nu}_\mu$-dominated mode, T2K has rejected the CP-conserving values $\delta_{CP} = 0, \pi$ at 2σ CL [2].

Figure 3.1 shows a schematic view of the T2K experiment. Neutrinos are produced at J-PARC (Japan Proton Accelerator Research Complex in Tokai, Ibaraki), and measured by the near detectors at 280 meters away before they oscillate. The neutrinos then journey through mainland Japan to reach Super-K on the west of Japan where the oscillated neutrino fluxes are measured again. As discussed in section 2.3, this near-far comparison is crucial for the measurement of neutrino oscillation parameters.

[1] T2K was proposed long before before θ_{13} was found to be relatively large.

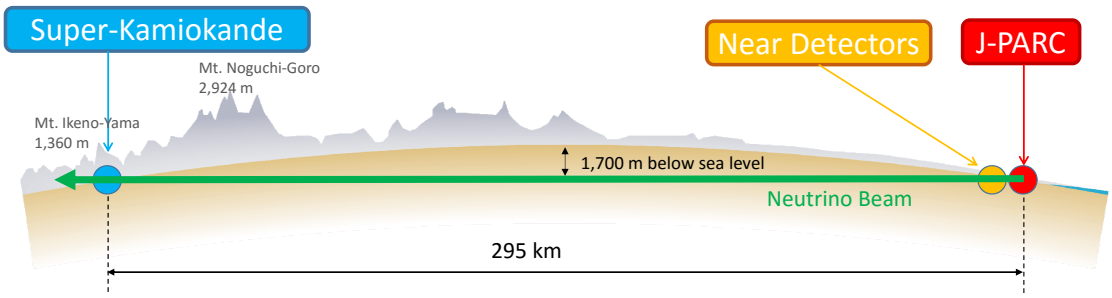

Figure 3.1: A schematic view of the T2K experiment. The green line indicates the neutrino propagation from its production at J-PARC through the near detectors to the far detector Super-Kamiokande. The baseline is 295 km.

T2K uses the MW-class [2] proton synchrotron at J-PARC to generate a 30 GeV proton beam. The collision between the proton beam and a graphite target produces hadrons which are focused by three magnetic horns and then decay in the decay volume. The pion decays shown in Eq. 2.31 are the dominant processes that produce beam neutrinos. T2K is the first experiment to adopt the off-axis technique, whereby the far detector does not align with the beam center. The off-axis angle is set at 2.5° (tunable to 2.0°) such that the neutrino energy is peaked at ~ 0.6 GeV, which maximizes the oscillation effects at 295 km baseline. It also eliminates much of the background in the appearance channel by reducing the intrinsic $\nu_e/\bar{\nu}_e$ contamination and the NC background rate. The lefthand side plot in Figure 3.2 shows the neutrino flux at 2.5°, 2.0° and 0° off-axis angle overlaid with oscillation probabilities. The flux at a higher off-axis angle is narrower than the on-axis flux due to the fact that the neutrino energy only depends weakly on the pion momentum for non-zero off-axis angles. The righthand-side plot in Figure 3.2 shows the neutrino energy as a function of the pion energy for three different off-axis angles based on the following equation:

$$E_\nu = \frac{m_\pi^2 - m_\mu^2}{2(E_\pi - p_\pi \cos\theta)} \tag{3.1}$$

where a maximum exists for a non-zero θ. Therefore, the allowed range of neutrino energy from off-axis pion decays is tightened regardless of the pion energy; the peak of the neutrino energy spectrum is tunable via the tuning of the off-axis angle.

The near detector complex consists of on-axis detectors and off-axis detectors both housed

[2] T2K has achieved stable running at ~480 kW; Main Ring upgrade is scheduled for 2019 to increase the beam power.

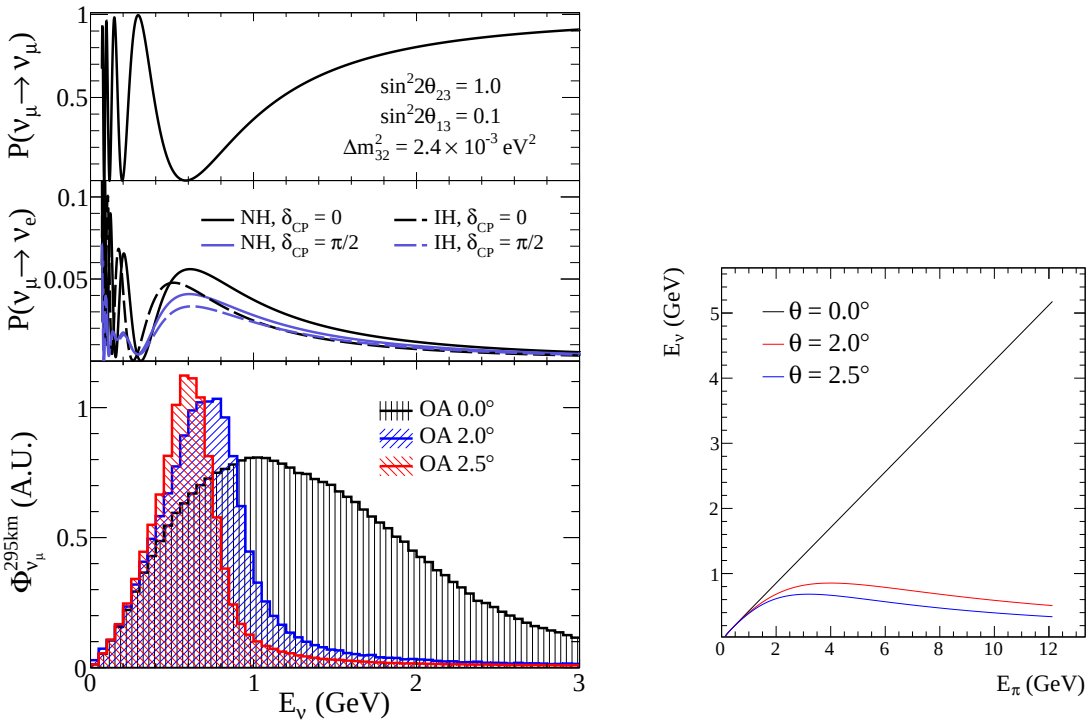

Figure 3.2: The T2K flux for different off-axis angles (left) and the neutrino energy as a function of the pion energy in the dominant pion decay processes which produce the beam neutrinos.

in the near detector hall shown in Figure 3.3. The on-axis INGRID detector has a structure of iron/scintillator sandwich and is used to measure the neutrino beam direction and beam profile. The off-axis ND280 detector is made of three sub-detectors: the PØD detector for the measurement of π^0; the gaseous time projection chambers (TPC) and the fine grained detectors (FGD) with excellent tracking capability. The sub-detectors are surrounded by electromagnetic calorimeters (ECal), and they are all placed inside a 0.2 T magnetic field generated by a magnet which also functions as part of a side muon range detector (SMRD). ND280 is used to measure the muon neutrino flux and electron neutrino contamination in the same direction as the far detector; it is also capable of measuring neutrino interaction cross sections in a wide energy range.

The far detector Super-K lies in the Mozumi mine of the Kamioka Mining and Smelting Company under Mt. Ikenoyama, with an overburden of 1000 m of rock (2700 meters-water-equivalent). Figure 3.4 shows the diagram of Super-K. It is a cylindrical water Cherenkov detector of 39 m in diameter and 42 m in height with a total mass of 50 kilotons. It is separated into two optically isolated regions: the inner detector (ID) and the outer detector

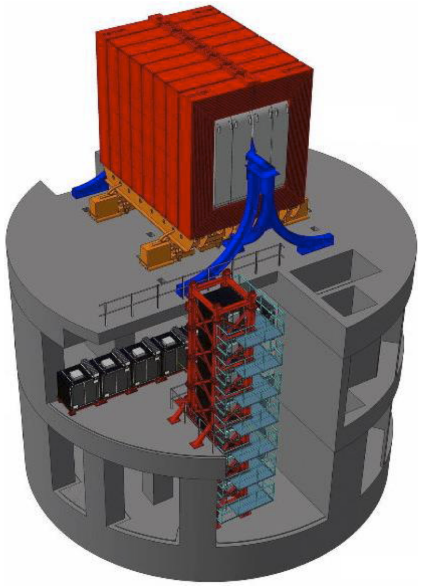

Figure 3.3: The ND280 detector complex. The off-axis ND280 detectors are on the top (enclosed in a magnetic) and the on-axis INGRID detector is on the bottom.

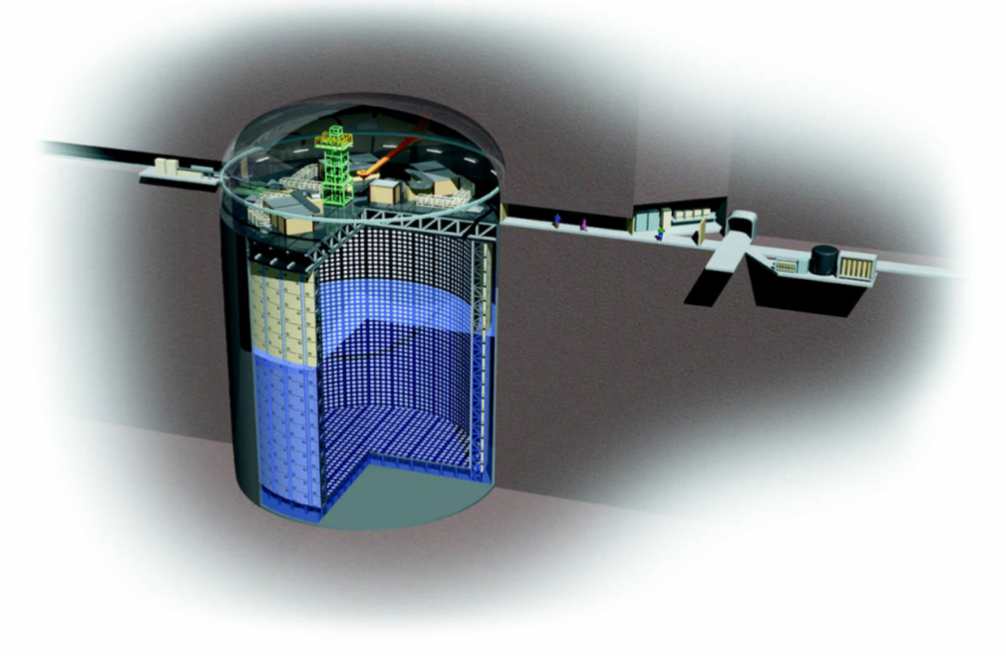

Figure 3.4: A schematic view of the Super-Kamiokande detector.

(OD); both are instrumented with PMTs. The OD is used to veto cosmic muons and exiting particles and the ID is used to study the interactions inside by measuring the Cherenkov light radiated by charged particles. Aside from functioning as the far detector for T2K, Super-K

also functions as an observatory for solar, atmospheric, and supernova neutrinos. Searches for proton decays [55] and WIMPs [56] are also being conducted at Super-K.

3.1 The T2K experiment

3.1.1 J-PARC

J-PARC consists of three accelerators: a linear accelerator (LINAC), a rapid-cycling synchrotron (RCS) and the main ring (MR) synchrotron. The LINAC accelerates a H^- beam up to 400 MeV, which is converted to H^+ at the RCS injection. The beam is then accelerated to 3 GeV by the RCS. About 5% of the bunches are diverted to the MR [3], in which the beam is accelerated to 30 GeV. Table 3.1 shows the design parameters of the J-PARC MR in the fast extraction mode [4], in which eight circulating proton bunches are extracted within a single turn.

Circumference	1567 m
Designed beam power	$\sim$ 750 kW
Beam kinetic energy	30 GeV
Beam intensity	$\sim 3 \times 10^{14}$ protons/spill
Spill cycle	$\sim$ 0.5 Hz
Number of bunches per spill	8
RF frequency	$1.67 - 1.72$ MHz
Spill width	~ 5 μsec

Table 3.1: The machine design parameters of the J-PARC Main Ring [53].

3.1.2 Neutrino beamline

Figure 3.5 shows the schematic of the sequential primary and secondary beamlines. The protons are extracted from the MR into the primary beamline, where they are redirected towards the direction of Kamioka. The beam is focused onto the target in the final focusing section by ten normal conducting magnets. The intensity, position, profile and loss of the

[3] The rest are supplied to the muon and neutron beamline for material and life science research.

[4] There are two extraction points in the MR: slow extraction for the hadron beamline and the fast extraction for the neutrino beamline.

proton beam in the primary beamline are monitored by a series of beam monitors in order to maintain a stable neutrino beam production and minimize the beam loss.

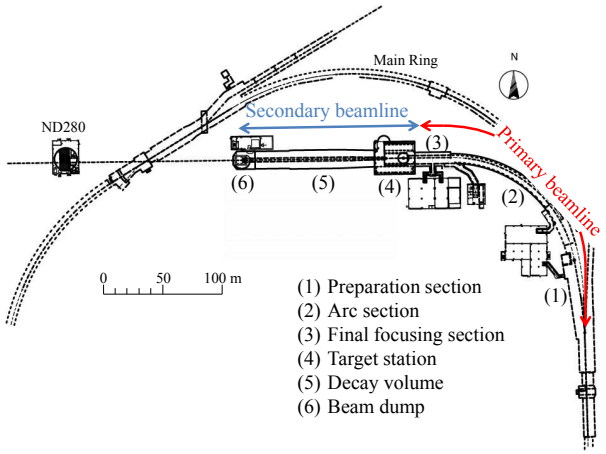

Figure 3.5: The T2K primary beamline and secondary beamline.

Figure 3.6 shows the sideview of the secondary beamline. In the secondary beamline, the protons strike a target to produce secondary hadrons (mostly pions) which are focused by magnetic horns and then decay into neutrinos. The target is a 91.4 cm long (1.9× interaction length), 2.6 cm in diameter and 1.8 g/cm^3 graphite rod. The target station also has (1) a beam window to separate the secondary beamline (filled with helium) and the vacuum in the primary beamline, (2) a baffle to protect the magnetic horns and (3) an optical transition radiation monitor (OTR) to monitor the proton beam profile just before they hit the target. The target is inside the first magnetic horn in a series of three; each magnetic horn consists of two coaxial conductors, between which a magnetic field is generated by feeding pulsed current through the conductors. The horn current is set at 250 kA (tunable to 320 kA which corresponds to stronger focusing) to focus the pions. The horn current can be reversed to focus the negatively charged pions, which decay into $\bar{\nu}_\mu$. The focused pions are left to decay in the 93-meter-long decay volume, which is filled with helium gas (1 atm) to reduce pion absorption. A beam dump consisting of 3.2 m of graphite and 2.4 m of iron at the end of the decay volume is used to absorbed the protons and secondary hadrons, and muons below ~ 5 GeV/c.

A muon monitor is placed just downstream of the beam dump to measure the neutrino beam intensity and direction on a bunch-by-bunch basis by measuring the muons that survive the beam dump. The muons are mostly from the pion two-body decay and have energy $\gtrsim 5$

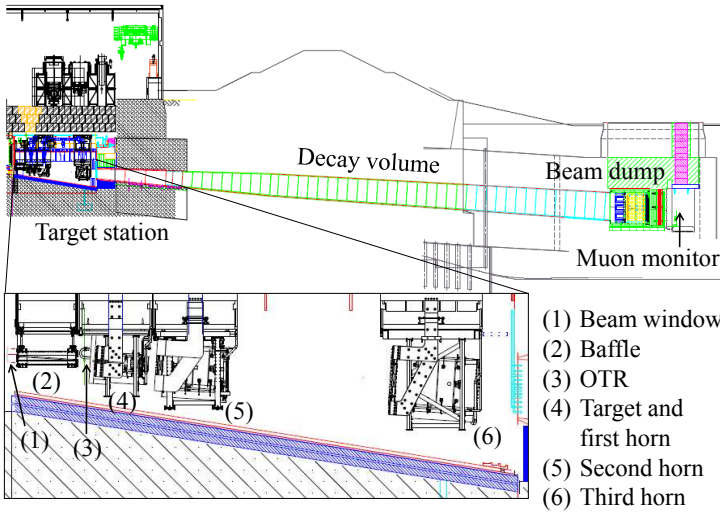

Figure 3.6: The secondary beamline. The length of the decay volume is 96 m.

GeV/c. The neutrino beam direction is determined to be the direction from the target to the center of the muon profile. The muon monitor measures the neutrino beam direction with a precision of $\lesssim$ 0.25 mrad. (3 cm) from the muon profile center. The detectors are made of arrays of ionization chambers and silicon PIN photodiodes at 117.5 m and 118.7 m from the target, respectively. A nuclear emulsion tracker is placed just downstream of the muon monitor to measure the absolute flux and momentum of the muons.

3.1.3 On-axis near detector

The INGRID (Interactive Neutrino GRID) detector is the on-axis near detector. It is made of 16 identical INGRID modules and one proton module. Figure 3.7 shows the configuration of the INGRID detector. 14 of the INGRID modules form a cross, the center of which is the designed beam center; two additional modules are placed at off-axis directions outside the main cross to check the beam axial symmetry. A proton module, which is similar in construction to the INGRID modules but without the iron plates, is place between the horizontal and vertical modules to detect the muons and protons produced by the beam neutrino in INGRID. The INGRID detector is used to monitor daily the neutrino beam direction and intensity via the neutrino interactions in the modules. The beam center is measured by the neutrino interaction rate in each module to a precision of $\lesssim$ 10 cm, or 0.4

mrad at the near detector pit. Figure 3.8 shows the daily event rate measured by the INGRID detector, and the horizontal and vertical directions measured by the INGRID detector and the muon monitor.

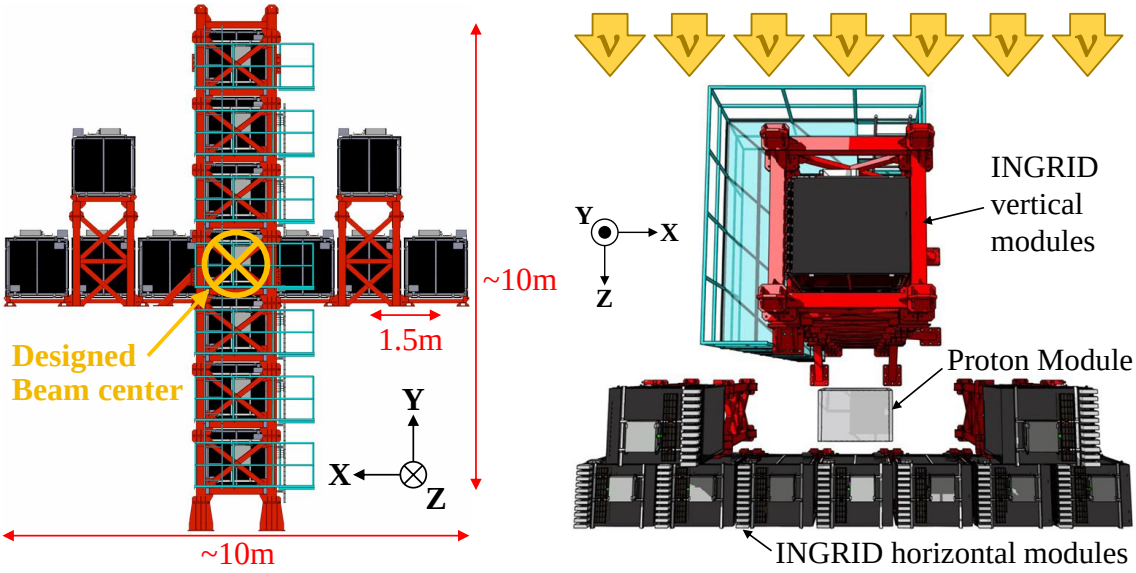

Figure 3.7: The on-axis INGRID detector from two viewing angles. The center of the INGRID detector is the designed beam center.

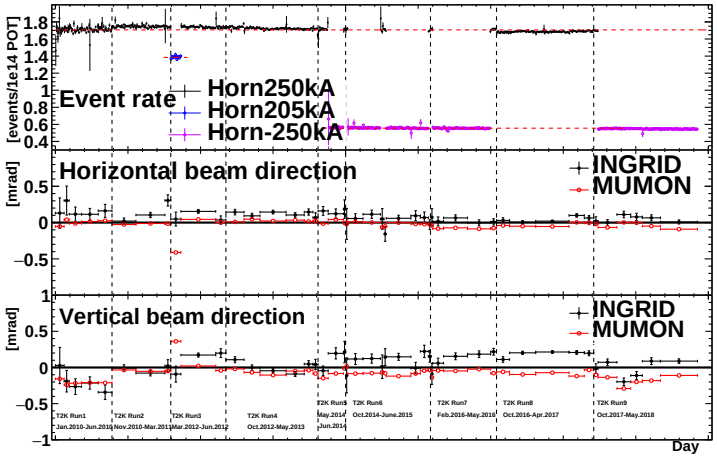

Figure 3.8: The event rate, horizontal and vertical beam directions measured by the INGRID detector and the muon monitor.

Each INGRID module is made of nine iron plates and 11 scintillator tracking planes sandwiched together as shown by Figure 3.9; they are surrounded by scintillator veto planes to reject interactions outside the module. Each iron plane is 1.24 m $\times$ 1.24 m in size and 6.5 cm in width; the total iron mass in each module is 7.1 tons. Each tracking plane is made of 24

horizontal scintillator bars and 24 vertical ones glued together. A wave-length shifting fiber (WLS) is inserted through a hole in each scintillator bar for light collection, and the signal is read out by an MPPC (Multi-Pixel Photon Counter) attached to the end of the WLS. The Hamamatsu MPPC has 667 pixels in a 1.3×1.3 mm^2 surface area; each pixel operates as an independent Geiger counter with a gain comparable to a vacuum photomultiplier. The compactness of MPPC and its ability to function inside a magnetic field makes it an ideal choice for the T2K near detectors. INGRID is calibrated using cosmic muon data; the mean light yield is determined to be larger than 10 p.e./cm (MIP).

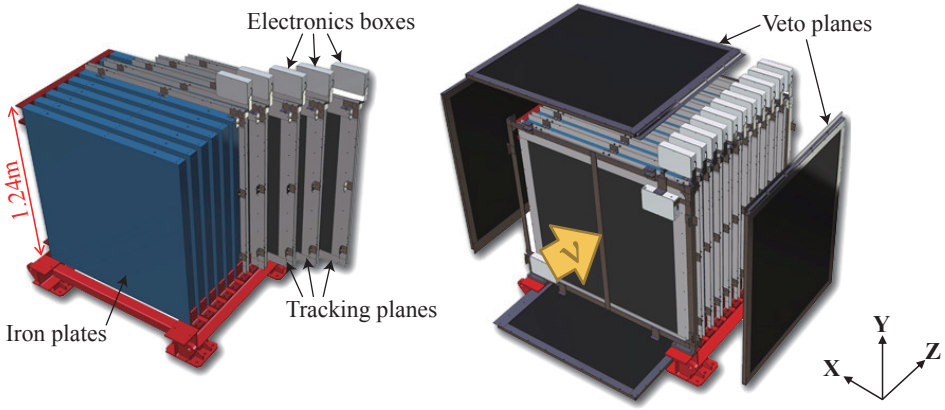

Figure 3.9: An INGRID module. The left image shows the tracking planes (blue) and iron plates. The right image shows the veto planes (black).

3.1.4 Off-axis near detector

The design of the T2K off-axis detector should meet the following requirements: (1) it should be able to provide information on the $\nu_\mu/\bar{\nu}_\mu$ flux, which will be extrapolated to Super-K for the measurement of neutrino oscillations; (2) it should measure the intrinsic $\nu_e/\bar{\nu}_e$ beam component, which is $\sim 1\%$ of the $\nu_\mu/\bar{\nu}_\mu$ flux and an irremovable background to the $\nu_e/\bar{\nu}_e$ appearance search at Super-K, as a function of neutrino energy; (3) it should measure the $\nu_\mu/\bar{\nu}_\mu$ interactions with such precision that the backgrounds (mainly neutral current π^0) to the ν_e appearance search at Super-K can be predicted. Figure 3.10 shows the components of the ND280 off-axis detector.

Most upstream is the PØD (i.e. π^0-detector), designed to measure the neutral current π^0 interactions on water, which is one of the two major backgrounds in the T2K ν_e appearance search (the other one being intrinsic ν_e). Figure 3.11 shows the cross section of the PØD.

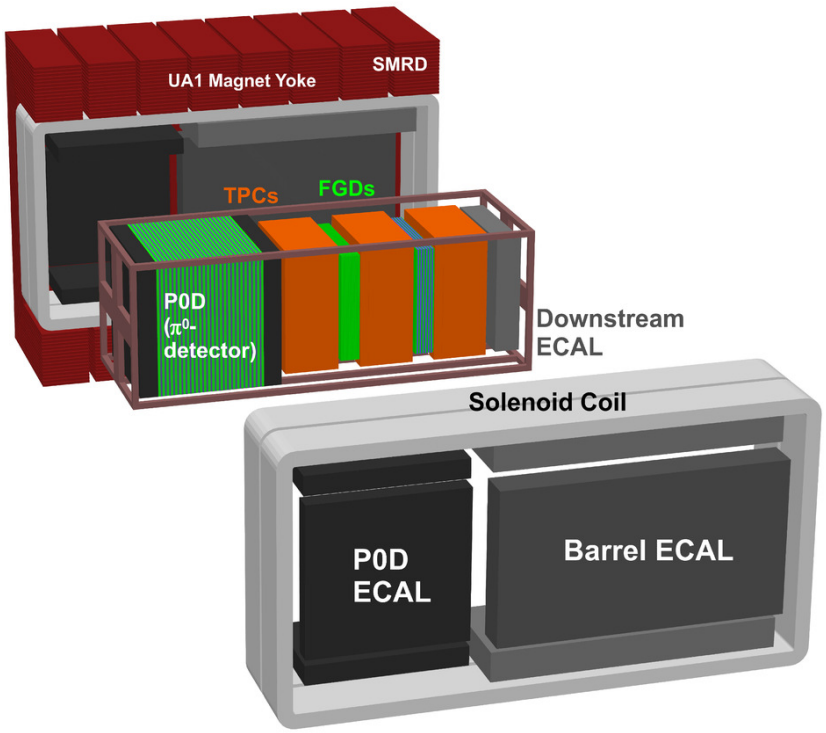

Figure 3.10: An exploded view of the ND280 off-axis detector. The metal frame which contains the PØD, TPCs and FGDs has a dimension of 6.5 m × 2.6 m × 2.5 m (length×width×height).

Perpendicular to the neutrino beam direction are layers of x-y scintillator bars, a light-tight cover, a lead or brass sheet, and a water bag which can be filled with water (water-in configuration) or emptied (water-out or air configuration). The "upstream ECal" and "downstream ECal" are used to veto events entering from outside and do not have water bags. There are 40 scintillator modules in the PØD, and each module consists of 134 vertical triangular scintillator bars and 126 vertical ones. The segmentation is sufficiently fine for the reconstruction of muon and pion tracks as well as electromagnetic showers. Each scintillator bar has a WLS fiber inserted and the optical signal is read out by Hamamatsu MPPCs attached to the one end (the other end is mirrored). There are a total of 50 water bags in PØD, making the total detector mass with water-in configuration 16.1 tons (13.3 tons without water). Binary (wet or dry) level sensors and pressure sensors are installed in the water volumes, which can measure the water depth within ±5 mm. The actual mass of the PØD water target can be estimated by the predetermined mass-depth relation. The designed fiducial water mass is 1944 ± 53 kg, and the measured mass is 1902 ± 16 kg.

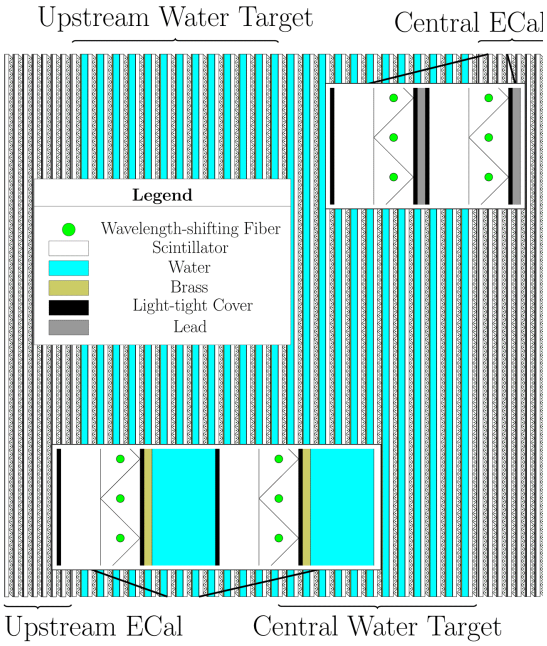

Figure 3.11: The PØD (π^0-detector). The beam is coming from the left and going right. The dimensions of the active target of PØD is 2103 mm × 2239 mm × 2400 mm (length×width×height).

Just downstream of the PØD are three Time Projection Chambers (TPC) and two Fine Grained Detectors (FGD). The two FGDs provide target mass for neutrino interactions as well as charged particle tracking. Each FGD has outer dimensions of 2300 mm × 2400 mm × 365 mm (width×height×depth in beam direction). They are made of layers of scintillator bars perpendicular to the beam in both horizontal and vertical directions, with WLS fiber inside. One end of the WLS fiber is mirrored by aluminum and the other end is attached to MPPCs and digitization electronics. The downstream FGD (FGD2) also contains six 2.5cm-thick water layers. The scintillator bars, WLS fibers and photosensors of each FGD is contained in a light-tight box. The calibration of photosensor response, saturation and non-linearity is enabled by the LED-based light injection system that flashes the exposed ends of the WLS fibers.

The emitted charged particles of the neutrino interactions that happen in the FGDs can be precisely measured by the TPCs. Each TPC has an inner box filled with argon-based drift gas, which is held inside an outer box filled with CO_2 as an insulating gas as shown by Figure 3.12. Charged particles ionize the argon atoms along their trajectories as they go through the TPC. A uniform electric field (roughly parallel to the magnetic field) is

applied which drives the ionization electrons to drift away from the central cathode plane. The drift time relative to the beam trigger, and the spatial and charge information of the ionization electrons can be measured at the readout plane on either side. The charge readout is achieved by the micromegas detectors [57] with 7.0 mm $\times$ 9.8 mm anode pad segmentation. The timing and spatial information combined is used to reconstruct a 3D image of the particle trajectory. A control pattern of electrons can be produced on the central cathode to calibrate and monitor the electron transport. The electron drift velocity and electric field distortion are determined by measuring the photoelectrons produced from the cathode (more precisely, from the thin aluminum discs glued to the copper surface of the cathode) by flashing it with a diffuse pulse of $\lambda = 266$ nm light.

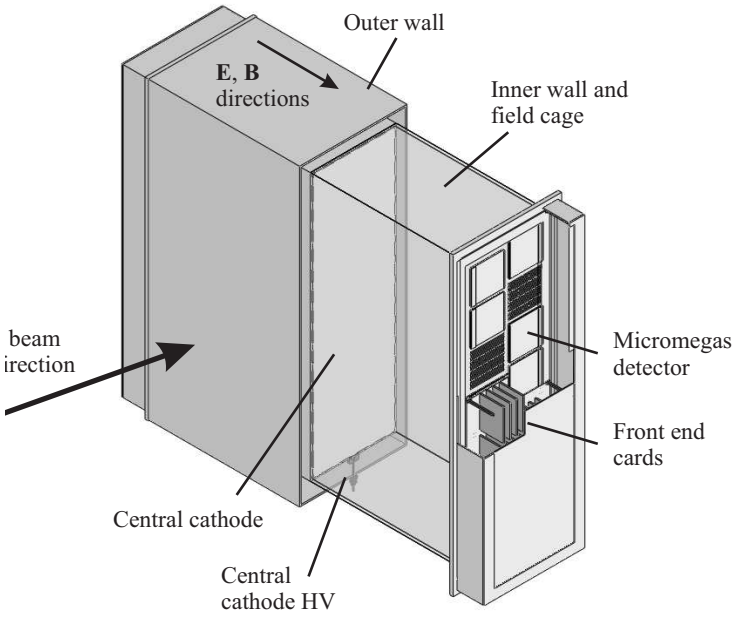

Figure 3.12: Simplified cut-away drawing of the TPC design. The outer dimensions of the TPC are approximately 2.3 m $\times$ 2.4 m $\times$ 1.0 m.

The TPCs play a crucial role in the measurement of neutrino interactions at ND280. The charged particle 3D trajectory and the amount of ionization per unit length along the trajectory can be precisely reconstructed in the TPCs, which is a powerful tool for identifying the particle type; the magnetic field enables the measurement of particle momentum and the sign of the charge.

The PØD, TPC and FGDs are surrounded by the electromagnetic calorimeter (ECal) as shown by Figure 3.10. The ECal is made of 13 independent modules: six barrel ECals surrounding the four sides of the trackers, one downstream ECal, and six PØD ECals covering the four sides of the PØD. Each module consists of layers of scintillator bars and lead absorber sheets, and the same WLS fiber-MPPCs configuration is used for the light detection. The main purpose of the ECals is to measure the energy of, and the direction at which, the photons and charged particles exiting from the inner detectors, in particular the photons from the π^0's produced in the tracker detectors.

The magnet in which the PØD, TPC, FGDs and the ECals are surrounded is recycled from the CERN UA1/NOMAD experiment; it provides a dipole magnetic field of 0.2 T for the determination of the sign of charged particles. The magnet consists of two mirror-symmetric halves which can be opened for access to the inner detectors or closed for data taking. Each half consists of water-cooled aluminum coils and 8 C-shaped flux return yokes, and each yoke consists of 16 4.8 cm-thick steel plates with 15 1.7 cm air gaps in the radial direction. 440 scintillator modules are inserted in these air gaps and on the top and bottom of the yokes, which make up the Side Muon Range Detector (SMRD). The scintillator modules can have different sizes in order to fit in the horizontal and vertical gaps. Each scintillator counter has an S-shaped WLS fiber glued into a grove cut into its surface, and the optical signal is read out by MPPCs. The purpose of the SMRD is three-fold: (1) to detect high-angle (w.r.t. the beam direction) muons and measure their momenta; (2) to identify cosmic ray muons; (3) to identify beam induced event interactions in the iron of the magnet and in the surrounding walls.

3.2 The Super-Kamiokande experiment

3.2.1 Cherenkov radiation

Super-K detects charged particles through their Cherenkov light emission in water – the particle type, direction and momentum can be inferred from the hit pattern of the PMTs mounted on the walls. Cherenkov radiation happens when a charged particle travels in a dielectric medium at a speed faster than the speed of light in said medium, much in the same way as a sonic boom is produced by sound waves emitted by an object that travels faster than the speed of sound. Let n be the dielectric constant and $v = \beta c$ be the speed of the charged particle, then the angle θ_C between the particle trajectory and direction at which

the electromagnetic shock wave travels has the following relation:

$$\cos\theta_C = \frac{1}{n\beta} \tag{3.2}$$

Pure water has $n \approx 1.34$, therefore ultra-relativistic particles have $\theta_C \approx 42°$. The number of photons emitted, N follows

$$\frac{\mathrm{d}^2 N}{\mathrm{d}L\mathrm{d}\lambda} = \frac{2\pi\alpha}{\lambda^2}\left(1 - \frac{1}{n^2\beta^2}\right) \tag{3.3}$$

where λ is the wavelength, L is the distance traveled by the particle, and α is the fine structure constant. Because Cherenkov radiation can only happen when $v = \beta c > c/n$, there exists a mass-dependent threshold of the particle energy/momentum, below which said particle would not be visible in a water Cherenkov detector.

3.2.2 OD and ID

The two concentric detector volumes – the inner detector (ID) and the outer detector (OD) are optically separated by a 55cm stainless steel support structure covered by black sheets. The ID has a diameter of 33.8m and height of 36.2m and holds 32 kilotons of water, which leaves approximately 2.5m on the other side of the support structure as the OD volume, which holds 18 kilotons of water. The OD serves as an active veto for entering events such as cosmic ray muons; it also functions as a shield for the cosmogenic neutrons and photons from the surrounding rocks. 1,885 outward-facing 8-inch OD PMTs [5] are mounted on the outer surface of the stainless steel support structure, and the OD volume is covered with highly reflective material Tyvek®(90% reflectivity at 400 nm, falling to 80% at 340 nm) to enhance light collection. To further enhance the light collection efficiency, each OD PMT is attached to a squared wavelength shifting plate of 60 cm in size, which absorbs the UV light from Cherenkov radiation and emits in the blue-green wavelengths to which the PMTs are more sensitive. The improvement in light collection due to the WLS plates is a factor of ~ 1.5 compared to bare PMTs, and the effect on PMT timing resolution is tolerable (from 13 ns without WLS plates to 15 ns with WLS plates) as the OD is only used as a calorimeter and veto counter and not as a particle tracker.

Particle type and kinematics of the particles produced in the neutrino interactions are measured by the ID. There are in total 11,129 inward-facing 20-inch ID PMTs [58] on the inner surface of the support structure. They are mounted on the stainless steel support

[5] Most of the OD PMTs are recycled from the IMB experiment.

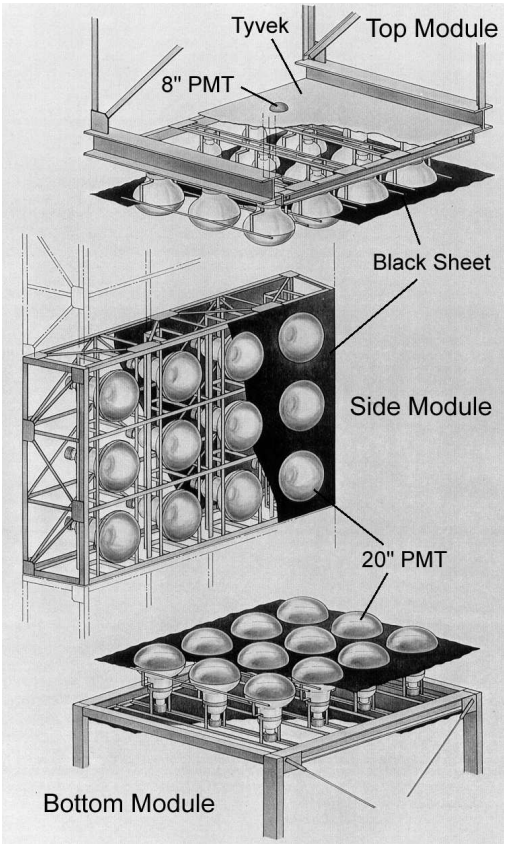

Figure 3.13: Schematic view of the support structures and the SK inner detector "supermodule".

structure in units of "supermodule" as shown by Figure 3.13. Each supermodule is 2.1m in height, 2.8m in width and 0.55m in thickness, and supports a 3×4 PMT array; it also has two OD PMTs mounted on the other side. The effective ID photocathode coverage is 40%. Figure 3.14 shows the ID PMT structure and its photocathode quantum efficiency (maximum of 21% at 360 nm-400 nm). The photoelectron collection efficiency at the first dynode is $> 70\%$; the transit time spread (r.m.s.) for a single photoelectron (p.e.) is 2.2 ns. The PMTs are operated with a gain of 10^7 with high voltage ranging from 1700 to 2000 volts. The dark noise threshold is 0.25 p.e., at which the rate in Super-K is about 3 Hz. In light of an accident in 2001 in which a single ID PMT imploded inside Super-K and triggered a chain reaction destroying ∼6600 PMTs, all ID PMTs are covered by an acrylic window which can contain the shock wave generated by one PMT implosion. In order to counter the potential bias the Earth magnetic field has on the PMTs, 26 sets of horizontal and vertical Helmholtz coils are arranged around the inner surface of the tank to reduce the magnetic field in the detector from 450 mG to about 50 mG.

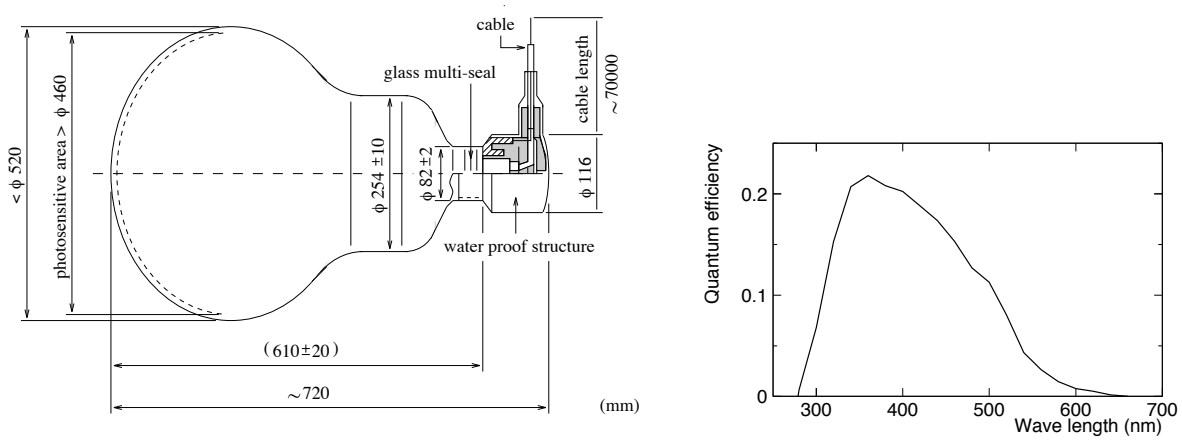

Figure 3.14: A schematic view of the Super-K ID PMT (left) and its photocathode quantum efficiency as a function of wavelength (right).

3.2.3 Data acquisition

When a photon hits a PMT, a photoelectron is generated from the photocathode and amplified by the dynodes. The analog signal from the PMT is fed into a charge-to-time converter (QTC) [6]; this signal is then digitized by a time-to-digital converter (TDC) to obtain the hit time and charge information [7]. Online PCs are continuously collecting the "hit" signals. A software trigger running on the online PCs is used at Super-K, in which the total number of PMT hits within a running time window of 200 ns is counted; an event trigger is issued once the count reaches a certain threshold. Only the events accompanied by a trigger are saved on the disk for physics analyses.

The detector activities induced by the T2K beam neutrinos can be extracted based on the neutrino arrival time. The timing signal synchronized with the MR extraction triggers the beam monitors and is logged at J-PARC; the timing and spill information is sent to Super-K through a VPN network, which is then returned from Super-K to J-PARC to check data corruption (the round-trip-time is measured). The synchronization between beam trigger timestamps at Super-K and J-PARC is at a scale of $\sim$ 50 ns. As shown in Figure 3.15, all PMT hit information within $\pm$500 μsec from the beam arrival time (with neutrino time-of-

[6]The new front-end boards named QBEE which stands for QTC Based Electronics with Ethernet [59] are an SK-IV upgrade in order to lower the trigger threshold, which is need for certain Solar neutrino and supernova relic neutrino searches. The QTC is a custom ASIC that responds to input PMT pulses by producing a square-wave pulse.

[7]The PMT "hit" threshold is set at 0.25 p.e.; the timing of a hit is registered as the time when the threshold is reached.

flight taken into account) are stored in order to eliminate potential trigger biases. The events within the 1 msec time window are later processed with the usual SK software triggers which are used to search for neutrino events; any candidate events found are used for T2K data analysis. Since the SK DAQ buffer can only store hit information for a few seconds, it is necessary to receive the spill information from J-PARC within $\sim$ 10 seconds such that the data can be promptly stored. This is monitored by the spill round-trip time (RTT) between Tokai-Kamioka-Tokai, which is typically 30-50 msec.

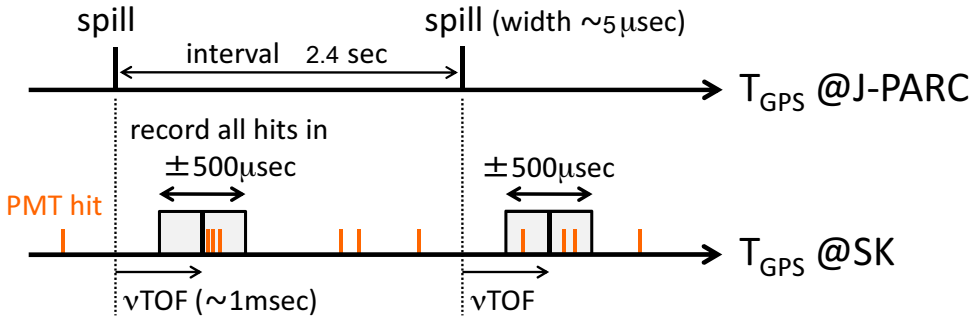

Figure 3.15: A schematic of T2K beam data acquisition at SK. Figure is modified from [60].

Chapter 4

Simulation and event reconstruction

This chapter will discuss the simulation of both the T2K and the Super-K experiments, including the neutrino beam/flux simulation, detector simulation and neutrino interactions. The second part will briefly discuss the Super-K event reconstruction which is relevant to this analysis.

4.1 Simulation

4.1.1 T2K beam simulation

In order to accurately predict the neutrino fluxes at the near and far detectors, all processes in the neutrino beamline need to be simulated, including the proton-target interactions, the subsequent focusing in the magnetic horns and pion decays in the decay volume. The intensity, position and beam profile of the proton beam pulses in the primary neutrino beamline are measured by a suite of proton beam monitors and used as an input to the beam simulation. The FLUKA 2008 [61] package is used to model the interactions between the proton beam and the graphite target, which produces pions and kaons. GEANT3 [62] is used to model the magnetic horns and decay volume and track the particles exiting the target; the GCALOR [63] package is used to model the subsequent hadron decays. This hadron production in the target is tuned to external data from the NA61/SHINE experiment [64] [65] and several other hadron experiments [66] [67] by weighting each simulated hadron interaction according to the measured multiplicity and particle production cross sections, using the true

initial and final state hadron kinematics [68]. Figure 4.1 shows the predicted neutrino-mode fluxes at ND280 and SK.

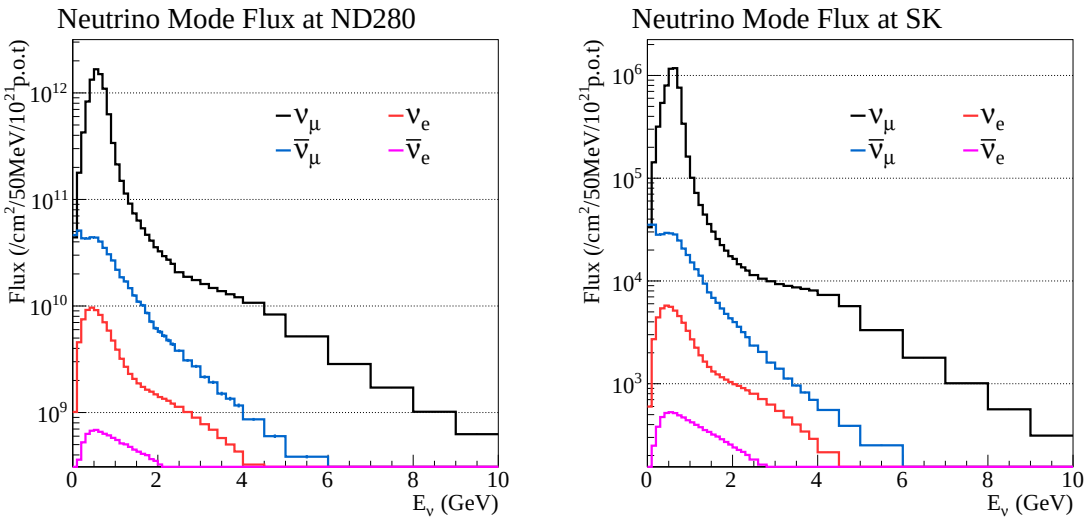

Figure 4.1: The predicted T2K beam neutrino fluxes in neutrino-mode at ND280 (left) and SK (right).

The hadron production model, proton beam profile, horn current, horn alignment etc. contribute to the uncertainties in the flux prediction. Figure 4.2 shows the error contributions to the ν_μ flux at SK in neutrino-mode from each different source. The largest contribution is from the uncertainties on the hadron production. The largest contribution from beam monitor calibrations comes from the beam current measurement, though its effect on oscillation analyses is reduced by ND280 data. A conservative 5 kA horn current fluctuation is assigned to estimate the horn current error; the uncertainty of horn magnetic field is defined by the deviation of the measurement by a Hall probe from the predicted horn magnetic field. The horn and target alignment uncertainties are obtained by survey measurements [68].

4.1.2 Super-K atmospheric neutrino flux prediction

The atmospheric neutrino flux predictions (absent neutrino oscillation) used to generate the SK atmospheric neutrino MC are provided by Honda et. al. [69] [70]. The model of the primary cosmic ray flux is tuned to the AMS [71] and BESS [72] measurements. The primary cosmic rays are deflected by the earth magnetic field [73]; the influence from the solar wind is also taken into account. The density profile of the Earth's atmosphere used in the simulation is based on the US-standard atmosphere 1976 model [74]. The interactions of the

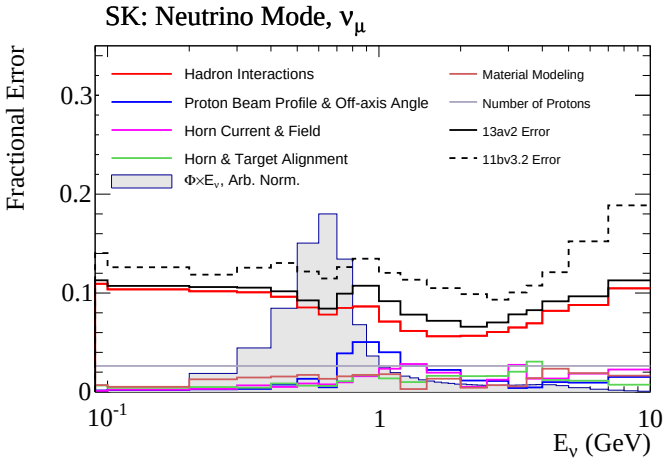

Figure 4.2: The uncertainties of the neutrino-mode ν_μ flux at SK broken down by sources. The total uncertainty is shown in the solid black line. The dashed line indicates the flux error from the previous flux tuning and is irrelevant to this analysis.

cosmic ray particles in the atmosphere is simulated using DPMJET-III [75] and JAM [76]; the hadron production model is further tuned to achieve better agreement with cosmic ray muons measurements [72] [77] [78].

Figure 4.3 shows the zenith angle distributions of the atmospheric neutrino flux averaged over azimuthal angles at SK in the absence of neutrino oscillation. The spectra are peaked at the horizontal direction because the cosmic ray particles traveling horizontally traverse a longer distance in the atmosphere and therefore have a high interaction rate. The up-down asymmetry is due to the geomagnetic field, the impact of which is greater for low energy cosmic rays and therefore neutrinos with lower energy. Figure 4.4 shows the unoscillated energy distributions of the atmospheric neutrinos at SK. The suppression at low energy is due to the fact that the low energy primary cosmic ray particles are deflected by the Earth's magnetic field and cannot enter Earth's atmosphere.

4.1.3 Detector simulation

The geometry of the T2K near detectors is implemented in GEANT4 [81]. GEANT4 is used to simulate the energy deposits from the particles coming out of the neutrino-nucleus interactions and to track their passage through the detector. The detector response, including that of the scintillator, WLS fibers, MPPCs and electronics, and TPC electron drift and electronics, is simulated in a customized T2K software package [53].

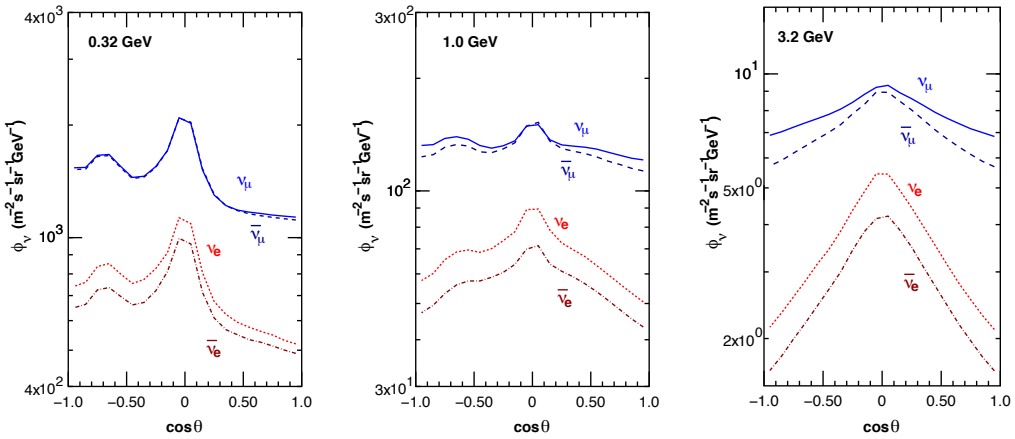

Figure 4.3: The zenith angle distributions of the atmospheric neutrino flux averaged over azimuthal angles at SK in the absence of neutrino oscillation. $\cos\theta = 1$ for downward-going neutrinos and $\cos\theta = -1$ if they are upward-going. Taken from [70].

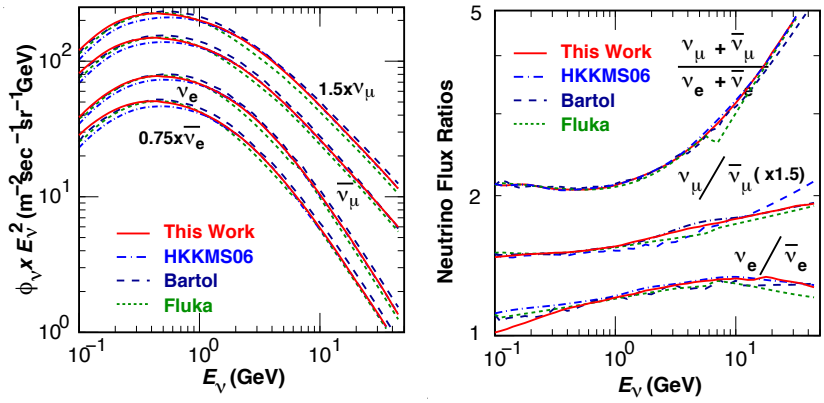

Figure 4.4: The energy distributions of the atmospheric neutrinos at SK in the absence of neutrino oscillation (left) and the flux ratios (right). The results from [70] are shown in red, and the previous results (HKKM06) [69] are shown by the dash-dot line. The calculation by the Bartol group [79] (dashed line) and FLUKA [80] (dotted line) are shown for comparison.

The software package that propagates the particles produced by the NEUT [82] neutrino interaction generator at Super-K is SKDETSIM [53]. The detector geometry and particle tracking are handled by GEANT3 [62]. The hadronic interactions in water in which the pion momenta are above 500 MeV/c is handled by the CALOR physics package [83]; the rest of the hadronic interactions are simulated by a custom routine [84]. Photon absorption, Rayleigh scattering and Mie scattering are considered for the photon propagation in SKDETSIM; the aforementioned processes involving photons are tuned to a number of laser calibration mea-

surements [51]. The PMT and electronics response is also implemented based on calibration measurements [52].

4.1.4 Neutrino interaction cross section modeling

In both ND280 and SK, the neutrino interactions are simulated by the NEUT event generator [82]. NEUT takes the input neutrino flux – whether it is the T2K beam neutrino flux or the SK atmospheric neutrino flux – and generates events, each of which consists of particles from neutrino-nucleus interactions based on the cross section models. Neutrino interactions can be classified by the weak interaction boson as Charged Current (CC) and Neutral Current (NC) as discussed in section 2.1. Figure 4.5 shows the neutrino and antineutrino per nucleon CC cross sections divided by neutrino energy as a function of neutrino energy. At lower energy ($E_\nu \lesssim 1$ GeV), quasi-elastic interactions dominate; as the energy goes up, resonant pion production processes start to dominate; for $E_\nu \gtrsim 10$ GeV, both the QE and resonance cross section decreases, and the interactions are almost exclusively DIS for $E_\nu \gtrsim 100$ GeV. This section will give a brief summary of the neutrino interactions incorporated in NEUT and used in this analysis.

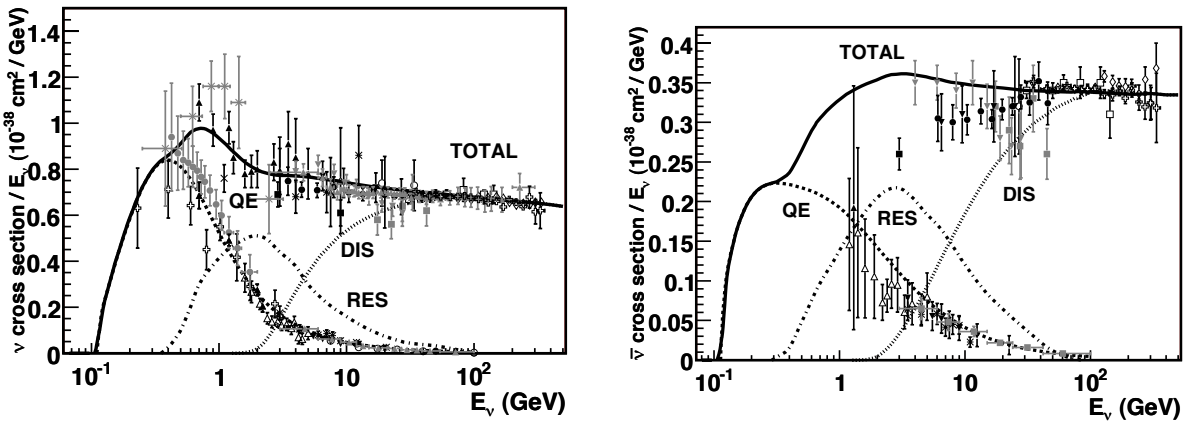

Figure 4.5: Total neutrino and antineutrino per nucleon CC cross sections (for an isoscalar target) divided by neutrino energy as a function of neutrino energy. Example predictions for each are provided by the NUANCE generator [85]. The quasi-elastic scattering data and predictions have been averaged over neutron and proton targets and hence have been divided by a factor of two. Taken from [86].

- **Charged Current quasi-elastic (CCQE) and Neutral Current elastic interactions**

In CCQE interactions, a neutrino (antineutrino) interacts with a neutron (proton), and the exchange of a W boson results in a charged lepton of the same flavor as the neutrino (antineutrino) and a proton (neutron). The differential cross section is given by Llewellyn-Smith [87] analytically; in addition to the particle kinematics, the cross section also depends on the electric, magnetic and axial form factors, all of which are usually assumed to have a dipole form. The electric and magnetic form factors are strongly constrained from electron-nucleon scattering; the axial form factor is also present in neutrino-nucleon interactions and is by far the dominant one in the neutrino-nucleon cross section [88]. It is usually parametrized with a dipole form

$$F_A(Q^2) = \frac{g_A}{\left(1 + Q^2/M_A^{QE2}\right)^2} \tag{4.1}$$

where $g_A = 1.2670 \pm 0.0035$ is well established from neutron β-decay [89], and the axial mass M_A^{QE} is constrained by neutrino-deuterium scattering experiments to be 1.026 ± 0.021 GeV [90]. In NC elastic interactions the neutrino or antineutrino transfer energy to the nucleon via the exchange of a Z boson and no lepton is produced, the cross section of which can also be calculated analytically.

For bound nuclei – in the case of T2K carbon and oxygen – the particles exiting the nucleus can be modified by nuclear effect. The following nuclear effects are considered in NEUT (details are described in [88] and [91]):

- A Fermi gas model is used to describe the nucleon momentum distribution inside the nucleus, on which the initial kinematics of the nucleon depends [88].
- The nuclear binding energy needed to extract the nucleon from the nucleus is subtracted from the energy available to the final state particles.
- Random Phase Approximation (RPA) is used to describe the overall long-range screening/enhancement of the neutrino-nucleon interaction by the nuclear potential. The modification to the CCQE cross section is dependent on E_ν and Q^2 as prescribed by the relativistic RPA model by Nieves et. al. [92]. The RPA correction is currently only considered for the CCQE interactions but not the pion production processes.
- The re-interactions of the hadrons with the remnant nucleus, or the final state interactions (FSI), are described by a semi-classical intra-nuclear cascade model which will be described later in this section.

Understanding nuclear effects is very difficult. M_A^{QE} has been used as an effective pa-

rameter to describe neutrino-nucleus CCQE interactions. Various experiments have attempted to measure the neutrino-nucleus CCQE interactions on different target nuclei, and the measured M_A^{QE} values often have disagreements due to the convolution with nuclear effects. Therefore, the parameters used to describe neutrino-nucleus CCQE interactions are left with no prior constraints in the fit to ND280 data.

- **Multi-nucleon effect**
  Multi-nucleon effect refers to processes in which two or more correlated nucleons are ejected from the nucleus together when a neutrino interacts with one of them. The MiniBooNE measurement of CCQE cross section [93] yields $M_A^{QE} = 1.35 \pm 0.17$ GeV, which is significantly different from other experiments. It is found that such a discrepancy in MiniBooNE can be resolved by the inclusion of multi-nucleon neutrino interactions. Predictions for the multi-nucleon-neutrino interactions arise from the multi-body expansion of the weak propagator in the medium: the first-order expansion corresponds to the CCQE interaction where the hadronic vertex involves a single nucleon-hole pair ("one particle, one hole", or 1p1h); the second-order terms involve additional nucleons or resonances in the hadronic current – the former is often called a "two particle, two hole" (2p2h) interaction, which means it involves two particles ejected from the nucleus and two holes in the nucleus [94]. Neutrino multi-nucleon interactions appear like CCQE interactions in SK but with different lepton kinematics. Therefore, failure to properly account for the multi-nucleon interactions can result in biases in the neutrino energy reconstruction as the energy reconstruction of the T2K beam neutrinos at SK is dependent on the lepton kinematics. Figure 4.6 shows the effect in reconstructed neutrino energy due to the multi-nucleon interactions. T2K (NEUT) adopts the multi-nucleon model given by Nieves et. al. [92]; the details of the implementation is described in [94].

- **CC/NC single pion production**
  CC and NC resonant pion production also happen in the energy range (the model cut-off is at $W < 2$ GeV, where W is the hadron invariant mass) of T2K beam neutrinos and SK atmospheric neutrinos. Figure 4.7 shows the Feynman diagrams of the charged current resonant pion production processes which involves a Δ (higher resonances are also considered in NEUT if kinematically allowed); the following neutral current resonant

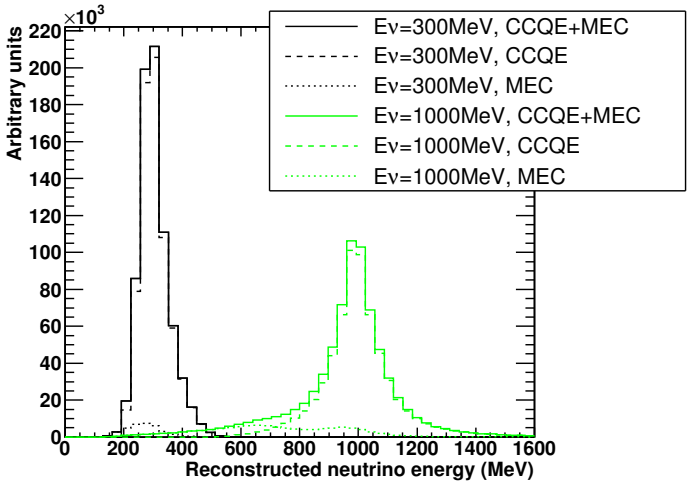

Figure 4.6: Neutrino energy reconstructed from final-state lepton, assuming stationary target nucleon. Two neutrino energies are shown; the multi-nucleon processes are label "MEC". Taken from [94].

pion production processes can also happen via the exchange of a Z boson

$$\begin{aligned} \nu_l + p &\rightarrow \nu_l + \pi^+ + n, \\ \nu_l + p &\rightarrow \nu_l + \pi^0 + p, \\ \nu_l + n &\rightarrow \nu_l + \pi^0 + n, \\ \nu_l + n &\rightarrow \nu_l + \pi^- + p. \end{aligned} \tag{4.2}$$

The model implemented in NEUT is given by Rein-Sehgal [95] with a modified form factor which emphasizes the $\Delta(1232)$ contribution [96] and takes into account the lepton mass effects [97]. The resonance-resonance intereference is also accounted for, while resonance-non-resonance is neglected. The non-resonant processes in which the pion is produced at the interaction vertex without going through a resonant stage is only modeled for isospin-1/2 ($I_{1/2}$) interaction channels [88]. The three parameters in the Rein-Sehgal model – the axial mass M_A^{Res}, the axial form factor at $Q^2 = 0$ $C_5^A(0)$ and the $I_{1/2}$ non-resonant background, are tuned by external bubble chamber data [98] [99]. This treatment is acceptable for the T2K energy range where generally speaking $W < 1.4$ GeV; more massive resonances, non-resonance processes and their interference become important at higher energy. Improvements have been made to significantly improve the Rein-Sehgal model by including amplitudes from $I_{3/2}$ and $I_{1/2}$ non-resonant backgrounds and the resonance-non-resonance interference that arises [100].

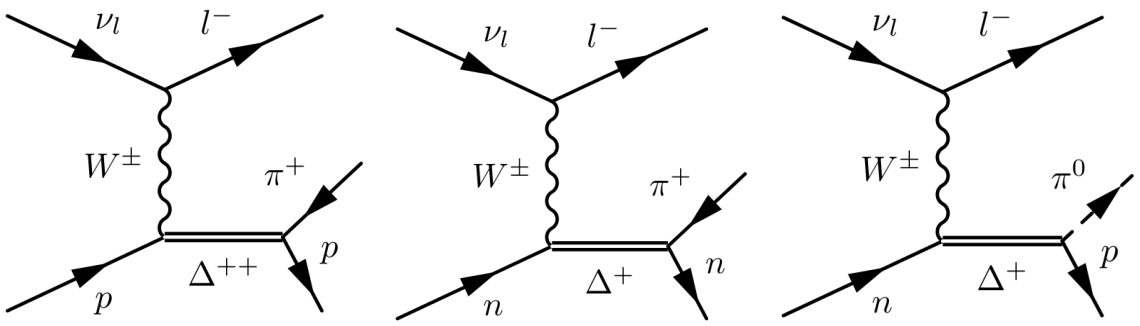

(a) CC1π^+1p (b) CC1π^+1n (c) CC1π^0

Figure 4.7: The Feynman diagrams of charged current resonant pion production [88].

- **Coherent pion production interaction**
  In the coherent pion production interactions, a neutrino scatters off the entire nucleus (rather than an individual nucleon) and produces a pion without exciting the nucleus, as shown by Figure 4.8. The energy transferred from the neutrino to the nucleus has to be small in order to satisfy this condition. Similar coherent pion production can also happen in the neutral current channels, in which a π^0 is produced. The cross sections of the coherent pion production processes are small compared to the resonant pion production channels. NEUT uses the Rein-Sehgal coherent model [101], which is shown to overestimate the cross section by the MINERνA coherent $\pi^\pm$ measurement [102]. An *ad hoc* reweighting is extracted from a comparison of the coherent pion production cross section in NEUT with that measured by MINERνA, and applied to T2K and SK MC events [88].

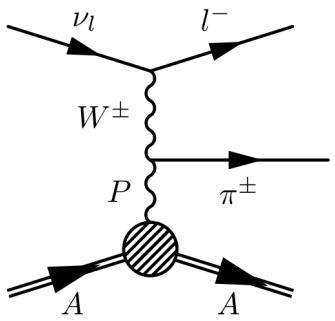

Figure 4.8: The Feynman diagram of coherent pion production [88].

- **Deep inelastic scattering**
  In deep inelastic scattering (DIS), the neutrino interacts with a quark inside a nu-

cleon by exchanging a W or Z boson, breaking the nucleon and producing hadrons from the quark fragmentations. The transition region (where the momentum transfer is $1.4 < W < 2.0$ GeV) is simulated by a superposition of different models: single pion production processes are handled by the model previously discussed; events with multiple pions are simulated by a DIS-like model called the multi-pion mode [88]. For $W > 2.0$ GeV, all events are generated using the PYTHIA [103] DIS model. The DIS double differential cross section with respect to Bjorken x (i.e. fraction of the nucleon momentum carried by the struck quark) and y (the fraction of the neutrino energy transferred to the hadronic system) formulation is given by [104] and modified to take into account the lepton mass. Because the Parton Distribution Functions (PDF) used in NEUT are relatively old [105], the Bodek-Yang correction [106] is applied to the low Q^2 region where the perturbative QCD techniques do not work.

- **Final state interactions (FSI) and secondary interaction (SI)**

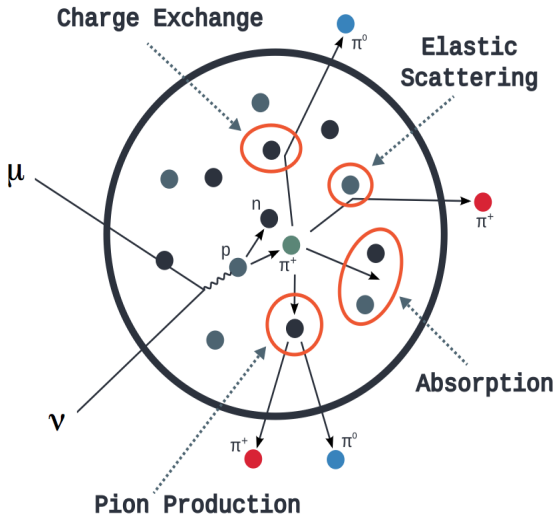

Figure 4.9: Illustration of the processes that can happen for a pion inside a nucleus. Taken from [107].

The final state interactions, or in other words the re-interaction of pions [1] from neutrino interactions before they exit the nucleus, can modify the topology of the observed events. The underlying physics behind secondary interactions in which the pions interact with a nucleus somewhere else in the detector is the same as FSI. Figure 4.9 shows

[1]NEUT also considers the FSI of other heavier mesons and nucleons, but their occurrence is much less frequent than pions.

the processes that can take place for a pion inside the nucleus on its way out: it can be elastically scattered, absorbed, gain or lose electric charge, or generate more hadrons. These pion interactions are simulated in NEUT using a semi-classical intra-nuclear cascade model. The starting point of the pion after it is produced by a neutrino interaction is chosen randomly from a nucleus density profile modeled by a three-parameter Fermi model [91], and said parameters can be determined by electron-nucleus scattering measurements [108]. The initial pion momentum is derived from the primary neutrino interaction. The pion propagation is then treated classically within the nucleus medium with a finite number of steps and the step size $\mathrm{d}x = R_N/100$, where R_N is the nucleus radius. At each step, a probability is assigned for each of the four processes and which process, if any, the pion will go through is determined through Monte Carlo. The pion cascade will continue until it is absorbed or exits the nucleus. Since the physics between FSI/SI and pion-nucleus scattering is modeled in a similar manner, the NEUT cascade model is tuned by external $\pi^{\pm}$-A scattering data as described in [91]. Table 4.1 summarizes the parameters which are used in the pion cascade model and constrained by the fit to external data; each parameter scales the macroscopic probability of the corresponding process.

Parameter	Description	Momentum region (MeV/c)
`FEFABS`	Absorption	< 500
`FEFQE`	Quasi-elastic scatter	< 500
`FEFCX`	Single charge exchange	< 500
`FEFQEH`	Quasi-elastic scatter	> 400
`FEFCXH`	Single charge exchange	> 400
`FEFINEL`	Hadron (N+nπ) production	> 400

Table 4.1: The NEUT FSI probability scaling parameters used in the pion scattering fit. The overlap in the momentum regions is due to blending of the high and low energy models in NEUT [91].

4.2 Super-K event reconstruction

A neutrino event observed at Super-K consists of the charge and time recorded for every PMT hit. This information needs to be parsed by the reconstruction algorithm, which identifies the type and kinematics of the outgoing particles, before it can be used in physics analyses. This section summarizes the reconstruction algorithm at SK named fiTQun: it employs a

maximum likelihood method, in which a prediction of the hit charge and time can be made for each PMT based on a particle hypothesis, and the best hypothesis can be found by a comparison between the prediction and the measurement. The core algorithm of fiTQun is based on the MiniBooNE reconstruction algorithm [109]. All discussions in the section is based on the references [110] and [111], in which more details about the fiTQun algorithm can be found.

4.2.1 Subevent algorithm

At the start of event reconstruction, an SK event (i.e. PMT hits) is first divided into time clusters of hits, or subevents; there can be at most one charge and one time for each PMT in each subevent. The subevent algorithm is meant to separate events that happen at different time. For example, a muon neutrino CCQE interaction produces a muon, which triggers the event; the subsequent decay electron from the muon may happen a few μsec later, and the hits induced by the decay electron will be in a different time cluster, or subevent, from the muon hits. An event in SK typically includes the detector activity in a ~ 10 μsec window around the trigger time and may contain several subevents. The subevent algorithm searches for subevents and associates the PMT hits with each of them; each subevent is then passed on to the maximum likelihood fit.

The subevent algorithm starts by performing a quick fit to obtain the event vertex, which can be done by searching for the vertex position $\boldsymbol{x}$ and time t that maximizes the following vertex goodness metric:

$$G(\boldsymbol{x}, t) = \sum_{i}^{\text{hit}} \exp\left(-\frac{\left(t_i - t - |\boldsymbol{R}^i_{\text{PMT}} - \boldsymbol{x}|/c_n\right)^2}{2\sigma^2} \right) \tag{4.3}$$

where $\boldsymbol{R}^i_{\text{PMT}}$ is the position of the i-th PMT, t_i the hit time, c_n the speed of light in water, and $\sigma = 4$ ns. Then the vertex position that maximizes Eq. 4.3 is fixed while a scan of the vertex goodness as a function of t is performed. Subevents appear as large peaks in the vertex goodness distribution as a function of t (the peak-finding algorithm is described in [110]) if the vertices of all subevents are in close proximity.

A time window near each peak is defined as the duration of each subevent such that a PMT has at most one hit within said time window. The time window of a given time peak is found by calculating the earliest and latest hit times t_i such that the following residual time

with respect to the peak time T_k

$$T^i_{res} = t_i - T_k - |\boldsymbol{R}^i_{\mathrm{PMT}} - \boldsymbol{x}|/c_n \tag{4.4}$$

satisfies $-180 < T^i_{res} < 800$ ns. Once the time window around each peak is found, a vertex fit using Eq. 4.3 is performed again – this time for each time window separately. This is important for identifying fake time peak if the vertices of the subevents are far apart. The remaining time peaks and their associated time windows are the final subevents which are then passed on to further reconstruction. The number of subevents is a good proxy for the number of decay electrons in an event (number of subevent = number of decay electrons + 1).

4.2.2 Likelihood function

The core of the fiTQun algorithm lies in the likelihood function which simultaneously takes into account the time and charge information of all PMTs in SK. For each subevent, the following likelihood function can be constructed given a particle hypothesis:

$$\mathcal{L} = \prod_{j}^{\mathrm{unhit}} P_j(\mathrm{unhit}|\mathbf{x}) \prod_{i}^{\mathrm{hit}} \{1 - P_i(\mathrm{unhit}|\mathbf{x})\} f_q(q_i|\mathbf{x}) f_t(t_i|\mathbf{x}) \tag{4.5}$$

where $\mathbf{x}$ is a hypothesis which includes the particle type, vertex, direction and momentum [2]. The index j runs over all unhit PMTs multiplying the probability of each PMT not registering a hit given the hypothesis $\mathbf{x}$. The index i runs over all the hit PMTs; $(1 - P_i(\mathrm{unhit}|\mathbf{x}))$ is the probability of the i-th PMT registering a hit; $f_q(q_i|\mathbf{x})$ is the likelihood of the i-th PMT observing q_i amount of charge, while $f_t(t_i|\mathbf{x})$ is the likelihood of it observing the hit at time t_i. Many hypotheses are tested, and the one that maximizes the likelihood function is deemed as the reconstructed event and used in the physics analyses.

4.2.3 Predicted charge calculation

In practice, the PMT and electronics response is separated from the particle and optical propagation by introducing the predicted charge μ_i – the mean number of photoelectrons

[2] The hypothesis can include more than one particle.

expected at the i-th PMT give a hypothesis. In this case Eq. 4.5 can be rewritten as

$$\mathcal{L} = \prod_{j}^{\text{unhit}} P_j(\text{unhit}|\mu_j) \prod_{i}^{\text{hit}} \{1 - P_i(\text{unhit}|\mu_i)\} f_q(q_i|\mu_i) f_t(t_i|\mathbf{x}) \tag{4.6}$$

where $f_q(q_i|\mu_i)$ now only explicitly depends on the PMT and electronics response, while $P_i(\text{unhit}|\mu_i)$ depends on μ_i through its relation with $\mathbf{x}$. Naturally the likelihood calculation can be divided into two steps: (1) the predicted charge μ_i at the position of each PMT is calculated based on the particle hypothesis $\mathbf{x}$ and then (2) $P_i(\text{unhit}|\mu_i)$ and $f_q(q_i|\mu_i)$ can be evaluated based on μ_i.

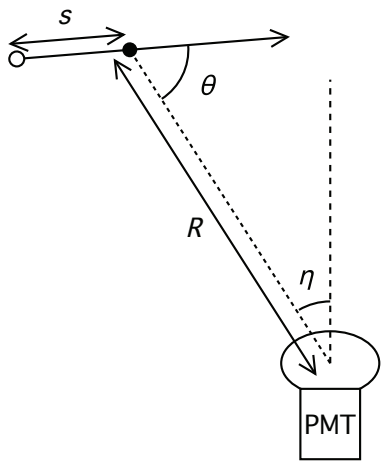

Figure 4.10: Schematic diagram describing the variables relevant to the predicted charge calculation. The white dot is the initial position of the particle. Taken from [110].

The predicted charge from both the direct Cherenkov radiation and the indirect light from processes such as light scattering in water and reflections from the walls and PMTs are taken into account when calculating μ_i. The predicted charge from direct light on the i-th PMT can be calculated by the following integrand:

$$\mu_i^{\text{dir}} = \Phi(p) \int \mathrm{d}s \; g(p, s, \cos\theta) \Omega(R) T(R) \epsilon(\eta) \tag{4.7}$$

where s, θ, R, η [3] are illustrated by Figure 4.10. The meaning and calculation of each term in Eq. 4.7 are listed below:

- $\Phi(p)$ is the charge normalization factor which is a function of the particle initial momen-

[3] R, θ, η are dependent on the event hypothesis $\mathbf{x}$ and s, and therefore the integration is over s only.

tum; it also absorbs other proportionality factors such as the PMT quantum efficiency, which is implemented PMT-by-PMT based on detector calibrations. The overall normalization of $\Phi(p)$ is also tuned by particle gun MC to achieve unbiased reconstructed momentum.

- $g(p, s, \cos\theta)$ is the Cherenkov emission profile which describes the number of photons emitted per unit track length per unit solid angle by a particle with initial momentum p, at an angle θ with respect to the particle direction and a distance s from the initial vertex. $g(p, s, \cos\theta)$ is pre-generated and saved by running SKDETSIM for different particle type and momentum hypotheses and then normalized to 1:

$$\int \mathrm{d}s\mathrm{d}\Omega \; g(p, s, \cos\theta) = 1 \tag{4.8}$$

Figure 4.11 shows an example of the Cherenkov emission profiles. Note that the PID information is encoded in $g(p, s, \cos\theta)$.

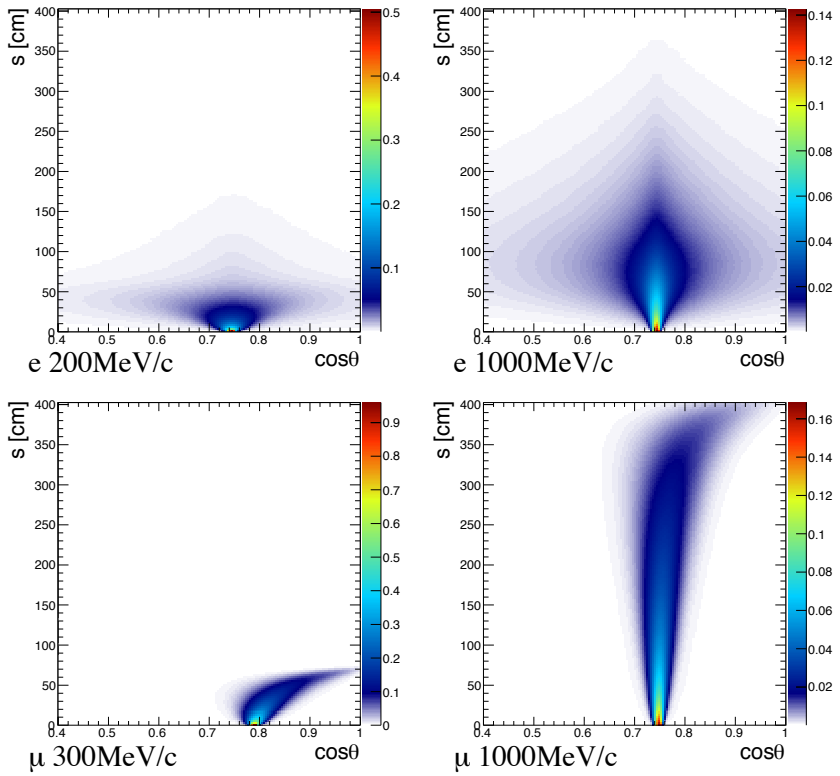

Figure 4.11: Cherenkov emission profile for electrons (top) and muons (bottom) at different initial momenta. Taken from [110].

- $\Omega(R)$ is the solid angle factor:

$$\Omega(R) = \frac{a^2}{2(R^2 + a^2)} \tag{4.9}$$

  where $a = 25.4$ cm is the PMT radius. It is a good approximation for $R > 1$ m.

- $T(R)$ is the light transmission factor which describes the attenuation of the direct light due to absorption and scattering in water. It takes the following form:

$$T(R) = \exp(-R/L^{\text{att}}) \tag{4.10}$$

  where L^{att} is the attenuation length. It is determined by MC studies to be 72 m.

- $\epsilon(\eta)$ is the PMT angular acceptance function, with the effect of shadowing by neighboring PMTs taken into account. It is obtained by detector simulation.

The predicted charge from indirect light due to light scattering in water or reflection from detector parts are calculated by the following integrand:

$$\mu_i^{\text{sct}} = \Phi(p) \int \mathrm{d}s \ \frac{1}{4\pi} \rho(p, s) \Omega(R) T(R) \epsilon(\eta) A(s) \tag{4.11}$$

where

$$\rho(p, s) = \int \mathrm{d}\Omega \ g(p, s, \cos\theta) \tag{4.12}$$

is the fraction of photons emitted per unit track length, at a distance s from the vertex along the particle trajectory; it amounts to an isotropic light source. Without the term $A(s)$, Eq. 4.11 is equivalent to the total charge of an isotropic light source traveling along the track with the same intensity as the Cherenkov radiation:

$$\mu_i^{\text{iso,dir}} = \Phi(p) \int \mathrm{d}s \ \frac{1}{4\pi} \rho(p, s) \Omega(R) T(R) \epsilon(\eta) \tag{4.13}$$

therefore,

$$A(s) = \frac{\mathrm{d}\mu_i^{\text{sct}}}{\mathrm{d}\mu_i^{\text{iso,dir}}} \ ^4 \tag{4.14}$$

In practice, $A(s)$ is tabularized by six parameters as illustrated by Figure 4.12:

$$A(s) = A(x_{\text{PMT}}, z_{\text{vtx}}, R_{\text{vtx}}, \varphi, \phi, \theta) \tag{4.15}$$

[4]There is an option in SKDETSIM to track the origin of each photon; the simulation of PMT response can be turned off for the direct light in order to calculate the predicted charge only from indirect light.

which is also referred to as the scattering table. If the Cherenkov opening angle does not depend on the momentum of the particle (a good assumption for electrons), then $A(s)$ has no dependence on the momentum, which means the scattering table are common for particles of any momentum given it only depends on the relative positioning of the PMT and the particle and its direction. The scattering table is linearly interpolated during the fit.

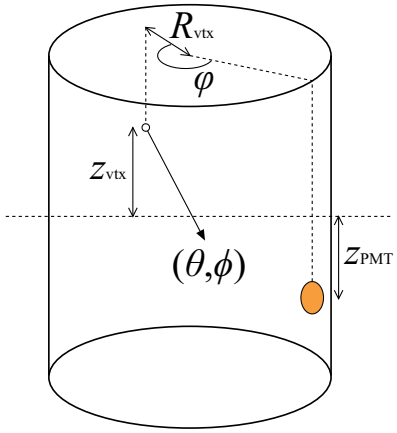

Figure 4.12: A schematic diagram which describes the relevant variables for the scattering table. Taken from [110].

Integrating Eq. 4.7 and Eq. 4.11 can be prohibitively slow. Therefore, the following approximation is employed when calculating the integrands:

$$J(s) = \Omega(R)T(R)\epsilon(\eta) \approx j_0 + j_1 s + j_2 s^2 \tag{4.16}$$

where the coefficient j_i are evaluated using three points on the particle trajectory. Since $A(s)$ changes slowly as a function of s, the following approximation is made for indirect light:

$$J(s)A(s) \approx k_0 + k_1 s + k_2 s^2 \tag{4.17}$$

The total predicted charge for each PMT is

$$\mu_i = \mu_i^{\text{dir}} + \mu_i^{\text{sct}} \tag{4.18}$$

4.2.4 Unhit probability and charge likelihood

The predicted charge in Eq. 4.18 is the averaged charge on a PMT, therefore the probability of producing no charge when the average is μ is $e^{-\mu}$. In order to take into account the threshold effect of PMTs, the following unhit probability is used:

$$P(\text{unhit}|\mu) = \left(1 + a_1\mu + a_2\mu^2 + a_3\mu^3\right) e^{-\mu} \tag{4.19}$$

where the coefficients are obtained from detector simulation.

The charge likelihood $f_q(q|\mu)$ is generated in the following way: photoelectrons are generated following a Poisson distribution with mean μ, and the observed charge q by the hit PMTs is obtained through detector simulation. Figure 4.13 shows an example of the normalized charge likelihood for different values of predicted charge. The charge likelihood is evaluated in the fit through interpolations.

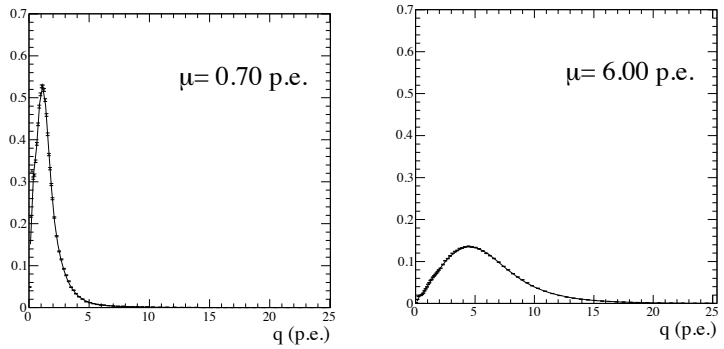

Figure 4.13: The normalized charge likelihood $f_q(q|\mu)$ with given predicted charge. The data points are obtained from detector simulation, and the polynomial fit is shown by the solid lines.

4.2.5 Time likelihood

The time likelihood $f_t(t_i|\mathbf{x})$ is expressed in terms of the predicted charge from direct and indirect light, particle momentum and the following residual time:

$$t_i^{\text{res}} = t_i - t - s_{\text{mid}}/c - |\boldsymbol{R}_i^{\text{PMT}} - \boldsymbol{x} - s_{\text{mid}}\boldsymbol{d}|/c_n \tag{4.20}$$

where $\boldsymbol{x}, t$ are the event vertex and time, d is the particle direction, s_{mid} is the half-length of the track, $\boldsymbol{R}_i^{\mathrm{PMT}}$ is the PMT position, c_n is the speed of light in water. The time likelihood is written as:

$$f_t(t_i^{\mathrm{res}}) = \omega f_t^{\mathrm{dir}}(t_i^{\mathrm{res}}) + (1-\omega) f_t^{\mathrm{sct}}(t_i^{\mathrm{res}}) \tag{4.21}$$

where

$$\omega = \frac{1 - e^{-\mu^{\mathrm{dir}}}}{1 - e^{-\mu^{\mathrm{dir}}} e^{-\mu^{\mathrm{sct}}}} \tag{4.22}$$

$f_t^{\mathrm{dir}}(t_i^{\mathrm{res}})$ and $f_t^{\mathrm{sct}}(t_i^{\mathrm{res}})$ are the time likelihood from direct and indirect light, respectively, which are dependent on the predicted charge and particle momentum as well (the width of the residual timing distribution is determined by the particle momentum and predicted charge).

Particle gun simulation studies are used to generate direct light residual time distributions for various values of particle momentum and predicted charge, and each distribution is fitted with a Gaussian. The evaluation of the direct light time likelihood is done through interpolation in the fit. The residual time distributions from indirect light is currently modeled by the following expression:

$$f_t^{\mathrm{sct}}(t^{\mathrm{res}}) = 1/\left(\sqrt{\frac{\pi}{2}}\sigma + 2\gamma\right) \times \begin{cases} \exp(-\tau^2/2\sigma^2) & (\tau < 0) \\ (\tau/\gamma + 1)\exp(-\tau/\gamma) & (\tau > 0) \end{cases} \tag{4.23}$$

where $\tau = t^{\mathrm{res}} - 25\mathrm{ns}$, $\sigma = 8\mathrm{ns}$, and $\gamma = 25\mathrm{ns}$ are obtained from a fit to indirect light-only simulation study. The functional shape is chosen to reproduce the typical shape of the indirect light time residual distribution which has a long tail on the right due to the reflected light.

4.2.6 Single-ring event reconstruction

After the vertex pre-fit and subevent finding algorithms described in section 4.2.1, for each subevent the fiTQun single-ring hypotheses consider three types of particles: electron, muon and $\pi^{\pm}$. Compared to the electron and muon hypotheses, the $\pi^{\pm}$ hypothesis has an extra parameter for the energy lost before it interacts hadronically. For each particle hypothesis, the best track parameters $\mathbf{x}$ are found by minimizing $-\ln\mathcal{L}$, where $\mathcal{L}$ is the likelihood described by Eq. 4.5. The minimizer program used in fiTQun is MINUIT [112]; aside from the best-fit track parameters it also returns the value of $-\ln\mathcal{L}$. The particle ID is determined by the comparison of the log likelihood of different particle type hypotheses. For example, if a track

has $\ln(\mathcal{L}_e/\mathcal{L}_\mu) > 0$, then it is more likely to be an electron track rather than a muon track. In practice, the following criteria is chosen to distinguish e-like and μ-like events:

$$\ln(\mathcal{L}_e/\mathcal{L}_\mu) > 0.2 \times p_e^{\text{rec}}[\text{MeV}/c] \tag{4.24}$$

where p_e^{rec} is the reconstructed momentum in the electron hypothesis. Figure 4.14 shows the $\ln(\mathcal{L}_e/\mathcal{L}_\mu)$ v.s. p_e^{rec} distributions from electron and muon particle gun studies. It can be clearly seen that the two species are well separated by such a cut line. In practice, the cut criteria such as the e v.s. μ, μ v.s. $\pi^\pm$, or single-ring v.s. multi-ring separation can be decided by the user based on the needs of individual analyses.

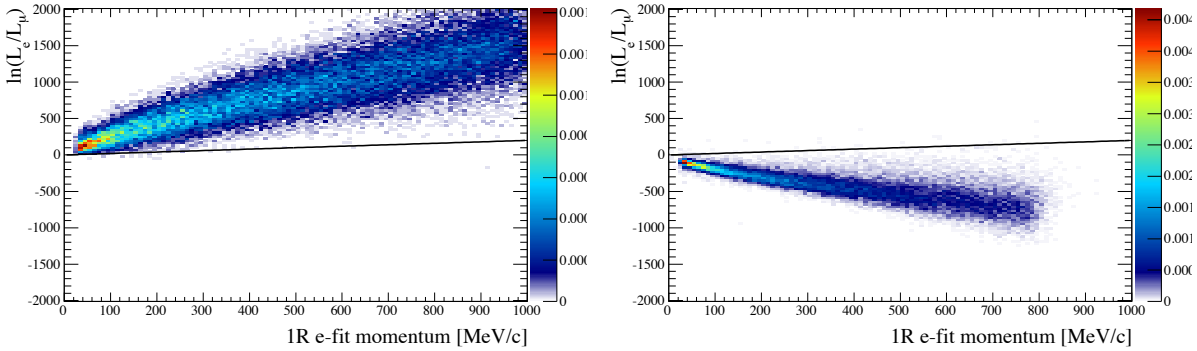

Figure 4.14: FiTQun likelihood separation of single-ring electron (left) and muon (right) particle gun events. The black lines show the cut criteria for the e/μ separation. Taken from [113].

4.2.7 Multi-ring fit

A dedicated π^0 fit is written in fiTQun by extending the single-ring fit formulation to include two γ's with a shared vertex. Figure 4.15 shows the π^0 hypothesis schematic: π^0 almost always decays instantly into two photons, and each photon then travels some distance before producing a e^+e^- pair that travel in the same direction as the photon. Therefore, the signature of a π^0 is two showering tracks that can be traced back to a common vertex. As a result, the π^0 hypothesis has 12 tracks parameters: the common vertex (x, y, z, t), the directions of both photons $(\theta_1, \phi_1), (\theta_2, \phi_2)$, the photon momenta p_1, p_2, and the distance d_1, d_2 the photons travel before converting into e^+e^-. The likelihood is evaluated by the same procedure as previously described and the best-fit track parameters are found through $-\ln\mathcal{L}$ minimization.

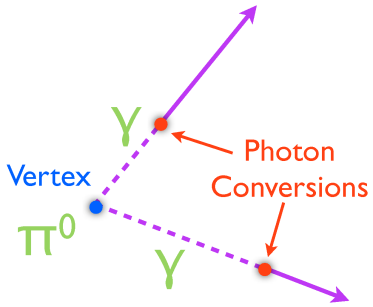

Figure 4.15: A diagram showing how the π^0 hypothesis is constructed [110].

Neutral current π^0 events are one of the two major backgrounds to T2K ν_e appearance analyses. T2K oscillation analyses have adopted a fiTQun π^0 rejection cut in the ν_e event selection, which reduces the NCπ^0 background by more than 60% [32] relative to the original reconstruction algorithm. Other dedicated fitters can and have been developed in fiTQun for studies such as proton decay search $p \to K^+\nu$ and selection of neutrino CC1π^+ interactions.

A more generic multi-ring fit is only performed on the first subevent to reconstruct up to six rings. Figure 4.16 shows the flow of the multi-ring fit. It starts with either an electron ring or a π^+ ring (the π^+ hypothesis can also fit for a muon), and adds one electron or π^+ ring to the same vertex; the best 2R hypothesis is chosen as the 2R fit outcome. A decision is made based on the best 2R likelihood and the best single-ring likelihood, and the added ring is accepted if the 2R hypothesis yields a better fit to the event. Then the algorithm goes on adding more rings following a similar procedure until adding a ring stops improving the fit. The raw outcome of this sequential multi-ring fit often contains fake rings; therefore followup fake ring reduction and ring merging algorithms are applied to identify and eliminate the fake rings. The details of the complete fiTQun multi-ring algorithm can be found in section 6.10 of [111].

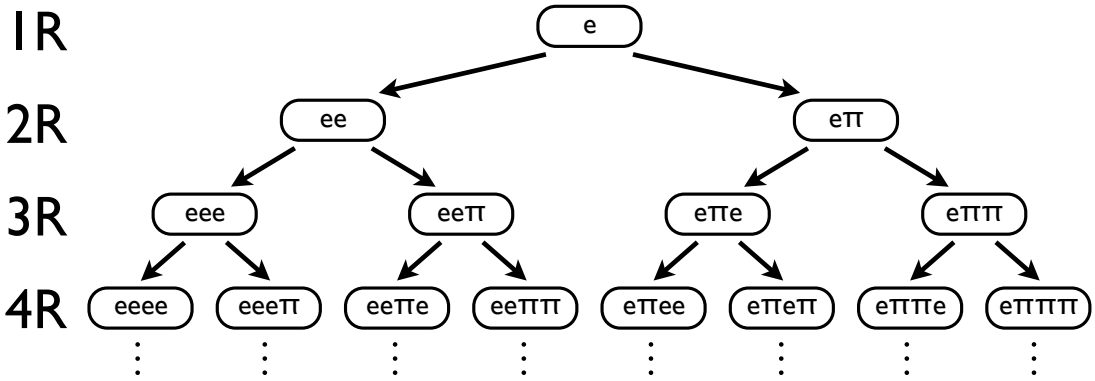

Figure 4.16: A diagram showing how the sequential multi-ring fit in fiTQun is evolved. The diagram assumes the first ring is an electron; the same procedure can be done assuming the first ring is a π^+. Taken from [111].

Chapter 5

Data reduction and T2K event selection

5.1 Data reduction

Data reduction is a process to trim down the raw data for physics analyses. The cosmic ray muon rate in SK is about 3 Hz; whereas there are the roughly 10 atmospheric neutrino events a day in the ID. Therefore, data reduction is needed in order to extract events that contain neutrino interactions from the vast background. This section describes the data reduction procedures for SK atmospheric neutrino data and the T2K beam neutrino data. The events used in this thesis are the neutrino interactions which happen in the ID and the outgoing particles all stop in the ID, or the fully contained (FC) events. In the standard SK atmospheric neutrino-only analyses, partially contained events and upward-going muon events are also used, but the data reduction procedures for selecting those events will not be discussed since they are not used in this analysis.

5.1.1 SK FC atmospheric neutrino event reduction

The SK atmospheric neutrino data FC reduction is done using the existing SK software. The FC reduction steps are summarized here directly following [114] and [111], in which more details can be found.

- **The first and second reduction** are designed to effectively filter out cosmic ray muons, electronic noise and low energy backgrounds. It is required that the total charge in ID PMT hits is more than 200 p.e. (the would-be energy deposit from a 22 MeV/c electron), and the number of OD hits within a 800 ns time window should not exceed 50 (such as in a typical cosmic ray muon event), or 30 for events with less than 100,000 p.e. ID charge. Furthermore, an event should not have more than half of the total ID charge originating from a single PMT within a 300 ns time window, as such events are likely due to PMT electronic discharge (they are called the "flasher" events). These cuts reduce the raw data from $\sim 10^6$ events/day to ~ 200 events/day.

- **The third reduction** is aimed at further removing the cosmic muon and low energy backgrounds. A cosmic muon can leave low OD activity, and such events would remain after the first and second stages of data reduction. A fast through-going muon fitter is applied to reconstruct the entering and exiting points; events that agree well with the through-going muon hypothesis are rejected, as well as those with more than 9 OD hits within 8 m from the entering or exiting point, as they are also likely to be true cosmic muon events. Similar rejection cuts can be done for cosmic muons that stop in the ID. Another type of cosmic muon event consists of muons which go through the twelve holes at the top of SK where the bundles of cables for the PMTs enter the ID. Such muons are indetectable in the OD. These muon events can be vetoed by the plastic scintillator plates installed on the top of each cable hole.

  The remaining low energy and noise background events are removed by requiring that the total number of ID hits within a 50 ns time-of-flight corrected time window is more than 50 (corresponding to a 9 MeV/c electron), in which the time-of-flight correction is calculated based on a rough vertex reconstruction using only PMT hit timing information. Flasher events tend to have a broader timing distribution and therefore can be removed by requiring that the total number of ID hits within a 100 ns running time window between 300-800 ns after the trigger is less than 20. Lastly, the coincidence events in which a cosmic ray muon event happens shortly after a low energy event trigger would leave no OD trigger in the triggering time but have high ID activity. These events can be removed by requiring that the total number of OD hits between 400-900 ns after the trigger is less than 20, and that the number of p.e. measured in the ID in the same time window is less than 5000. The third reduction further reduces the number of events to ~ 45 events/day.

- **The fourth reduction** further removes flasher events, which tend to repeat similar PMT hit patterns in the detector. Therefore, a pattern matching algorithm is applied

to identify and remove flasher events, in which the charge correlations among 10,000 neighboring events are calculated and the highly correlated events are removed. ~ 18 events/day are left after the fourth reduction.

- **The fifth reduction** is designed to remove the remaining cosmic ray muon and flasher backgrounds. When a cosmic ray muon below Cherenkov threshold enters the detector, its decay electron can be detected in the ID with hits in the OD prior to the triggering time. Events of which the total charge in the ID is less than 1000 p.e. and the OD activity before the ID trigger is high are rejected as invisible muons. Finally, the remaining flasher events can be removed by the same method used in the third reduction but with a tighter cut. ~ 16 events/day remain after all the five reduction stages.

5.1.2 T2K beam neutrino event reduction

The T2K event reduction begins by selecting events induced by "good spills" sent from J-PARC. The following criteria are required of a good spill [60]:

1. SK DAQ should be alive during the spill.
2. It is not a bad subrun. A "subrun" in SK is a data block approximately one minute long. A subrun can be discarded if there are known reasons for concern such as flasher events or DAQ errors.
3. The number of ID and OD PMT dark noise hits during the 1 msec around beam spill arrival time should be approximately constant; a spill is discarded if this is not the case, which usually indicates DAQ problems. An error in the GPS reading would also disqualify a spill for data analysis.
4. The spill shouldn't coincide with a special data block. There are two kinds of special data block in SK: the "pedestal block" for taking pedestal data of all the channels on the front-end electronics modules which happens every 1.1 sec and lasts for 17 μsec; the "TDC reset block" for resetting the counters in the TDC chips which happens every ~ 70 msec and also lasts for 17 μsec.
5. Finally, there should not be any detector activity in the 100 μsec before the spill arrival time. This is aimed at removing the accidental contamination by Michel electrons from cosmic muon decays.

The total number of spills in T2K Runs 1-8 after each good-spill cut and the corresponding inefficiency is shown in Table 5.1. The overall SK inefficiency for T2K data taking is about 1%.

	Number of spills	Inefficiency
Beam good spills	16,295,856	
(1) SK DAQ alive	16,262,927	0.20 %
(2) Bad subrun cut	16,226,930	0.22 %
(3) Incomplete data/GPS error cut	16,217,652	0.06 %
(4) Special data block cut	16,204,459	0.08 %
(5) Pre-activity cut	16,131,492	0.45 %
Total	16,131,492	1.01 %

Table 5.1: Number of spills after each cut used to select the good spills for physics analyses of the T2K data observed at SK during the T2K beam Runs 1-8.

The events found in the ± 500 μsec T2K timing window from good spills are classified into four categories: calibration events, OD events, LE (low energy) events and FC events. Although SK calibration is normally scheduled when T2K beam is not running, whether a T2K event has happened during a calibration run is still checked. Among the remaining events, those with more than 15 OD hits are classified as OD events. Most of the OD events are from cosmic ray muons. Events with less than 200 p.e. (corresponding to a 20 MeV/c electron) total charge in the ID within a 300 ns time window from the trigger are classified as LE; the remainder are FC events. The flasher cut is deemed unnecessary for T2K events as the timing information is sufficient in removing this background. The OD, LE and FC events are further divided by the event timing with respect to the spill arrival time: events that arrive between -2 μsec and 10 μsec are called on-timing events, which are passed on to T2K analyses; the remaining events in the ± 500 μsec window are off-timing events. Only the FC on-timing events are used in the T2K three-flavor oscillation analyses. Figure 5.1 shows the ΔT_0 (ΔT_0 is the time-of-flight corrected time difference between a neutrino event and the beam trigger) distribution for all the on-timing FC events. The T2K events observed at SK clearly exhibit the bunch structure of the beam spills; the 581 ns bunch interval is evident in the FC events.

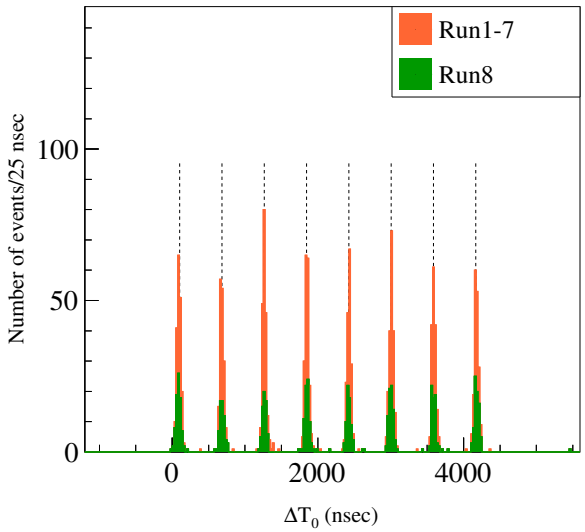

Figure 5.1: ΔT_0 distribution of all the T2K FC events (zoomed into the spill on-timing window) observed during Runs 1-7 (orange) and Run 8 (green). The eight dotted vertical lines represent bunch centre positions fit to the observed FC event times preserving the inter-bunch spacing of 581 ns. The two histograms are stacked.

5.2 T2K event selection optimization

This section presents an event selection optimization study using the fiTQun reconstruction algorithm at Super-K. It has been demonstrated that fiTQun can effectively remove π^0 background, which is the major background in the electron neutrino appearance samples [32]. However, the π^0 cut was previously chosen to remove as much NC π^0 background as possible while keeping the same ν_e CC signal efficiency as the previous cut. In addition, one of the major backgrounds in the disappearance samples – the NC1π^+ background – can be removed by using the single-ring π^+ fit provided by fiTQun, which cannot be done with the previous reconstruction algorithm (APfit). In order to move to fiTQun-based oscillation analysis, we decided to revisit the π^0 cut for the appearance samples, and optimize the π^+ cut for the disappearance samples.

It is always a concern when developing event selections, that we will not necessarily obtain results that yield the best sensitivity by using simple metrics such as $S/\sqrt{S+B}$ because they largely ignore the details of the systematic uncertainties and their effect on the sensitivity. For example, the T2K ν_μ disappearance sample has a large $NC1\pi^+$ background near the oscillation dip, and its fractional uncertainty is 55% compared to $\sim$ 3% signal

uncertainty [115]. A simple metric may not cut out $NC1\pi^+$ background as aggressively as it should. This motivated us to develop a framework that uses sensitivity or precision of certain measurements as the metric to optimize event selections and that takes into account systematic uncertainties.

This study aims to optimize the π^+ cut based on the T2K sensitivity to $\sin^2\theta_{23}$ and the π^0 cut based on the δ_{CP} sensitivity assuming full T2K statistics with 50% FHC running and 50% RHC running. The optimization strategy will be discussed, as will the comparison between the new fiTQun-based samples and the APfit-based samples.

5.2.1 Optimization strategy

The software used to calculate sensitivities is essentially a joint fit with four CCQE-like samples: the SK reconstructed energy spectra in both appearance and disappearance channels, and both FHC and RHC modes are used in the fit. Since the selected events are predominantly CCQE, the neutrino energy can be reconstructed based on the lepton kinematics:

$$E_{rec} = \frac{m_p^2 - (m_n - E_b)^2 - m_l^2 + 2(m_n - E_b)E_l}{2(m_n - E_b - E_l + p_l\cos\theta)} \tag{5.1}$$

where m_p is the proton mass, m_n is the neutron mass, E_b is the oxygen nucleus binding energy, E_l is the lepton energy and p_l is the lepton momentum. Because the beam direction is known, the lepton direction relative to the incoming neutrino direction, θ, can be reconstructed. The number of events for each neutrino type in each 50 MeV reconstructed energy bin E_r is calculated by the following formula:

$$N_i(E_r) = \sum_{E_t}\sum_{j} R_{ij}(E_t, E_r)P_{ij}(E_t) \tag{5.2}$$

where

- Index i indicates neutrino type: $\nu_\mu \to \nu_\mu$, $\nu_e \to \nu_e$, $\bar{\nu}_\mu \to \bar{\nu}_\mu$, $\bar{\nu}_e \to \bar{\nu}_e$, $\nu_\mu \to \nu_e$, $\bar{\nu}_\mu \to \bar{\nu}_e$.
- Index j indicates interaction types: CCQE (including 2p2h), CC1π, CCother, NC1π, NCother.
- E_t is the true energy, and E_r is the reconstructed energy.
- $R_{ij}(E_r, E_t)$ is the unoscillated E_t v.s. E_r map for neutrino type i and interaction type

j built from looping through T2K MC events that have passed all cuts, which has the beam flux, cross section and detector efficiency information encoded. $R_{ij}(E_r, E_t)$ is re-evaluated for each new event selection.

- $P_{ij}(E_t)$ is the oscillation probability for neutrino type i and interaction type j calculated using Prob3++ [116].

The approved T2K full statistics, namely 7.8×10^{21} POT is assumed, with 50% in FHC-mode and 50% in RHC-mode. T2K Run1-4 best fit oscillation parameters as shown in Table 5.2 are assumed as the truth in the optimization.

parameter	Nominal value	Treatment
$\sin^2 2\theta_{13}(\sin^2 \theta_{13})$	0.0849 (0.0217)	fitted
δ_{CP}	-1.601	fitted
$\sin^2 \theta_{23}$	0.528	fitted
$\sin^2 \theta_{12}$	0.304	fixed
Δm^2_{32}	2.509^{-3} eV^2	fitted
Δm^2_{21}	7.53×10^{-5} eV^2	fixed
Hierarchy	Normal	fixed
Earth matter density	2.6 g/cm^3	
Base-line	295 km	

Table 5.2: Values of oscillation parameters used in this study as well as the treatment in the fit.

The χ^2 curve of $\sin^2 \theta_{23}$ or δ_{CP} is obtained in the following steps: (1) The "nominal" reconstructed energy spectra are generated using the oscillation parameters in Table 5.2, and the minimum χ^2 with respect to the nominal reconstructed energy spectra is calculated for a number of "trial" values of oscillation parameter $\sin^2 \theta_{23}$ or δ_{CP}; (2) for a given "trial", the parameter in question is fixed at its trial value while the remaining oscillation parameters are allow to vary to match with the "nominal" spectra, which is done by minimizing the χ^2 without systematic uncertainties; (3) all oscillation parameters are fixed at the best-fit values from the previous step, and systematic error nuisance parameters are allowed to vary in the fit to obtain minimum χ^2; (4) the same minimization in step (2) and (3) are repeated for all trial values of the parameter, and the χ^2 curve as a function of the parameter value can be made. The sequential fitting method in step (2) and (3) was used to save computation time; it ignores the correlation between oscillation parameters and systematic error nuisance parameters.

The following constraint on $\sin^2 2\theta_{13}$ from reactor experiments is also included in the fit:

$$\chi^2_{reactor} = \frac{(\sin^2 2\theta_{13} - \sin^2 2\theta'_{13})^2}{\sigma^2}, \tag{5.3}$$

where $\sigma = 0.005$ and $\sin^2 2\theta_{13}$ ($\sin^2 2\theta'_{13}$) is the true (test) value of $\sin^2 2\theta_{13}$. An example of the constant $\Delta\chi^2$ curves generated by the fitter is shown in Figure 5.2. Also shown are the optimization metrics: the 1σ width of $\sin^2\theta_{23}$ $\Delta\chi^2$ and $\delta_{CP} \neq 0$ significance $\chi^2(\delta_{CP} = 0) - \chi^2(\delta_{CP} = \delta^{true}_{CP})$.

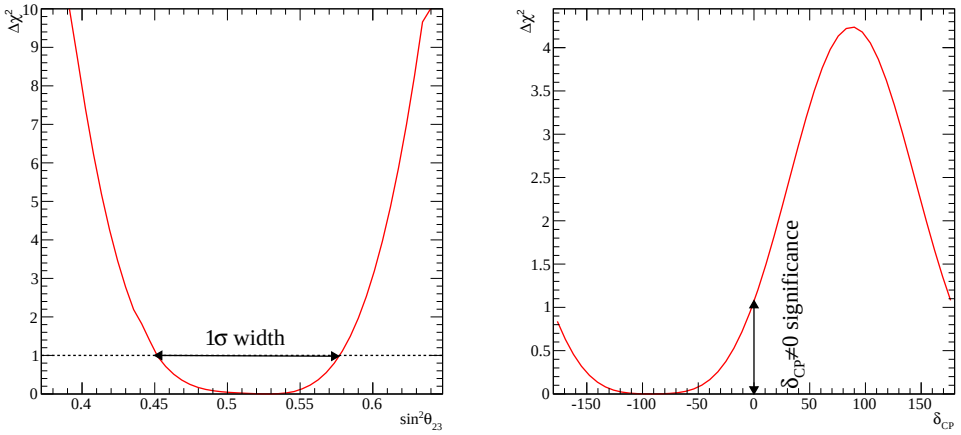

Figure 5.2: Example 1D $\Delta\chi^2$ maps with 7.8×10^{21} POT, 50% FHC-mode and 50% RHC-mode, including systematics errors and using the oscillation parameter shown in Tab.5.2. Left: the 1σ width of the $\sin^2\theta_{23}$ 1D contour; right: significance of $\delta_{CP} \neq 0$.

In T2K official analyses, systematic uncertainties can be categorized into three groups: cross section uncertainties, flux uncertainties, and SK related uncertainties as shown in Figure 5.3. The cross section and flux systematic error parameters can alter the reconstructed energy spectra in a non-trivial way ("shape" parameters in Table 5.3). Typically systematic errors are applied on an event-by-event [117] or bin-by-bin [118] basis as a function of neutrino energy, lepton angle/momentum etc.; splines [1] are introduced for certain cross section parameters that can change the shape of the energy spectra [117].

In order for this study to be computationally feasible, the same treatment of systematic errors as implemented by the official analyses cannot be used. Instead, one can use the total systematic uncertainties on reconstructed energy and their bin-by-bin correlation, which are generated based on the 2015 version of T2K systematic uncertainties. The procedures, more

[1] A spline is a function defined by segments of polynomials stitched together.

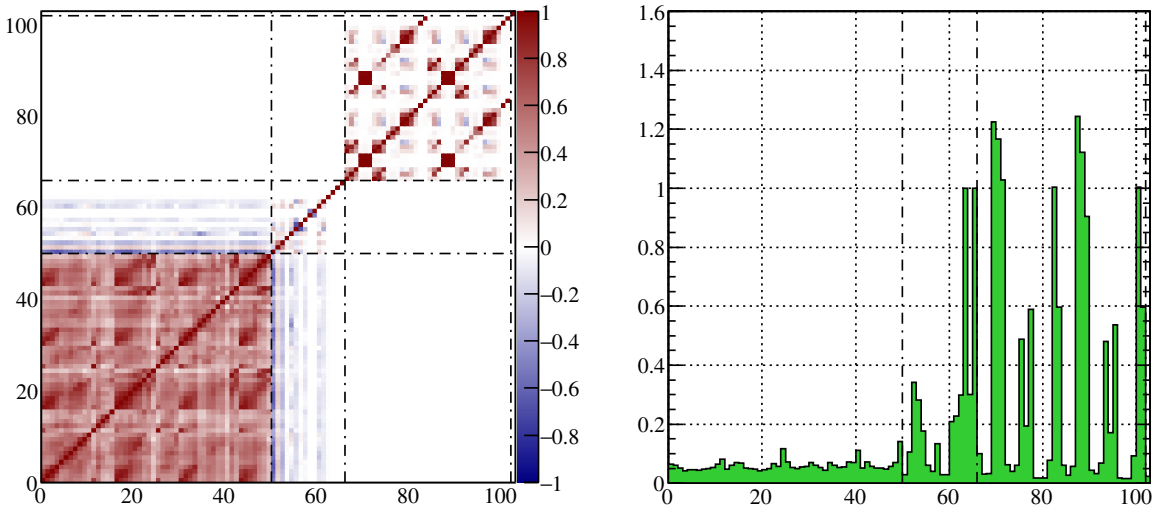

Figure 5.3: Correlation matrix (left) describing the relationship between the 103 systematic parameters of the analysis and the square root of the diagonal elements of the covariance matrix (right). Parameters are 0-49: beam flux, 50-65: interaction and cross section parameters, 66-101: SK FHC 1Re, FHC 1Rμ, RHC 1Re, RHC 1Rμ, 102: SK energy scale parameter (not considered in this study).

specifically, are as follows:

- 1,000 sets of systematic error parameters are randomly generated from the post-ND280 fit flux and cross section best fit and covariance matrix [119]. For each set of systematic error parameters generated, a weight is generated and saved for each MC event using T2KReWeight [120]; the weights from systematic error parameters (2p2h anti-ν normalization, $\sigma_{\nu_e}/\sigma_{\nu_\mu}$, $\sigma_{\bar{\nu}_e}/\sigma_{\bar{\nu}_\mu}$, NC 1$\gamma$ normalization) that are not included in T2KReWeight are later added manually.

- 1,000 sets of systematic error parameters are randomly generated from SK detector error [121] and FSI+SI+PN (photonuclear effect) error covariance matrix, which is binned in APfit reconstructed energy, neutrino flavor and interaction mode. For each set of systematic error parameter generated, a weight is generated and saved for each MC event based on APfit reconstructed energy (as well as neutrino flavor and interaction mode). This is an approximation that has to be made for there was no SK+FSI/SI+PN errors available for fiTQun analysis. It is a reasonable one because SK+FSI/SI+PN systematic uncertainties are not expected to change significantly by switching from one reconstruction algorithm to another.

Parameter	Interaction category	type
M_A^{QE}	CCQE	shape
p_F	CCQE	shape
E_b	CCQE	shape
2p2h ^{16}O norm.	2p2h	norm
2p2h anti-ν norm.	2p2h	norm
C_A^{RES}	CC1π and NC1π	shape
M_A^{RES}	CC1π and NC1π	shape
BG_A^{RES}	CC1π and NC1π	shape
CC other shape	CC other	shape
CC coherent norm.	CC coherent	norm
NC coherent norm.	NC cohereht	norm
NC 1γ norm.	NC 1γ	norm*
NC other norm.	NC other	norm*
$\sigma_{\nu_e}/\sigma_{\nu_\mu}$	CC	norm*
$\sigma_{\bar{\nu}_e}/\sigma_{\bar{\nu}_\mu}$	CC	norm*

Table 5.3: Summary of the neutrino interaction parameters using the results of ND280 fit. Starred errors are not constrained by the near detector. Table is based on the 2015 version of T2K analyses.

- For each one of the 1,000 sets of systematic error parameters and for each event, the total weight is a product of the weight from the flux and cross section parameters and the weight from SK+FSI/SI/PN parameters.

- A reconstructed energy distribution is generated for each one of the 1,000 parameter sets. The covariance matrix is made according to the bin-by-bin correlation of the 1,000 reconstructed energy distributions. Each matrix element in the covariance matrix is calculated as follows:

$$\mathrm{COV}_{ij}^{E_{rec}} = \frac{1}{1000}\sum_{k=1}^{1000}(N_i^k - N_i^0)(N_j^k - N_j^0) \tag{5.4}$$

  where N_i^k is the expected number of events in the i^{th} reconstructed energy bin (the binning is show in Table 5.4) from the k^{th} systematic parameter set, and N_i^0 is that of the nominal distribution. It is the fractional error matrix that is used in the fit:

$$\mathrm{COV}_{ij}^{err} = \frac{\mathrm{COV}_{ij}^{E_{rec}}}{N_i^0 N_j^0} \tag{5.5}$$

The covariance matrix and fractional error matrix are re-generated for each trial fiTQun cut,

as it modifies the number of events in each bin.

	Binning (GeV)	Bin number
Appearance	0.0-0.35, 0.35-0.45, 0.45-0.55, 0.55-0.65, 0.65-0.75, 0.75-0.85, 0.85-1.05, 1.05-1.25	1-8 & 21-28
Disappearance	0.0-0.4, 0.4-0.5, 0.5-0.6, 0.6-0.7,0.7-0.8, 0.8-1.0, 1.0-1.25, 1.25-1.5, 1.5-3.5, 3.5-6.0, 6.0-10, 10-30	9-20 & 29-40

Table 5.4: Binning of the reconstructed energy distributions used to build covariance matrix. The first 20 bins are for FHC-mode, and the rest RHC-mode.

All T2K systematic errors except for the energy scale uncertainty are taken into account. This is because energy scale uncertainty has to be treated in a different way than the rest. Its impact on sensitivity is negligible [117] in comparison, and it is not the absolute sensitivity but the relative sensitivities of different cuts that we are after. Therefore it was dropped. An example of the covariance matrix and correlation matrix of the systematic errors are shown in Figure 5.4.

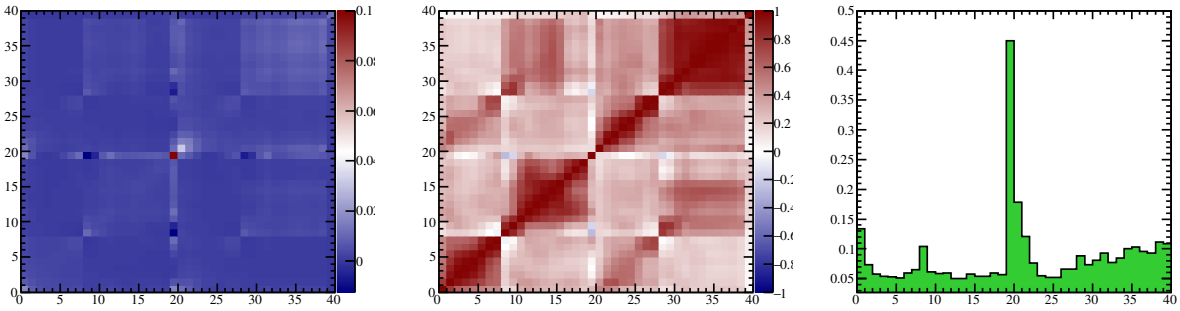

Figure 5.4: Covariance matrix as defined by Eq 5.5 (left), correlation matrix (middle) and magnitude (right) of systematic uncertainties binned in reconstructed energy.

5.2.2 Cut Parameterization

The main background in the ν_μ disappearance samples is the NC1π^+ background near the oscillation dip. It has a systematic uncertainty of 55% [115], which is much larger than the signal uncertainty. FiTQun offers the possibility to reduce the NC1π^+ background by providing a single-ring π^+ likelihood. This NC1π^+ cut is parameterized as a straight line ($y = a_\mu x + b_\mu$) in $\ln(\mathcal{L}_{\pi^+}/\mathcal{L}_\mu)$ v.s. the reconstructed μ momentum phase space as shown

by Figure 5.5, where $\mathcal{L}_{\pi^+}$ is the likelihood of the single-ring π^+ hypothesis, and $\mathcal{L}_\mu$ of the single-ring μ hypothesis.

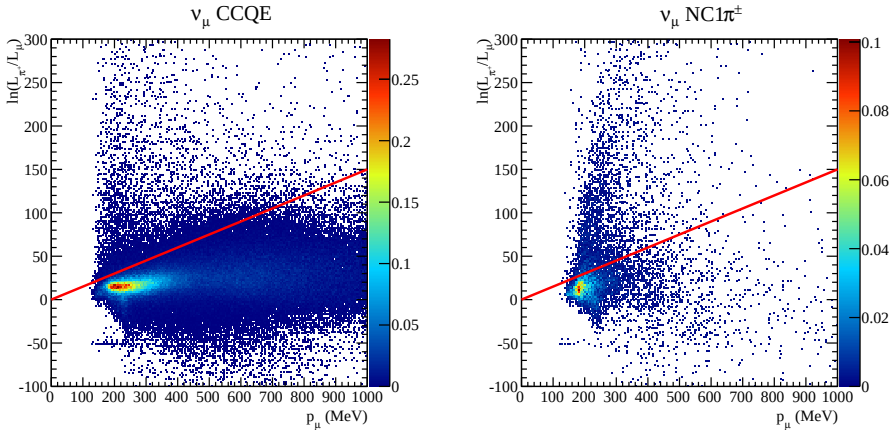

Figure 5.5: The $\ln(\mathcal{L}_{\pi^+}/\mathcal{L}_\mu)$ v.s. p_μ distributions. Left: signal ν_μ CCQE+2p2h; right: background NC1$\pi^\pm$ background. Only FC cut is applied. The π^+ cut is parameterized as a straight line in $\ln(\mathcal{L}_{\pi^+}/\mathcal{L}_\mu)$ v.s. p_μ phase space as indicated by the red lines, events above which are rejected.

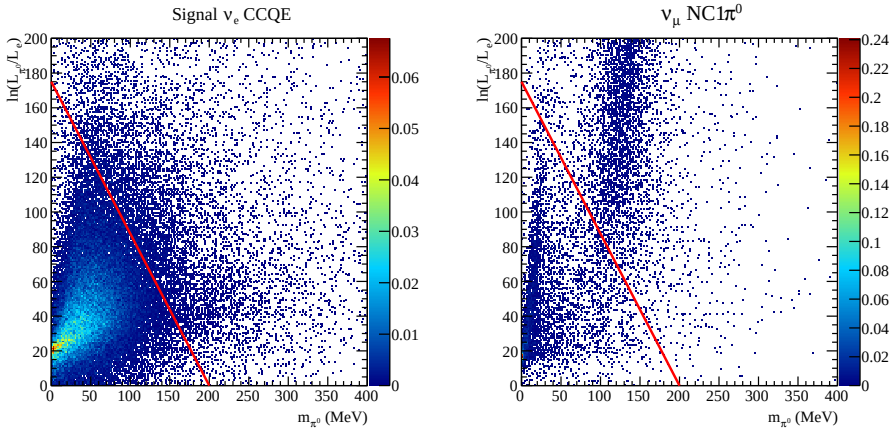

Figure 5.6: The $\ln(\mathcal{L}_{\pi^0}/\mathcal{L}_e)$ v.s. reconstructed π^0 mass distributions. Left: signal ν_e CCQE+2p2h (oscillated); right: background NC1π^0 background. Only FC cut is applied. The π^0 cut is parameterized as a straight line in $\ln(\mathcal{L}_{\pi^0}/\mathcal{L}_e)$ v.s. m_{π^0} phase space as indicated by the red lines, events above which are rejected.

FiTQun π^0 cut has previously been applied to the APfit-selected ν_e appearance sample. However it was chosen based on a rough signal/background separation. This study adopted the same π^0 cut parameterization ($y = a_e x + b_e$) in $\ln(\mathcal{L}_{\pi^0}/\mathcal{L}_e)$ v.s. reconstructed π^0 mass

phase space as shown by Figure 5.6, where $\mathcal{L}_{\pi^0}$ is the π^0 likelihood from fiTQun dedicated π^0 fitter [110]. For fiTQun π^+ cut optimization, pairs of (a_μ, b_μ) parameters are chosen from a grid. For each set of (a_μ, b_μ), a new systematic error covariance matrix is generated, and $\sin^2\theta_{23}$ sensitivity is evaluated. Aside from the π^+ cut, following criteria are also applied to select the $\nu_\mu/\bar{\nu}_\mu$ CCQE-like sample:

1. Fully-contained in SK fiducial volume: classified by OD activity and total PMT hits as fully contained events; $wall > 50$ cm, $towall > 250$ cm. Here "wall" is the distance between vertex and the nearest ID wall; "towall" is the distance between the vertex and ID wall along the direction at which the particle (in the case of multiple rings, it refers to the particle with the most energetic ring) travels. The SK fiducial volume cut is optimized for $\sin^2\theta_{23}$ measurement [122].

2. Number of rings found by the fiTQun fitter is one.

3. The ring is identified as muon-like by the single-ring fitter: $\ln(\mathcal{L}_e/\mathcal{L}_\mu) < 0.2 \times p_e$, where $\ln L_e$ is the fiTQun single-ring e-like hypothesis log likelihood, $\ln L_\mu$ is the single-ring μ-like log likelihood, and p_e is the reconstructed electron momentum of single-ring e-like hypothesis.

4. Reconstructed muon momentum of the single-ring μ-like hypothesis p_μ is larger than 200 MeV/c. This is to eliminate the proton background.

5. Number of sub-events (identified by hits timing clusters) is 1 or 2 (i.e. number of decay electrons is 0 or 1).

The result of π^+ cut optimization is shown in Figure 5.7. A pair of cut parameters, $a_\mu = 0.15$ and $b_\mu = 0$ are chosen from the center of the favored region, within which the difference in $\sin^2\theta_{23}$ precision is negligible. It should also be noted that compared with the result without systematic uncertainties, the optimization with systematics favors more aggressive cuts. In other words, it is beneficial to sacrifice efficiency in exchange for lower background, which is what one would expect from cases where background has a much larger systematic uncertainty than signal. Figure 5.8 shows the sensitivity of the parameters relevant to π^+ cut. Improvements in both $\sin^2\theta_{23}$ and Δm^2_{32} are expected from better NC background rejection and consequently better energy reconstruction, and indeed are achieved. Note that the APfit event selection uses a different fiducial volume definition – $dwall > 200$ cm, which has been the fiducial volume definition for all the previous APfit-based T2K analyses.

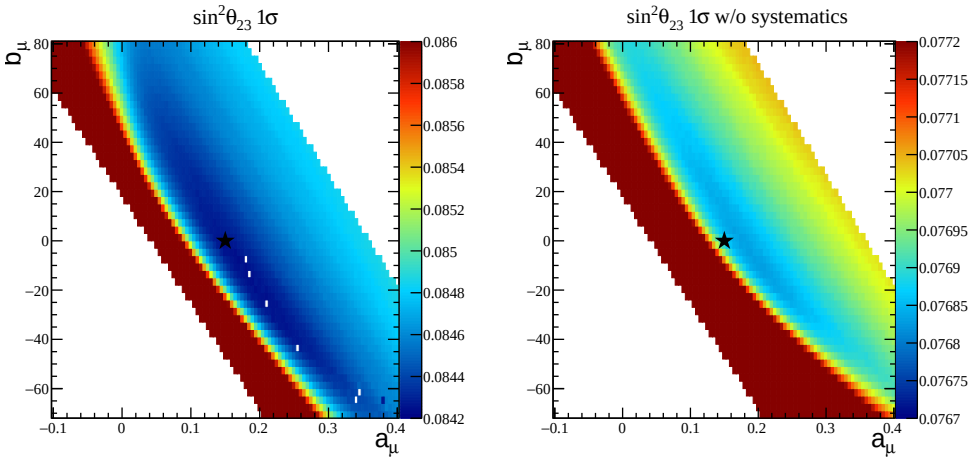

Figure 5.7: 1σ width of $\sin^2\theta_{23}$ $\Delta\chi^2$ curve (z-axis) as a function of the π^+ cut parameters a_μ and b_μ. Left: with systematics; right: without systematics. The star denotes the chosen value for fiTQun π^+ cut $a_\mu = 0.15$, $b_\mu = 0$

Similarly for the fiTQun π^0 cut optimization, pairs of (a_e, b_e) parameters are chosen from a grid. For each set of (a_e, b_e), a new systematic error covariance matrix is generated, and $\delta_{CP} \neq 0$ significance is evaluated. The following criteria are applied to select the $\nu_e/\bar{\nu}_e$ CCQE-like samples:

1. Fully-contained in SK fiducial volume: $wall > 80$ cm, $towall > 170$ cm.
2. Number of rings found by the fiTQun is one.
3. The ring is identified as electron-like by the single-ring fitter: $\ln(\mathcal{L}_e/\mathcal{L}_\mu) > 0.2 \times p_e$, where $\ln\mathcal{L}_e$ is the fiTQun single-ring e-like log likelihood, $\ln\mathcal{L}_\mu$ single-ring μ-like log likelihood, and p_e reconstructed electron momentum of single-ring e-like hypothesis.
4. Visible energy (fiTQun single-ring e-like hypothesis reconstructed energy) is greater than 100 MeV. In practice, we use fiTQun reconstructed single-ring electron momentum as the visible energy.
5. Number of decay electron is 0, i.e. 1 subevent.
6. Reconstructed neutrino energy E_{rec} is less than 1250 MeV

The result of π^0 cut optimization is shown in Figure 5.9. Because the current cut – $a_e = -0.875$ and $b_e = 175$ – yields negligible difference in significance ($< 0.05\sigma$) compared to

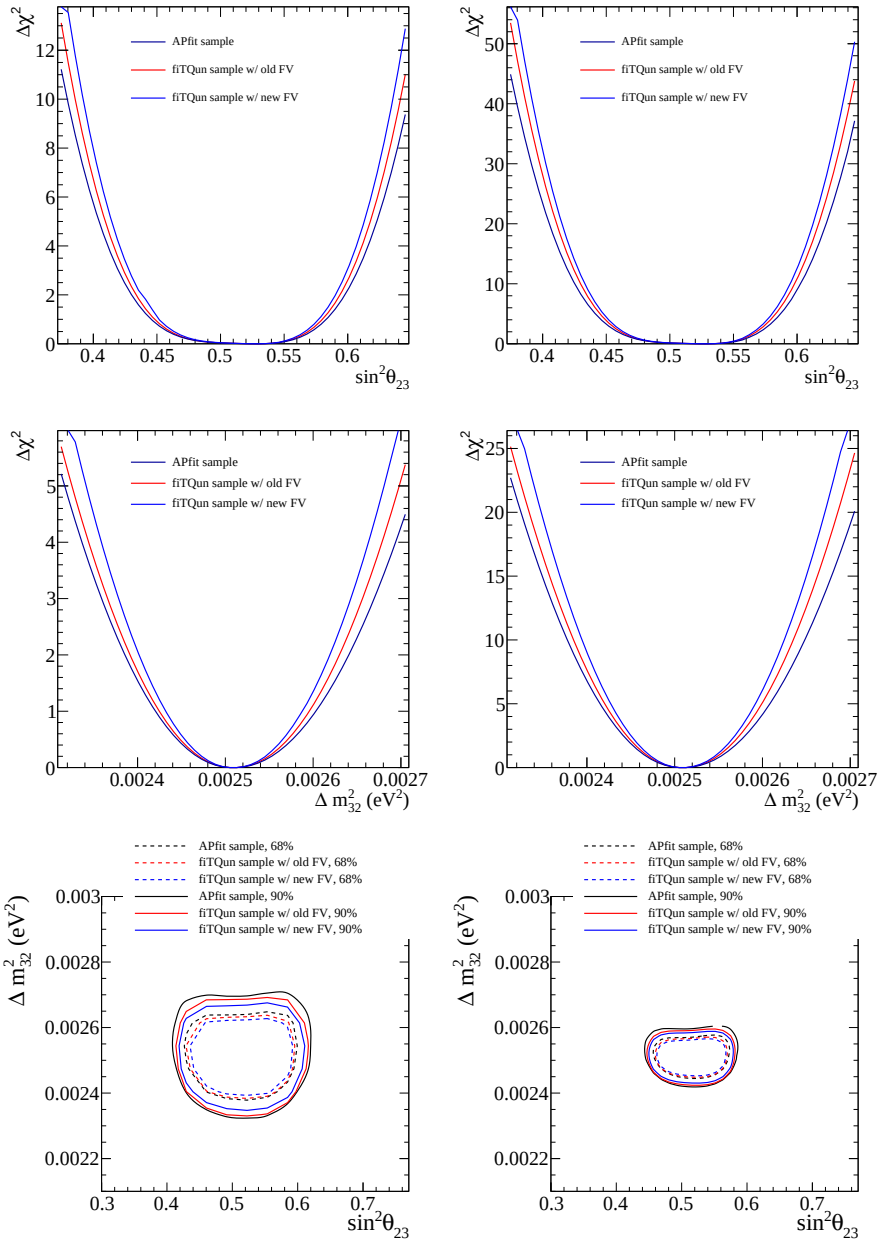

Figure 5.8: Sensitivity comparison between APfit samples and fiTQun samples. Left: T2K Run1-7 statistics (7.482×10^{20} FHC, 7.471×10^{20} RHC), right: T2K full statistics (3.9×10^{21} FHC, 3.9×10^{21} RHC). Top: $\sin^2\theta_{23}$, middle: Δm^2_{32}, bottom: $\sin^2\theta_{23}$ v.s. Δm^2_{32}. The values of oscillation parameters are shown in Table 5.2. The "new FV" refers to the cut *dwall* > 50 cm, *towall* > 250 cm; and the "old FV" refers to the cut *dwall* > 200 cm.

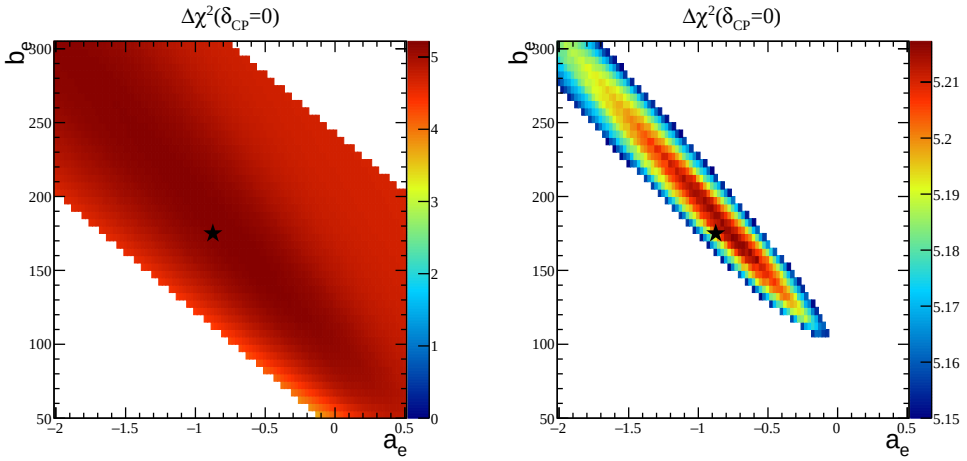

Figure 5.9: $\delta_{CP} \neq 0$ rejection significance (z-axis) as a function of π^0 cut parameters a_e and b_e. Right plot is left plot zoomed in. The star denotes the chosen value for fiTQun π^0 cut $a_e = -0.875$, $b_e = 175$.

the absolute optimum, we chose not to change it for now. Figure 5.10 shows the sensitivity relevant to the π^0 cut. The improvement in δ_{CP} sensitivity is not as significant as $\sin^2\theta_{23}$ and Δm^2_{32} because π^0 cut has already been applied to APfit ν_e selection. Note that APfit samples have the original fiducial cut $wall > 200$ cm applied, whereas fiTQun samples use the new fiducial cuts.

5.2.3 Comparison with APfit samples

Figure 5.11 shows the number of events after each cut in the ν_μ CCQE-like sample, and the corresponding numbers are shown in Table 5.5. We observe a $\sim 13\%$ increase in $\nu_\mu + \bar{\nu_\mu}$ signal, a $\sim 40\%$ reduction in CC non-QE background and a 50% reduction in NC background. The improvement is even more significant in sub-GeV region, which drives the sensitivities to $\sin^2\theta_{23}$ and Δm^2_{32}. Figure 5.12 shows the reconstructed energy distribution fo the fiTQun and APfit ν_μ CCQE-like samples. The POT assumed is the T2K Run1-7 FHC POT: 7.482×10^{20}.

Figure 5.13 shows the number of events after each cut in the $\bar{\nu}_\mu$ CCQE-like sample, and the corresponding numbers are shown in Table 5.6. Figure 5.14 shows the reconstructed energy distribution fo the fiTQun and APfit ν_μ CCQE-like samples. The POT assumed is the T2K Run1-7 RHC POT: 7.471×10^{20}.

Figure 5.15 shows the number of events after each cut in the ν_e CCQE-like sample,

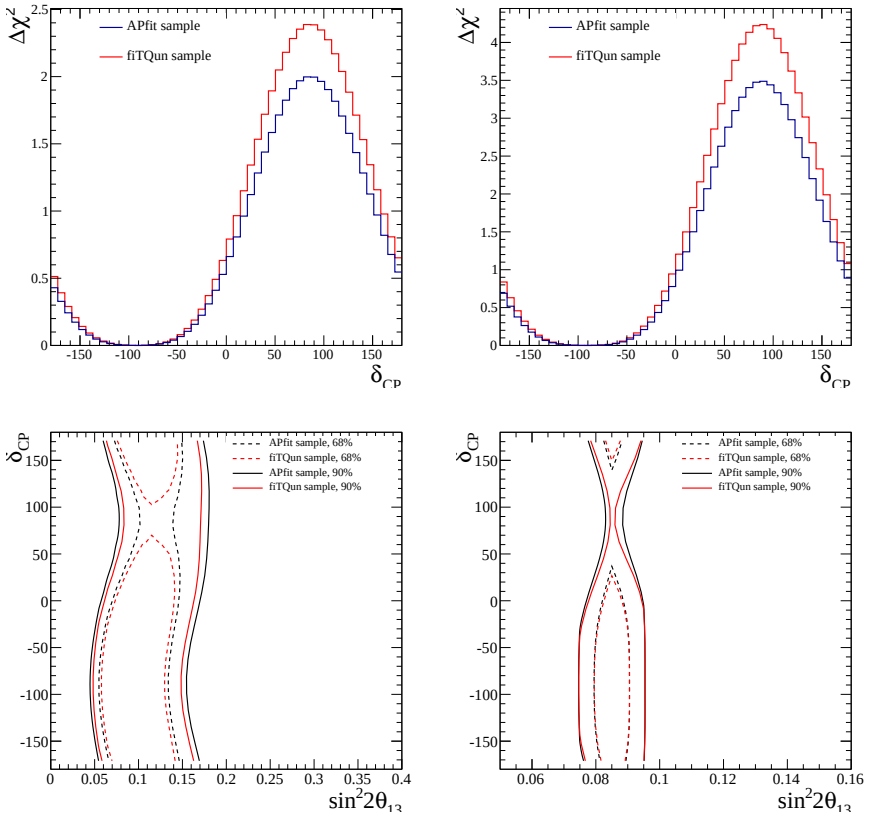

Figure 5.10: Sensitivity comparison between APfit samples and fiTQun samples. T2K Run1-7 statistics (7.482×10^{20} FHC, 7.471×10^{20} RHC) is assumed. Left: without reactor constraint; right: with reactor constraint. Top: δ_{CP}, bottom: δ_{CP} v.s. $\sin^2 2\theta_{13}$. The values of oscillation parameters are shown in Table 5.2. FiTQun selection with the original FV cut yields similar δ_{CP} sensitivity as does the APfit selection.

	CCQE + 2p2h				CC other				NC			
	$\nu_\mu+\bar{\nu}_\mu$	$\nu_e+\bar{\nu}_e$	$\nu_\mu+\bar{\nu}_\mu$	$\nu_e+\bar{\nu}_e$	$\nu_\mu+\bar{\nu}_\mu$	$\nu_e+\bar{\nu}_e$	$\nu_\mu+\bar{\nu}_\mu$	$\nu_e+\bar{\nu}_e$	$\nu_\mu+\bar{\nu}_\mu$	$\nu_e+\bar{\nu}_e$	$\nu_\mu+\bar{\nu}_\mu$	$\nu_e+\bar{\nu}_e$
	fiTQun		APfit		fiTQun		APfit		fiTQun		APfit	
FCFV	131.347	40.816	106.691	32.834	207.303	24.483	171.059	19.722	120.771	3.497	96.355	2.789
1ring	114.929	37.707	100.452	31.636	31.881	9.551	50.915	9.183	21.938	0.633	28.216	0.798
mu-like	112.791	0.029	98.499	0.355	29.774	0.019	46.443	0.108	8.647	0.257	8.877	0.284
$p_\mu > 200$MeV/c	112.691	0.029	98.283	0.355	29.754	0.019	46.414	0.108	8.587	0.255	8.808	0.281
0,1 Michel	111.512	0.029	97.372	0.355	19.192	0.019	29.848	0.107	8.303	0.246	8.510	0.271
not π^+	110.074	0.025			18.566	0.014			4.054	0.107		
Final sample	110.074	0.025	97.372	0.355	18.566	0.014	29.848	0.107	4.054	0.107	8.510	0.271
Only erec< 1 GeV	55.234	0.012	46.062	0.130	6.735	0.010	6.834	0.076	3.963	0.104	8.248	0.265
signal	110.074		97.372									
background	22.766		39.090									
purity	82.86%		71.35%									

Table 5.5: Expected number of signal and background events passing each cut in the ν_μ CCQE-like sample. *wall* $>$ 50 cm and *towall* $>$ 250 cm are used as FV cut for the fiTQun sample; 7.482×10^{20} POT is assumed.

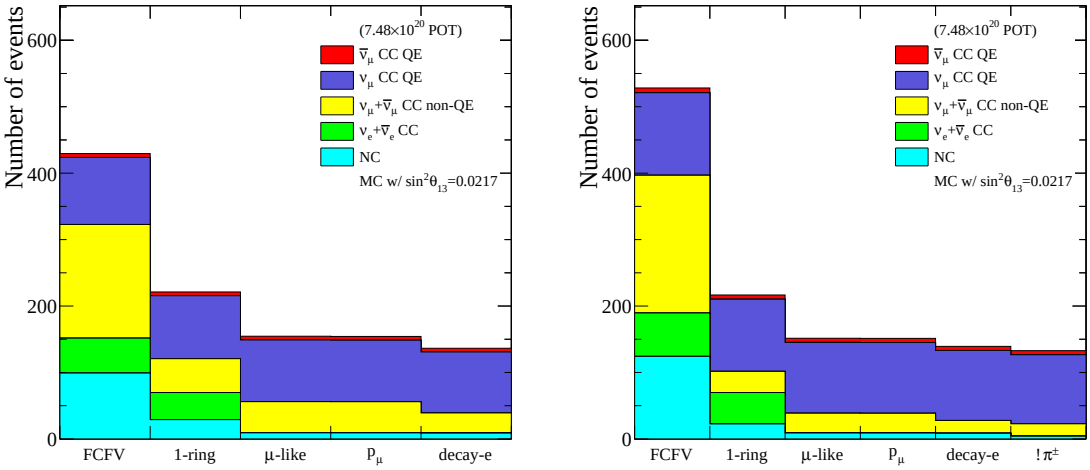

Figure 5.11: Event selection breakdown of the ν_μ CCQE-like sample by APfit (left) and fiTQun (right). All the ν_μ selection criteria are applied. Oscillation parameters used are shown in Table 5.2; 7.482×10^{20} POT in FHC-mode is assumed.

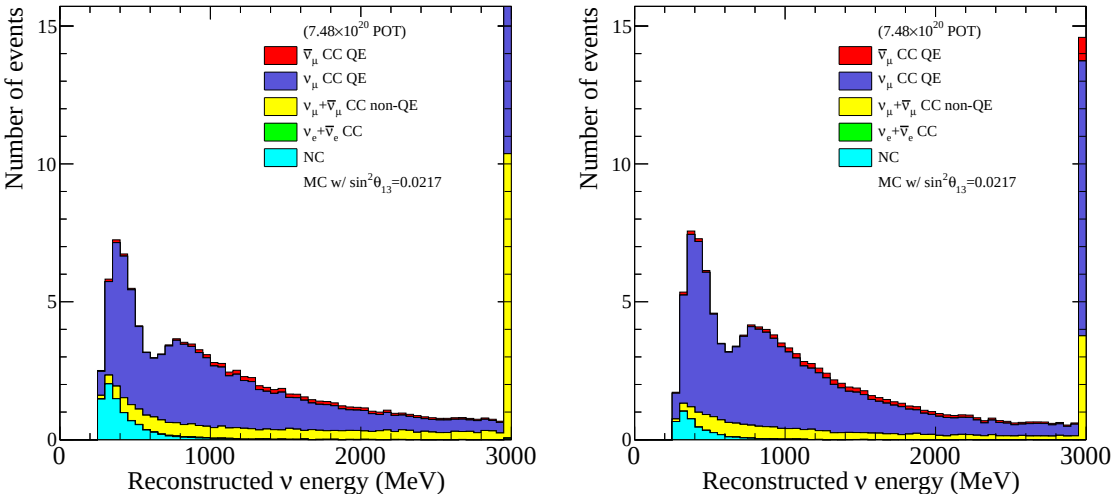

Figure 5.12: Reconstructed energy distributions of the final ν_μ CCQE-like sample by APfit (left) and fiTQun (right). All the ν_μ selection criteria are applied. Oscillation parameters used are shown in Table 5.2; 7.482×10^{20} POT in FHC-mode is assumed.

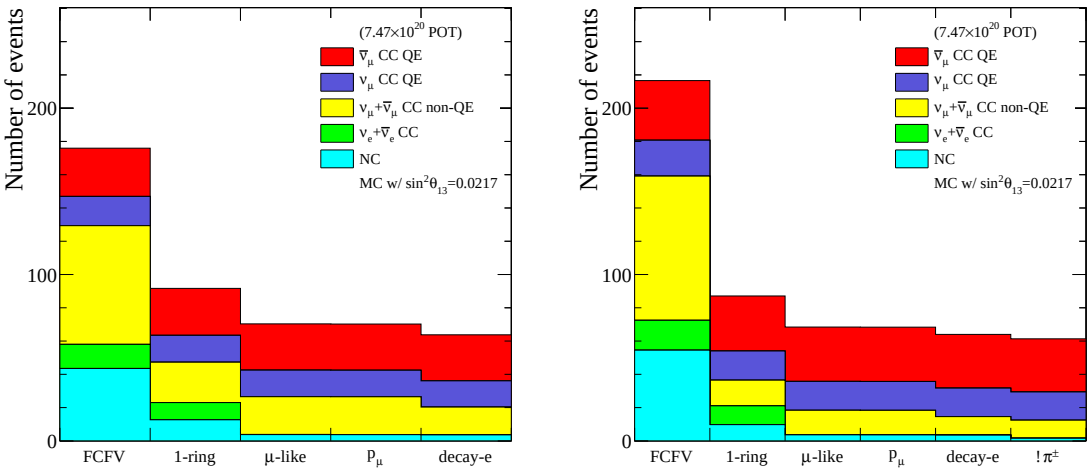

Figure 5.13: Event selection breakdown of the $\bar{\nu}_\mu$ CCQE-like sample by APfit (left) and fiTQun (right). All the ν_μ selection criteria are applied. Oscillation parameters used are shown in Table 5.2; 7.471×10^{20} POT in RHC-mode is assumed.

	CCQE + 2p2h				CC other				NC			
	$\nu_\mu+\bar{\nu}_\mu$	$\nu_e+\bar{\nu}_e$	$\nu_\mu+\bar{\nu}_\mu$	$\nu_e+\bar{\nu}_e$	$\nu_\mu+\bar{\nu}_\mu$	$\nu_e+\bar{\nu}_e$	$\nu_\mu+\bar{\nu}_\mu$	$\nu_e+\bar{\nu}_e$	$\nu_\mu+\bar{\nu}_\mu$	$\nu_e+\bar{\nu}_e$	$\nu_\mu+\bar{\nu}_\mu$	$\nu_e+\bar{\nu}_e$
	fiTQun		APfit		fiTQun		APfit		fiTQun		APfit	
FCFV	57.409	9.870	46.591	7.944	86.691	8.080	71.344	6.541	52.758	1.775	42.108	1.422
1ring	50.605	8.945	44.368	7.622	15.444	2.363	24.288	2.719	9.434	0.314	12.264	0.404
mu-like	50.022	0.005	43.784	0.064	14.772	0.003	22.694	0.024	3.494	0.124	3.627	0.133
$p_\mu > 200$MeV	49.997	0.005	43.732	0.064	14.768	0.003	22.688	0.024	3.359	0.123	3.589	0.132
0,1 Michel	49.434	0.005	43.433	0.064	11.099	0.003	16.637	0.023	3.344	0.118	3.467	0.125
not π^+	48.894	0.004			10.857	0.002			1.524	0.054		
Final sample	48.894	0.004	43.433	0.064	10.857	0.002	16.637	0.023	1.624	0.054	3.467	0.125
Only erec< 1 GeV	19.892	0.001	16.497	0.032	3.320	0.001	3.384	0.012	1.486	0.052	3.364	0.12
signal	48.894		43.433									
background	12.442		20.317									
purity	79.72%		68.13%									

Table 5.6: Expected number of signal and background events passing each cut for the $\bar{\nu}_\mu$ CCQE-like sample. *wall* > 50 cm and *towall* > 250 cm are used as FV cut for the fiTQun sample; 7.471×10^{20} POT is assumed.

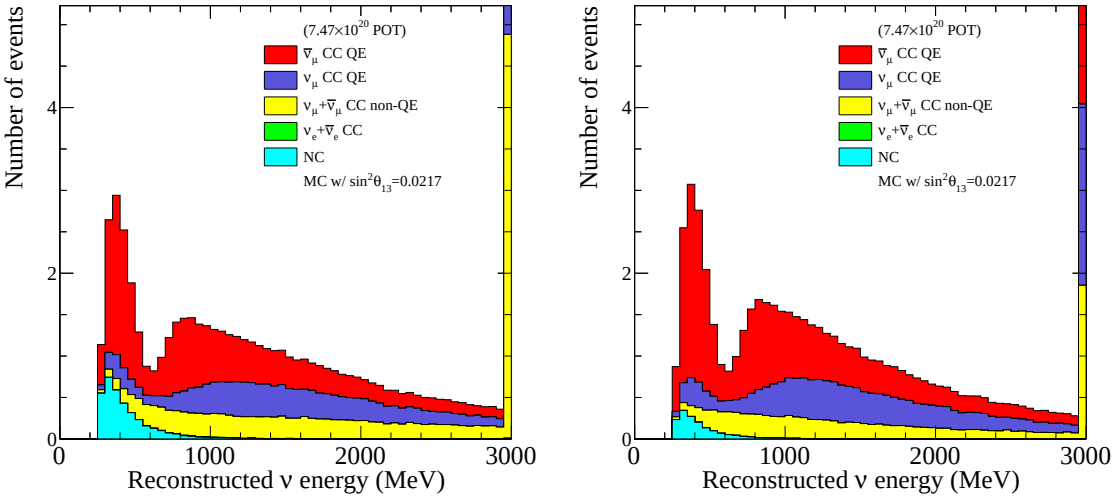

Figure 5.14: Reconstructed energy distributions of the final $\bar{\nu}_\mu$ CCQE-like sample by APfit (left) and fiTQun (right). All the ν_μ selection criteria are applied. Oscillation parameters used are shown in Table 5.2; 7.471×10^{20} POT in RHC-mode is assumed.

and the corresponding numbers are shown in Table 5.7. We observe an $\sim$ 22% increase in $\nu_e + \bar{\nu_e}$ signal, and a proportional increase in backgrounds. This change in mainly due to the expansion of the fiducial volume relative to the APfit sample. Figure 5.16 shows the reconstructed energy distribution fo the fiTQun and APfit ν_e CCQE-like samples. T2K Run1-7 FHC POT (7.482×10^{20}) is assumed in the figures and table.

Figure 5.17 shows the number of events after each cut of the $\bar{\nu}_e$ CCQE-like sample, and the corresponding numbers are shown in Table 5.8. We observe a $\sim$ 22% increase in $\nu_e + \bar{\nu_e}$ signal, and a $\sim$ 29% increase in backgrounds. Figure 5.14 shows the reconstructed energy distributions of the fiTQun and APfit $\bar{\nu}_e$ CCQE-like samples. T2K Run1-7 RHC POT (7.471×10^{20}) is assumed in the figures and table.

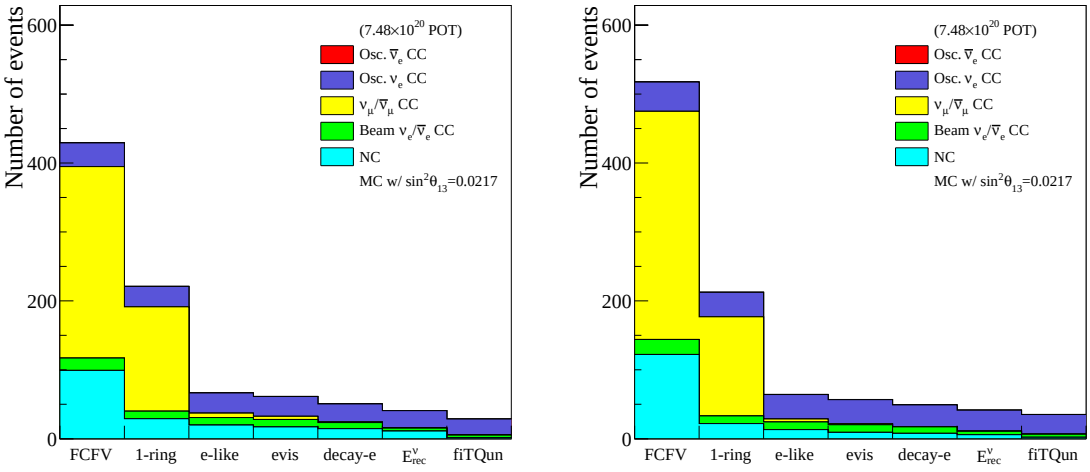

Figure 5.15: Event selection breakdown of the ν_e CCQE-like sample by APfit (left) and fiTQun (right). All the ν_e selection criteria are applied. Oscillation parameters used are shown in Table 5.2; 7.482×10^{20} POT in FHC-mode is assumed.

	fiTQun			APfit		
	$\nu_\mu + \bar{\nu}_\mu$	beam $\nu_e + \bar{\nu}_e$	signal $\nu_e + \bar{\nu}_e$	$\nu_\mu + \bar{\nu}_\mu$	beam $\nu_e + \bar{\nu}_e$	signal $\nu_e + \bar{\nu}_e$
	CC					
FCFV	330.957	21.771	42.830	277.750	17.886	34.671
1ring	143.778	11.108	35.820	151.367	10.950	29.869
e-like	4.305	11.103	35.779	6.425	10.867	29.489
evis> 100MeV	1.617	11.023	35.080	4.583	10.812	28.980
0 Michel	0.439	9.383	31.696	0.967	8.863	26.319
Erec< 1.25GeV	0.278	4.953	30.560	0.255	4.224	25.273
not π^0	0.135	4.403	28.658	0.089	3.648	23.365
	NC					
FCFV	118.810	3.441	signal	96.355	2.789	signal
1ring	21.349	0.621	28.66	28.216	0.789	23.36
e-like	12.842	0.534	background	19.338	0.514	background
evis> 100MeV	8.592	0.388	6.65	16.680	0.454	5.35
0 Michel	7.590	0.210	purity	14.184	0.373	purity
Erec< 1.25GeV	5.687	0.143	81.18%	10.896	0.264	81.36%
not π^0	2.059	0.048		1.580	0.037	

Table 5.7: Expected number of signal and background events passing each cut in the ν_e CCQE-like sample. *wall* $>$ 80 cm and *towall* $>$ 170 cm are used as FV cut for the fiTQun sample; 7.482×10^{20} POT is assumed.

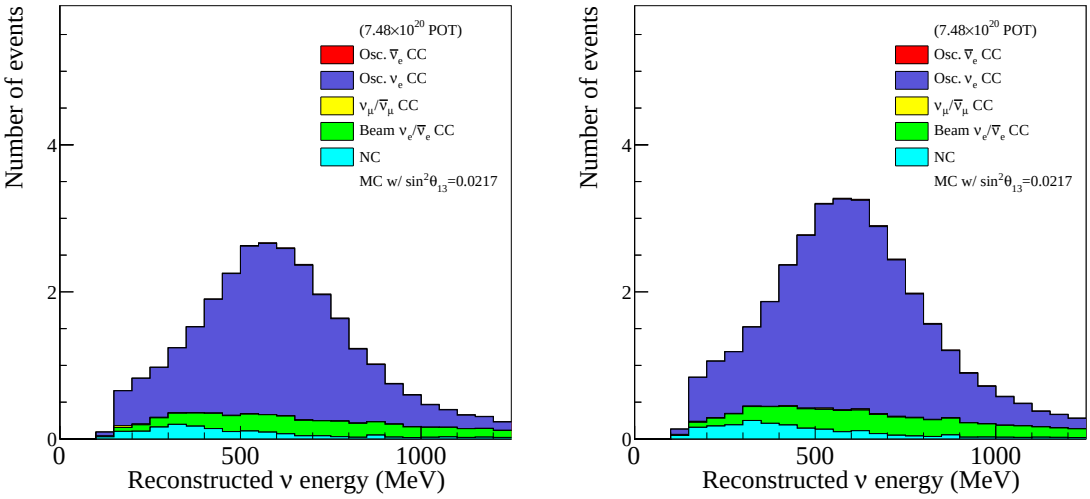

Figure 5.16: Reconstructed energy distributions of the final ν_e CCQE-like sample by APfit (left) and fiTQun (right). All the ν_e selection criteria are applied. Oscillation parameters used are shown in Table 5.2; 7.482×10^{20} POT in FHC-mode is assumed.

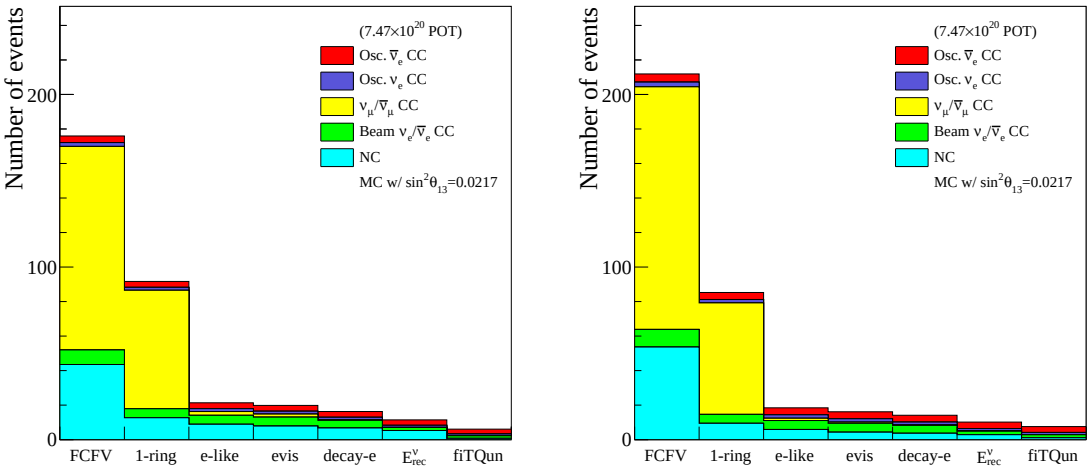

Figure 5.17: Event selection breakdown of the $\bar{\nu}_e$ CCQE-like sample by APfit (left) and fiTQun (right). All the ν_e selection criteria are applied. Oscillation parameters used are shown in Table 5.2; 7.471×10^{20} POT in RHC-mode is assumed.

	fiTQun			APfit		
	$\nu_\mu + \bar{\nu}_\mu$	beam $\nu_e + \bar{\nu}_e$	signal $\nu_e + \bar{\nu}_e$	$\nu_\mu + \bar{\nu}_\mu$	beam $\nu_e + \bar{\nu}_e$	signal $\nu_e + \bar{\nu}_e$
	CC					
FCFV	140.554	10.221	7.473	117.935	8.432	6.053
1ring	64.588	5.175	6.038	68.656	5.217	5.123
e-like	1.329	5.171	6.033	2.178	5.185	5.068
evis> 100MeV	0.679	5.152	5.983	1.759	5.171	5.031
0 Michel	0.194	4.575	5.666	0.315	4.446	4.797
Erec< 1.25GeV	0.131	2.026	5.158	0.079	1.745	4.318
not π^0	0.062	1.759	4.684	0.018	1.464	3.851
	NC					
FCFV	51.897	1.748	signal	42.108	1.422	signal
1ring	9.154	0.306	4.68	12.264	0.404	3.85
e-like	5.706	0.184	background	8.637	0.271	background
evis> 100MeV	4.179	0.134	2.87	7.629	0.240	2.23
0 Michel	3.579	0.110	purity	6.544	0.197	purity
Erec< 1.25GeV	2.773	0.075	61.99%	5.159	0.136	63.31%
not π^0	1.022	0.029		0.730	0.020	

Table 5.8: Expected number of signal and background events passing each cut in the $\bar{\nu}_e$ CCQE-like sample. $wall > 80$ cm and $towall > 170$ cm are used as FV cut for the fiTQun sample; 7.471×10^{20} POT is assumed.

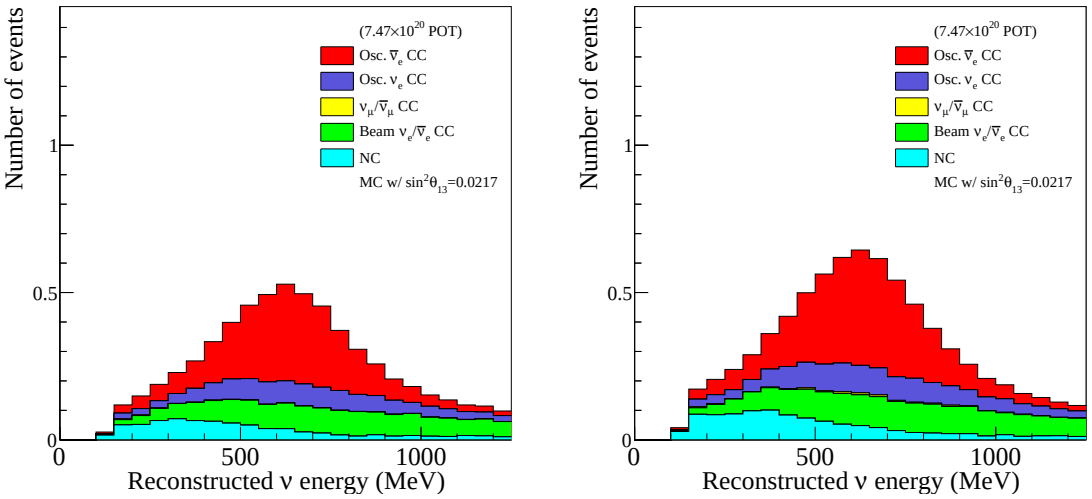

Figure 5.18: Reconstructed energy distributions of the final $\bar{\nu}_e$ CCQE-like sample by APfit (left) and fiTQun (right). All ν_e selection criteria are applied. Oscillation parameters used are shown in Table 5.2; 7.471×10^{20} POT in RHC-mode is assumed.

The most significant difference between the fiTQun samples and APfit samples comes from the ring-counting. Naively speaking, events with only one muon, one electron, or one charged pion in the final state with energy above Cherenkov threshold should produce one visible ring in the detector; events with other final states should produce multiple rings. It can be illustrated by Figure 5.19, where only final state particles whose energy is above Cherenkov threshold are counted. For example, "1μ" means only one final state particle is above Cherenkov threshold and that particle is a muon; "1μ+other" means that there are more than one final state particle above Cherenkov threshold and at least one of them is a muon. Sometimes the reconstruction can miss one or more rings when, for instance, two particles travel in a similar direction and produce overlapping rings. In addition, it is not trivial to state unambiguously how many true rings should be visible to the detector. Despite all the caveats, however, Figure 5.19 shows qualitatively that compared to APfit, fiTQun identifies true multi-ring events as single-ring less often. Figure 5.20 shows that in general fiTQun correctly finds the number of rings more often than APfit does.

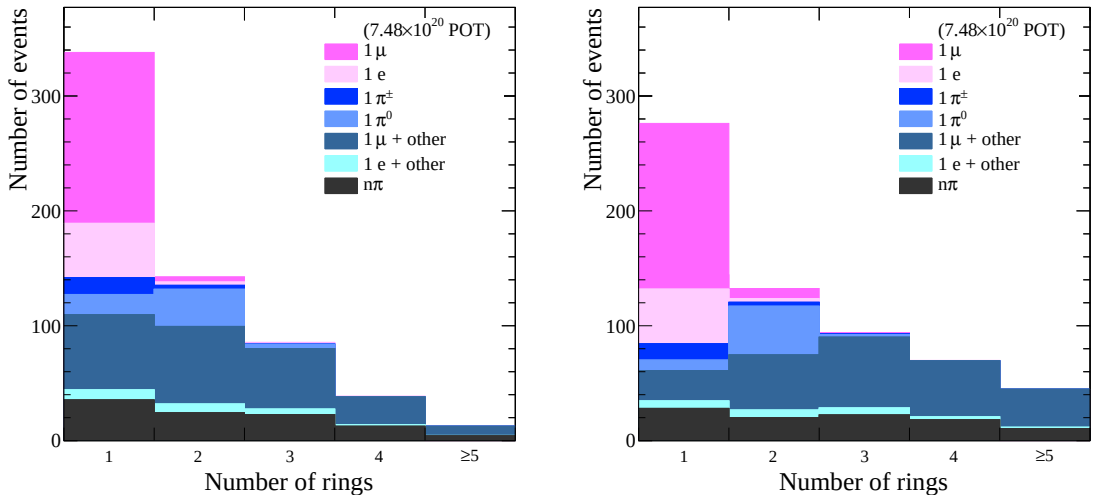

Figure 5.19: Number of rings found breaking down in final states. Left: APfit; right: fiTQun. 7.482×10^{20} POT in FHC-mode is assumed; oscillation parameter values are shown in Table 5.2. Only fully contained cut is applied.

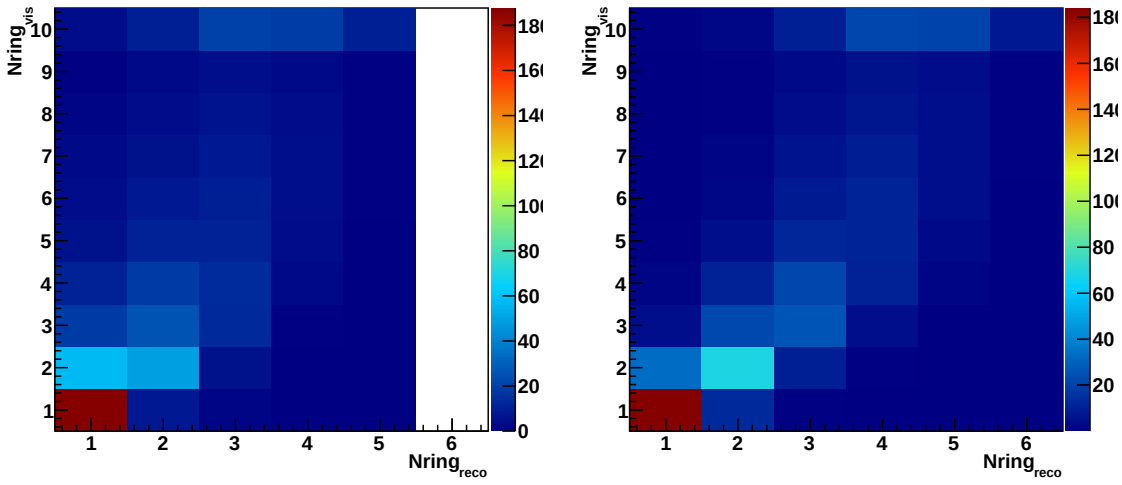

Figure 5.20: Number of true rings v.s. number of rings found by reconstruction. Left: APfit; right: fiTQun. 7.482×10^{20} POT in FHC-mode is assumed; oscillation parameter values are shown in Table 5.2. Only events with true *dwall* > 200 cm are counted.

Chapter 6

Joint fit analysis of T2K $CC0\pi$ samples and Super-K atmospheric neutrino sub-GeV $CC0\pi$ samples

Both the T2K beam neutrinos and the SK atmospheric neutrinos are sensitive to the oscillation parameters $\sin^2\theta_{23}$, $\sin^2\theta_{13}$, $|\Delta m^2_{32}|$ and δ_{CP}. SK in particular, also has an advantage over T2K in that atmospheric neutrino samples have sensitivity to the mass hierarchy. However, the mass hierarchy measurement by atmospheric neutrinos is limited by the precision of $\sin^2\theta_{23}$, of which T2K has the world's most precise measurement. Therefore, combining the T2K beam neutrinos and SK atmospheric neutrinos can improve the sensitivity to the mass hierarchy, which in turn will improve the measurement of δ_{CP}. In addition, combining two experiments which are sensitive to the same parameters will improve the measurement as it amounts to an increase in statistics. This chapter will describe the first combined analysis of T2K and SK data.

Although T2K and SK share a common detector, the neutrino oscillation analyses are conducted in a different fashion – different statistical methods and different treatment of systematic uncertainties have been used. T2K beam neutrinos and SK atmospheric neutrinos also have very different energy spectra: T2K beam neutrino energy is narrowly peaked at ~ 0.6 GeV, whereas SK atmospheric neutrino energy ranges from tens of MeV to a few TeV as shown by Figure 6.1. Therefore T2K has mainly focused on the CCQE-and CC1π-like samples so far, whereas SK has to consider interactions that happen at much higher energy and even ν_τ interactions. To simplify the problem, this analysis will only focus on the CCQE-like

samples at both T2K and SK. Although this analysis choice sacrifices the sensitivity to mass hierarchy, it should still provide an improvement to the δ_{CP} measurement. The SK samples at higher energy can be added once the treatment of cross section systematic uncertainties associated with DIS, pion multiplicity, etc. are unified between the two experiments in the future.

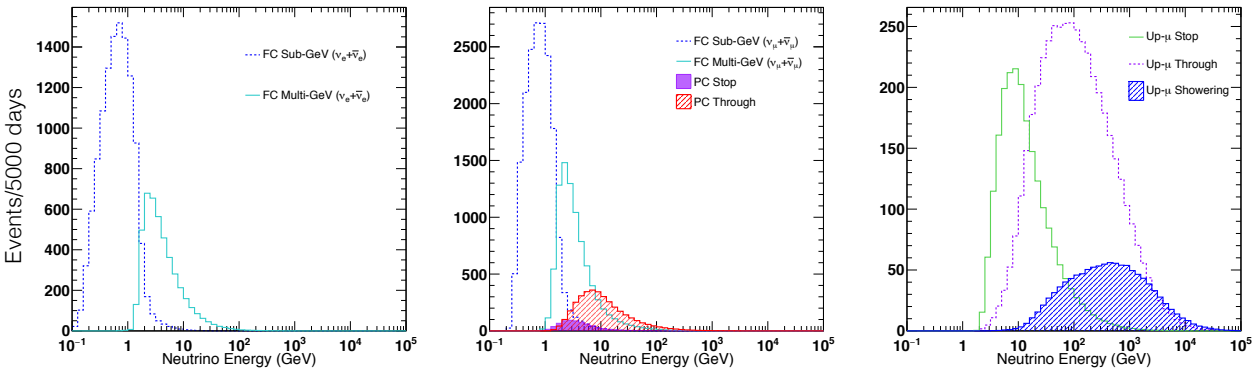

Figure 6.1: Atmospheric neutrino unoscillated fluxes. Figure is taken from [123]

Prior to this analysis, the SK atmospheric neutrinos have always been used to estimate the detector systematic uncertainties by both the T2K and SK analyses prior to the fit, which is not an ideal way in which the detector systematic errors should be treated. In particular, the SK detector systematic uncertainties in the T2K analysis are estimated by a three-step procedure [124]: (1) A fit to SK atmospheric neutrino data is done which includes SK flux systematic uncertainties and cross section systematic uncertainties parametrized with a more simplistic model than what is used in either T2K or SK oscillation analyses; (2) the posterior distributions of the detector parameters is translated into errors on the T2K event selection efficiency with flux and cross section errors marginalized; (3) a toy MC is performed to generate detector systematic errors binned in visible energy and neutrino interaction categories, using the results from step (2) and the error estimates of other background components as its input. This way of estimating detector uncertainties would inevitably erase the correlations between the cross section and the effective detector systematic error parameters; it also over-estimates the detector errors by double-counting the cross section errors. This joint-fit analysis will also address these problems.

It should be pointed out the MINOS collaboration was the first to perform a simultaneous fit to their FHC-mode beam neutrino and atmospheric neutrino data [125], and that such joint-fit analyses have been attempted within both the T2K and the SK collaborations [123] [126]. But this analysis is the first one in T2K and SK to treat the systematic

uncertainties in a consistent manner between the two experiments. In this chapter, the Bayesian analysis technique used by this analysis will be introduced, followed by a mathematical formulation of the likelihood function and a discussion about the analysis strategy. Then the neutrino event samples will be defined, and the implementation of systematic uncertainties will be detailed. The sensitivity of this T2K-SK combined fit will be shown and compared with the respective T2K-only sensitivity. Finally, the data-fit results will be shown and interpretations provided.

6.1 Bayesian statistic and Markov Chain Monte Carlo

Generally speaking, there are two schools of statistics – frequentist and Bayesian, and their philosophies on how to interpret probability results in a fundamental difference in the methodology used to perform data analysis. For a frequentist, probability is defined as the limit of frequency: if an experiment is conducted N times under the exact same circumstances, then the fraction of times when outcome A is achieved $P(A)$ approaches a limit as N becomes sufficiently large:

$$P(A) = \lim_{N\to\infty} \frac{N(A)}{N} \tag{6.1}$$

where $P(A)$ is the probability. When one quotes a frequentist probability, it is always necessary to specify what the circumstances are, or against which ensemble the outcomes are measured.

To a Bayesian, however, probability is a subjective matter that does not necessarily rely on repeated tests. Take the example in [127]: one can have a personal probability, or a degree-of-belief $P(A)$ for winning a bet whereby the penalty of losing is \$1 and the reward for winning is \$$G$. Obviously one would choose to take the bet if $P(A) > 1/(1+G)$ and otherwise decline it. There is no requirement for everybody's personal probability to be the same, therefore Bayesian probability is often described as subjective probability.

This analysis takes a Bayesian approach – the question we ask is this: given our prior knowledge and the measured data, what is the probability of parameter θ taking certain values? Mathematically, suppose θ is the parameter of interest and x is the data, then the probability we are trying to evaluate is $f(\theta|x)$. Using Bayes' Theorem,

$$f(\theta|x) = \frac{f(x|\theta)\pi(\theta)}{f(x)} \tag{6.2}$$

where $\pi(\theta)$ describes the prior knowledge or belief in the value of θ, and

$$f(x) = \int f(x|\theta)\pi(\theta)\mathrm{d}\theta \tag{6.3}$$

which is a constant that no longer depends on θ. If we ignore the normalization constant, the posterior estimate on θ can be written as

$$f(\theta|x) \propto f(x|\theta)\pi(\theta) \tag{6.4}$$

In reality, there are always many (sometimes hundreds, even thousands) nuisance parameters that are also present in the likelihood function, in which case the posterior probability becomes

$$f(\theta, \alpha|x) \propto f(x|\theta, \alpha)\pi(\theta)\pi(\alpha) \tag{6.5}$$

where α are the nuisance parameters, and $\pi(\alpha)$ the prior probability distribution of α.

After establishing the posterior probability distribution $f(\theta, \alpha|x)$, one can proceed to answer such question as "what is the most probable value of parameter θ", or "what is the range in which θ has a 68% probability of being". Since the values of α is not of our interest, a process called marginalization is done to obtain the marginal probability of θ:

$$f(\theta|x) = \int f(\theta, \alpha|x)\ \mathrm{d}\alpha = \int f(x|\theta, \alpha)\pi(\theta)\pi(\alpha)\ \mathrm{d}\alpha \tag{6.6}$$

Note that the normalization constant is again ignored as can be done at any stage of the calculation without affecting the final probability distribution function. In this way, any correlations between α and θ are taken into account in $f(\theta|x)$. The "best-fit" value of θ is usually quoted as the mode of $f(\theta|x)$.

The parameter range with a given probability content is called the credible interval. There are many schemes with which credible intervals can be calculated [127]. This analysis quotes the "highest-posterior-density regions (HPD)" as the credible interval:

$$\frac{\int_{\theta_{low}}^{\theta^{high}} f(\theta|x)\ \mathrm{d}\theta}{\int_{\text{lower bound}}^{\text{upper bound}} f(\theta|x)\ \mathrm{d}\theta} = 68\% \tag{6.7}$$

where $f(\theta|x)$ has a higher probability everywhere inside $[\theta_{low}, \theta_{high}]$ than anywhere outside of it. $[\theta_{low}, \theta_{high}]$ is the 1σ credible interval of θ. Two-dimensional credible intervals can be obtained in the same way. A credible interval is not necessarily a continuous region in the parameter space; it can be multiple separated regions. Last but not least, it should be

stressed that the output of a Bayesian analysis is the entire posterior distribution of the parameter(s) of interest; providing the best-fit values or credible intervals is for the purpose of easier interpretation.

Calculating Eq. 6.6 can be formidably difficult in practice. One way around it is to sample in the θ-α phase space using Monte Carlo methods. However, many Monte Carlo techniques would not work for problems with high dimensionality as their sampling efficiencies often drop exponentially as the dimensionality increases. In this case the Markov Chain [1] Monte Carlo (MCMC) methods can be used.

There are many MCMC algorithms on the market; a review on the subject can be found in [128]. This analysis uses the Metropolis-Hastings algorithm [129] [130] to sample from the probability distribution function. It takes the following steps to generate a set of points that follow the equilibrium probability distribution $p(\vec{\theta})$:

1. Suppose a chain is at its current step $\vec{\theta}_0 = (\theta_0, \theta_1, \cdots, \theta_N)$, then the next step $\vec{\theta}$ can be proposed based on a proposal function $q(\vec{\theta}, \vec{\theta}_0)$.

2. Define the following Hastings test ratio

$$\alpha = \min\left[1, \frac{p(\vec{\theta})q(\vec{\theta}_0, \vec{\theta})}{p(\vec{\theta}_0)q(\vec{\theta}, \vec{\theta}_0)}\right] \tag{6.9}$$

   In this analysis, the proposal function $q(\vec{\theta}, \vec{\theta}_0)$ is symmetric around $\vec{\theta}_0$, therefore $q(\vec{\theta}, \vec{\theta}_0) = q(\vec{\theta}_0, \vec{\theta})$, and Eq. 6.9 becomes

$$\alpha = \min\left[1, \frac{p(\vec{\theta})}{p(\vec{\theta}_0)}\right] \tag{6.10}$$

3. Compare α with a random number r between 0 and 1; if $r \leq \alpha$, take the step $\vec{\theta}$; otherwise, stay at step $\vec{\theta}_0$ (i.e. step $\vec{\theta}_0$ is included in the ensemble again).

4. Repeat from Step 1 until sufficient statistics is reached in the sampling.

[1] A Markov Chain is a stochastic process in which the probability of the current event only depends on the state in the immediate past but nothing previous to that; in other words, for a given event, its past and future events are independent. Suppose a given state in a process $X_n = i$, then the probability of the next state $X_{n+1} = j$ is

$$P(X_{n+1} = j | X_n = i, X_{n-1} = i_{n-1}, \cdots, X_1 = i_1, X_0 = i_0) = P(X_{n+1} | X_n = j) \tag{6.8}$$

It is easy to see from Eq. 6.10 that it is more favorable for the MCMC to step towards regions in the phase space with higher probability densities, therefore the Metropolis-Hastings MCMC can be seen as a directed random walk. The choice of proposal density $q(\vec{\theta}, \vec{\theta}_0)$ is arbitrary; however, it can greatly affect the sampling efficiency. For this analysis, nuisance parameters are proposed at each step according to their correlated prior constraints to increase sampling efficiency. With enough steps, the MCMC would reach an equilibrium distribution designated by $p(\vec{\theta})$. In other words, the set of points produced by the MCMC are distributed according to $p(\vec{\theta})$, and from there characteristics of the probability distribution can be inferred.

The rate at which a proposed step is accepted is important for the success of a MCMC analysis. If the proposed step is always too close to the current step, and therefore the difference in $p(\vec{\theta})$ and $p(\vec{\theta}_0)$ is always small, the acceptance rate would be high; however, this could lead to the MCMC not fully exploring the parameter space, or taking too many iterations to achieve a proper coverage. On the contrary, if the proposed step is always too far from the current step, the rate of acceptance would drop too low, and the MCMC could stay at one step for a very long time, making it difficult to reach the equilibrium distribution. Therefore, the step size has to be carefully tuned such that only a reasonable chain length is needed to achieve proper sampling in the parameter space.

Since the chains normally do not start from a region with high probability density, it takes a certain number of steps for them to reach equilibrium. It is customary to discard a number of steps from the beginning of the chain, or a "burn-in" period, such that a proper sampling of the parameter space can be achieved with a finite number of steps. Typically the "burn-in" period is determined to be the steps it takes for each parameter to reach its stationary distribution.

6.2 The likelihood function

An essential part of this analysis is to evaluate the posterior probability function at each MCMC step. Suppose the parameters (both the parameters of interest and the nuisance parameters) are $\mathbf{p}$, the experimental observables are D; using the Bayes theorem, the posterior

probability function can be expressed as

$$\mathcal{L}(\mathbf{p}|D) = \frac{\mathcal{L}(D|\mathbf{p})P(\mathbf{p})}{\int \mathcal{L}(D|\mathbf{p})P(\mathbf{p})\,\mathrm{d}\mathbf{p}} \tag{6.11}$$

where $P(\mathbf{p})$ is the probability distribution function of $\mathbf{p}$ based on the prior knowledge of $\mathbf{p}$. The denominator is the normalization constant.

In practice, a likelihood function as shown by the numerator of Eq. 6.11 is constructed, which is different from the Bayesian posterior probability function only by a scaling constant as shown by the denominator. The total likelihood for the joint-fit analysis can be separated into four parts:

$$\mathcal{L}_{Tot}(D|\theta,\alpha) = \mathcal{L}_{SK}(D|\theta,\alpha) \times \mathcal{L}_{T2K}(D|\theta,\alpha) \times \mathcal{L}_{Syst}(\alpha) \times \mathcal{L}_{osc}(\theta) \tag{6.12}$$

where θ are the oscillation parameters θ_{12}, θ_{13}, θ_{23}, Δm^2_{12}, Δm^2_{13}, Δm^2_{23} and δ_{CP}, and α represents the systematic error parameters, or nuisance parameters. The detailed SK likelihood function $\mathcal{L}_{SK}(\theta,\alpha)$ and the T2K likelihood function $\mathcal{L}_{T2K}(\theta,\alpha)$ will be shown later in this section by Eq. 6.13 and Eq. 6.18, respectively. The likelihood contribution from the prior constraints on the systematic errors $\mathcal{L}_{Syst}(\alpha)$ will be discussed in section 6.3.

In Eq. 6.12, the term $\mathcal{L}_{osc}(\theta)$ represents the prior constraints on the oscillation parameters. In this analysis, we use the results from solar neutrino and reactor neutrino measurements on $\sin^2\theta_{12}$ and Δm^2_{12} as the prior constraints; $\sin^2\theta_{23}$, Δm^2_{23} and δ_{CP} have flat priors; there is a 50%-50% probability for normal and inverted hierarchy *a priori*. In addition, two cases – with and without prior constraints on $\sin^2 2\theta_{13}$, are both considered; it is termed "with reactor constraint" or "without reactor constraint" as $\sin^2 2\theta_{13}$ is measured most precisely by reactor experiments. The prior constraints on oscillation parameters are summarized in Table 6.1. It is assumed that neutrinos and anit-neutrinos are described by the same set of oscillation parameters as prescribed by the PMNS framework. All oscillation parameters are uncorrelated prior to the fit, and are allowed to vary in the MCMC.

$\sin^2\theta_{12}$	0.304 ± 0.017
$\sin^2 2\theta_{13}$*	$0.0857 \pm .0046$
$\sin^2\theta_{23}$	Flat prior
Δm^2_{12}	$7.53 \pm 0.20 \times 10^{-5}$ eV^2
Δm^2_{23}	Flat prior
δ_{CP}	Flat prior
Mass hierarchy	$P(NH) = P(IH) = 0.5$

Table 6.1: The prior constraints on oscillation parameters. *The prior constraint on $\sin^2 2\theta_{13}$ is optional. For parameters with a prior constraint, the central value and error are taken from PDG 2016 [131].

Eq. 6.13 shows the likelihood function of the SK samples.

$$
\begin{aligned}
\mathcal{L}_{SK}(D|\theta,\alpha) \approx & \prod_{\substack{k=0,1,2\\ n_e=0}} P_{\substack{1\text{ring}\\ e\text{-like}}}\left(N_{k,n_e}|\theta,\alpha\right) \left(\prod_{\substack{m\in[1\text{ring}\\ e\text{-like events}]\\ E_m\in[e_k,e_{k+1}]}} \rho\left(z_m|E_k,\theta,\alpha\right) \right) \\
& \times \prod_{\substack{k=0,1,2,3\\ n_e=0,\geq 1}} \left(\prod_{\substack{m\in[1\text{ring}\\ e\text{-like events}]\\ E_m\in[e_k,e_{k+1}]}} \rho\left(R_m|E_k,\theta,\alpha\right) \rho\left(P_m^{e/\mu}|E_k,\theta,\alpha\right) \rho\left(P_m^{e/\pi^0}|E_k,\theta,\alpha\right) \rho\left(P_m^{\mu/\pi^+}|E_k,\theta,\alpha\right) \right) \\
& \times \prod_{\substack{k=0,1,2\\ n_e=0,1}} P_{\substack{1\text{ring}\\ \mu\text{-like}}}\left(N_{k,n_e}|\theta,\alpha\right) \left(\prod_{\substack{n\in[1\text{ring}\\ \mu\text{-like events}]\\ E_n\in[e_k,e_{k+1}]}} \rho\left(z_n|E_k,\theta,\alpha\right) \right) \\
& \times \prod_{\substack{k=0,1,2,3\\ n_e=0,1,\geq 2}} \left(\prod_{\substack{n\in[1\text{ring}\\ \mu\text{-like events}]\\ E_n\in[e_k,e_{k+1}]}} \rho\left(R_n|E_k,\theta,\alpha\right) \rho\left(P_n^{e/\mu}|E_k,\theta,\alpha\right) \rho\left(P_n^{e/\pi^0}|E_k,\theta,\alpha\right) \rho\left(P_n^{\mu/\pi^+}|E_k,\theta,\alpha\right) \right) \\
& \times \prod_{\substack{k=0,1,2,3\\ n_e=0,1,\geq 2}} \left(\prod_{\substack{l\in[\text{Multi-ring}\\ \text{events}]\\ E_l\in[e_k,e_{k+1}]}} \rho\left(R_l|E_k,\theta,\alpha\right) \rho\left(P_l^{e/\mu}|E_k,\theta,\alpha\right) \rho\left(P_l^{e/\pi^0}|E_k,\theta,\alpha\right) \rho\left(P_l^{\mu/\pi^+}|E_k,\theta,\alpha\right) \right)
\end{aligned}
\tag{6.13}
$$

One may notice the "≈" symbol in Eq. 6.13. Approximations are needed to reduce the original six-dimensional likelihood function $\mathcal{L}_{SK}^{n^{th}\ \text{sample}}(E, z, R, P^{e/\mu}, P^{e/\pi^0}, P^{\mu/\pi^+}|\theta, \alpha)$ into one-dimensional distributions. By categorizing events into different visible energy categories, the likelihood function can be broken down into normalization likelihoods and shape likelihoods

$$\begin{aligned}\mathcal{L}(E, z, R, P^{e/\mu}, P^{e/\pi^0}, P^{\mu/\pi^+}|\theta, \alpha) = \prod_k P(N_k|\theta, \alpha) \\ \times \rho(z, R, P^{e/\mu}, P^{e/\pi^0}, P^{\mu/\pi^+}|E_k, \theta, \alpha)\end{aligned} \tag{6.14}$$

where it should be noted that this only refers to the n-th SK sample even though the symbol is dropped. Further factorizing the multi-dimensional distribution requires the variables to be independent, i.e. for a given pair of observables x and y,

$$\mathcal{L}(x, y|E_k, \theta, \alpha) = \mathcal{L}(x|E_k, \theta, \alpha)\mathcal{L}(y|E_k, \theta, \alpha) \tag{6.15}$$

where x, y are $R, P^{e/\mu}, P^{e/\pi^0}, P^{\mu/\pi^+}$ or z. Although this is generally true when one of the parameters is z, as the event reconstruction should not be different for events coming from different zenith angles, the ring-counting and PID parameters themselves are somewhat correlated, as shown by Figure 6.2. Even though the correlation is generally weak, it is indeed a compromise to collapse the five-dimensional distribution into five one-dimensional distributions. The posterior correlations amongst SK detector error parameters will be affected by such approximations. Although this is one of the modest weaknesses of this analysis, it should be noted that it is already an improvement compared to how the detector systematic uncertainties are estimated currently [124].

The first and third lines in Eq. 6.13, i.e. the normalization and zenith angle distributions are where the sensitivities to oscillation parameters originate, and only the "core" samples, i.e. events with 0 decay electron (e-like) and 0 or 1 decay electron (μ-like) and visible energy < 1.33 GeV, are considered. This is because these are the most important samples for the δ_{CP} measurement, and also the best understood – the underlying cross section model of the dominant CCQE process has been tested by not only T2K, but other external measurements [132]. Sub-GeV single-ring e-like events with one or more decay electrons, and μ-like events with two or more decay electrons are dominated by CC1π^+, the cross section model of which is known to have discrepancies with data [133]. Since the measurement of δ_{CP} relies heavily on a correct cross section modeling, it was decided that it is safer to not include them until the discrepencies are understood.

Lines 2, 4, and 5 of Eq. 6.13 show the control distributions, namely the distributions of

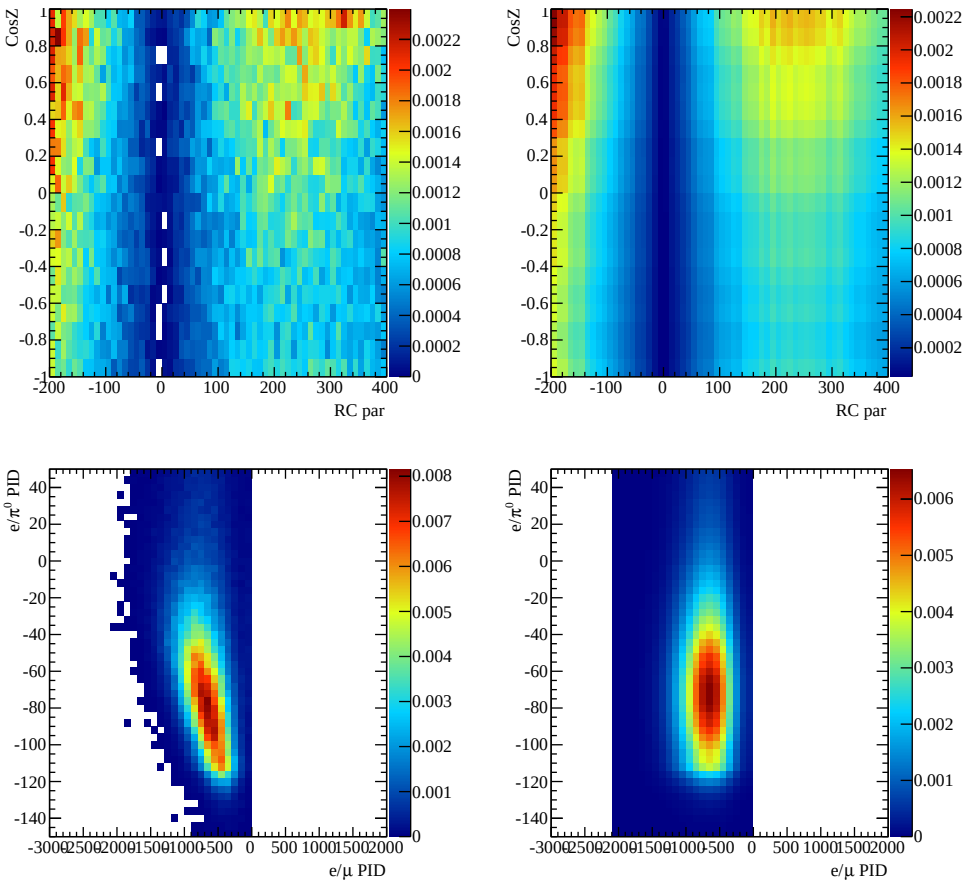

Figure 6.2: An example of the parameter correlation test. Top-left: $\rho(z, R|\theta, \alpha)$ for single-ring, e-like events with 0 decay electron and $0.3 < E_{vis} < 0.7$ GeV; top-right: $\rho(z|\theta, \alpha)\rho(R|\theta, \alpha)$ for single-ring, e-like events with 0 decay electron and $0.3 < E_{vis} < 0.7$ GeV; bottom-left: $\rho(P^{e/\pi^0}, P^{\mu/\pi^+}|\theta, \alpha)$ for single-ring, μ-like events with 1 decay electron and $0.3 < E_{vis} < 0.7$ GeV; bottom-right: $\rho(P^{e/\pi^0}|\theta, \alpha)\rho(P^{\mu/\pi^+}|\theta, \alpha)$ for single-ring, μ-like events with 1 decay electron and $0.3 < E_{vis} < 0.7$ GeV. All distributions are normalized to 1. If there is no correlation between the two parameters x and y, then $\rho(x, y) = \rho(x)\rho(y)$. Therefore the top two plots are an example of cases where there is no correlation between the two parameters, whereas the bottom two plots are an extreme case where there is a relatively strong correlation. All samples used in this analysis are checked; most distributions do not show strong correlation.

ring-counting parameter R, e/μ PID parameter $P^{e/\mu}$, e/π^0 PID parameter P^{e/π^0}, and μ/π^+ PID parameter P^{μ/π^+}, which are used to constrain the SK detector systematic errors (more discussion in section 6.3). The control distributions are made for events with any number of decay electrons and energy up to 3 GeV. Since only a very small number of T2K events that make it into the final samples have visible energy larger than 3 GeV, there is an upper limit of 3 GeV for atmospheric neutrinos in this analysis. Moreover, events with any given

number of decay electrons are needed to constrain the detector systematic errors. This is in contrast to the events that go into the visible energy and zenith angle distributions. Sub-GeV single-ring e-like events with one or more decay electrons and μ-like events with two or more decay electrons are the side-band samples, and are needed to constrain the detector systematic errors of events with a single hadron or more than one visible particles in the final state. Although the cross section parameters can change the shape of the control distributions (albeit moderately) and therefore potentially cause biases in the detector systematic errors of events with a hadron or more than one visible particles in the final state, such events only make up a small fraction of the "core" atmospheric samples and T2K samples, and therefore have very little effect on the measurement of oscillation parameters.

SK atmospheric neutrino events are categorized by the number of decay electrons (n_e), single-ring v.s. multi-ring, e-like v.s. μ-like, and the visible energy E. Table 6.2 shows the visible energy bin indices k and the corresponding bin edges. Note that only events with visible energy less than 3 GeV are considered, the reason for which is twofold. First, the T2K cross section modeling is developed to best describe neutrinos at the energy range of the T2K beam, which means it may be insufficient to adequately determine systematic uncertainties for higher-energy SK samples. High energy atmospheric neutrino samples can and should be included in the joint analysis in the future. Secondly, since the focus of this analysis is on the δ_{CP} measurement, sub-GeV samples are sufficient as they contribute the most to the sensitivity to δ_{CP}.

	Sub-GeV			Multi-GeV
Bin index k	0	1	2	3
Bin edge (GeV)	0-0.3	0.3-0.7	0.7-1.33	1.33-3

Table 6.2: Visible energy binning of SK samples.

The term $P(N_{k,n_e}|\theta,\alpha)$ in Eq. 6.13 is the Poisson probability for observing N_{k,n_e} events with n_e decay electrons at the k-th visible enery bin, given oscillation parameters θ and nuisance parameters α. Suppose the number of predicted events in the same category is $N^0_{k,n_e}(\theta,\alpha)$, then the Poisson probability can be described by the following equation:

$$P(N_{k,n_e}|\theta,\alpha) = N^0_{k,n_e}(\theta,\alpha)^{N_{k,n_e}} \frac{e^{-N^0_{k,n_e}(\theta,\alpha)}}{N_{k,n_e}!} \tag{6.16}$$

$\rho\,(z|E_k,\theta,\alpha)$ is the zenith angle shape distribution of events in the k-th visible energy bin.

The shape likelihood associated with it is shown by Eq. 6.17,

$$\prod_{\substack{m\in[n^{th}\text{ sample}]\\ E_m\in[e_k,e_{k+1}]}} \rho\left(z_m|E_k,\theta,\alpha\right) = \prod_{i=1}^{\#\text{ of }z\text{ bins}} \left(\frac{N^0_{k,i}(\theta,\alpha)}{\sum_{j=1}^{\#\text{ of }z\text{ bins}} N^0_{k,j}(\theta,\alpha)} \right)^{N^i_k} \tag{6.17}$$

where $N^0_{k,i}(\theta,\alpha)$ is the predicted number of events in a particular event sample, in the k-th visible energy bin and the i-th zenith energy bin, N^i_k the observed number of events. Similarly, $\rho\left(x|E_k,\theta\alpha\right)$ is the shape likelihood of parameter x for events in the k-th visible energy bin given θ and α, where x can be the ring-counting parameter R, e/μ PID parameter $P^{e/\mu}$, e/π^0 PID parameter P^{e/π^0}, or μ/π^+ PID parameter P^{μ/π^+}.

The following equation describes the likelihood function of the T2K samples:

$$\begin{aligned}\mathcal{L}_{T2K}(D|\theta,\alpha) = &\left(\prod_{k_1=1}^{\#\text{ of bins}} P^{\nu_e\text{CC0}\pi}\left(N_{k_1}|\theta,\alpha\right)\right)\left(\prod_{k_2=1}^{\#\text{ of bins}} P^{\nu_\mu\text{CC0}\pi}\left(N_{k_2}|\theta,\alpha\right)\right)\\ &\times\left(\prod_{k_3=1}^{\#\text{ of bins}} P^{\bar{\nu}_e\text{CC0}\pi}\left(N_{k_3}|\theta,\alpha\right)\right)\left(\prod_{k_4=1}^{\#\text{ of bins}} P^{\bar{\nu}_\mu\text{CC0}\pi}\left(N_{k_4}|\theta,\alpha\right)\right)\end{aligned} \tag{6.18}$$

where $P_k\left(N_k|\theta,\alpha\right)$ is the Poisson probability of observing N_k events in the k-th reconstructed energy bin with given θ and α.

6.3 Systematic uncertainties

The term $\mathcal{L}_{Syst}(\alpha)$ in Eq. 6.12 is the contribution from systematic error parameters based on their prior constraints:

$$\begin{aligned}\ln \mathcal{L}_{Syst}(\alpha) = &- \left(\sum_{i}^{\text{BANFF}} \sum_{j}^{\text{BANFF}} \Delta b_i (V_b^{-1})_{ij} \Delta b_j \right) \\ &- \left(\sum_{i}^{\text{det}} \sum_{j}^{\text{det}} \Delta d_i (V_d^{-1})_{ij} \Delta d_j \right) \\ &- \left(\sum_{i}^{\text{flux}} \sum_{j}^{\text{flux}} \Delta f_i (V_f^{-1})_{ij} \Delta f_j \right) \\ &- \left(\sum_{i}^{\text{Other}} \sum_{j}^{\text{other}} \Delta o_i (V_o^{-1})_{ij} \Delta o_j \right)\end{aligned} \tag{6.19}$$

where the V_x is the covariance matrix of a given systematic error category, and Δx_i is the deviation of parameter x_i from its nominal values. The systematic error parameters can be roughly divided into four categories: T2K beam flux and cross section systematic errors (termed "BANFF" in the equation), SK detector systematic error (det), atmospheric neutrino flux systematic errors ($flux$), and all the rest. The systematic error parameters can also affect the likelihood function by modifying the predicted number of events in a given sample. This section will describe the systematic error parameters and how they can modify the event rates.

6.3.1 Beam flux and cross section systematic uncertainties

The T2K beam flux and cross section systematic error parameters used by the far detector analysis are termed "BANFF" parameters because they are the result of the so-called "BANFF" (Beam And ND280 Flux extrapolation task Force) fit, or the near detector fit. At the near detector, we select events with vertices in FGD1 (carbon target) or FGD2 (42% water target) and separate them into different samples based on the number of pion tracks (FHC), or simply the number of tracks (RHC) in the TPCs to enhance different neutrino interaction modes. A fit is then performed to constrain the flux and cross section systematic uncertainties simultaneously, the result of which is propagated to the far detector for oscillation analyses. The BANFF fit used as the input to this analysis is described in [134]. It should be noted that the T2K beam flux systematic uncertainties are only applied to T2K

samples, whereas the cross section systematic uncertainties are applied to both T2K and SK samples.

There are 100 flux systematic error parameters, among which 50 describe the flux uncertainties at ND280, 50 at SK. Each parameter represents the scaling of neutrinos of a certain flavor in a certain energy range. Table 6.3 shows the details of the 50 flux systematic error parameters at SK. The pre-fit values and pre-fit errors are from the flux prediction prior to the near detector fit; and the post-fit values and post-fit errors are obtained after the near detector fit.

Table 6.4 shows the details of the cross section systematic error parameters [2] Figure 6.3 shows the pre-BANFF and post-BANFF correlations among the flux and cross section parameters. It must be noted that the pre-BANFF constraints are used in the fits to ND280 data, and that the post-BANFF parameter values and correlations are used as input to this analysis. Among the 21 cross section parameters, 10 are normalization parameters, and the rest are "shape" parameters which can change sample distributions in non-trivial ways. Take the axial mass parameter M_A^{QE} for example as shown by Figure 6.4. M_A^{QE} can modify the CCQE interaction cross section, which also depends on the neutrino energy, outgoing lepton momentum and angle, etc. Re-calculating the cross sections during the fit as we vary the shape parameters would be prohibitively time-consuming. Instead, we can consider the ratio of the new cross section σ' as we change M_A^{QE} from its nominal value to the nominal cross section σ^0; the σ'/σ^0 is calculated for many different values of M_A^{QE} prior to the fit, and a polynomial fit is performed on the σ'/σ^0 v.s. M_A^{QE} curve. During the fit, a MC event is weighted by the σ'/σ^0 corresponding to the current M_A^{QE} value, and said weight is calculated by the M_A^{QE} polynomial of this particular MC event; this is done for every MC event and all 11 shape parameters.

[2] The $BeRPA\_U$ parameter is set to have a 0.1 prior uncertainty in the fit whereas in other T2K analyses it is fixed at its nominal value. However, its impact on the final results is negligible as shown in Appendix A.1.

Id	Horn current	ν flavor	ν energy (GeV)	pre-fit	pre-fit error	post-fit	post-fit error
0	FHC	ν_μ	$0.00 \sim 0.40$	1.000	0.103	1.012	0.059
1	FHC	ν_μ	$0.40 \sim 0.50$	1.000	0.102	1.033	0.054
2	FHC	ν_μ	$0.50 \sim 0.60$	1.000	0.093	1.016	0.047
3	FHC	ν_μ	$0.60 \sim 0.70$	1.000	0.084	0.976	0.044
4	FHC	ν_μ	$0.70 \sim 1.00$	1.000	0.102	0.929	0.056
5	FHC	ν_μ	$1.00 \sim 1.50$	1.000	0.085	0.951	0.050
6	FHC	ν_μ	$1.50 \sim 2.50$	1.000	0.067	1.021	0.044
7	FHC	ν_μ	$2.50 \sim 3.50$	1.000	0.072	1.038	0.046
8	FHC	ν_μ	$3.50 \sim 5.00$	1.000	0.085	1.029	0.044
9	FHC	ν_μ	$5.00 \sim 7.00$	1.000	0.097	0.989	0.044
10	FHC	ν_μ	$7.00 \sim 30.00$	1.000	0.114	0.969	0.053
11	FHC	$\bar{\nu}_\mu$	$0.00 \sim 0.70$	1.000	0.103	0.979	0.075
12	FHC	$\bar{\nu}_\mu$	$0.70 \sim 1.00$	1.000	0.078	0.969	0.049
13	FHC	$\bar{\nu}_\mu$	$1.00 \sim 1.50$	1.000	0.082	0.982	0.059
14	FHC	$\bar{\nu}_\mu$	$1.50 \sim 2.50$	1.000	0.082	1.032	0.063
15	FHC	$\bar{\nu}_\mu$	$2.50 \sim 30.00$	1.000	0.085	1.097	0.066
16	FHC	ν_e	$0.00 \sim 0.50$	1.000	0.091	1.016	0.048
17	FHC	ν_e	$0.50 \sim 0.70$	1.000	0.087	1.017	0.044
18	FHC	ν_e	$0.70 \sim 0.80$	1.000	0.083	1.016	0.043
19	FHC	ν_e	$0.80 \sim 1.50$	1.000	0.077	1.006	0.041
20	FHC	ν_e	$1.50 \sim 2.50$	1.000	0.076	1.025	0.042
21	FHC	ν_e	$2.50 \sim 4.00$	1.000	0.082	1.025	0.044
22	FHC	ν_e	$4.00 \sim 30.00$	1.000	0.093	1.034	0.061
23	FHC	$\bar{\nu}_e$	$0.00 \sim 2.50$	1.000	0.072	1.044	0.055
24	FHC	$\bar{\nu}_e$	$2.50 \sim 30.00$	1.000	0.129	1.084	0.115
25	RHC	ν_μ	$0.00 \sim 0.70$	1.000	0.094	0.983	0.067
26	RHC	ν_μ	$0.70 \sim 1.00$	1.000	0.076	0.989	0.050
27	RHC	ν_μ	$1.00 \sim 1.50$	1.000	0.075	1.003	0.047
28	RHC	ν_μ	$1.50 \sim 2.50$	1.000	0.078	1.050	0.051
29	RHC	ν_μ	$2.50 \sim 30.00$	1.000	0.078	1.043	0.046
30	RHC	$\bar{\nu}_\mu$	$0.00 \sim 0.40$	1.000	0.109	0.999	0.066
31	RHC	$\bar{\nu}_\mu$	$0.40 \sim 0.50$	1.000	0.102	1.013	0.054
32	RHC	$\bar{\nu}_\mu$	$0.50 \sim 0.60$	1.000	0.093	0.994	0.047
33	RHC	$\bar{\nu}_\mu$	$0.60 \sim 0.70$	1.000	0.083	0.973	0.043
34	RHC	$\bar{\nu}_\mu$	$0.70 \sim 1.00$	1.000	0.102	0.972	0.054
35	RHC	$\bar{\nu}_\mu$	$1.00 \sim 1.50$	1.000	0.088	0.987	0.049
36	RHC	$\bar{\nu}_\mu$	$1.50 \sim 2.50$	1.000	0.068	1.029	0.044
37	RHC	$\bar{\nu}_\mu$	$2.50 \sim 3.50$	1.000	0.070	1.058	0.049
38	RHC	$\bar{\nu}_\mu$	$3.50 \sim 5.00$	1.000	0.092	1.063	0.065
39	RHC	$\bar{\nu}_\mu$	$5.00 \sim 7.00$	1.000	0.085	1.039	0.059
40	RHC	$\bar{\nu}_\mu$	$7.00 \sim 30.00$	1.000	0.115	0.997	0.094
41	RHC	ν_e	$0.00 \sim 2.50$	1.000	0.066	1.043	0.048
42	RHC	ν_e	$2.50 \sim 30.00$	1.000	0.083	1.038	0.066
43	RHC	$\bar{\nu}_e$	$0.00 \sim 0.50$	1.000	0.095	1.005	0.053
44	RHC	$\bar{\nu}_e$	$0.50 \sim 0.70$	1.000	0.089	1.004	0.045
45	RHC	$\bar{\nu}_e$	$0.70 \sim 0.80$	1.000	0.086	1.002	0.045
46	RHC	$\bar{\nu}_e$	$0.80 \sim 1.50$	1.000	0.079	1.007	0.042
47	RHC	$\bar{\nu}_e$	$1.50 \sim 2.50$	1.000	0.075	1.035	0.053
48	RHC	$\bar{\nu}_e$	$2.50 \sim 4.00$	1.000	0.086	1.038	0.066
49	RHC	$\bar{\nu}_e$	$4.00 \sim 30.00$	1.000	0.153	1.075	0.134

Table 6.3: Systematic uncertainties of the T2K beam flux parameters at SK. Pre-fit refers to pre-ND280 fit; post-fit refers to post-ND280 fit.

Id	Parameter	type	nominal	upper	lower	pre-fit	pre-fit error	post-fit	post-fit error
50	M_A^{QE}	shape	1.0 (1.2)	0.000	9999.000	1.000	N/A	0.943	0.066
51	$p_F(O)$	shape	1.0 (225 MeV/c)	0.889	1.222	1.000	N/A	0.911	0.067
52	σ_ν^{2p2h}	norm	1.000	0.000	9999.000	1.000	N/A	1.502	0.195
53	$\sigma_{\bar{\nu}}^{2p2h}$	norm	1.000	0.000	9999.000	1.000	N/A	0.726	0.231
54	$\sigma^{2p2h}(C)/\sigma^{2p2h}(O)$	norm	1.000	0.000	9999.000	1.000	0.200	0.964	0.167
55	$f^{2p2h}(O)$	shape	0.000	-1.000	1.000	0.000	3.000	0.997	0.347
56	C_A^5	shape	1.0 (1.01)	0.000	9999.000	0.950	0.149	0.966	0.064
57	M_A^{RES}	shape	1.0 (0.95)	0.000	9999.000	1.126	0.158	0.848	0.047
58	$I_{BKG}^{1/2}$	shape	1.0 (1.30)	0.000	9999.000	0.738	0.308	1.011	0.197
59	$\sigma_{\nu_e}/\sigma_{\nu_\mu}$	norm	1.000	0.000	9999.000	1.000	0.028	1.000	0.028
60	$\sigma_{\bar{\nu}_e}/\sigma_{\bar{\nu}_\mu}$	norm	1.000	0.000	9999.000	1.000	0.028	1.000	0.028
61	f^{CCDIS}	shape	0.000	-9999.000	9999.000	0.000	0.400	0.385	0.197
62	$f^{CCCoh}(O)$	norm	1.000	0.000	9999.000	1.000	0.300	0.874	0.282
63	f^{NCCoh}	norm	1.000	0.000	9999.000	1.000	0.300	0.938	0.297
64	$f^{NC1\gamma}$	norm	1.000	0.000	9999.000	1.000	1.000	1.000	1.000
65	$f^{NCother}$	norm	1.000	0.000	9999.000	1.000	0.300	1.000	0.300
66	$BeRPA\_A$	shape	0.590	0.000	9999.000	0.590	0.118	0.688	0.057
67	$BeRPA\_B$	shape	1.050	0.000	9999.000	1.050	0.210	1.599	0.117
68	$BeRPA\_D$	shape	1.130	0.000	9999.000	1.130	0.170	0.962	0.134
69	$BeRPA\_E$	shape	0.880	0.000	9999.000	0.880	0.352	0.875	0.353
70	$BeRPA\_U$	shape	1.200	0.000	9999.000	1.200	Fixed	1.200	0.100

Table 6.4: cross section systematic error parameters used in this analysis. The nominal values are the default values in NEUT, which are used to generated the MC. The numbers in brackets in column "nominal" are the nominal values of these parameters in NEUT, and the fractional values are used in the fit; otherwise the nominal values of the parameters used in the fit are the same as their nominal values in NEUT.

More details are listed below on the cross section systematic error parameters considered in this analysis (listed in Tab. 6.4):

- $\mathbf{M_A^{QE}}$: M_A^{QE} is the axial mass in the axial form factor of CCQE neutrino-nucleon interaction. The measured CCQE cross section is a convolution of neutrino-nucleon interaction and nuclear effect. Therefore, M_A^{QE} is used as an effective parameter to describe neutrino-nucleus interactions. Due to the observed tension between MiniBooNE and MINERνA data [132], a flat prior on M_A^{QE} is used in the near detector fit; in other words, M_A^{QE} is only constrained by ND280 data.

- $\mathbf{p_F(O)}$: The average Fermi momentum of a nucleon in an oxygen nucleus in the relativistic Fermi gas model. Similar to M_A^{QE}, $p_F(O)$ is also only constrained by ND280 data due to the tension between MiniBooNE and MINERνA data [132].

- $\sigma_\nu^{\mathbf{2p2h}}$ and $\sigma_{\bar{\nu}}^{\mathbf{2p2h}}$: The normalization of 2p2h interaction for ν and $\bar{\nu}$, respectively.

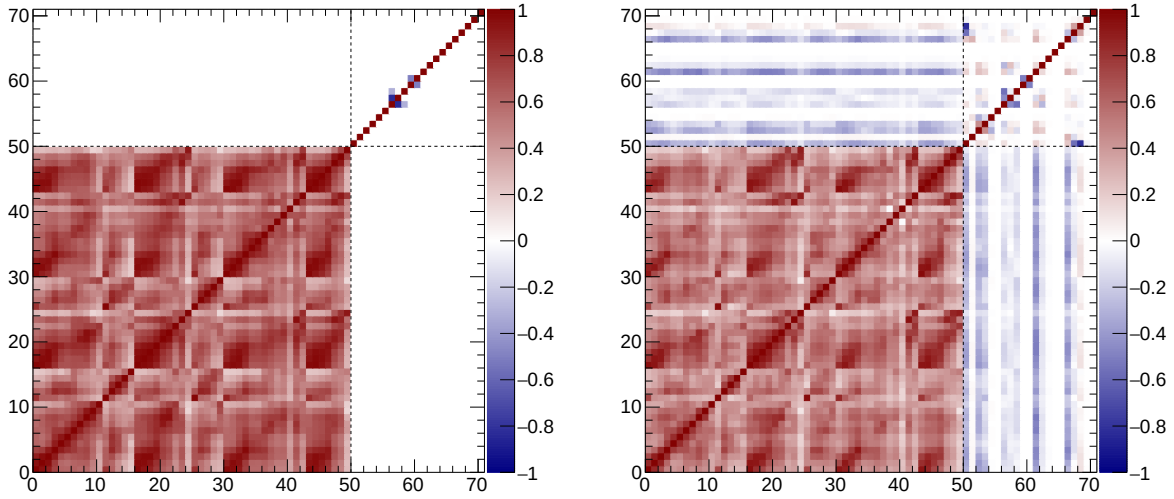

Figure 6.3: The correlation matrix of the T2K beam flux parameters and cross section parameters used in this analysis, taken from [134]. Left: pre-ND280 fit; right: post-ND280 fit. The first 50 bins correspond to the flux parameters, and the last 21 bins correspond to the cross section parameters.

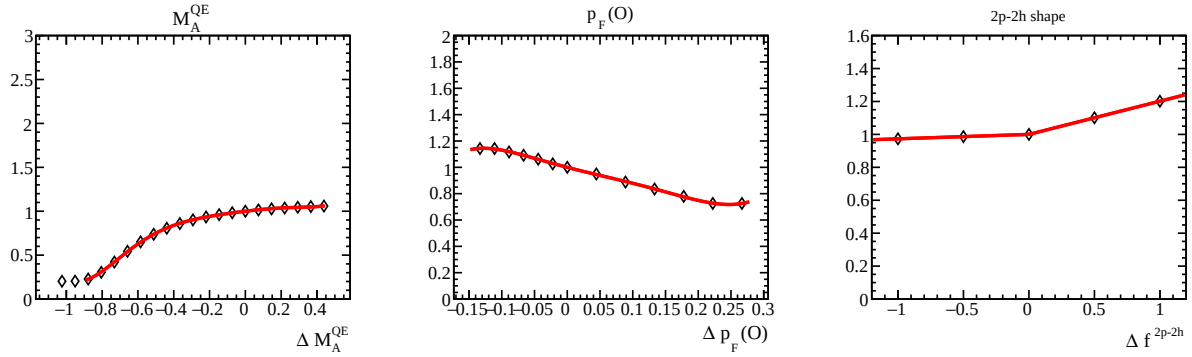

Figure 6.4: An example of the event-by-event weight polynomials for the shape cross section parameters. Left: M_A^{QE}; middle: $p_F(O)$; right: $f^{2p2h}(O)$ shape parameter. There are 11 cross section polynomials per MC event, but only 3 are shown here. The black triangles are the event-by-event weights generated using T2KReWeight v1r27p3; the red curves are the fitted polynomials.

They are assigned flat priors in the ND280 fit because neither T2K nor external data has enough constraining power on the 2p2h process. No correlation is assigned between σ_{ν}^{2p2h} and $\sigma_{\bar{\nu}}^{2p2h}$ because different models predict very different $\nu/\bar{\nu}$ 2p2h cross sections [88].

- $\sigma^{\mathbf{2p2h}}(\mathbf{C})/\sigma^{\mathbf{2p2h}}(\mathbf{O})$ and : The C/O ratio of the 2p2h cross section. A 0.2 prior constraint is assigned in the ND280 fit based on a study which estimated the uncertainty on the extrapolation from Carbon to Oxygen using electron scattering data [135].

- $\mathbf{f}^{\mathbf{2p2h}}(\mathbf{O})$: The shape parameter that modified the differential shape of the 2p2h process by changing the relative contribution from meson exchange current (MEC) and nucleon-nucleon correlations (NN) [88]. $+1$ means it is fully MEC, and -1 means it is fully NN.

- $\mathbf{C}_{\mathbf{A}}^{\mathbf{5}}$, $\mathbf{M}_{\mathbf{A}}^{\mathbf{RES}}$ and $\mathbf{I}_{\mathbf{BKG}}^{\mathbf{1/2}}$: C_A^5 is the axial form factor in the single pion production channel of the neutrino-nucleon interaction, while M_A^{RES} is the axial mass; $I_{BKG}^{1/2}$ is the isospin=1/2 non-resonant background. The prior constraints on the three parameters are obtained by fits to external data on neutrino interaction with a free nucleon from the ANL [98] and BNL [99] bubble chamber experiments [88].

- $\sigma_{\nu_\mathbf{e}}/\sigma_{\nu_\mu}$ and $\sigma_{\bar{\nu}_\mathbf{e}}/\sigma_{\bar{\nu}_\mu}$: These parameters are included to account for the fact that $\nu_e(\bar{\nu}_e)$ and $\nu_\mu(\bar{\nu}_\mu)$ interaction cross sections are not the same. The following covariance matrix is used:

$$V_{\nu_e,\bar{\nu}_e} = V_{rad.corr.} + V_{SCC} = \begin{pmatrix} \sigma^2_{\nu_e} & \sigma_{\nu_e}\sigma_{\bar{\nu}_e} \\ \sigma_{\nu_e}\sigma_{\bar{\nu}_e} & \sigma^2_{\bar{\nu}_e} \end{pmatrix} = \begin{pmatrix} 2\times 0.02^2 & -0.02^2 \\ -0.02^2 & 2\times 0.02^2 \end{pmatrix} \quad (6.20)$$

  The covariance matrix takes into account the uncorrelated 2% contribution from radiative corrections, and an anti-correlated contribution to account for second class currents (SCC) [136][137]. The constraints are added after the ND280 fit is performed as ND280 does not provide constraints on these parameters.

- $\mathbf{f}^{\mathbf{CCDIS}}$: It is the only systematic error parameter assigned to the DIS process because DIS events rarely make it into T2K samples. The uncertainty is parameterized as

$$\sigma_{DIS} = \frac{0.4}{E_\nu} \quad (6.21)$$

  as the uncertainty on the Bodek-Yang corrections have a larger error at low energy [88]. The numerator is 0.4 because external data shows that the uncertainty is $\sim$ 10% at 4 GeV [138]. Future improvements in the DIS systematic error parameterization is crucial for the inclusion of SK multi-GeV atmospheric neutrino samples.

- $\mathbf{f}^{\mathbf{CCCoh}}(\mathbf{O})$ and $\mathbf{f}^{\mathbf{NCCoh}}$: The normalization parameters for CC coherent and NC coherent neutrino-nucleus pion production interactions. A 30% prior error is assigned

to $f^{CCCoh}(O)$ based on comparisons to MINERνA data [102]. The 30% prior error on f^{NCCoh} is motivated by a 15% NEUT/data discrepancy from the measurement in [139], which has a 20% systematic uncertainty.

- $\mathbf{f^{NC1\gamma}}$: The normalization parameters for non-pion resonant NC interactions that produce a γ. It has a 100% error and is not constrained by ND280 fit because there is no external data or control sample that could constrain it.

- $\mathbf{f^{NCother}}$: The normalization parameter for the NC interactions which consist of NC elastic interactions, NC resonant interactions that produce a γ, η, or K, NC DIS and multi-π interactions. A 30% error is assigned based on studies in ref. [120], and it is not constrained by the ND280 fit because the NC other category at the near detector has different components than the equivalent category at SK.

- Bernstein RPA ($\mathbf{BeRPA\_(A, B, D, E, U)}$) shape parameters: The BeRPA parameters are used to mock up the Random Phase Approximation (RPA) correction uncertainty provide by the Nieves relativistic RPA model [92] as shown by Figure 6.5. The parameterization of Nieves' RPA correction uncertainty is based on Bernstein polynomials [140], hence the name "BeRPA". RPA is a non-perturbative method to describe microscopic quantum mechanical interactions in a complex many-body system which has recently been used to describe the collective effects due to the interactions and correlations of the nucleons inside the nucleus in neutrino-nucleus interaction [92][141]. The RPA correction yields modification to the neutrino-nucleus interaction cross section described as a function of Q^2, and the uncertainties come from pion-nucleus scattering data constraints as well as a large theoretical uncertainty.

6.3.2 Final state interaction (FSI) and secondary interaction (SI) systematic uncertainties

As described in section 4.1, T2K uses the cascade model to describe final state interactions. Because the underlying physics principles that govern hadronic interactions inside and outside the nucleus are the same, the pion cascade model is tuned to external $\pi^{\pm}$-nucleus scattering measurements. The tuning of the model to external data sets and the data sets themselves are described in [91]. The parameters used in the pion scattering fit, and the fit results are summarized in Table 6.5. The quasi-elastic scattering, absorption and hadron production parameters scale the probability of the corresponding microscopic interaction at each step;

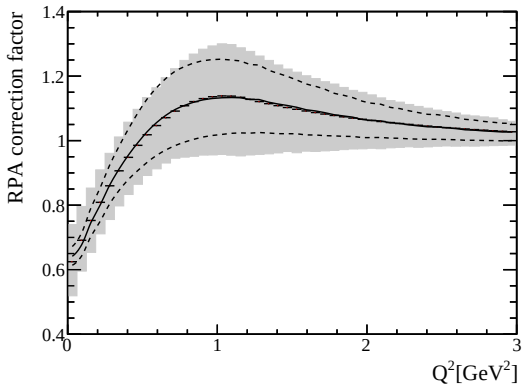

Figure 6.5: The BeRPA best fit value is shown (black data points) compared to the Nieves nominal RPA model as a function of Q^2 (black solid line). The nominal BeRPA uncertainties given in Table 6.4 (gray band) are also shown with the theoretical uncertainties from Nieves for comparison (dashed black lines) [88].

the charge exchange parameters scale the fraction of charge exchange in low momentum QE scattering. Table 6.6 shows the correlation among the five FSI/SI parameters used in this analysis.

Id	Parameter	description	momentum region	nominal	lower	upper	best-fit	error
0	FEFQE	Quasi-elastic scattering	< 500 MeV/c	1.000	0.100	1.700	1.069	0.313
1	FEFABS	Absorption	< 500 MeV/c	1.100	0.350	1.950	1.404	0.432
2	FEFCX	Single charge exchange	< 500 MeV/c	1.000	0.100	1.600	0.697	0.305
3	FEFINEL	Hadron (N+n) production	> 400 MeV/c	1.000	0.200	2.600	1.002	1.101
4	FEFQEH	Quasi-elastic scattering	> 400 MeV/c	1.800	0.800	2.800	1.824	0.859
5	FEFCXH	Single charge exchange	> 400 MeV/c	Not used in this analysis				

Table 6.5: The NEUT FSI probability scaling parameters used in the pion scattering fit; the same parameters are used in this analysis with the exception of FEFCXH. The best-fit values and errors are taken from [91]. The last parameter is not incorporated in this analysis for its small effect.

A reweighting scheme [142][91] was developed to calculate the escape probability after FSI and SI relative to the nominal escape probability as a function of each parameter value. For each MC event with at least one pion at the primary interaction vertex, a set of five reweighting functions are generated. A 5^{th}-order polynomial fit is performed to each reweighting function as an approximation of the direct output of the reweighting software. The event-by-event polynomials are used in the analysis to avoid having to re-run the FSI/SI simulation each time. An example of the reweighting functions is shown in Fig. 6.7.

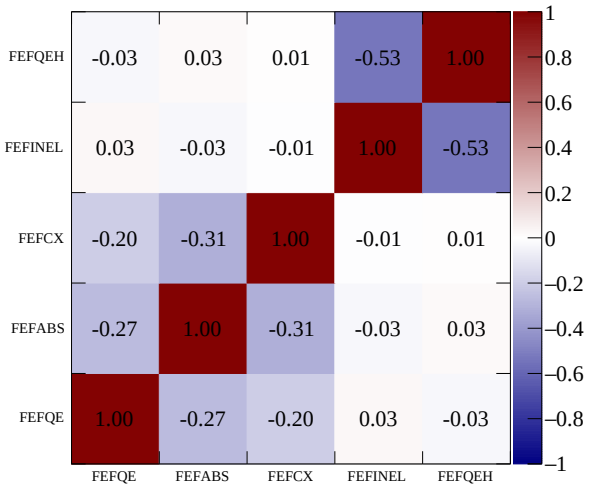

Figure 6.6: The correlation matrix of the FSI/SI systematic error parameters used in this analysis, as it is taken from [91].

6.3.3 SK detector systematic uncertainties

A proper detector model would be able to tell us how a given event is affected by the variations in detector characteristics. For example, a change in water transparency, if unaccounted for, will incur a bias in the energy reconstruction, and potentially in other reconstructed quantities such as the reconstructed vertex position and direction; it is therefore necessary to quantify such effects as a function of the change in water transparency. The ideal detector model would include such quantifications of all the detector characteristics which have an impact on the observed events. However, an effective detector model has been used in the past and present SK and T2K analyses. The justification is that our lack of understanding of the detector characteristics would manifest in the form of data/MC discrepancy in reconstructed quantities; in other words, uncertainties in the detector performance can be quantified by the such data/MC discrepancies.

In this analysis, the SK detector systematic uncertainties are parameterized as the smearing and biasing of the fiTQun [110] reconstructed quantities:

$$L^i_{jk} \rightarrow \alpha^i_{jk} L^i_{jk} + \beta^i_{jk}, \tag{6.22}$$

where L^i are the fiTQun ring-counting parameter, the e/μ PID parameter, the e/π^0 PID

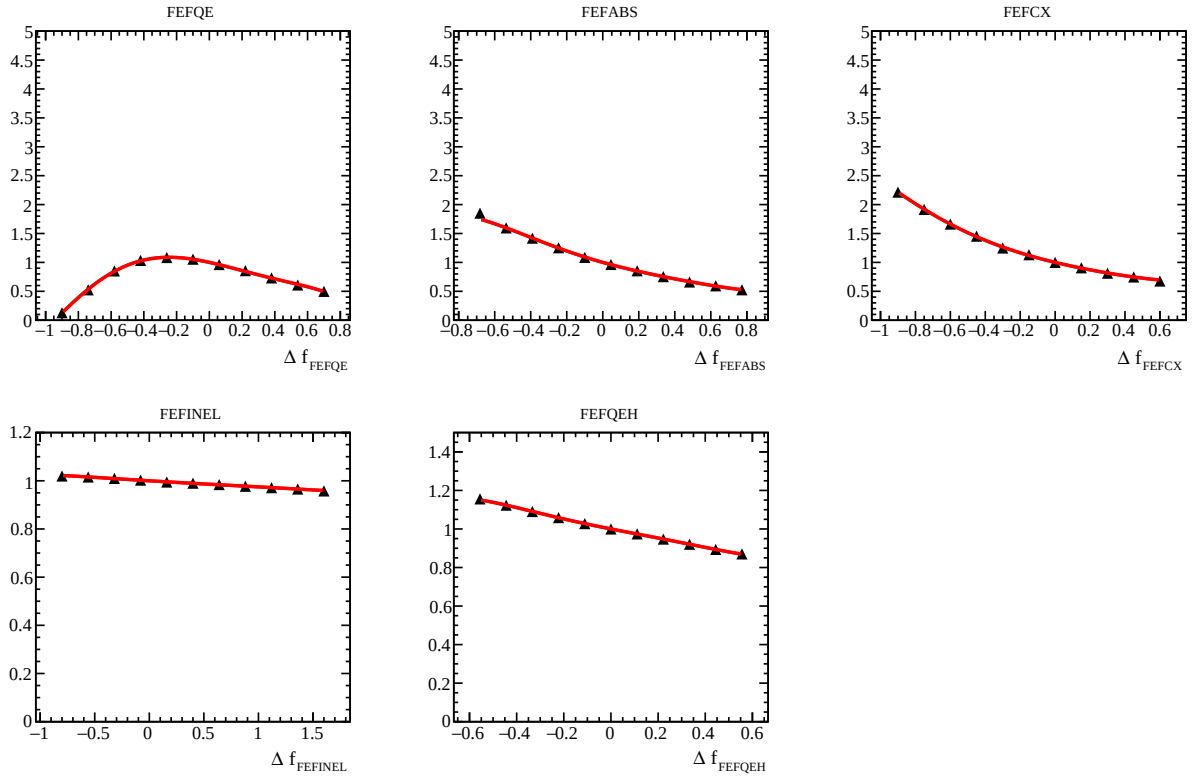

Figure 6.7: An example of the event-by-event weight polynomials for the FSI/SI parameters. Clock-wise from the top left: FEFQE, FEFABS, FEFCX, FEFQEH and FEFINEL. The black triangles are the event-by-event weights generated using T2KReWeight v1r27p3 and the fitter described in [91]; the red curves are the fitted 5^{th}-order polynomials used in this analysis. The parameter values here are the fractional change relative to the nominal values shown in Table 6.5.

parameter or the μ/π^+ PID parameter, j is the event topology index, and k is the visible energy bin index. The L^i's are chosen because the event selection is based on them. It should be pointed out that this effective detector model assumes that we can only bias and smear these parameters. Unless changes in the low-level detector parameter manifests themselves in ways that cannot be described by the biases and smears, this model is a reasonable depiction of the detector. Table 6.6 summarizes the seven event topology categories; they are chosen because the detector systematic uncertainties are not expected to be the same for events with distinctively different final state topologies. For example, the particle identification capability gets worse if there are two overlapping rings, compared to the case where there is only one lepton in the final state; therefore, they should be assigned different systematic uncertainties. Four visible energy ranges are considered: 30 $\sim$ 300 Mev, 300 $\sim$ 700 Mev, 700 $\sim$ 1330 Mev, 1330 $\sim$ 3000 Mev. Therefore, there are 112 smearing (α) parameters and

112 bias (β) parameters in total.

Index	category	description
0	1e	Only one electron above Cherenkov threshold in the final state
1	1μ	Only one muon above Cherenkov threshold in the final state
2	1e+other	One electron and one or more other charged particle above Cherenkov threshold in the final state
3	1μ+other	One muon and one or more other charged particle above Cherenkov threshold in the final state
4	1π^0	Only one π^0 in the final state
5	1π^+	Only one $\pi^\pm$ above Cherenkov threshold in the final state
6	Other	All the other cases (mostly multiple hadrons)

Table 6.6: The event categorization on which the SK detector systematic errors are based.

Two ring-counting parameter distributions are shown in Figure 6.8 as an example of the control distributions. Note that the ring-counting parameter value is not always below (above) zero for the 1R (MR) samples. This is because the ring-counting parameter defined here corresponds to an intermediate step at which fiTQun compares the best single-ring hypothesis and the best two-ring hypothesis, after which more steps are taken to determine whether the additional ring should be kept or merged. Therefore, the eventual reconstructed number of rings (single-ring v.s. multi-ring) does not correspond to the intermediate ring-counting parameter exactly, neither does fiTQun provide a ring-counting parameter that does. Nonetheless, the data/MC differences of this ring-counting parameter provides a good approximation for the detector systematic uncertainties associated with ring-counting.

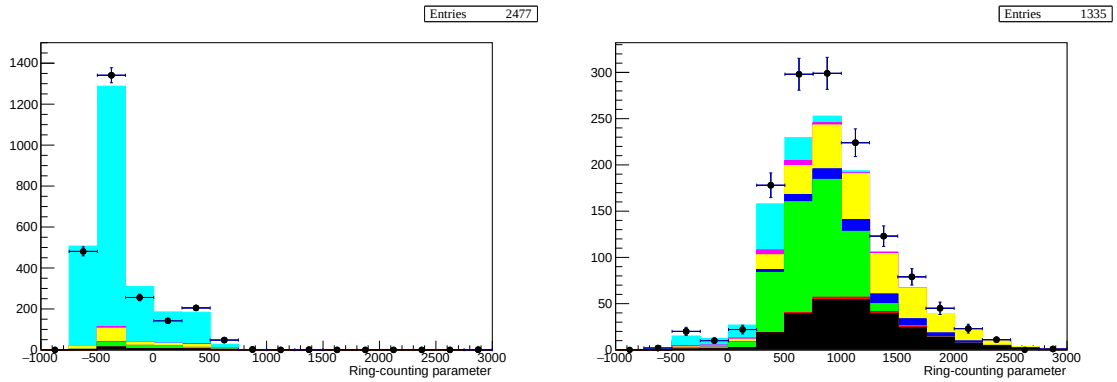

Figure 6.8: The pre-fit ring-counting parameter distribution of the 1Re 0_{dcy} sample (left) and the MR 0_{dcy} sample (right) in the visible energy range $300 < E_{vis} < 700$ MeV. Data points are shown with statistical errors.

Since the single-ring selection is based on the fiTQun final output of the number of rings, whereas the ring-counting related detector systematic errors are estimated by the data/MC discrepancies of the aforementioned ring-counting parameter, a change in the latter should reflect in the change in the former. Ideally this should be done by re-running fiTQun reconstruction every time the ring-counting parameter is varied ($L \to \alpha L + \beta$) to obtain the reconstructed number of rings. However, doing so would take a prohibitively long time for each MCMC step. In practice, this is done by the following re-weighting procedure, which mimics the effect of re-running fiTQun:

- 2D look-up tables of the ring-counting parameter v.s. the number of rings are generated prior to the fit with all parameters fixed at nominal values (oscillation parameter values shown in Table 6.11). An example of the look-up tables are shown by Figure 6.9. Each row is normalized to 1, which means each bin represents the fraction of the events with a given ring-counting parameter value being reconstructed as n-ring, where n is the x-axis bin index. Let ω_{nL} be the weight for events with ring-counting parameter value L and reconstructed as n-ring.
- The ring-counting parameter is varied in the MCMC as $L' = \alpha L + \beta$; the corresponding weight for being reconstructed as n-ring becomes $\omega_{nL'}$. Each MC event would then take an additional weight $\omega = \omega_{nL'}/\omega_{nL}$.

The hybrid-π^0 samples [124] are used to assign prior constraints on the α and β parameters of the e/π^0 PID parameters of the $1\pi^0$ category. Figure 6.10 shows the χ^2 map obtained from a fit to the primary and secondary hybrid-π^0 samples, which are used as the prior constraints in this analysis.

6.3.4 Atmospheric neutrino flux systematic uncertainties

This analysis uses the atmospheric neutrino flux model provided by Honda et. al. [69]. 16 atmospheric flux systematic error parameters are used in this analysis as summarized by Table 6.7.

The following sources of flux systematic uncertainties are considered:

- **Absolute normalization**
  The absolute normalization errors are given by the Honda flux model [69]. It factors

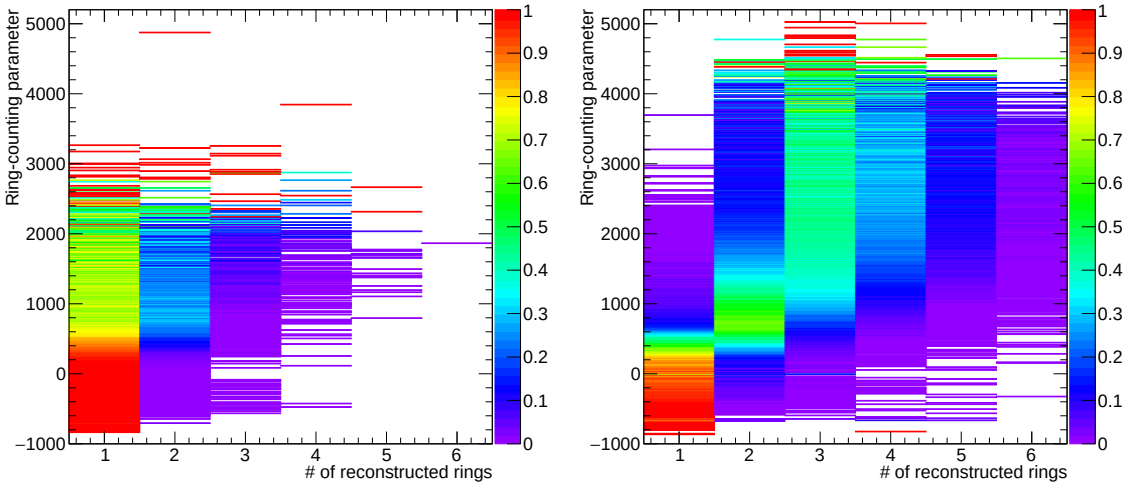

Figure 6.9: 2D look-up tables of the ring-counting parameter v.s. the number of reconstructed rings. Left: atmospheric neutrino ν_μ flavor with only one muon above Cherenkov threshold (index 1 in Table 6.6); right: atmospheric neutrino ν_μ flavor with one muon and one or more other particles above Cherenkov threshold (index 3 in Table 6.6).

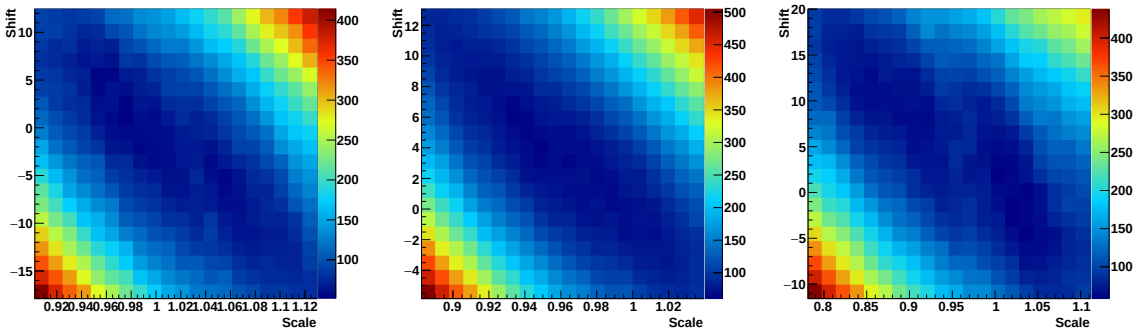

Figure 6.10: χ^2 as a function of the α and β parameters of the e/π^0 PID parameters of the $1\pi^0$ category based on a fit to the hybrid-π^0 samples. Left: $100 < E_{vis} < 300$ MeV; middle: $300 < E_{vis} < 700$ MeV; right: $700 < E_{vis} < 1250$ MeV. The x-axis is the smearing (α) parameter, y-axis the bias parameter (β), z-axis the χ^2. Plots are provided by Miao Jiang.

in the contributions from uncertainties on pion production in the hadronic interaction model (δ_π, calibrated with atmospheric muon measurements), Kaon production (δ_K), hadronic interaction cross sections (δ_σ) and air density profile (δ_{air}). Figure 6.11 shows the fractional uncertainties as a function of neutrino energy. In this analysis, two independent normalization parameters are assigned to neutrinos with energy smaller and larger than 1 GeV, respectively, and the fractional change when the flux parameters

Parameter	Description
abs_norm_E_lt_1GeV	Normalization constant for events with $E < 1$GeV
abs_norm_E_gt_1GeV	Normalization constant for events with $E > 1$GeV
nu_nubar_ratio_E_lt_1GeV	$\nu/\bar{\nu}$ for events with $E < 1$GeV
nu_nubar_ratio_1_E_10GeV	$\nu/\bar{\nu}$ for events with $1 < E < 10$GeV
nu_nubar_ratio_E_gt_10GeV	$\nu/\bar{\nu}$ for events with $E > 10$GeV
nuebar_nue_E_lt_1GeV	$\bar{\nu}_e/\nu_e$ for events with $E < 1$GeV
nuebar_nue_1_E_10GeV	$\bar{\nu}_e/\nu_e$ for events with $1 < E < 10$GeV
nuebar_nue_E_gt_10GeV	$\bar{\nu}_e/\nu_e$ for events with $E > 10$GeV
numubar_numu_E_lt_1GeV	$\bar{\nu}_\mu/\nu_\mu$ for events with $E < 1$GeV
numubar_numu_1_E_10GeV	$\bar{\nu}_\mu/\nu_\mu$ for events with $1 < E < 10$GeV
numubar_numu_E_gt_10GeV	$\bar{\nu}_\mu/\nu_\mu$ for events with $E > 10$GeV
up_down_ratio	Upward and downward flux ratio
horizontal_vertical_ratio	Horizontal and vertical flux ratio
k_pi_ratio	K/π ratio
solar_activity	Solar activity
nu_path	Neutrino path length

Table 6.7: Atmospheric neutrino flux systematic uncertainty parameters. The prior constraints on the flux parameters follow $\sim N(0, 1)$.

are changed by 1σ are given by the combined contribution from pion production and hadronic interaction cross sections as shown by Figure 6.11.

- **Flux ratio**
  Systematic uncertainties on the flux ratio of $(\nu_\mu+\bar{\nu}_\mu)/(\nu_e+\bar{\nu}_e)$ is given by the difference between the Honda flux model [69] and the flux predictions by FLUKA [80] and the Bartol model [79]. Three flux parameters are assigned for neutrinos with energy smaller than 1GeV, between 1GeV and 10 GeV, and above 10 GeV. The fractional change by changing these flux parameters by 1σ is 2% for $E_\nu < 1$ GeV, 3% for $1 < E_\nu < 10$ GeV, and 5% for $10 < E_\nu < 30$ GeV; above 30 GeV, the fractional change increases linearly as a function of $\log E_\nu$ from 5% at 30 GeV up to 30% at 1 TeV.

- **$\nu/\bar{\nu}$ ratio**
  The uncertainties in π^+/π^- and K^+/K^- lead to uncertainties in $\nu_\mu/\bar{\nu}_\mu$ and $\nu_e/\bar{\nu}_e$. Three systematic error parameters are assigned to $\nu_\mu/\bar{\nu}_\mu(\nu_e/\bar{\nu}_e)$ at $E_\nu < 1$ GeV, $1 < E_\nu < 10$ GeV and $E_\nu > 10$ GeV. The following fractional errors are assigned according to the differences between the Honda model [69] and FLUKA [80] and the Bartol model [79]: for $\nu_\mu/\bar{\nu}_\mu$, the uncertainties are 2% for $E_\nu < 1$ GeV, 6% for $1 < E_\nu < 10$ GeV, 6% for $10 < E_\nu < 50$ GeV, and then linearly increases as a function of $\log E_\nu$ to 30% at 1 TeV;

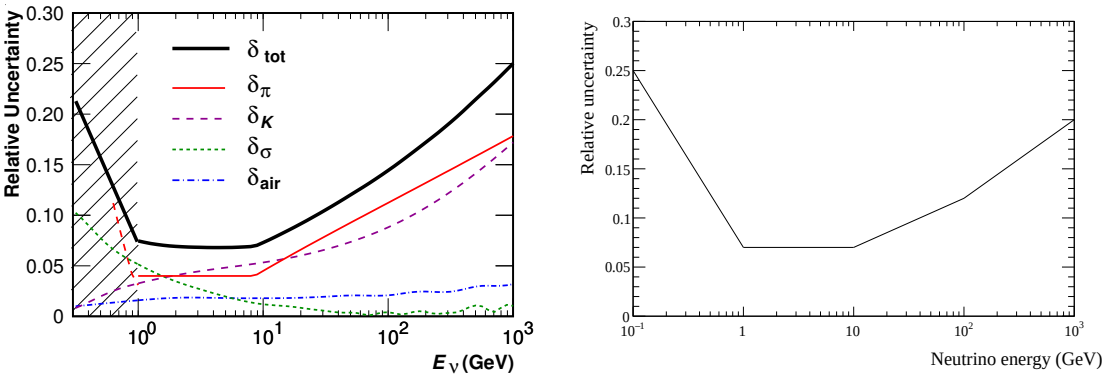

Figure 6.11: Left: absolute flux uncertainties by source as a function of neutrino energy given by [69]. Right: absolute flux uncertainties as a function of neutrino energy used in this analysis, which only into account the contributions from pion production (δ_π) and hadronic interaction cross section (δ_σ); the constributions from kaon production and air density profile are considered separately.

for $\nu_e/\bar{\nu}_e$, the uncertainties are 5% for $E_\nu < 1$ GeV, 5% for $1 < E_\nu < 10$ GeV, 8% for $10 < E_\nu < 100$ GeV, and then linearly increases as a function of $\log E_\nu$ to 30% at 1 TeV

- **Up/down ratio and horizontal/vertical ratio**
  Both the up/down ratio and horizontal/vertical ratio systematic uncertainties are assigned by comparing the zenith angle distributions calculated by the Honda model [69], FLUKA [80] and the Bartol model [79]. The up/down asymmetry in the unoscillated neutrino flux is due to the Earth magnetic field; it is small at low energy because the lepton zenith angle is not a good proxy for neutrino direction, therefore the uncertainty is largely smeared out. As for the horizontal/vertical ratio, the uncertainty is dominated by the differences in the 3D calculation methods used in the models below 3 GeV, and by the differences in the underlying hadronic interaction K/π ratio above 3 GeV. The 1σ errors are summarized in Table 6.8. The error values are originally calculated for each analysis sample but assigned to true neutrino flavor here because purities are high ($> 90\%$) for the sub-GeV samples considered in this analysis.

- **K/π ratio**
  The dominant source of atmospheric neutrinos is π^+/π^- when $E_\nu < 10$ GeV; above a few tens of GeV, the contributions from Kaon become dominant. Using the measurement of K/π ratio from 450 GeV/c protons on beryllium by the SPY experiment [143], the uncertainties on atmospheric neutrino flux due to the K/π ratio uncertainty is

Up/down ratio			Horizontal/vertical ratio		
1σ error $= -0.02\sigma \cos\theta_{zenith}$			1σ error $= 0.01\sigma(1 - 2\lvert\cos\theta_{zenith}\rvert)$		
Neutrino energy	Flavor	σ	Neutrino energy	Flavor	σ
< 400 MeV	ν_e, $\bar{\nu}_e$	0.1	< 400 MeV	ν_e, $\bar{\nu}_e$	0.1
	ν_μ, $\bar{\nu}_\mu$	0.3		ν_μ, $\bar{\nu}_\mu$	0.1
$[400, 1330]$ MeV	ν_e, $\bar{\nu}_e$	0.8	$[400, 1330]$ MeV	ν_e, $\bar{\nu}_e$	1.4
	ν_μ, $\bar{\nu}_\mu$	0.5		ν_μ, $\bar{\nu}_\mu$	1.9
> 1330 MeV	ν_e, $\bar{\nu}_e$	0.7	> 1330 MeV	ν_e, $\bar{\nu}_e$	3.2
	ν_μ, $\bar{\nu}_\mu$	0.2		ν_μ, $\bar{\nu}_\mu$	2.3

Table 6.8: The up/down ratio and horizontal/vertical ratio systematic errors.

determined to be 5% for $E_\nu < 100$ GeV, 20% for $E_\nu > 1$ TeV, and increase linearly as a function of E_ν between 100 GeV and 1 TeV.

- **Solar activity**
  Solar activity has a 11-year cycle, and it can affect the Earth magnetic field, and therefore the primary cosmic rays arriving at the Earth atmosphere. The variation in neutrino fluxes as a result of a ± 1 year variation in the Solar cycle is taken as the uncertainty, which is 10% for the SK-IV period.

- **Neutrino path length**
  Neutrino oscillation probability is dependent on the height at which atmospheric neutrinos are produced, especially for the downward-going and horizontal-going neutrinos. The average neutrino path length depends on the atmosphere density profile, the uncertainty of which is determined to be 10% by comparing the US-standard '76 and the MSISE-90 atmosphere models [144]. The calculation of neutrino oscillation probability factors in the variation of neutrino production height as a result of the air density uncertainty.

6.3.5 Other systematic uncertainties

The remaining systematic uncertainties are summarized by Table 6.9.

- **T2K and SK energy scale errors**
  The T2K and SK energy scale errors are fully correlated; it is calibrated using a number of natural sidebands ranging from tens of MeV to a few TeV, including cosmic muons

which stop inside the detector and the associated decay electrons and neutral current π^0 events. The absolute energy scale is taken as the relative data/MC difference of the most discrepant sample. The time variations of the reconstructed decay electron momentum and the muon momentum divided by range in the stopping muon sideband are also considered. The final energy scale error is the quadratic sum of the absolute energy scale error and the time variation error. It is estimated to be 2.1% for SK-IV [123].

- **SK up-down energy calibration**
  The up-down asymmetry in energy scale is estimated to be 0.3% based on the data/MC directional difference in the decay electrons from stopping cosmic muons.

- **SK FC reduction**
  The uncertainty related to the FC reduction efficiency is estimated to be 1.3% based on comparisons between data/MC after FC reduction.

- **SK FV**
  The fiducial volume uncertainty is estimated by the change of number of events inside the fiducial volume by shifting each MC event inward and outward by 10 cm. It is estimated to be 2% for SK samples.

- **SK decay-e tagging efficiency**
  The decay electron tagging efficiency is estimated using the cosmic stopping muon sideband samples. The error is estimated to be 0.8% for the efficiency in identifying a decay electron when there is one, and 1.6% for identifying two decay electrons when there is one. The fractional error of each SK sample is then calculated based on the event rate. For example, the uncertainty on the 1Re 0_{dcy} sample is $-(0.008 \times N^{1Re\ 1_{dcy}}/N^{1Re\ 0_{dcy}}$, where $N^{1Re\ 0_{dcy}}$ is the number of events in the 1Re 0_{dcy} sample.

- **SK background**
  The background error is estimated by the eye-scanning of non-neutrino background events such as cosmic muons and PMT flashers. It is determined to be 0.02% for the sub-GeV samples.

- **T2K FV and decay electron tagging efficiency**
  The decay electron tagging efficiency and fiducial volume uncertainties for the T2K samples are estimated in the same way as the SK samples. The decay electron tagging efficiency is estimated to be 0.22% for the CCQE-like samples, and the FV uncertainty

is 0.43% [124]. Since each T2K sample has similar errors in both, a quadratic sum is taken and a 0.5% normalization error is assigned to all four T2K samples.

Parameter	Nominal	Error
sk_energy_scale	0	0.021
sk_up_down_calibration	0	0.003
sk_fc_reduction	0	0.013
sk_non_nue_bg_elike	0	0.0002
sk_nu_bg_mulike	0	0.0002
sk_FV	0	0.02
sk_decay_e_tagging	0	0.03
t2k_energy_scale	0	0.021
t2k_FV_decay_e_tagging	0	0.005

Table 6.9: The remaining systematic error parameters. The T2K energy scale error is fully correlated with the SK energy scale error.

6.4 Event samples

As shown in section 6.2, three "core" samples and four "side-band" samples of SK atmospheric neutrinos, and four samples of T2K beam neutrinos are used in this analysis. This section describes the event selection for the samples used as input for the oscillation analysis. The pre-fit sample data/MC distributions are shown, as well as the effect of systematic error parameters on the number of events.

6.4.1 MC predictions and pre-fit data/MC comparison

The pre-fit MC prediction is generated assuming the same exposure as the data used in this analysis, as shown by Table 6.10, and neutrino oscillation is assumed using the parameters shown in Table 6.11. The 3-flavor (with matter effect) oscillation probabilities are calculated using the software Prob3++ [116]. Since the MC events are generated assuming no oscillation, each MC event can be weighted according to the unoscillated flux and oscillation probabilities.

For each T2K run mode (FHC/RHC), six independent MC samples are generated with their respective unoscillated flux, each for a different oscillation channel: $\nu_\mu \to \nu_\mu$ with ν_μ flux, $\bar{\nu}_\mu \to \bar{\nu}_\mu$ with $\bar{\nu}_\mu$ flux, intrinsic $\nu_e \to \nu_e$ with intrinsic ν_e flux, intrinsic $\bar{\nu}_e \to \bar{\nu}_e$ with intrinsic

	Exposure
T2K Run1-8 FHC	14.734×10^{20} POT
T2K Run1-8 RHC	7.557×10^{20} POT
SK-IV atmospheric	2519.89 days

Table 6.10: The exposure used in this analysis.

$\sin^2\theta_{12}$	0.304
$\sin^2\theta_{13}$	0.0219
$\sin^2\theta_{23}$	0.528
Δm^2_{21}	7.53×10^{-5} eV^2
Δm^2_{32}	2.509×10^{-3} eV^2
δ_{CP}	-1.601 (rad.)

Table 6.11: Default neutrino oscillation parameters used to make pre-fit data/MC distributions and Asimov data fit.

$\bar{\nu}_e$ flux, $\nu_\mu \to \nu_e$ with ν_μ flux, and $\bar{\nu}_\mu \to \bar{\nu}_e$ with $\bar{\nu}_\mu$ flux. The oscillation weight applied to each MC event in the $\overset{(-)}{\nu}_\alpha \to \overset{(-)}{\nu}_\beta$ channel is calculated by Prob3++. Channels $\nu_e \to \nu_\mu$ and $\bar{\nu}_e \to \bar{\nu}_\mu$, or any oscillations into $\overset{(-)}{\nu}_\tau$ are ignored because of their negligible contributions to the observed events at SK.

For SK atmospheric neutrinos, all oscillation channels should be considered. The oscillation weight applied to each MC event is

$$\omega_{\nu_\alpha} = \frac{f_{\nu_\mu} P(\nu_\mu \to \nu_\alpha) + f_{\nu_e} P(\nu_e \to \nu_\alpha)}{f_{\nu_\alpha}} \tag{6.23}$$

where $\nu_\alpha = \nu_e, \nu_\mu$ or ν_τ, f_{ν_α} is the nominal ν_α flux without oscillation, and $P(\nu_\beta \to \nu_\alpha)$ is the $\nu_\beta \to \nu_\alpha$ oscillation probability. Anti-neutrinos are treated in the same way. $P(\nu_\beta \to \nu_\alpha)$ can be calculated by Prob3++ given zenith angle (hence the average baseline).

Aside from oscillation probabilities, additional T2K flux tuning and post-BANFF tuning are applied to each MC event. The flux tuning [145] is obtained by the in-situ measurements during the data-taking period, and therefore is updated after each T2K run period and only applied to T2K MC events. Adding the flux tuning is equivalent to re-generating the T2K MC using updated fluxes without having to do so. The post-BANFF tuning refers to the adjustment made to each MC event based on the post-ND280 fit flux and cross section best-fit values. The post-BANFF flux tuning is only applied to T2K MC, and the post-BANFF cross

section tuning is applied to both the T2K MC and the SK atmospheric neutrino MC. It should also be pointed out that although the MC was generated using the spectral function (SF) model for the CCQE interaction, each MC event is weighted to mock up the RFG+rel.RPA model [88]. This is also done to avoid the CPU-consuming process of generating new MC.

For each step in the Markov chain during the fit, the oscillation probabilities are re-calculated, and each MC event is weighted according to the current oscillation parameters and nuisance parameters. For SK atmospheric neutrinos in particular, when the unoscillated flux is changed by the flux systematic error parameters, the weight applied to each MC event becomes

$$\omega'_{\nu_\alpha} = \frac{f'_{\nu_\mu} P(\nu_\mu \to \nu_\alpha) + f'_{\nu_e} P(\nu_e \to \nu_\alpha)}{f_{\nu_\alpha}} \tag{6.24}$$

where f'_{ν_α} is the ν_α flux modified by the flux systematic error parameters.

6.4.2 T2K samples

The T2K event selections have been discussed in detail in Chapter 5. Tables 6.12 6.13 6.14 6.15 show the event rate predictions for each T2K sample. Figures 6.12 6.13 show the T2K sample reconstructed energy distributions.

	ν_μ	$\bar{\nu}_\mu$	ν_e	$\bar{\nu}_e$	Signal ν_e	Signal $\bar{\nu}_e$
CCQE	0.15997	0.00632	6.26493	0.25353	46.01964	0.27627
MEC	0.03009	0.00117	1.59737	0.04277	8.68482	0.03896
CC1π	0.05192	0.00295	1.05792	0.07173	5.11422	0.05027
CC coherent	0.00014	0.00017	0.00901	0.00412	0.03873	0.00336
CC DIS	0.00833	0.00038	0.10691	0.00808	0.07079	0.00274
CC other	0.00044	0.00000	0.01883	0.00092	0.00874	0.00023
NCπ^0	1.67171	0.05897	0.03649	0.00351	0.00000	0.00000
NC$\pi^\pm$	0.15441	0.00985	0.00450	0.00058	0.00000	0.00000
NC coherent	0.52817	0.04794	0.00715	0.00294	0.00000	0.00000
NCγ	0.94222	0.04983	0.01687	0.00233	0.00000	0.00000
NC other	0.34206	0.02264	0.01870	0.00140	0.00000	0.00000
Total	3.88944	0.20022	9.13869	0.39191	59.93694	0.37183
Total MC	73.92903					
Total data	74					

Table 6.12: Expected numbers of signal and background events passing the event selections broken down in oscillation channel and interaction mode. Oscillation parameters are set to the values in Table 6.11. Expectations are normalized to 14.734×10^{20} POT.

	ν_μ	$\bar{\nu}_\mu$	ν_e	$\bar{\nu}_e$	Signal ν_e	Signal $\bar{\nu}_e$
CCQE	0.01289	0.02394	0.50634	0.84101	1.02054	2.83338
MEC	0.00294	0.00222	0.14383	0.11306	0.23304	0.33048
CC1π	0.00814	0.00792	0.11440	0.15266	0.16267	0.35266
CC coherent	0.00003	0.00042	0.00113	0.01101	0.00125	0.03212
CC DIS	0.00295	0.00058	0.01877	0.01016	0.00904	0.00512
CC other	0.00091	0.00069	0.00226	0.00076	0.00125	0.00044
NCπ^0	0.13578	0.17261	0.00537	0.00465	0.00000	0.00000
NC$\pi^\pm$	0.02354	0.01807	0.00120	0.00076	0.00000	0.00000
NC coherent	0.04803	0.20260	0.00221	0.00317	0.00000	0.00000
NCγ	0.07984	0.17490	0.00438	0.00383	0.00000	0.00000
NC other	0.06002	0.02883	0.00243	0.00105	0.00000	0.00000
Total	0.37507	0.63278	0.80231	1.14213	1.42779	3.55421
Total MC	7.93429					
Total data	7					

Table 6.13: Expected numbers of signal and background events passing the event selection broken down in oscillation channel and interaction mode. Oscillation parameters are set to the values in Table 6.11. Expectations are normalized to 7.557×10^{20} POT.

	ν_μ	$\bar{\nu}_\mu$	ν_e	$\bar{\nu}_e$	Signal ν_e	Signal $\bar{\nu}_e$
CCQE	174.15107	10.92992	0.00364	0.00020	0.02268	0.00016
MEC	35.54530	1.41150	0.00152	0.00008	0.02542	0.00004
CC1π	30.56042	2.78749	0.00186	0.00008	0.02642	0.00008
CC coherent	0.30470	0.09503	0.00000	0.00000	0.00000	0.00000
CC DIS	4.92405	0.36394	0.00035	0.00006	0.00000	0.00000
CC other	0.77193	0.04728	0.00042	0.00000	0.00000	0.00000
NCπ^0	0.50364	0.01796	0.01576	0.00128	0.00000	0.00000
NC$\pi^\pm$	4.73899	0.16952	0.09572	0.00946	0.00000	0.00000
NC coherent	0.00000	0.00043	0.00000	0.00003	0.00000	0.00000
NCγ	0.00000	0.00000	0.00000	0.00000	0.00000	0.00000
NC other	2.12757	0.13326	0.07528	0.00917	0.00000	0.00000
total	253.62767	15.95633	0.19456	0.02035	0.07452	0.00028
Total MC	269.87372					
Total data	240					

Table 6.14: Expected numbers of signal and background events passing the event selections broken down in oscillation channel and interaction mode. Oscillation parameters are set to the values in Table 6.11. Expectations are normalized to $14.734 \times 10^{20}\,POT$.

	ν_μ	$\bar{\nu}_\mu$	ν_e	$\bar{\nu}_e$	Signal ν_e	Signal $\bar{\nu}_e$
CCQE	15.17378	29.66529	0.00084	0.00088	0.00080	0.00137
MEC	4.47557	2.84247	0.00026	0.00027	0.00034	0.00021
CC1π	4.34817	4.82419	0.00036	0.00021	0.00063	0.00068
CC coherent	0.04957	0.18034	0.00000	0.00005	0.00000	0.00006
CC DIS	0.85520	0.54380	0.00004	0.00000	0.00000	0.00000
CC other	0.11859	0.06928	0.00006	0.00000	0.00000	0.00000
NCπ^0	0.05234	0.05034	0.00196	0.00149	0.00000	0.00000
NC$\pi^\pm$	0.34920	0.44624	0.01503	0.01191	0.00000	0.00000
NC coherent	0.00000	0.00201	0.00000	0.00000	0.00000	0.00000
NCγ	0.00000	0.00000	0.00000	0.00000	0.00000	0.00000
NC other	0.32676	0.20423	0.01721	0.00816	0.00000	0.00000
Total	25.74918	38.82819	0.03576	0.02296	0.00177	0.00232
Total MC	64.64018					
Total data	68					

Table 6.15: Expected numbers of signal and background events passing the event selections broken down in oscillation channel and interaction mode. Oscillation parameters are set to the values in Table 6.11. Expectations are normalized to $7.557 \times 10^{20}\,POT$.

6.4.3 SK samples

The following is a list summarizing the criteria used to select the SK samples:

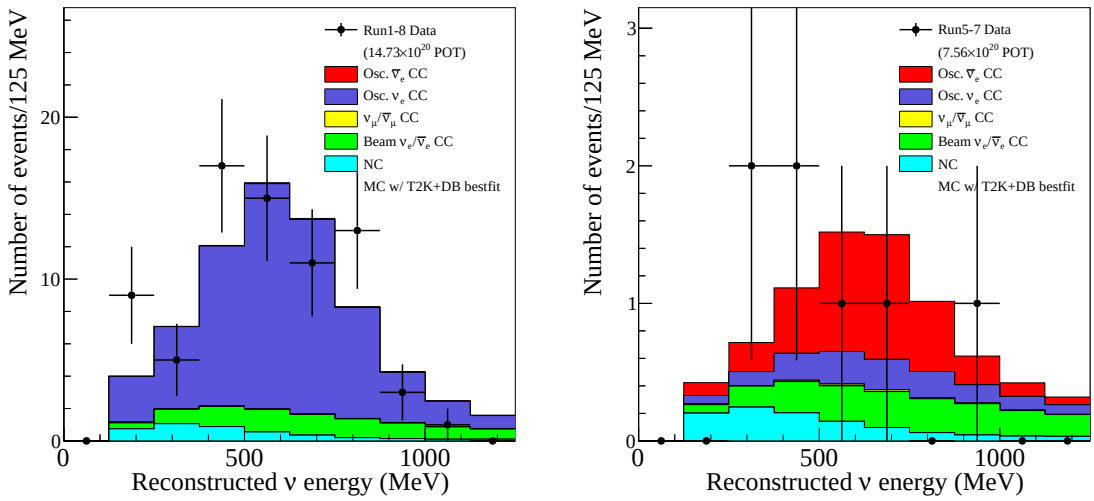

Figure 6.12: Reconstructed neutrino energy distribution for the final selected ν_e candidates (left) and $\bar{\nu}_e$ candidates (right) for Run1-8 data. MC distributions are made using oscillation parameters shown in Table 6.11 and are POT-normalized to data. Data is shown with statistical errors only.

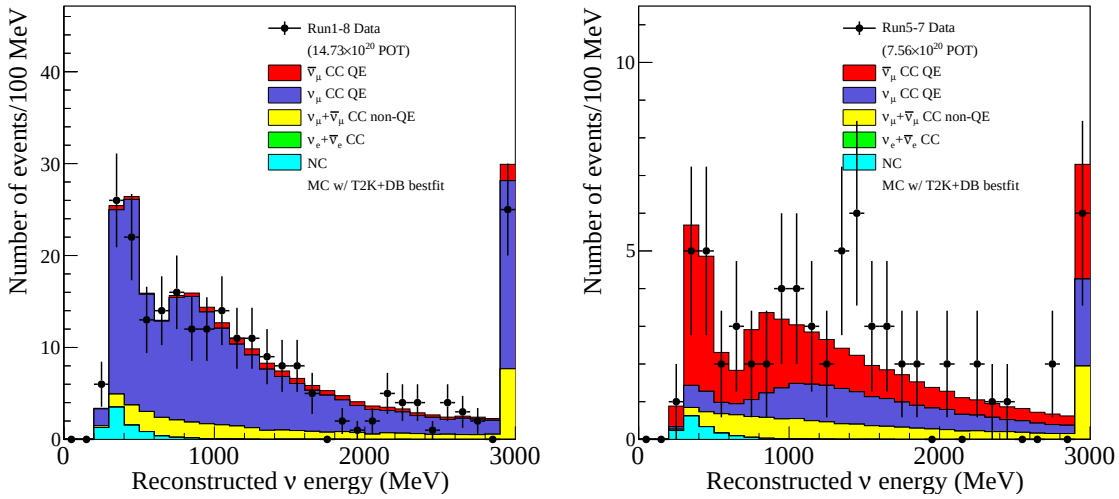

Figure 6.13: Reconstructed neutrino energy distribution for the final selected ν_μ candidates (left) and $\bar{\nu}_\mu$ candidates (right) for Run1-8 data. MC distributions are made using oscillation parameters shown in Table 6.11 and are POT-normalized to data. Data is shown with statistical errors only.

- Pre-selection (applied to both core and side-band samples):
  - Fully contained: pass the FC reduction described in section 5.1

  - Inside fiducial volume: $dwall > 50$ cm, $E_{vis} > 30$ MeV

- Core samples:

  1. **Sub-Gev 1Re $0_{\mathbf{dcy}}$**
     $0.1 < E_{vis} < 1.33$ GeV, single-ring, e-like, one sub-event (0 decay electron)
  2. **Sub-Gev 1Rμ $0_{\mathbf{dcy}}$**
     $E_{vis} < 1.33$ GeV, single-ring, μ-like, reconstructed μ momentum $p_\mu > 200$ MeV/c, one sub-event
  3. **Sub-Gev 1Rμ $1_{\mathbf{dcy}}$**
     $E_{vis} < 1.33$ GeV, single-ring, μ-like, reconstructed μ momentum $p_\mu > 200$ MeV/c, two sub-events (1 decay electron)

- Side-band samples:

  1. **Sub-Gev 1Re $\geq 1_{\mathbf{dcy}}$**
     $0.1 < E_{vis} < 1.33$ GeV, single-ring, e-like, two or more sub-events (≥ 1 decay electron)
  2. **Sub-Gev 1Rμ $\geq 2_{\mathbf{dcy}}$**
     $E_{vis} < 1.33$ GeV, single-ring, μ-like, reconstructed μ momentum $p_\mu > 200$ MeV/c, three or more sub-events (≥ 2 decay electrons)
  3. **Sub-Gev MR $0_{\mathbf{dcy}}$**
     $E_{vis} < 1.33$ GeV, multi-ring, one sub-event (0 decay electron)
  4. **Sub-Gev MR $\geq 1_{\mathbf{dcy}}$**
     $E_{vis} < 1.33$ GeV, multi-ring, two or more sub-events (≥ 1 decay electron)

Table 6.16 shows the statistics and the breakdown by interaction mode of the core samples. Note that $\nu_\tau/\bar{\nu_\tau}$ components are not shown in the table although $\overset{(-)}{\nu}_{\mu/e} \rightarrow \overset{(-)}{\nu}_\tau$ oscillations happen and that there is evidence of $\overset{(-)}{\nu}_\tau$ interactions from atmospheric neutrinos in SK [146]. This is because $\overset{(-)}{\nu}_\tau$ charged current interactions have a threshold of $E_\nu > 3.5$ GeV, and therefore almost never make it into the sub-GeV samples, while neutral current interactions are agnostic to flavors.

Figure 6.14 shows the pre-fit zenith angle distributions of the core samples. The pre-fit control distributions are shown in Appendix A.2.

%	Sub-GeV 1Re 0_{dcy}			Sub-GeV 1Rμ 0_{dcy}			Sub-GeV 1Rμ 1_{dcy}		
E_{vis} (GeV)	< 0.3	$0.3 \sim 0.7$	$0.7 \sim 1.33$	< 0.3	$0.3 \sim 0.7$	$0.7 \sim 1.33$	< 0.3	$0.3 \sim 0.7$	$0.7 \sim 1.33$
ν_e CC	78.56%	74.65%	67.68%	1.78%	0.88%	0.24%	0.03%	0.01%	0.02%
$\bar{\nu}_e$ CC	18.40%	20.46%	29.12%	0.50%	0.23%	0.11%	0.00%	0.00%	0.00%
ν_μ CC	0.71%	0.72%	0.17%	64.56%	83.68%	79.08%	75.54%	69.07%	61.56%
$\bar{\nu}_\mu$ CC	0.19%	0.27%	0.06%	2.69%	11.22%	20.29%	20.95%	30.36%	38.34%
NC	2.14%	3.90%	2.96%	30.47%	3.98%	0.28%	3.47%	0.56%	0.09%
Total									
Total MC	2662.78	2561.01	1133.72	476.42	310.81	211.13	2538.45	1784.79	917.90
Total Data	2510	2477	1105	451	311	182	2603	1892	936

	1Re 0_{dcy}	1Rμ 0_{dcy}	1Rμ 1_{dcy}
ν_e CC	75.04%	1.17%	0.02%
$\bar{\nu}_e$ CC	21.14%	0.33%	0.00%
ν_μ CC	0.62%	73.58%	70.89%
$\bar{\nu}_\mu$ CC	0.20%	9.07%	27.20%
NC	3.00%	15.84%	1.89%
Total MC	6357.52	998.37	5241.14
Total Data	6092	944	5431

Table 6.16: Event rates and interaction mode breakdown for each SK "core" sample. The oscillation parameters shown in Table 6.11 are used to calculate the MC predictions. 2519.89 days of SK-4 data is used, and MC is scaled to the same exposure as data.

6.4.4 Effect of systematic uncertainties on T2K and SK samples

The fractional uncertainties on the number of events in the T2K and SK samples are calculated to identify the contributions from each source of systematic uncertainties. For all error sources except for the SK detector systematic uncertainties, 2,500 parameter sets are randomly thrown from each source based on its pre-fit constraints; the number of events is calculated for each throw, and the R.M.S to nominal event rate ratio is taken as the fractional uncertainty. For the SK detector systematic uncertainties, 2,500 SK detector parameter sets are randomly sampled from the post-data fit Markov chain posterior, and the number of events calculated for each parameter set, R.M.S. to nominal event rate ratio taken as the fractional uncertainty.

Table 6.17 shows the effect of systematic uncertainties on the event rate in each T2K sample. The cross section and flux combined uncertainty is smaller than either the cross section or flux uncertainty individually because they are anti-correlated after the ND280 fit. The T2K flux and cross section are the dominant source of systematic error for T2K. The SK detector error has been reduced compared to the current T2K analysis [147] because the

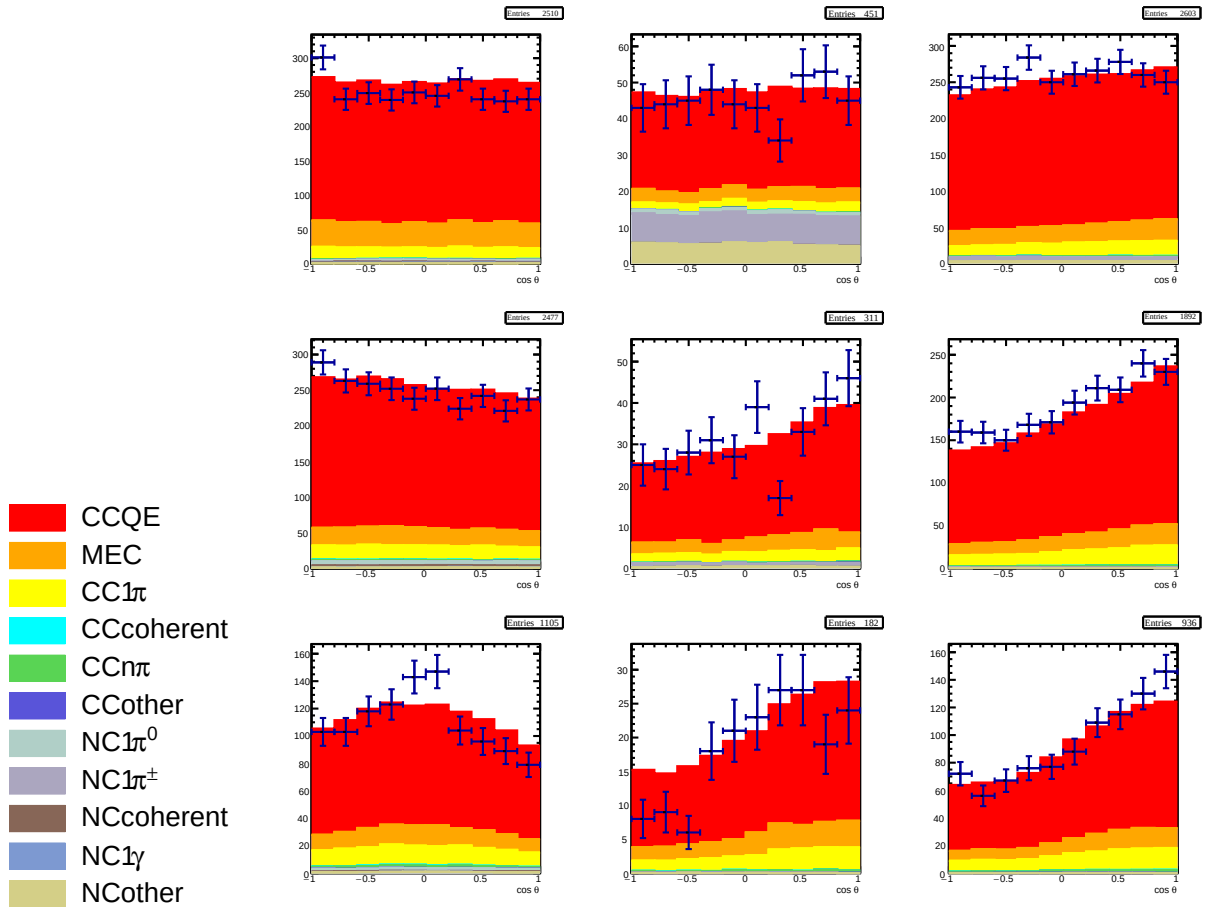

Figure 6.14: The pre-fit cosine zenith angle distributions. The samples from left to right are: 1Re 0_{dcy}, 1Rμ 0_{dcy}, 1Rμ 1_{dcy}. The energy ranges from top to bottom are: $E_{vis} < 400$ MeV, $400 < E_{vis} < 700$ MeV, $700 < E_{vis} < 1330$ MeV. Data is shown with statistical errors only. The oscillation parameters shown in Table 6.11 are used to calculate the MC predictions. 2519.89 days of SK-4 data is used, and MC is scaled to the same exposure as data. $\cos\theta = 1$ for downward going events; $\cos\theta = -1$ for upward going events.

evaluation of SK detector systematic error is done simultaneously with the oscillation fit and no longer incorrectly folds in atmospheric neutrino flux and cross section uncertainties.

Table 6.18 shows the effect of systematic uncertainties on the event rate in each SK core sample. The biggest source of uncertainty for the 1Rμ 0_{dcy} sample comes from FSI and SI due to the significant NC1π^+ background at low energy. For the 1Re 0_{dcy} sample and the 1Rμ 1_{dcy} sample, the dominant systematic errors are from the atmospheric neutrino flux prediction.

	FHC ν_e	FHC ν_μ	RHC $\bar{\nu}_e$	RHC $\bar{\nu}_\mu$
cross section	5.28%	4.40%	5.28%	3.97%
T2K flux	4.29%	4.22%	3.95%	3.88%
cross section and flux	4.26%	3.12%	4.41%	2.74%
FSI/SI	1.55%	2.02%	1.28%	1.88%
Energy scale and reduction	0.59%	0.49%	0.86%	0.49%
SK Detector	1.19%	0.69%	1.70%	0.59%
Total	4.61%	3.92%	4.73%	3.53%

Table 6.17: Fractional uncertainties on the number of events in each T2K sample due to each source of systematic uncertainties.

	1Re 0_{dcy}	1Rμ 0_{dcy}	1Rμ 1_{dcy}
cross section	4.73%	4.37%	4.48%
FSI/SI	1.63%	9.35%	3.35%
cross section and FSI/SI	4.97%	10.49%	5.52%
Atmospheric flux	10.95%	6.44%	7.13%
Energy scale and reduction	2.43%	2.55%	4.86%
SK Detector	0.31%	1.71%	1.36%
Total	12.22%	13.10%	10.39%

Table 6.18: Fractional uncertainties on the number of events in each SK sample due to each source of systematic uncertainties.

6.5 Asimov sensitivities

Sensitivity to the oscillation parameters can be evaluated by a fit to the so-call "Asimov" data set, which is a mock data set generated by setting all the nuisance parameters to their nominal values (the post-ND280 best-fit for the BANFF parameters). The oscillation parameters used in the sensitivity study are shown in Table 6.11, and the exposure assumed is shown in Table 6.10. The Asimov data set represents an average expectation of the experiment with given true oscillation parameters; the fit itself is also a sanity check of the fitting framework before analyzing data. Only the posterior distributions of the oscillation parameters will be shown; those of the nuisance parameters are included in Appendix A.3, which show that the nuisance parameters behave as expected.

6.5.1 Asimov sensitivity without reactor constraint

The MCMC algorithm as described in section 6.1 is used, and credible intervals are calculated. The burn-in is chosen to be 50,000 steps, and a total number of $\sim$ 10 million post burn-in steps are used. Figure 6.15 shows the 68% and 90% credible intervals; the color scale shows the number of post burn-in steps in each bin; the best-fit point is the mode of the marginalized 2D posterior probability distribution. The best-fit point of Δm^2_{23} v.s. $\sin^2\theta_{23}$ is significantly different from the input values because of the marginalization effect; the differences in probability between the bin which corresponds to the best-fit point and the bin which corresponds to the input values is less than 10%. Figure 6.16 shows the posterior probability distribution of δ_{CP} and credible intervals. The δ_{CP} 68% (1σ) credible interval is $[-3.016, -0.691]$, and the 90% credible is $[-\pi, 0.063], [2.388, \pi]$.

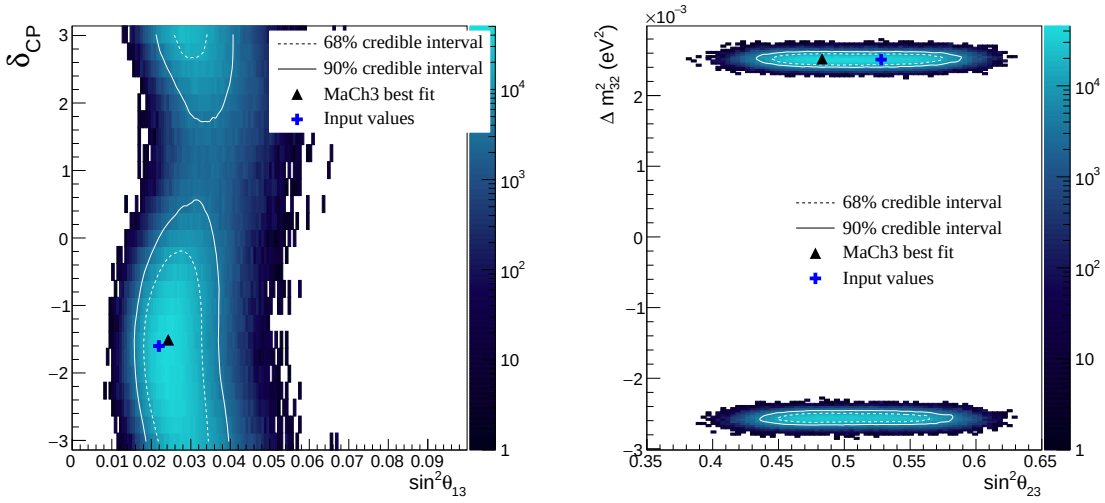

Figure 6.15: Posterior probability distributions and credible intervals of the Asimov fit using parameters shown in Table 6.11. Left: δ_{CP} v.s. $\sin^2\theta_{13}$; right: Δm^2_{32} v.s. $\sin^2\theta_{23}$.

Table 6.19 shows the posterior probabilities in each θ_{23} and MH octant. The prior on the mass hierarchy is $\pi(NH) = \pi(IH) = 0.5$, i.e. the sign of Δm^2_{32} is allowed to flip between positive and negative with equal probabilities. With input values $\sin^2\theta_{23} = 0.5208$ and $\Delta m^2_{32} = 2.509 \times 10^{-3}$ eV^2, only a slight preference to the $\theta_{23} > 45°$ (56.1%) and normal hierarchy (59.1%) is observed. This shows that the T2K samples and the three SK sub-GeV CCQE-like atmospheric neutrino samples have little sensitivity to the θ_{23} octant and MH (i.e. NH and IH).

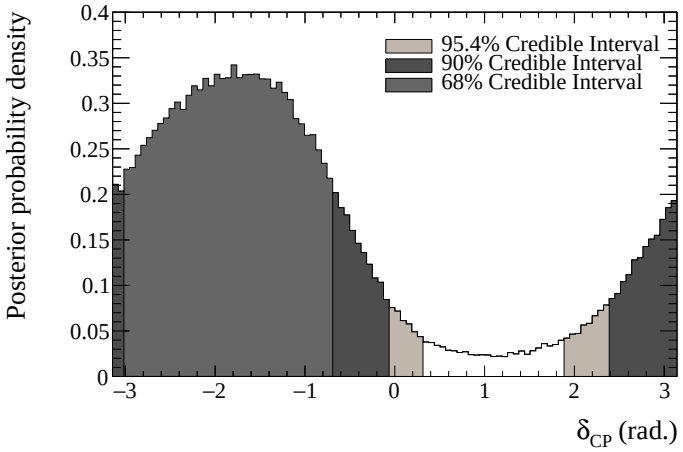

Figure 6.16: δ_{CP} posterior probability distribution and credible intervals of the Asimov fit using parameters shown in Table 6.11.

	$\sin^2\theta_{23} < 0.5$	$\sin^2\theta_{23} > 0.5$	Sum
$\Delta m^2_{32} < 0$	0.185	0.225	0.409
$\Delta m^2_{32} > 0$	0.254	0.336	0.591
Sum	0.439	0.561	1

Table 6.19: Posterior probabilities for each θ_{23} and MH octant of the Asimov fit using parameters shown in Table 6.11.

6.5.2 Asimov sensitivity with reactor constraint

Using the same Markov chain posterior, one can also study the impact of applying a prior constraint on $\sin^2 2\theta_{13}$ provided by the reactor neutrino experiments [39]. This is done by assigning a weight for each step in the posterior chain based on the value of $\sin^2 2\theta_{13}$ in said step

$$\omega = \frac{1}{\sqrt{2\pi}\sigma} e^{-\left(\sin^2 2\theta_{13} - 0.0857\right)^2 / 2\sigma^2} \tag{6.25}$$

where $\sigma = 0.0046$. Mathematically, it is equivalent to running a separate Markov Chain with the same constraint on $\sin^2 2\theta_{13}$.

Figure 6.17 shows the 2D posterior probability distributions and credible intervals; Figure 6.18 shows the 1D δ_{CP} posterior probability distribution and credible intervals. The reactor constraint on $\sin^2 2\theta_{13}$ improves the sensitivity to δ_{CP}, $\sin^2\theta_{23}$ and $|\Delta m^2_{32}|$. This is easy to understand, as they are all present in the leading term in the appearance and disappearance probabilities, therefore a tighter constraint on one parameter will enable the others

to be measured more precisely. The δ_{CP} 68% credible interval now becomes $[-2.513, -0.880]$, and the 90% credible interval is $[-3.016, -0.377]$. Note that the CP-conserving value $\delta_{CP} = 0$ now lies outside of the 2σ interval, while $\delta_{CP} = \pi$ is outside of the 90% interval.

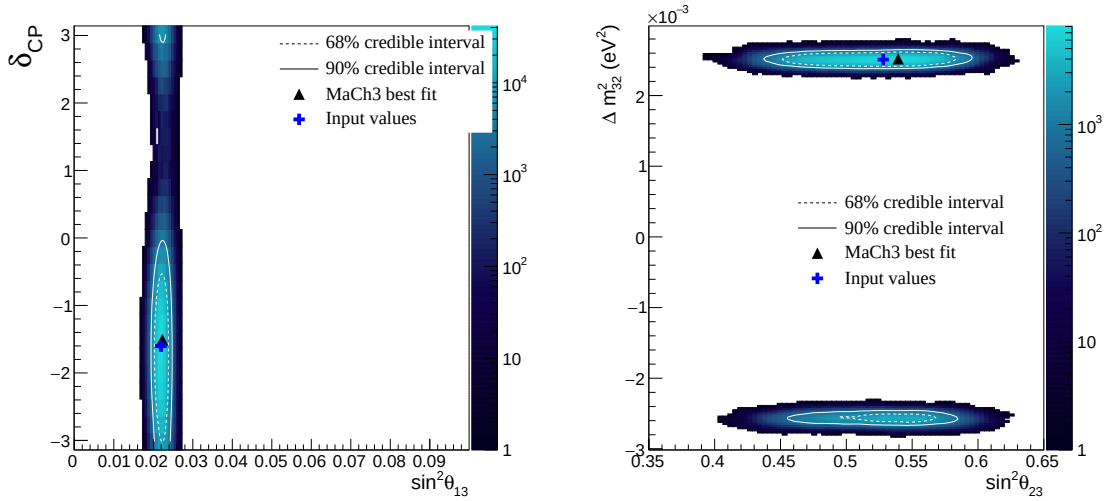

Figure 6.17: Posterior probability distributions and credible intervals of the Asimov fit using parameters shown in Table 6.11 with additional constraint $\sin^2 2\theta_{13} = 0.0857 \pm 0.0046$ applied. Left: δ_{CP} v.s. $\sin^2\theta_{13}$; right: Δm^2_{32} v.s. $\sin^2\theta_{23}$.

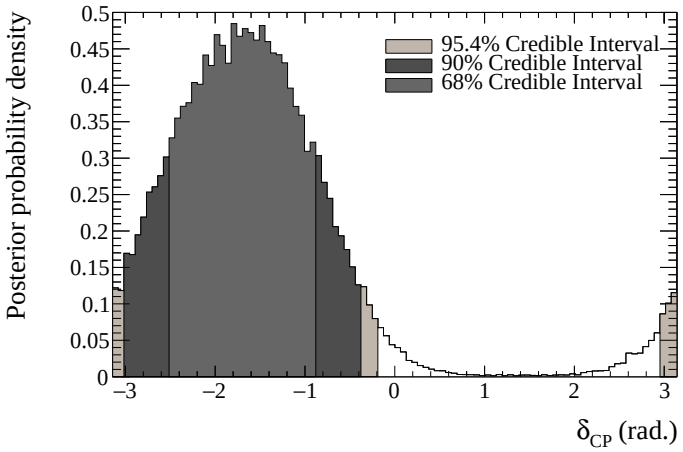

Figure 6.18: δ_{CP} posterior probability distribution and credible intervals of the Asimov fit using parameters shown in Table 6.11 with additional constraint $\sin^2 2\theta_{13} = 0.0857 \pm 0.0046$ applied.

Table 6.20 shows the posterior probabilities for each θ_{23} octant and MH with reactor constraint $\sin^2 2\theta_{13} = 0.0857 \pm 0.0046$ applied. In this case, the experiments have a stronger

preference for normal hierarchy (73.4%) and $\theta_{23} > 45°$ (79.6%) compared to the case without the reactor constraint.

	$\sin^2\theta_{23} < 0.5$	$\sin^2\theta_{23} > 0.5$	Sum
$\Delta m^2_{32} < 0$	0.0685	0.197	0.266
$\Delta m^2_{32} > 0$	0.225	0.509	0.734
Sum	0.294	0.706	1

Table 6.20: Posterior probabilities for each θ_{23} and MH octant of the Asimov fit using parameters shown in Table 6.11 with additional constraint $\sin^2 2\theta_{13} = 0.0857 \pm 0.0046$ applied.

6.5.3 Sensitivity compared to T2K-only analysis

Figures 6.19 and 6.20 show a comparison between this study and the T2K-only study [147] using the same T2K exposure. Note that the T2K-only study uses five T2K samples (four CCQE-like samples and the ν_e CC1π^+ sample), whereas the T2K+SK joint fit analysis only uses the four CCQE-like samples from T2K. Sizable improvements in sensitivity are obtained by combing sub-GeV CCQE-like SK atmospheric neutrino samples with the T2K CCQE-like samples, particularly for the δ_{CP} measurement without reactor constraint. T2K is much more sensitive to $|\Delta m^2_{32}|$ and $\sin^2\theta_{23}$ than SK because of the fixed baseline; therefore, the improvement in the measurement of those parameters is much less significant compared to δ_{CP}.

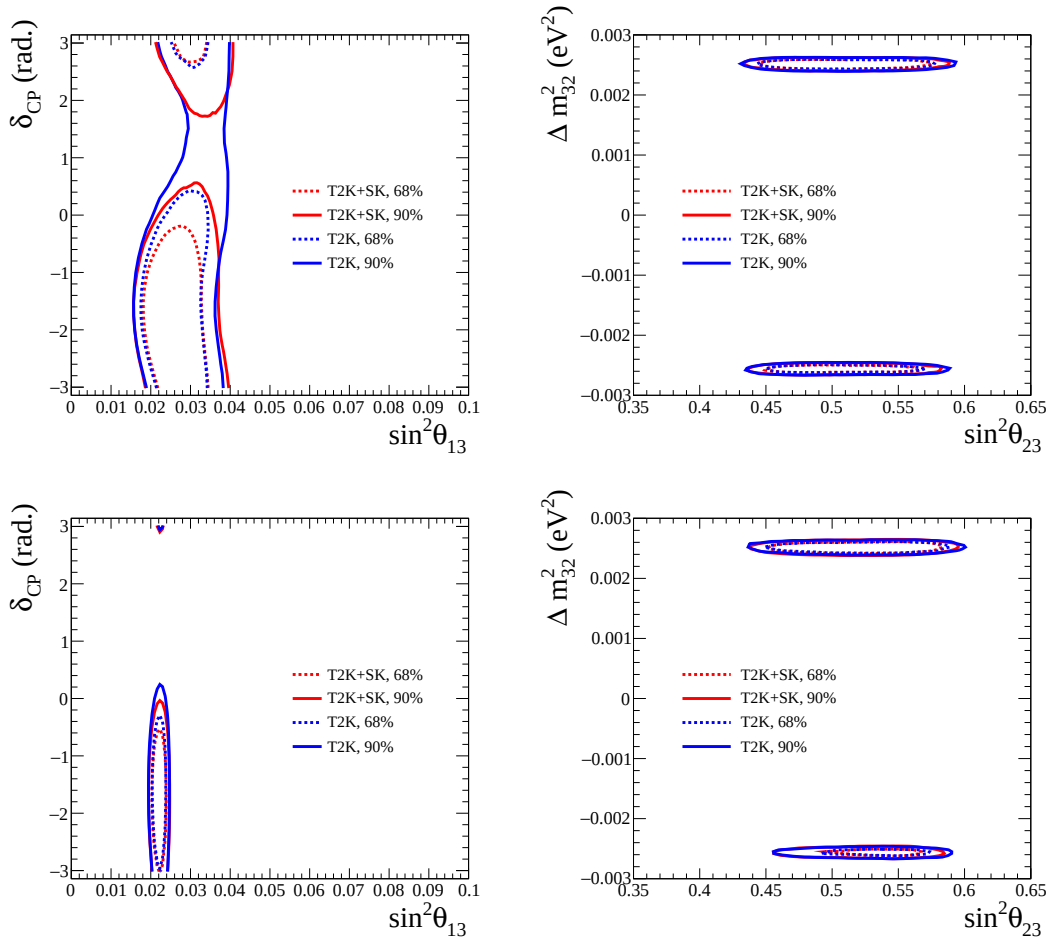

Figure 6.19: A comparison between the T2K+SK sensitivity with the T2K-only sensitivity. Top left: δ_{CP} v.s. $\sin^2\theta_{13}$ without reactor constraint; top right: Δm^2_{32} v.s. $\sin^2\theta_{23}$ without reactor constraint; bottom left: δ_{CP} v.s. $\sin^2\theta_{13}$ with reactor constraint $\sin^2 2\theta_{13} = 0.0857 \pm 0.0046$; bottom right: Δm^2_{32} v.s. $\sin^2\theta_{23}$ with reactor constraint $\sin^2 2\theta_{13} = 0.0857 \pm 0.0046$. The T2K-only sensitivities are taken from [147]. Note that the T2K-only study uses five T2K samples (four CCQE-like samples and the ν_e CC1π^+ sample), whereas the T2K+SK joint fit analysis only uses the four CCQE-like samples from T2K.

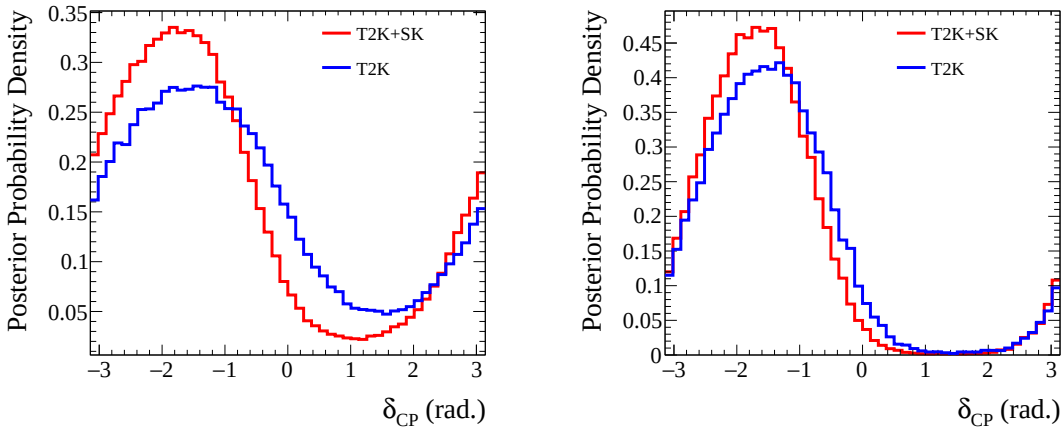

Figure 6.20: A comparison between the T2K+SK sensitivity to δ_{CP} with the T2K-only sensitivity. Left: without reactor constraint; right: with reactor constraint $\sin^2 2\theta_{13} = 0.0857 \pm 0.0046$. The T2K-only sensitivities are taken from [147]. Note that the T2K-only study uses five T2K samples (four CCQE-like samples and the ν_e CC1π^+ sample), whereas the T2K+SK joint fit analysis only uses the four CCQE-like samples from T2K.

6.6 Data fit results

The data fit is performed on the T2K and SK data with the exposure shown in Table 6.10. The burn-in is chosen to be 100,000 steps to be conservative. The results shown in this chapter are based on 15.7M post burn-in steps. Again, a fit without reactor constraint is performed; the results labeled "with reactor constraint" are obtained by adding an additional weight to each step based on the value of $\sin^2 2\theta_{13}$ as described in the previous chapter.

6.6.1 Data fit results on oscillation parameters

Figures 6.21 and 6.22 show the 2D posterior probability distributions and credible intervals, both with and without reactor constraint. The addition of reactor constraint pushes δ_{CP} towards maximum CP-violating value $-\pi/2$ and $\sin^2\theta_{23}$ towards higher value. Even without the reactor constraint, certain parts of the δ_{CP}-$\sin^2\theta_{13}$ phase space are ruled out at 90%. Figure 6.23 shows the δ_{CP} 1D posterior probability distribution and credible intervals in normal hierarchy, inverted hierarchy, and with mass hierarchy marginalized. It is clear that if mass hierarchy is known to be either normal or inverted, the preferred δ_{CP} range would be

different than the case in which mass hierarchy is marginalized. The double-peak in the top left δ_{CP} probability distribution is due to such mass hierarchy-dependent preference as well. In all three cases, the addition of reactor constraint improves the constraint on δ_{CP}, and the CP-conserving value $\delta_{CP} = 0$ is ruled out at 2σ.

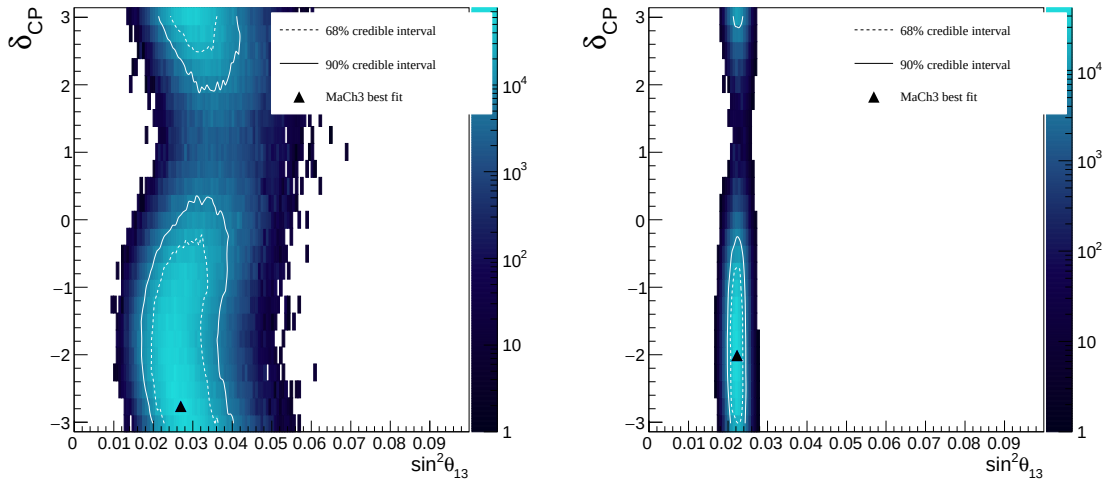

Figure 6.21: Posterior probability distributions and credible intervals of δ_{CP} v.s. $\sin^2\theta_{13}$ from the data fit. Left: without reactor constraint; right: with reactor constraint $\sin^2 2\theta_{13} = 0.0857 \pm 0.0046$.

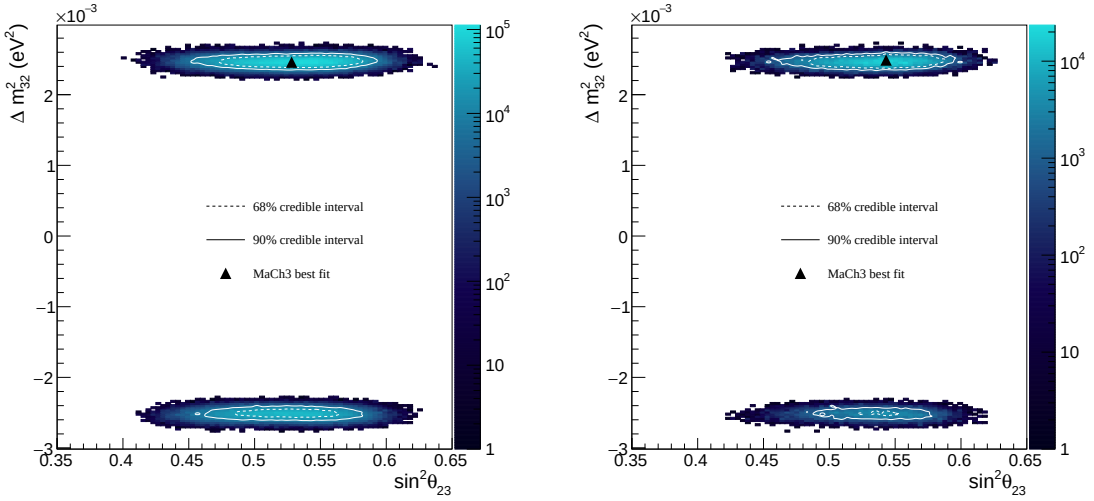

Figure 6.22: Posterior probability distributions and credible intervals of Δm^2_{32} v.s. $\sin^2\theta_{23}$ from the data fit. Left: without reactor constraint; right: with reactor constraint $\sin^2 2\theta_{13} = 0.0857 \pm 0.0046$.

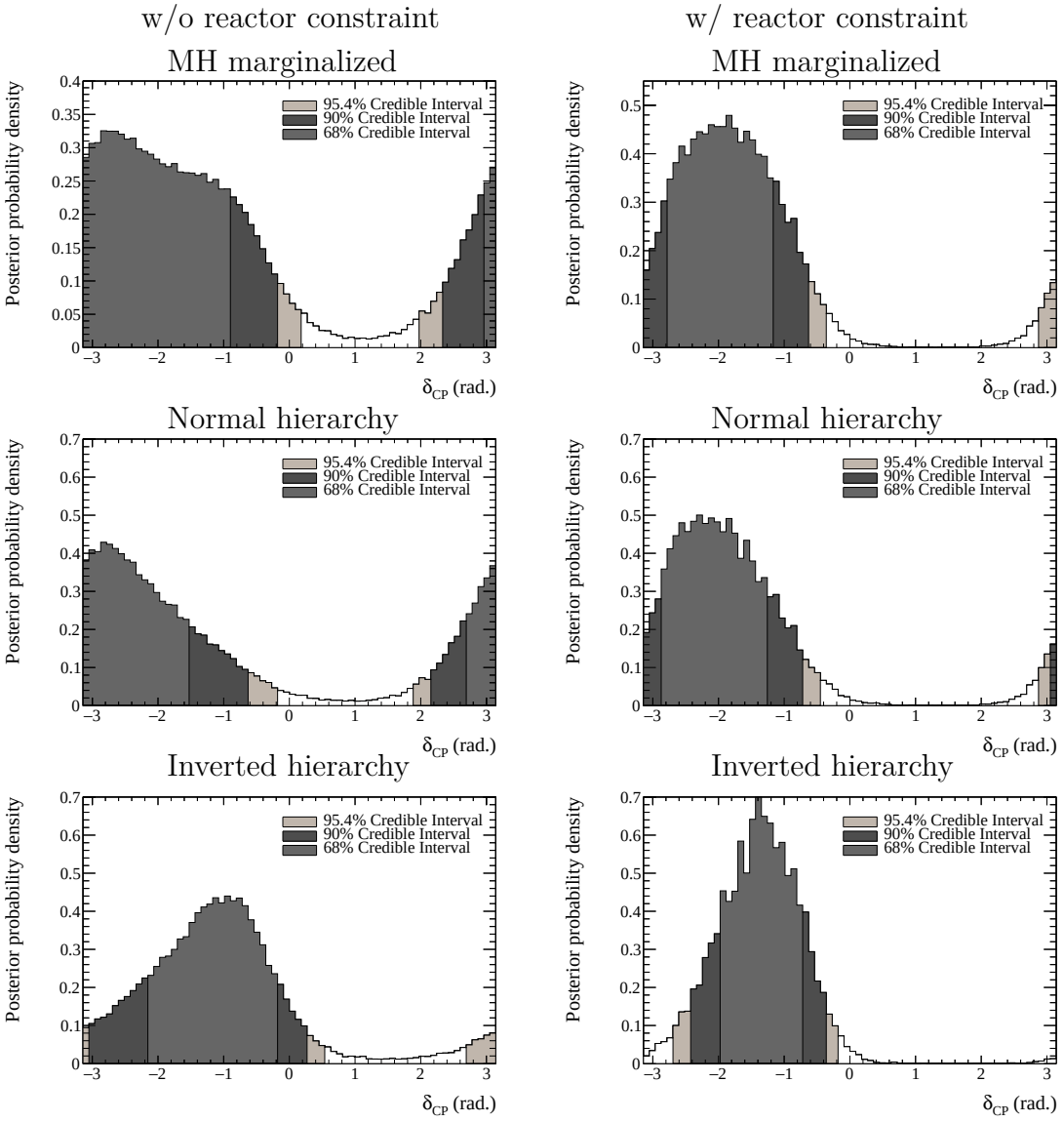

Figure 6.23: δ_{CP} posterior probability distribution and credible intervals of the data fit. Left column: without reactor constraint; right column: with reactor constraint $\sin^2 2\theta_{13} = 0.0857 \pm 0.0046$. From top to bottom: mass hierarchy marginalized; normal hierarchy only; inverted hierarchy only.

Figure 6.24 shows the 1D posterior distributions and credible intervals of Δm^2_{32}, $\sin^2\theta_{23}$ and $\sin^2\theta_{13}$ with mass hierarchy marginalized. T2K+SK itself prefers a slightly larger $\sin^2\theta_{13}$ than what the reactor constraint dictates; nevertheless the T2K+SK measurement of $\sin^2\theta_{13}$ is consistent with the reactor measurements. The best-fit values, 68% and 90% credible intervals of Δm^2_{32}, $\sin^2\theta_{23}$, δ_{CP} and $\sin^2\theta_{13}$ are shown in Table 6.21 with marginalized mass hierarchy, normal hierarchy and inverted hierarchy. The effect of reactor constraint is also listed. The best-fit values of $\sin^2\theta_{23}$ and Δm^2_{32} ($\sin^2\theta_{13}$ and δ_{CP}) are the mode of the 2D

posterior probability distribution of $\sin^2\theta_{23}$ v.s. Δm^2_{32} ($\sin^2\theta_{13}$ v.s. δ_{CP}). The best-fit values without reactor constraint in separate mass hierarchy is more different than they are with reactor constraint. The 68% and 90% credible intervals are calculated based on their respective marginalized 1D posterior distributions.

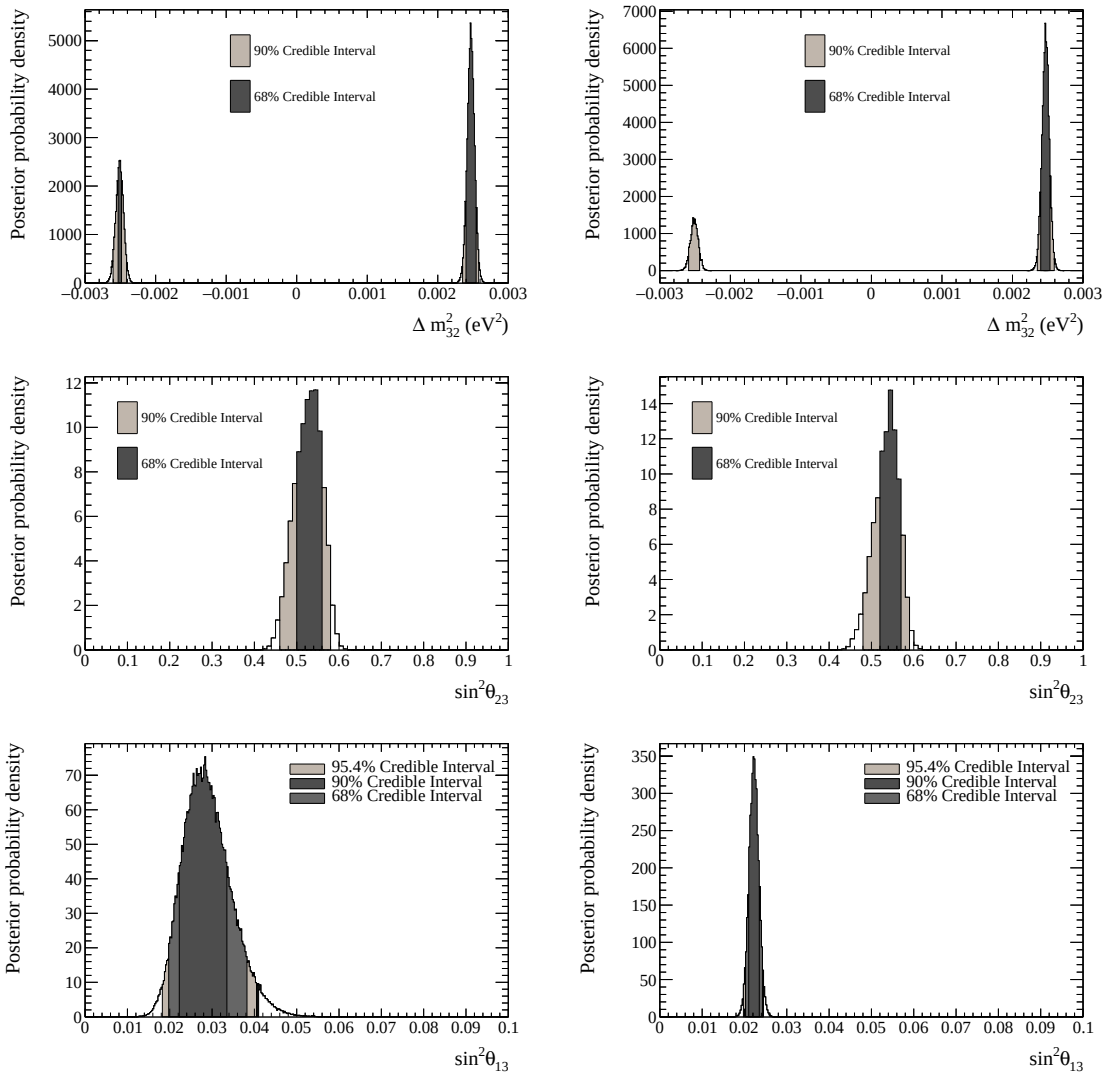

Figure 6.24: 1D posterior probability distributions and credible intervals of the data fit. Left column: without reactor constraint; right column: with reactor constraint $\sin^2 2\theta_{13} = 0.0857 \pm 0.0046$. From top to bottom: Δm^2_{32}; $\sin^2\theta_{23}$; $\sin^2\theta_{13}$.

Table 6.22 shows the posterior probabilities in each θ_{23} octant and MH without reactor constraint. The prior on the mass hierarchy is $\pi(NH) = \pi(IH) = 0.5$. Only a slight preference to $\theta_{23} > 45°$ (78.4%) and normal hierarchy (66.3%) is observed. The preferences are slightly stronger than the sensitivity. Table 6.23 shows the θ_{23} and MH octant preference

	$\sin^2\theta_{23}$	Δm^2_{32} (10^{-3}eV^2)	$\sin^2\theta_{13}$	δ_{CP}
Mass hierarchy marginalized, w/o reactor constraint				
2D best-fit	0.528	2.46	0.0270	-2.765
68% C.I. range	$[0.50, 0.56]$	$[-2.532, -2.484], [2.400, 2.544]$	$[0.0223, 0.0335]$	$[-\pi, -0.898], [2.96, \pi]$
90% C.I. range	$[0.46, 0.58]$	$[-2.604, -2.412], [2.352, 2.580]$	$[0.0198, 0.0382]$	$[-\pi, -0.180], [2.333, \pi]$
Mass hierarchy marginalized, w/ reactor constraint				
2D best-fit	0.543	2.49	0.0223	-2.011
68% C.I. range	$[0.52, 0.57]$	$[2.400, 2.532]$	$[0.0210, 0.0235]$	$[-2.783, -1.167]$
90% C.I. range	$[0.48, 0.59]$	$[-2.592, -2.436], [2.352, 2.592]$	$[0.0202, 0.0243]$	$[-\pi, -0.628]$
Normal hierarchy, w/o reactor constraint				
2D best-fit	0.528	2.46	0.027	-2.765
68% C.I. range	$[0.52, 0.56]$	$[2.424, 2.520]$	$[0.0218, 0.0323]$	$[-\pi, -1.526], [2.693, \pi]$
90% C.I. range	$[0.47, 0.59]$	$[2.364, 2.568]$	$[0.0190, 0.0363]$	$[-\pi, -0.628], [2.154, \pi]$
Inverted hierarchy, w/o reactor constraint				
2D best-fit	0.524	-2.52	0.0283	-0.754
68% C.I. range	$[0.50, 0.56]$	$[-2.568, -2.460]$	$[0.0245, 0.0348]$	$[-2.154, -0.180]$
90% C.I. range	$[0.46, 0.58]$	$[-2.616, -2.400]$	$[0.0218, 0.0403]$	$[-3.052 - -0.269]$
Normal hierarchy, w/ reactor constraint				
2D best-fit	0.543	2.49	0.0223	-2.011
68% C.I. range	$[0.52, 0.57]$	$[2.424, 2.520]$	$[0.0210, 0.0235]$	$[-2.872, -1.257]$
90% C.I. range	$[0.48, 0.59]$	$[2.364, 2.568]$	$[0.0198, 0.0382]$	$[-\pi, -0.718], [3.052, \pi]$
Inverted hierarchy, w/ reactor constraint				
2D best-fit	0.543	-2.49	0.023	-1.257
68% C.I. range	$[0.52, 0.57]$	$[-2.556, -2.448]$	$[0.0213, 0.0238]$	$[-1.975, -0.718]$
90% C.I. range	$[0.48, 0.59]$	$[-2.604, -2.400]$	$[0.0205, 0.0245]$	$[-2.424, -0.359]$

Table 6.21: The 68% and 90% credible interval range of $\sin^2\theta_{23}$, Δm^2_{32}, $\sin^2\theta_{13}$ and δ_{CP}. The best-fit values of $\sin^2\theta_{23}$ and Δm^2_{32} are the mode of the 2D posterior probability distribution of $\sin^2\theta_{23}$ v.s. Δm^2_{32}; the best-fit values of $\sin^2\theta_{13}$ and δ_{CP} are the mode of the 2D posterior probability distribution of $\sin^2\theta_{13}$ v.s. δ_{CP}. The 68% and 90% credible interval ranges are calculated based on the marginalized 1D posterior distributions.

with reactor constraint applied. The preference to $\theta_{23} > 45°$ (87.4%) and normal hierarchy (81.3%) becomes slightly stronger. However, the preference to normal hierarchy is still very weak, and no decisive conclusion can be drawn regarding the mass hierarchy.

6.6.2 Posterior predictive distributions

Figure 6.25 shows the reconstructed energy distributions of the four T2K samples using the so-called posterior predictive method. Since there are 325 nuisance parameters and 6 oscilla-

	$\sin^2\theta_{23} < 0.5$	$\sin^2\theta_{23} > 0.5$	Sum
$\Delta m^2_{32} < 0$	0.0837	0.254	0.337
$\Delta m^2_{32} > 0$	0.132	0.530	0.663
Sum	0.216	0.784	1

Table 6.22: Posterior probabilities for each θ_{23} and MH octant of the data fit.

	$\sin^2\theta_{23} < 0.5$	$\sin^2\theta_{23} > 0.5$	Sum
$\Delta m^2_{32} < 0$	0.0238	0.163	0.187
$\Delta m^2_{32} > 0$	0.102	0.712	0.813
Sum	0.126	0.874	1

Table 6.23: Posterior probabilities for each θ_{23} and MH octant of the data fit with additional constraint $\sin^2 2\theta_{13} = 0.0857 \pm 0.0046$ applied.

tion parameters in the fit, it is neither feasible nor prudent to make the distributions which correspond to the best-fit in the 331-dimensional space. Instead, the posterior predictive method is used, where a large number of steps, in this case 2,500 steps, are randomly sampled from the fit posterior; this ensemble of steps is representative of the multi-dimensional posterior probability distribution. Then for each sampling, the reconstructed energy spectra are calculated using the set of nuisance and oscillation parameters in that step. In the end, the 2,500 reconstructed energy spectra for each T2K sample present a probabilistic representation of how the post-fit reconstructed energy spectrum would be, shown by the blue colored 2D histograms. The orange (green) lines show the spectra made by setting all parameters at the mode of their respective 1D posterior distribution without (with) reactor constraint. This is different from a frequentist "best-fit" prediction, because the multi-dimensional correlations are simply ignored; this is why the orange or green line in some bins does not sit in the highest probability region. Nonetheless, they, as well as the posterior predictive distributions indicate good post-fit model agreement with data.

Figure 6.26 shows the similar posterior predictive (zenith angle) distributions of the SK samples. Good post-fit model and data agreement is also seen in the SK fit. The normalized posterior predictive of the control distributions are shown in Appendix A.4.

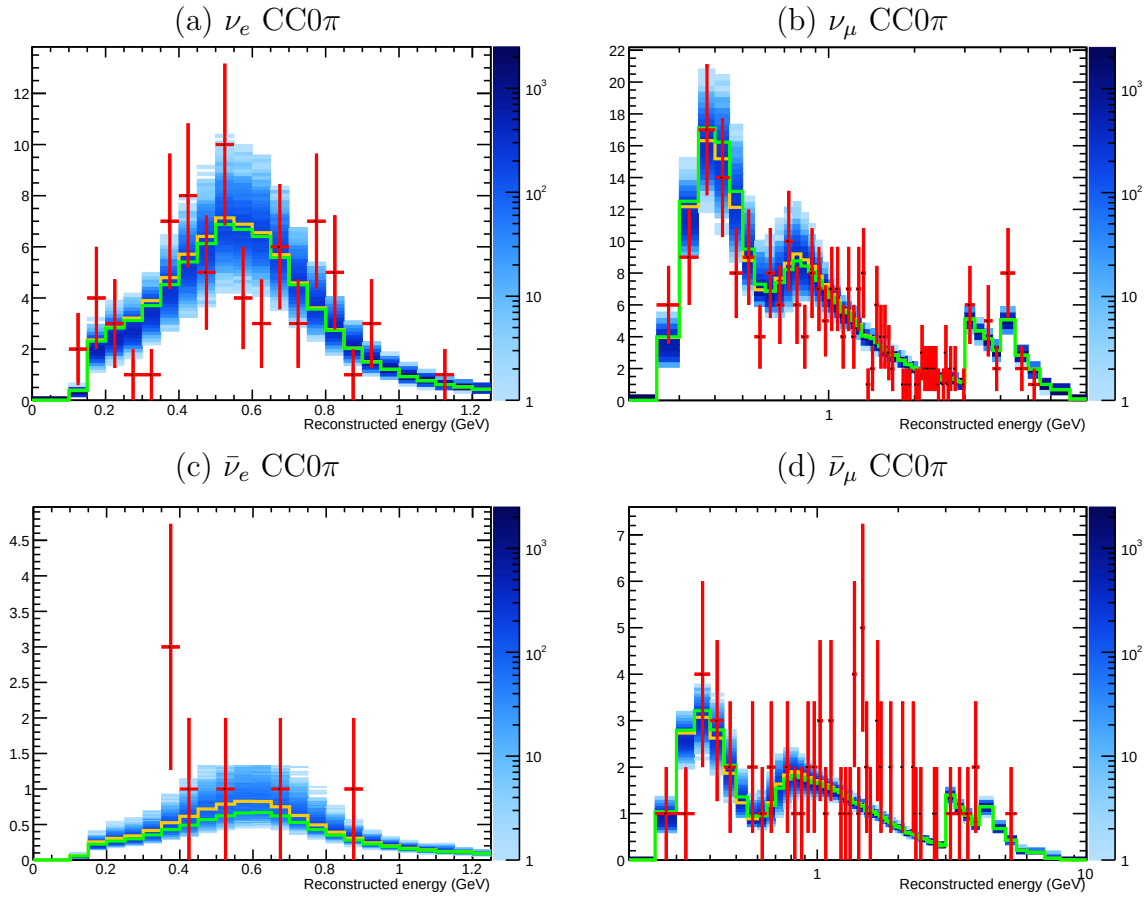

Figure 6.25: The posterior predictive spectra of T2K samples. The blue 2D histogram is made by sampling 2,500 steps from the fit posterior distribution without reactor constraint. Data is shown in red with statistical errors only. Orange shows the spectra made by setting all parameters at the mode of their respective 1D posterior distribution without reactor constraint; green shows the spectra made by setting all parameters at the mode of their respective 1D posterior distribution with reactor constraint.

6.6.3 Post-fit nuisance parameters

Although the purpose of this study is to measure the oscillation parameters $\sin^2\theta_{23}$, Δm^2_{32}, $\sin^2\theta_{13}$ and δ_{CP}, it is necessary to understand the behavior of the systematic error parameters (i.e. nuisance parameters) post-fit as they can influence the marginal posterior distributions of the oscillation parameters.

Figure 6.27 shows the pre- and post-fit values of the T2K flux parameters, cross section parameters, atmospheric neutrino flux parameters, and the energy scale and reduction related

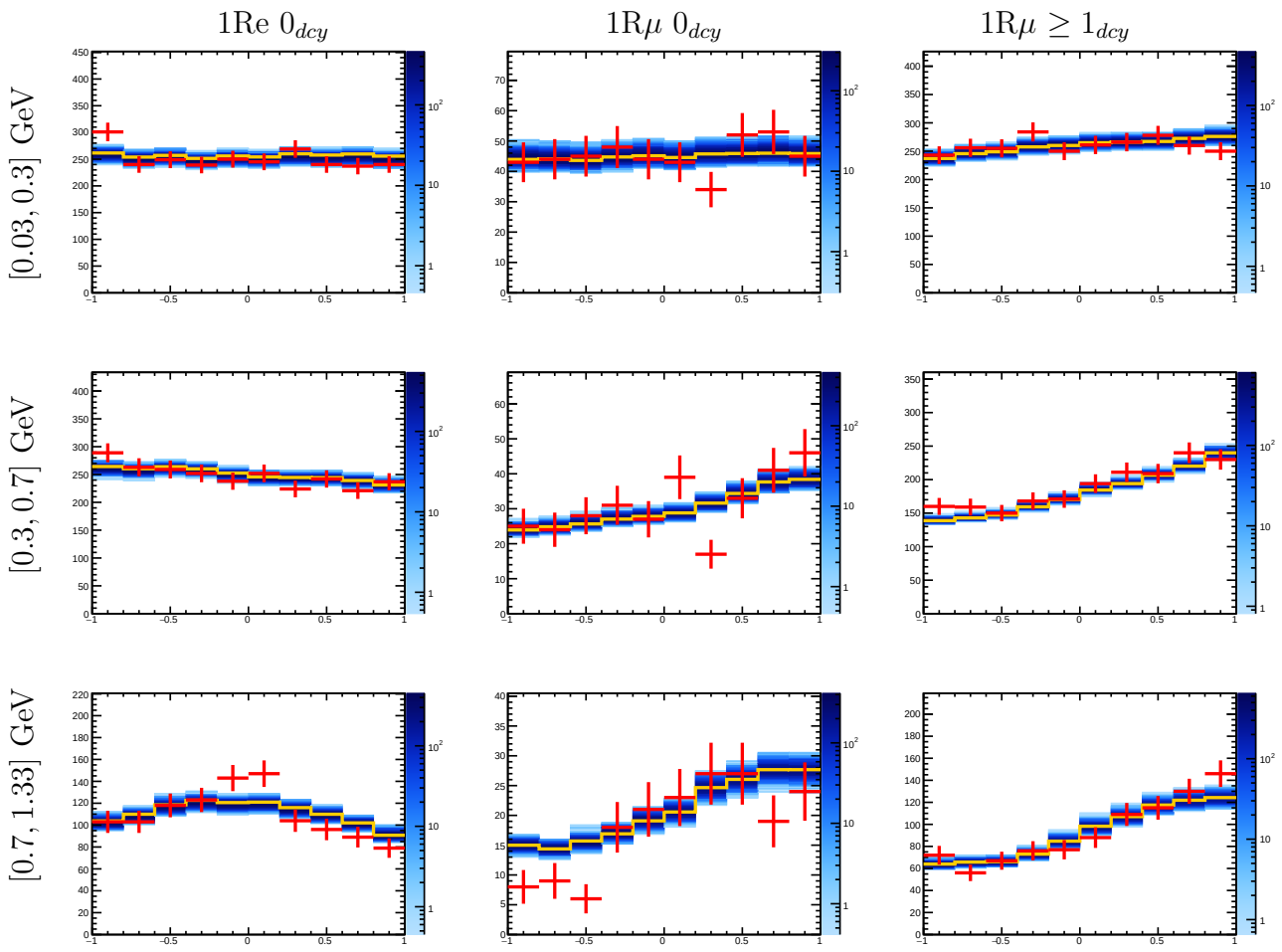

Figure 6.26: The posterior predictive zenith angle distributions of SK samples. The blue 2D histogram is made by sampling 2,500 steps from the fit posterior distribution without reactor constraint. Data is shown in red with statistical errors only. Orange shows the spectra made by setting all parameters at the mode of their respective 1D posterior distribution without reactor constraint.

parameters. The 1σ pre-fit values are shown in red; the mean and R.M.S of the post-fit parameter values are shown in blue by the diamond and shaded area respectively. Most of the parameter post-fit values agree with the pre-fit values within 1σ. The parameter most pulled from its pre-fit value is the NC other normalization parameter.

Figure 6.28 shows the post-fit detector systematic error parameters; the priors on these parameters are flat, and therefore are not shown. Each bin in the plot corresponds to a α or β parameter of a category in Table 6.6 of a reconstructed variable in an energy range in Table 6.2. If the detector simulation and event reconstruction were perfect, all α parameters

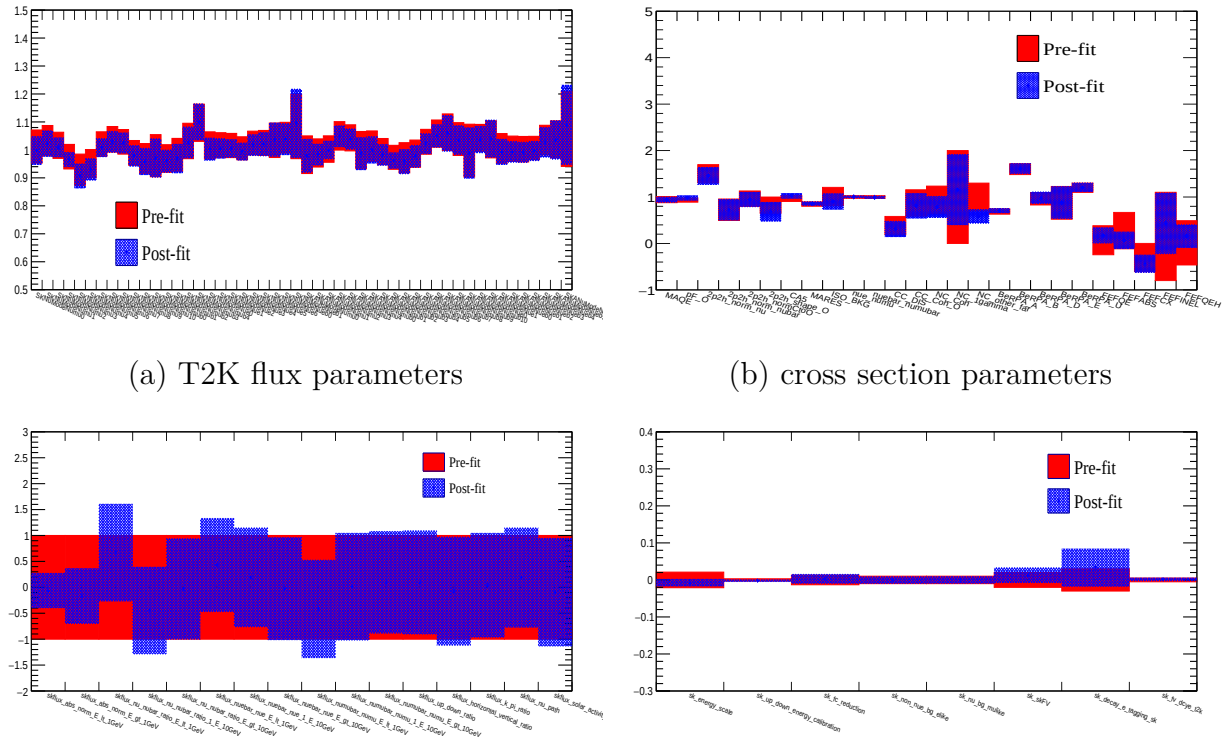

(a) T2K flux parameters

(b) cross section parameters

(c) SK atmospheric flux parameters

(d) Energy scale and reduction parameters

Figure 6.27: The pre- and post-fit nuisance parameters. The pre-fit uncertainties are shown in red; post-fit mean and R.M.S are shown in blue.

should be centered around 1 and all β parameters should be centered around 0. Some α (β) parameters are pulled away from 1 (0) after the fit as dictated by the SK atmospheric data. The parameters which correspond to categories with higher statistics are more tightly constrained (bins 1, 2, 3 and 4 in each energy block) than the ones with low statistics (bins 5, 6 and 7). The only exceptions are bins 5, 12 and 19 in (c1) and (c2) thanks to the prior constraints obtained by a fit to the hybrid-π^0 samples.

6.6.4 Goodness-of-fit

In order to check how well the fit has performed, a Bayesian goodness-of-fit test following the method described in [148] is used to calculate the p-value. It works as follows: 2,500 steps are randomly sampled from the fit posterior; for each set of parameters a nominal MC prediction is made, from which a fake data set is generated by allowing statistical fluctuation; the likelihood $-\ln \mathcal{L}_{Throw}$ can be calculated from the nominal MC prediction and the fake data set; the likelihood $-\ln \mathcal{L}_{Data}$ can be calculated from the nominal MC prediction and the

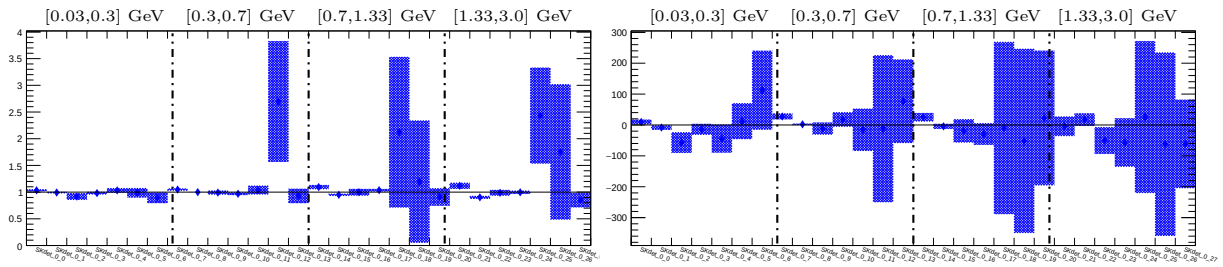

(a1) Smearing parameters of ring-counting (a2) Bias parameters of ring-counting

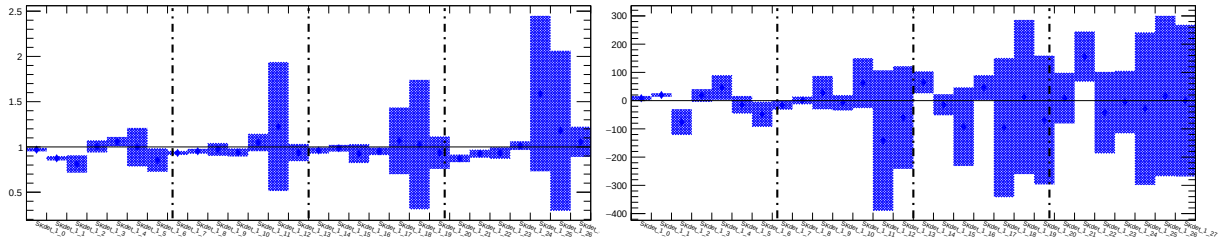

(b1) Smearing parameters of e/μ PID (b2) Bias parameters of e/μ PID

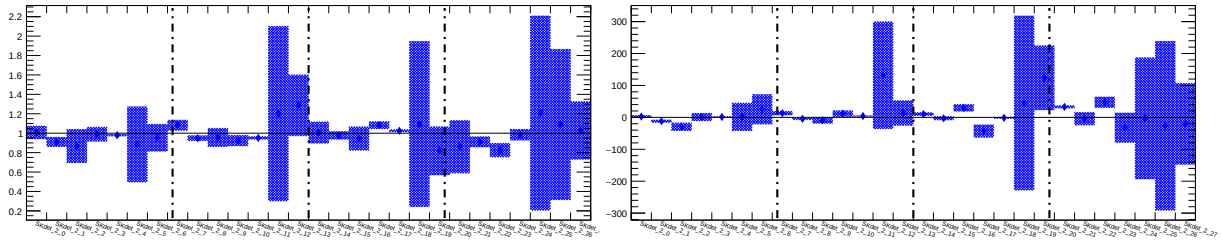

(c1) Smearing parameters of e/π^0 PID (c2) Bias parameters of e/π^0 PID

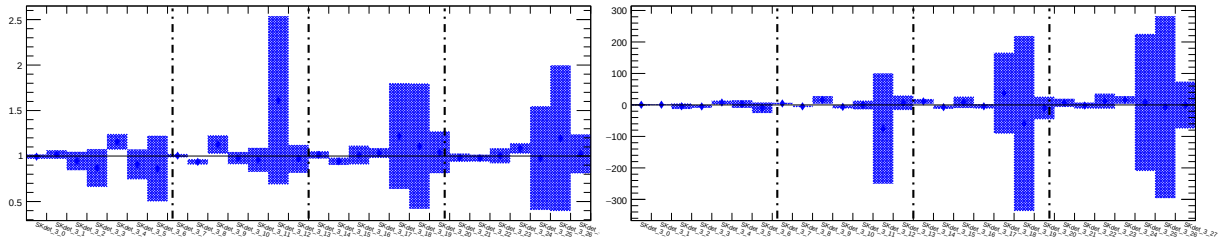

(d1) Smearing parameters of μ/π^+ PID (d2) Bias parameters of mu/π^+ PID

Figure 6.28: The post-fit SK detector error nuisance parameters (mean and R.M.S). Each plot represents a smearing (bias) parameter of a reconstructed variable in four energy ranges; in each energy range, the first to last bins represent the smearing (bias) parameter for events with the final state topology $1e$, 1μ, $1e$+other, 1μ+other, $1\pi^0$, $1\pi^+$, and *Other*, respectively.

observed data set. This is repeated 2,500 times, and the p-value corresponds to the fraction of steps with which the observed data set fits the MC prediction better than the fake data

set generated from the very same MC prediction ($\ln \mathcal{L}_{Data} > \ln \mathcal{L}_{Throw}$). Generally speaking a p-value greater than 5% is deemed acceptable.

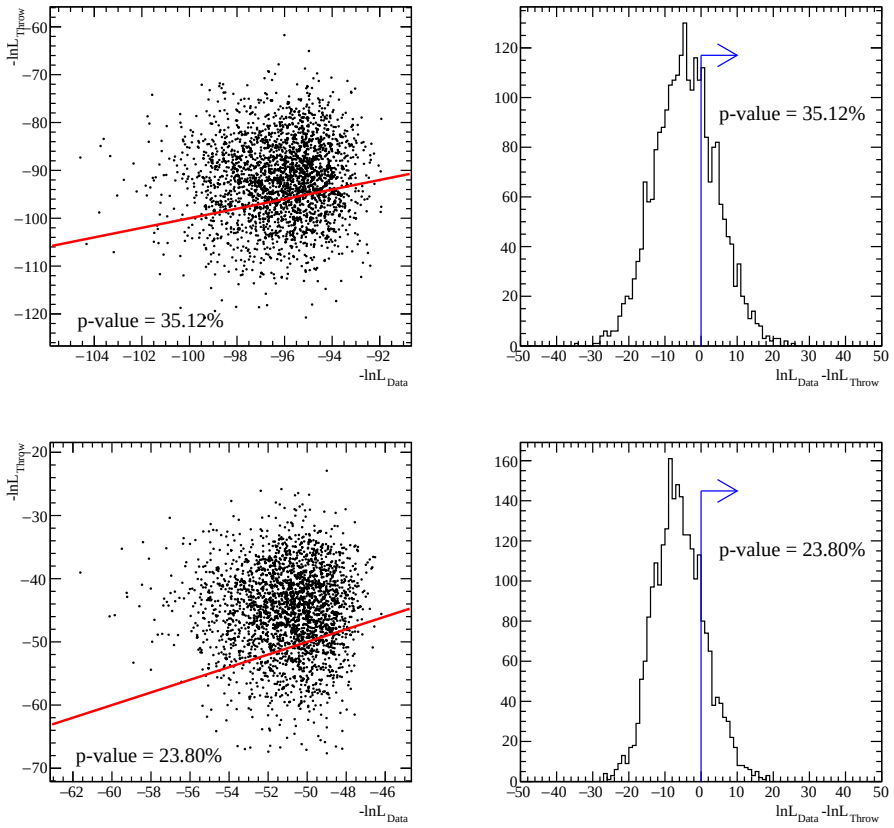

Figure 6.29: The goodness-of-fit of the T2K (top) and SK (bottom) samples. The red line represents $\ln \mathcal{L}_{Data} = \ln \mathcal{L}_{Throw}$. The lefthand-side plots are the 1D projections of $\ln \mathcal{L}_{Data}/\mathcal{L}_{Throw}$.

Figure 6.29 shows the goodness-of-fit of the T2K and SK samples. The plots on the lefthand side are distributions of $-\ln \mathcal{L}_{Data}$ v.s. $-\ln \mathcal{L}_{Throw}$, and righthand side plots distributions of $\ln \mathcal{L}_{Data}/\mathcal{L}_{Throw}$. The T2K likelihoods are calculated in the same way as defined in the fit, i.e. a binned likelihood function. It should be noted that the SK control distributions are not included in the goodness-of-fit test for two reasons: first of all, only the zenith angle distributions are relevant to the oscillation parameters, which is the focus of this study, hence a binned likelihood function of the zenith angle distributions are used; secondly, the unbinned likelihood functions of the control distributions in Eq. 6.13 are not good test statistic in this case – a proper test statistic for the control distributions would reflect how well the shape of the data distributions matches those of the model regardless of the data statistics. In the future, a test statistic such as the Kolmogorov-Smirnov test statistic or the Anderson-Darling

test statistic can be used to test the goodness-of-fit of the control distributions, although its implementation in the framework would not be straightforward. Nevertheless, it can be seen from the posterior predictive distributions A.4 that the post-fit detector model and data have good agreement. The p-value is found to be 35.1% for the T2K samples, and 23.8% for the SK samples.

6.6.5 Data fit results compared with T2K-only analysis

Figures 6.30 and 6.31 show a comparison between this study and the T2K-only study [147] using the same T2K exposure. Note that the T2K-only study uses five T2K samples (four CCQE-like samples and the ν_e CC1π^+ sample), whereas the T2K+SK joint fit analysis only uses the four CCQE-like samples from T2K. The addition of SK atmospheric neutrino samples only slightly shifted the Δm^2_{32}-$\sin^2\theta_{23}$ contours and best-fit values, which is similar to what the Asimov sensitivity suggests.

However, contrary to the expected sensitivity improvement from combining T2K and SK, the constraint on δ_{CP} has become weaker, especially in the case without reactor constraint. This is likely due to the fact that T2K data and SK data prefer different δ_{CP} values; as a consequence, the Markov chain steps toward both preferred values, making the posterior probability distribution wider. Ideally a fit using only the three SK samples should be performed to confirm this hypothesis, but this was not done due to the limitation in computing resources. Nevertheless, a Bayesian analysis on all SK-IV fully contained atmospheric neutrino events [111] was previously performed, and can confirm that even with reactor constraint applied, the prefered δ_{CP} value is close to π, as shown by Figure 6.32. It must be pointed out that the analysis in [111] used a different version of SK reconstruction software and drastically different systematic uncertainty modeling; it also included multi-GeV samples. With that said, the sub-GeV samples have the most δ_{CP} sensitivity, so the results of the prior analysis are expected to be similar to an SK-only fit using the framework described in this thesis.

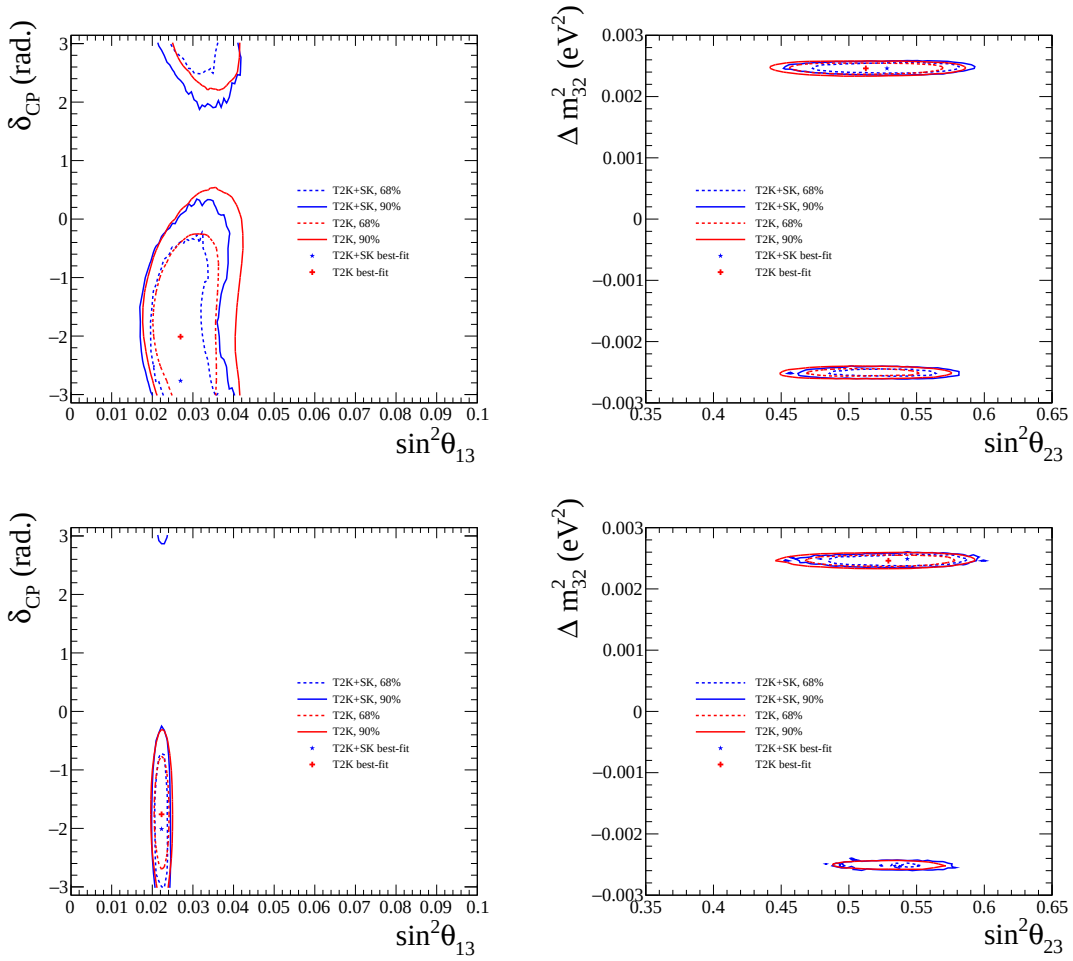

Figure 6.30: A comparison between the T2K+SK data fit with the T2K-only data fit. Top left: δ_{CP} v.s. $\sin^2\theta_{13}$ without reactor constraint; top right: Δm^2_{32} v.s. $\sin^2\theta_{23}$ without reactor constraint; bottom left: δ_{CP} v.s. $\sin^2\theta_{13}$ with reactor constraint $\sin^2 2\theta_{13} = 0.0857 \pm 0.0046$; bottom right: Δm^2_{32} v.s. $\sin^2\theta_{23}$ with reactor constraint $\sin^2 2\theta_{13} = 0.0857 \pm 0.0046$. The T2K-only sensitivities are taken from [147]. Note that the T2K-only fit uses five T2K samples (four CCQE-like samples and the ν_e CC1π^+ sample), whereas the T2K+SK joint fit only uses the four CCQE-like samples from T2K.

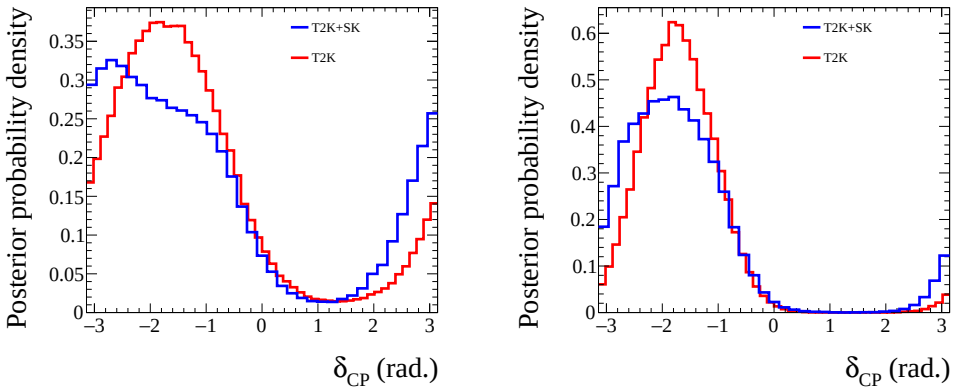

Figure 6.31: A comparison between the T2K+SK data fit to δ_{CP} with the T2K-only data fit. Left: without reactor constraint; right: with reactor constraint $\sin^2 2\theta_{13} = 0.0857 \pm 0.0046$. The T2K-only sensitivities are taken from [147]. Note that the T2K-only fit uses five T2K samples (four CCQE-like samples and the ν_e CC1π^+ sample), whereas the T2K+SK joint fit only uses the four CCQE-like samples from T2K.

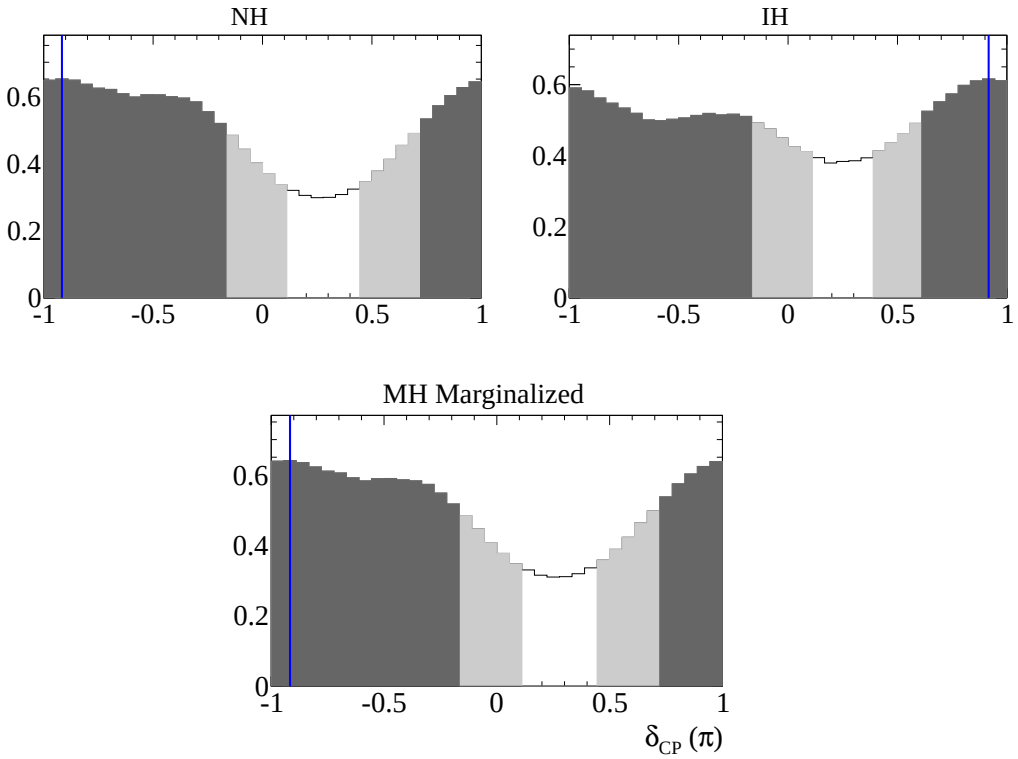

Figure 6.32: The δ_{CP} posterior probability distributions and credible intervals from all SK FC samples taken from [111]. The blue lines indicate the mode of the 1D probability distribution. It is a fit to all SK-IV fully contained atmospheric neutrino events with reactor constraint $\sin^2\theta_{13} = 0.0219 \pm 0.0012$.

Chapter 7

Conclusions and outlook

The first simultaneous analysis of the Super-K atmospheric neutrino data and the T2K beam neutrino data has been performed. 2519 days of SK-IV data, and the T2K Runs 1-8 data amounting to 14.7×10^{20} POT and 7.6×10^{20} POT in neutrino-mode and antineutrino-mode, respectively, are used. This analysis employs a Bayesian technique in which the nuisance parameters are marginalized to obtain credible intervals of the oscillation parameters. When the constraint on $\sin^2 2\theta_{13}$ from reactor neutrino experiments is included, the oscillation parameters are measured to be $\sin^2 \theta_{23} = 0.543^{+0.026}_{-0.023}$ and $|\Delta m^2_{32}| = 2.49^{+0.042}_{-0.090}(10^{-3}\text{eV}^2)$; the 90% credible interval of δ_{CP} is $[-\pi, -0.628]$, and the CP-conserving value $\delta_{CP} = 0$ is excluded at 2σ. Even though the sensitivity to δ_{CP} is expected to increase relative to the T2K-only analysis, the data constraint on δ_{CP} in the joint analysis is somewhat weaker. The overall results from the joint fit are consistent with the sensitivity.

Three sub-GeV CCQE-like atmospheric neutrino samples and four CCQE-like beam neutrino samples are used in this analysis, which excludes some of the samples that each experiment uses in their respective official analyses [123] [1]. However, as discussed in section 2.3, the SK multi-GeV ν_e and $\bar{\nu}_e$ samples are important in resolving the mass hierarchy problem. The added constraint on $\sin^2 \theta_{23}$ from T2K will improve the mass hierarchy sensitivity from the SK multi-GeV samples, which in turn will benefit the measurement of δ_{CP}. In addition, this analysis only used the SK-IV data, whereas SK has been taking data since 1996 (with a few brief interruptions) with different detector configurations and electronics [52]. Table 7.1 shows the live time of each SK run period – SK-IV only makes up just over 50% of the total statistics. An analysis of SK-I to IV atmospheric neutrino data including the sub-GeV and multi-GeV samples as well as the partially contained and upward-going muon samples found

that the inverted mass hierarchy is disfavored by between 80.6% and 96.7% for SK (with constraint on θ_{13} from reactor experiments) over the range of parameters allowed at 90% C.L. [123]. Therefore, it is desirable to include the multi-GeV samples as well as SK-I to III data in the joint analysis.

	SK-I	SK-II	SK-III	SK-IV
Live time (days)	1489.2	798.6	518.1	3118.5

Table 7.1: The live time of each SK run period. 2519 days of SK-IV data is used in this analysis.

Improvements in the cross section modeling are needed in order to incorporate the non-CCQE and multi-GeV samples from both experiments. Single-pion production is known to be poorly simulated in the version of the NEUT (v5.3.2) used in this analysis. Recently efforts have been made to improve the modeling of the single-pion production in neutrino-nucleon interactions [100]. Moreover, T2K has used a simpler DIS model compared to SK atmospheric neutrino analyses since the T2K neutrino beam has a much lower energy range than atmospheric neutrinos. Therefore, a more precise parameterization of the DIS systematic uncertainties will be needed. For example, there should be systematic error parameters of the Bodek-Yang corrections and pion multiplicity [88].

SK-I and III have the same photocathode coverage as SK-IV but different electronics, while both the photocathode coverage and electronics of SK-II are different from SK-IV. The event reconstruction relies heavily on the accuracy of the simulation, and so far the effort to improve the simulation has mostly been focused on SK-IV. As a result, there exist somewhat larger data/MC discrepancies in SK-I to III atmospheric neutrinos [111]. Once the discrepancies are mitigated through improvements in the detector simulation, the data from SK-I to III can be included in the analysis.

The next generation neutrino experiments such as DUNE and Hyper-Kamiokande are poised to determine the mass hierarchy and leptonic CP-violation conclusively. In the meantime, with T2K and NOνA accumulating data rapidly, a simultaneous fit of the data from SK, T2K and NOνA will be able be improve the constraints on the oscillation parameters considerably. Such an analysis poses quite a challenge. It is my humble wish that this study will be a valuable first step towards the eventual global fit.

Appendix A

T2K-SK joint fit analysis

A.1 Impact of $BeRPA\_U$ parameter

Contrary to other T2K analyses, the value of $BeRPA\_U$ parameter was not fixed at 1.2 but instead has a Gaussian prior uncertainty of 0.1. Since $BeRPA\_U$ parameter only has a negligible effect on the likelihood, and that re-running the entire is very computationally expensive and time consuming, it was decided that studies should be done to assess the impact of $BeRPA\_U$ parameter on the final results – if the impact is sufficiently small, the data fit results can thusly be trusted.

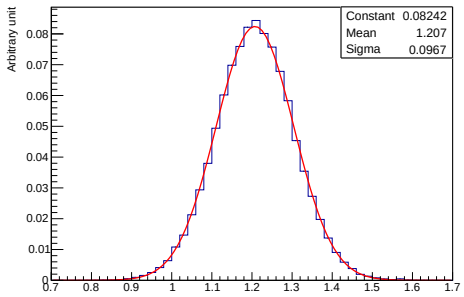

Figure A.1: The post-fit distribution of the $BeRPA\_U$ parameter. The red line is a Gaussian fit to the post-fit distribution.

Figure A.1 shows the post-fit distribution of the $BeRPA\_U$ parameter with a Gaussian fit. The post-fit Gaussian mean (1.207) and r.m.s. (0.0967) are very close to the pre-fit values (1.2 and 0.1 respectively). Therefore, the data does not have constraining power on the $BeRPA\_U$ parameter and vice versa. Figure A.2 shows the correlation factors between the $BeRPA\_U$ parameter and the rest of the nuisance and oscillation parameters. $BeRPA\_U$

only has negligibly small correlations with the rest of the parameters. Figure A.3 shows the post-fit oscillation parameter distributions in black, and the same distributions made with $BeRPA\_U \in [1.18, 1.22]$ in red. Note that the red histograms only have 17% of the statistics of the black histograms. For each oscillation parameter, the two distributions do not have differences greater than the differences in statistics. In conclusion, the $BeRPA\_U$ parameter does not have any visible effects on the fit results, and therefore the fit results can be trusted.

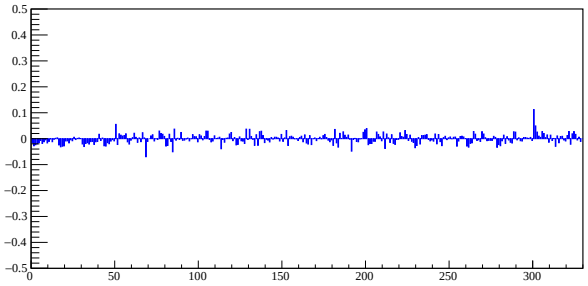

Figure A.2: The correlation factors (y-axis) between the $BeRPA\_U$ parameter and the rest of the nuisance and oscillation parameters (parameter index shown in x-axis).

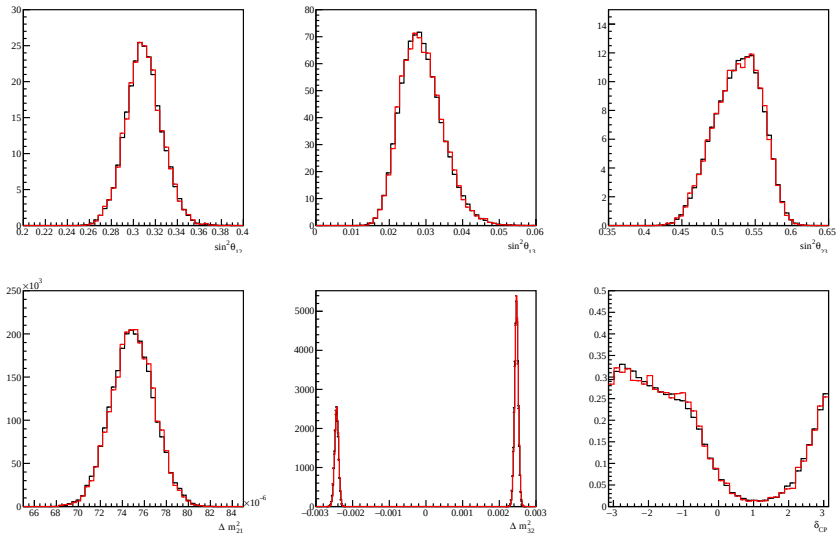

Figure A.3: The post-fit oscillation parameter distributions. The black histograms are made with all the steps in the fit posterior, whereas the red histograms are made only with the steps in which $BeRPA\_U \in [1.18, 1.22]$.

A.2 Pre-fit data/MC comparison of control distributions

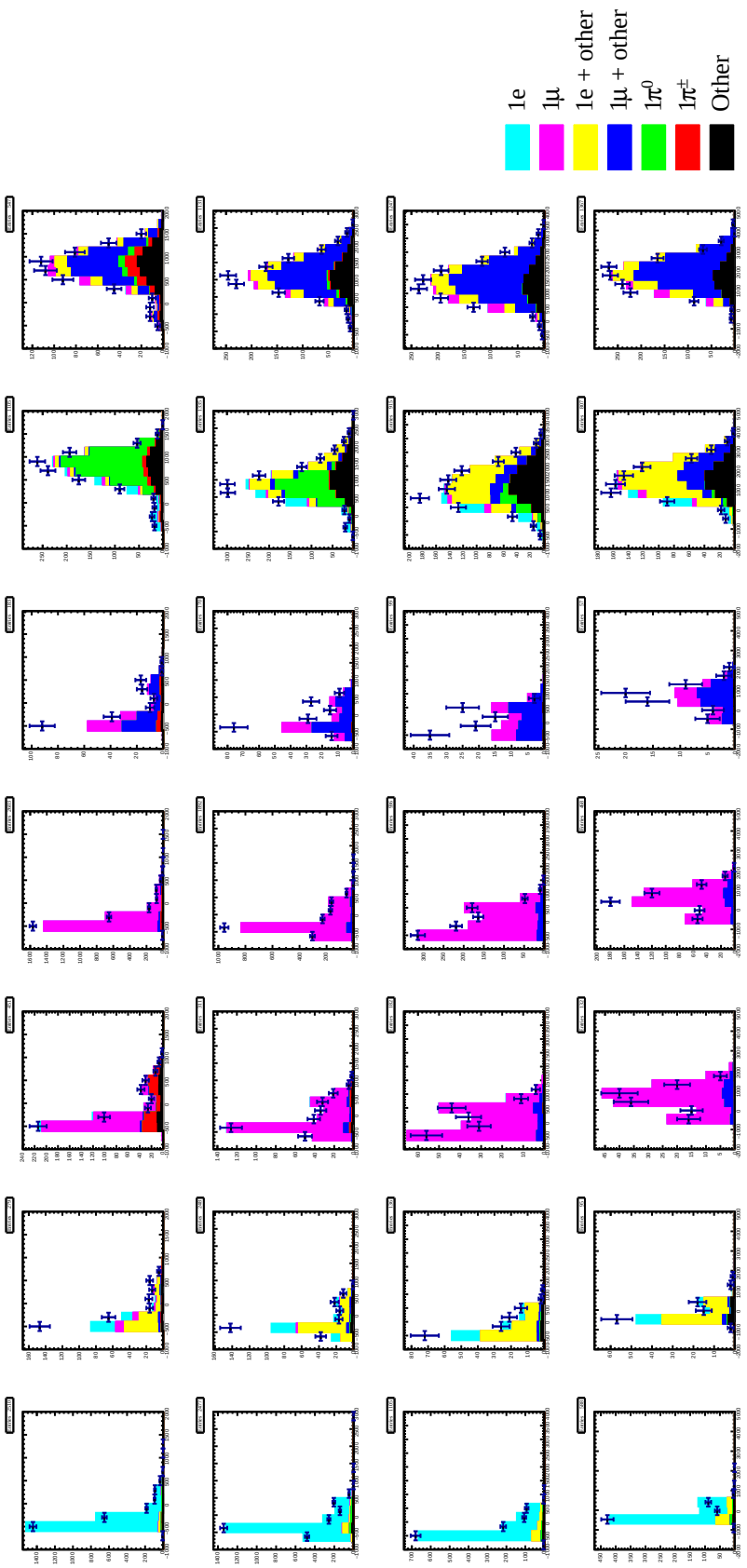

Figure A.4: The pre-fit ring-counting parameter distributions. The samples from left to right are: 1Re 0_{dcy}, 1Re $\geq 1_{dcy}$, 1Rμ 0_{dcy}, 1Rμ 1_{dcy}, 1R$\mu \geq 2_{dcy}$, MR 0_{dcy}, MR $\geq 1_{dcy}$. The energy ranges from top to bottom are: $E_{vis} < 400$ MeV, $400 < E_{vis} < 700$ MeV, $700 < E_{vis} < 1330$ MeV, $1330 < E_{vis} < 3000$ MeV. Data is shown with statistical errors only. The oscillation parameters shown in Tb. 6.11 are used to calculate the MC predictions. 2519.89 days of SK-4 data is used, and MC is scaled to the same exposure as data.

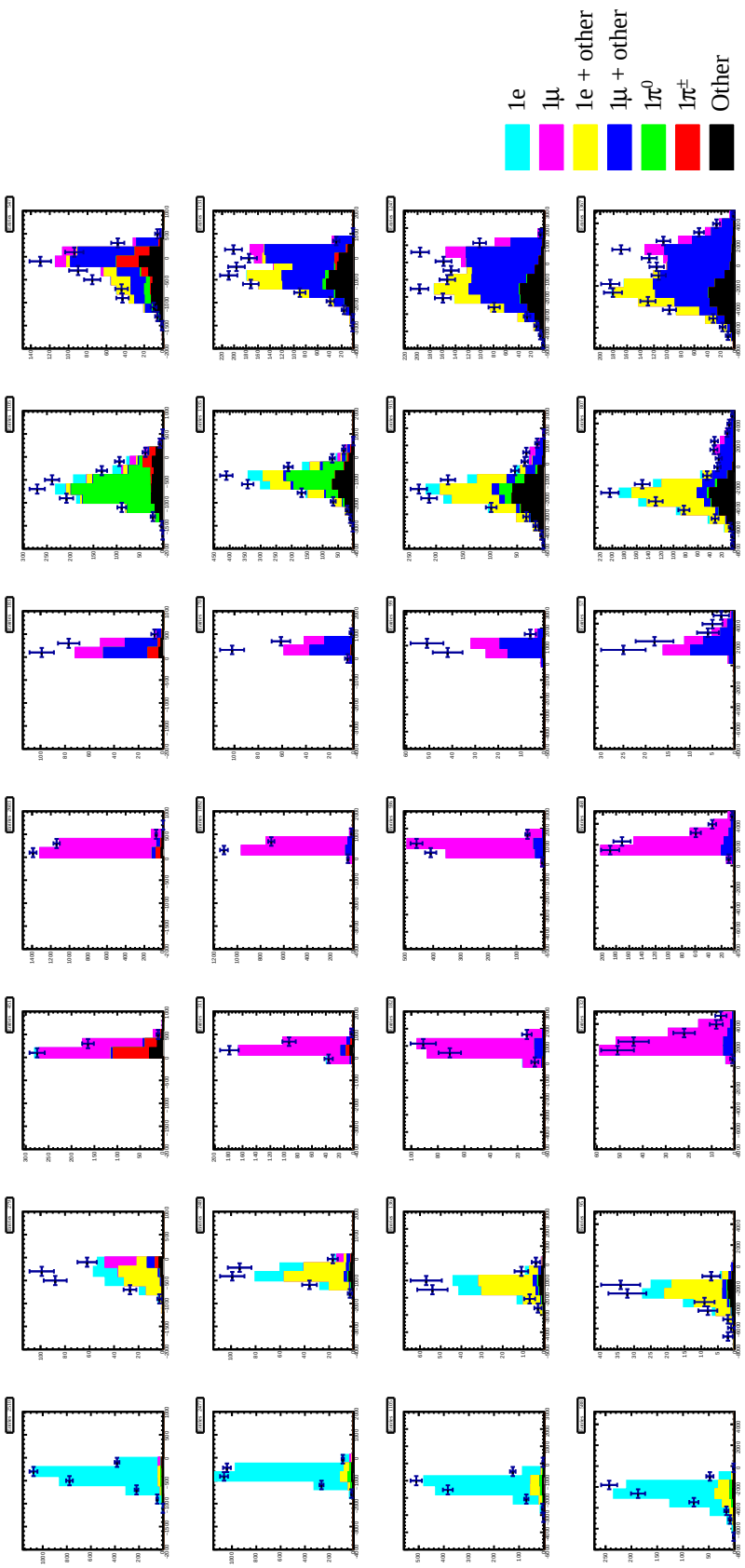

Figure A.5: The pre-fit e/μ PID parameter distributions. The samples from left to right are: 1Re 0_{dcy}, 1Re $\geq 1_{dcy}$, 1Rμ 0_{dcy}, 1Rμ 1_{dcy}, 1Rμ $\geq 2_{dcy}$, MR 0_{dcy}, MR $\geq 1_{dcy}$. The energy ranges from top to bottom are: $E_{vis} < 400$ MeV, $400 < E_{vis} < 700$ MeV, $700 < E_{vis} < 1330$ MeV, $1330 < E_{vis} < 3000$ MeV. Data is shown with statistical errors only. The oscillation parameters shown in Tb. 6.11 are used to calculate the MC predictions. 2519.89 days of SK-4 data is used, and MC is scaled to the same exposure as data.

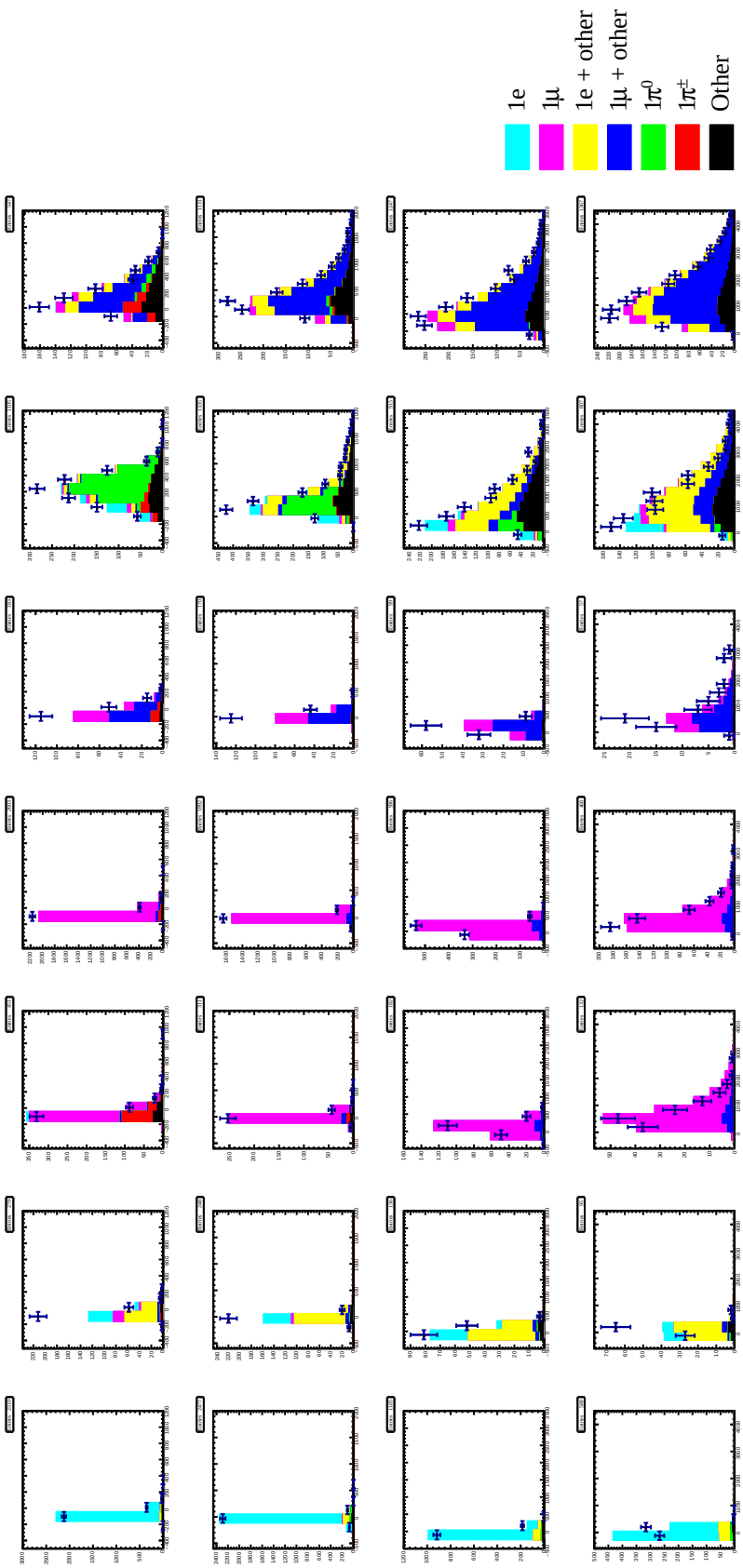

Figure A.6: The pre-fit e/π^0 PID parameter distributions. The samples from left to right are: 1Re 0_{dcy}, 1Re $\geq 1_{dcy}$, 1Rμ 0_{dcy}, 1Rμ 1_{dcy}, 1Rμ $\geq 2_{dcy}$, MR 0_{dcy}, MR $\geq 1_{dcy}$. The energy ranges from top to bottom are: $E_{vis} < 400$ MeV, $400 < E_{vis} < 700$ MeV, $700 < E_{vis} < 1330$ MeV, $1330 < E_{vis} < 3000$ MeV. Data is shown with statistical errors only. The oscillation parameters shown in Tb. 6.11 are used to calculate the MC predictions. 2519.89 days of SK-4 data is used, and MC is scaled to the same exposure as data.

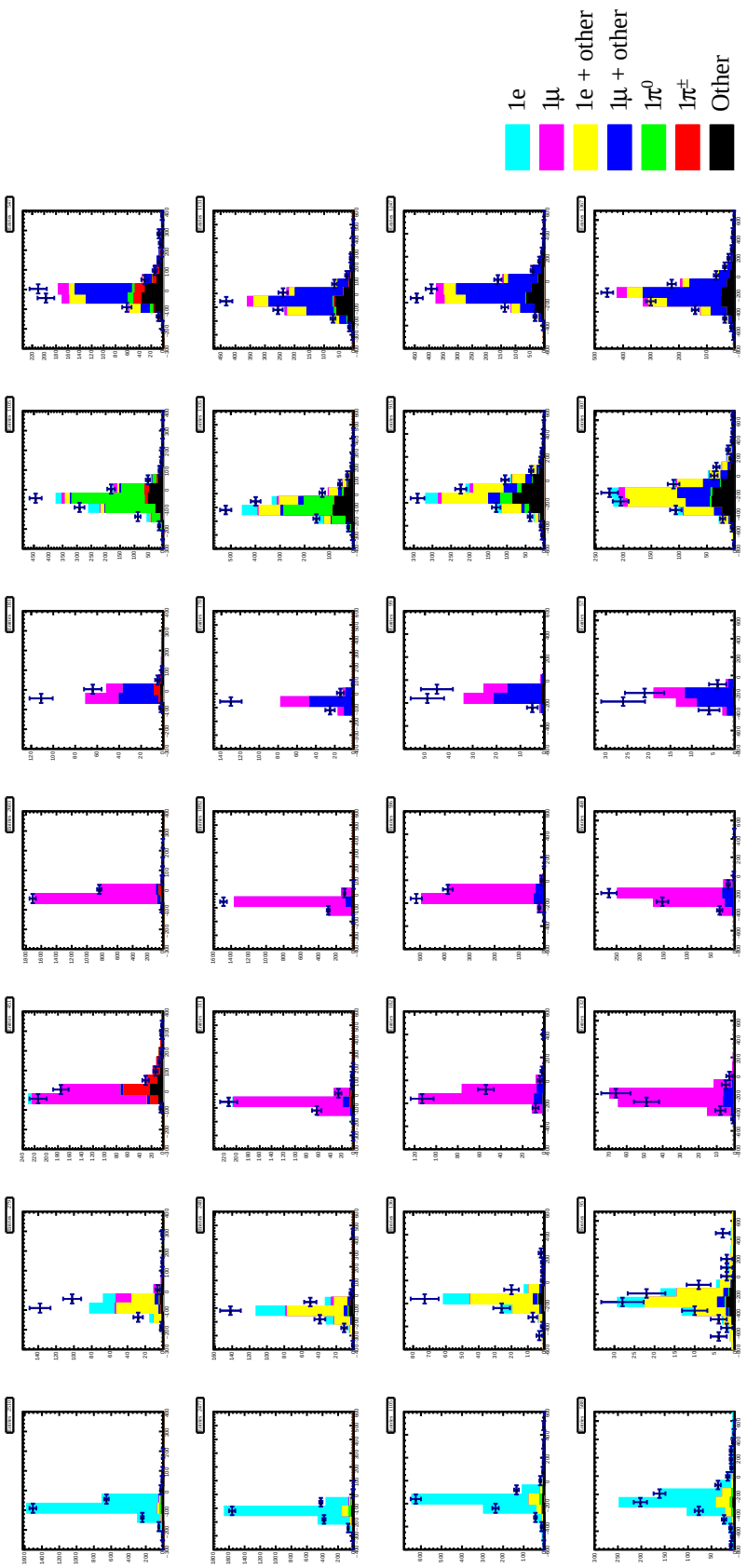

Figure A.7: The pre-fit μ/π^+ parameter distributions. The samples from left to right are: 1Re 0_{dcy}, 1Re $\geq 1_{dcy}$, 1Rμ 0_{dcy}, 1Rμ 1_{dcy}, 1Rμ $\geq 2_{dcy}$, MR 0_{dcy}, MR $\geq 1_{dcy}$. The energy ranges from top to bottom are: $E_{vis} < 400$ MeV, $400 < E_{vis} < 700$ MeV, $700 < E_{vis} < 1330$ MeV, $1330 < E_{vis} < 3000$ MeV. Data is shown with statistical errors only. The oscillation parameters shown in Tb. 6.11 are used to calculate the MC predictions. 2519.89 days of SK-4 data is used, and MC is scaled to the same exposure as data.

A.3 Asimov fit post-fit nuisance parameters

Figure A.8 shows the Asimov fit pre- and post-fit values of the T2K flux parameters, cross-section parameters, atmospheric neutrino flux parameters and the energy scale can reduction related parameters. The 1σ pre-fit values are shown in red; the mean and R.M.S of the post-fit parameter values are shown in blue by the diamond and shaded area respectively. Figure A.9 shows the Asimov fit post-fit detector systematic error parameters; the priors on these parameters are flat, and therefore are not shown. Each bin in the plot corresponds to a α or β parameter of a category in Table 6.6 of a reconstructed variable in an energy range in Table 6.2. All α parameters are expected to be centered around 1 and all β parameters centered around 0. The parameters which correspond to categories with higher statistics are more tightly constrained (bins 1, 2, 3 and 4 in each energy block) than the ones with low statistics (bins 5, 6 and 7). Bins 5, 12 and 19 in (c1) and (c2) are tightly constrained because of the prior constraints obtained by a fit to the hybrid-π^0 samples.

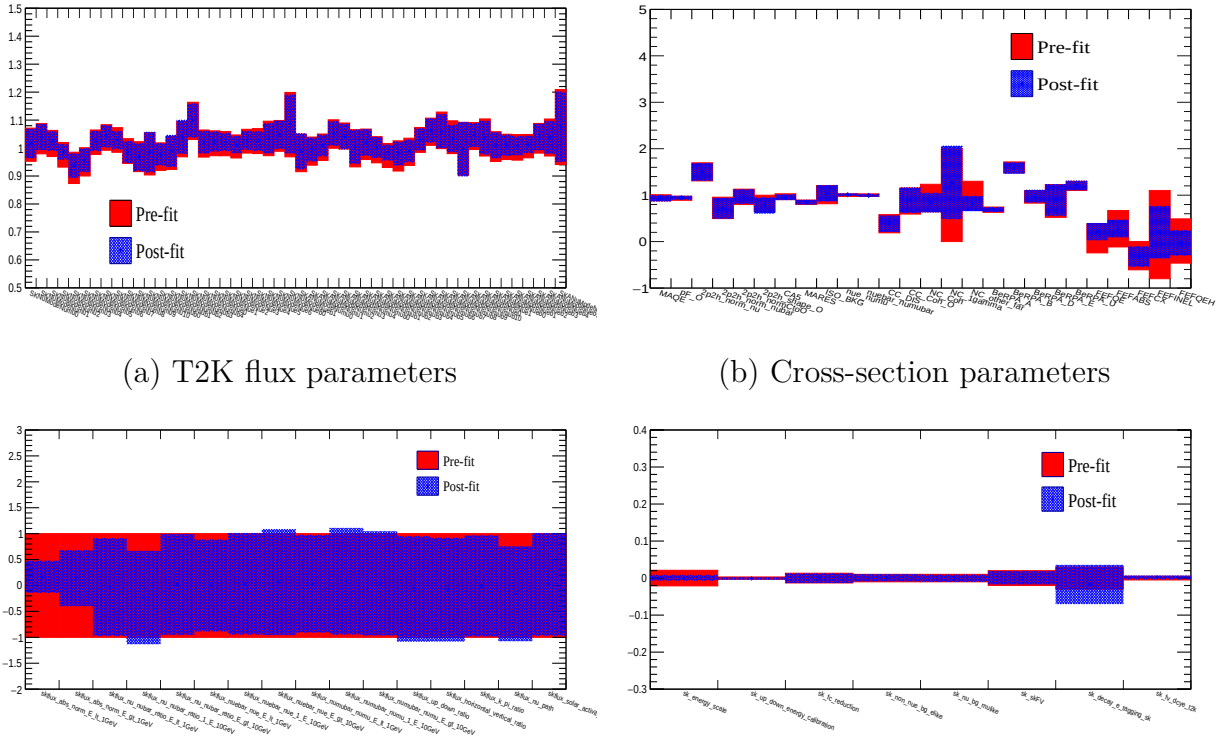

(a) T2K flux parameters

(b) Cross-section parameters

(c) SK atmospheric flux parameters

(d) Energy scale and reduction parameters

Figure A.8: The Asimov fit pre- and post-fit nuisance parameters. The pre-fit uncertainties are shown in red; post-fit mean and R.M.S are shown in blue.

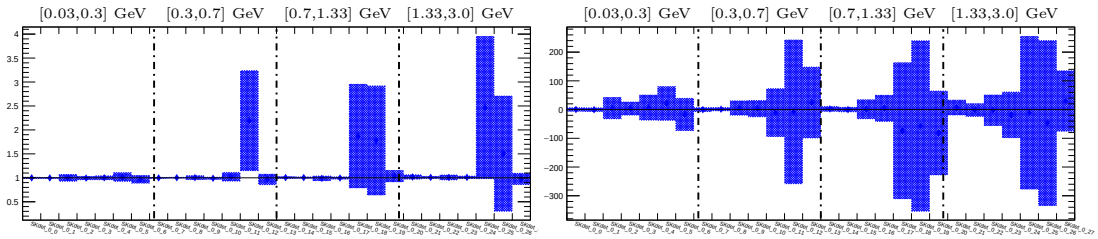

(a1) Smearing parameters of ring-counting (a2) Bias parameters of ring-counting

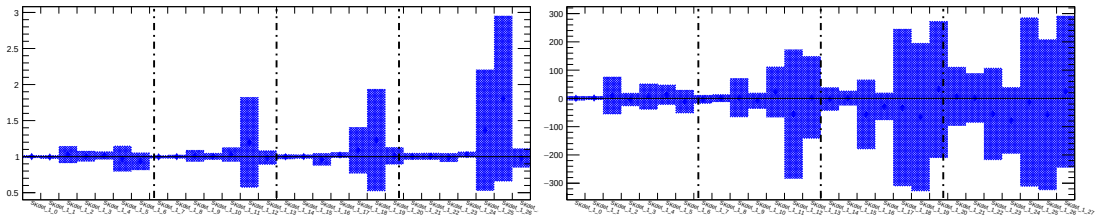

(b1) Smearing parameters of e/μ PID (b2) Bias parameters of e/μ PID

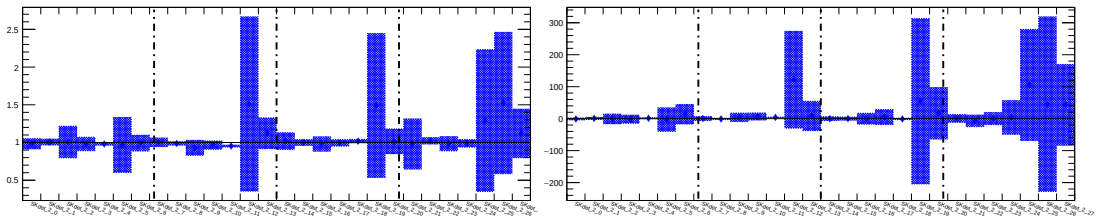

(c1) Smearing parameters of e/π^0 PID (c2) Bias parameters of e/π^0 PID

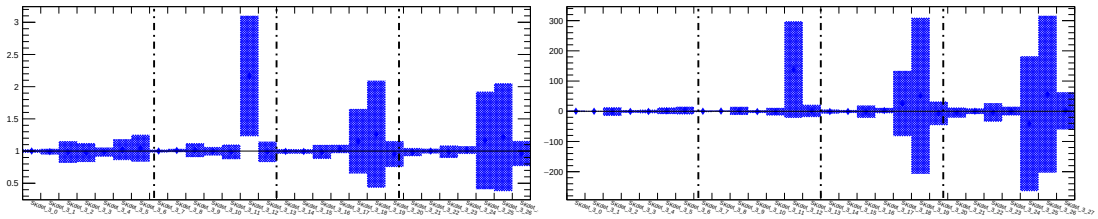

(d1) Smearing parameters of μ/π^+ PID (d2) Bias parameters of mu/π^+ PID

Figure A.9: The Asimov fit post-fit SK detector error nuisance parameters (mean and R.M.S). Each plot represents a smearing (bias) parameter of a reconstructed variable in four energy ranges; in each energy range, the first to last bins represent the smearing (bias) parameter for events with the final state topology $1e$, 1μ, $1e$+other, 1μ+other, $1\pi^0$, $1\pi^+$, and *Other*, respectively.

A.4 SK posterior predictive control distributions

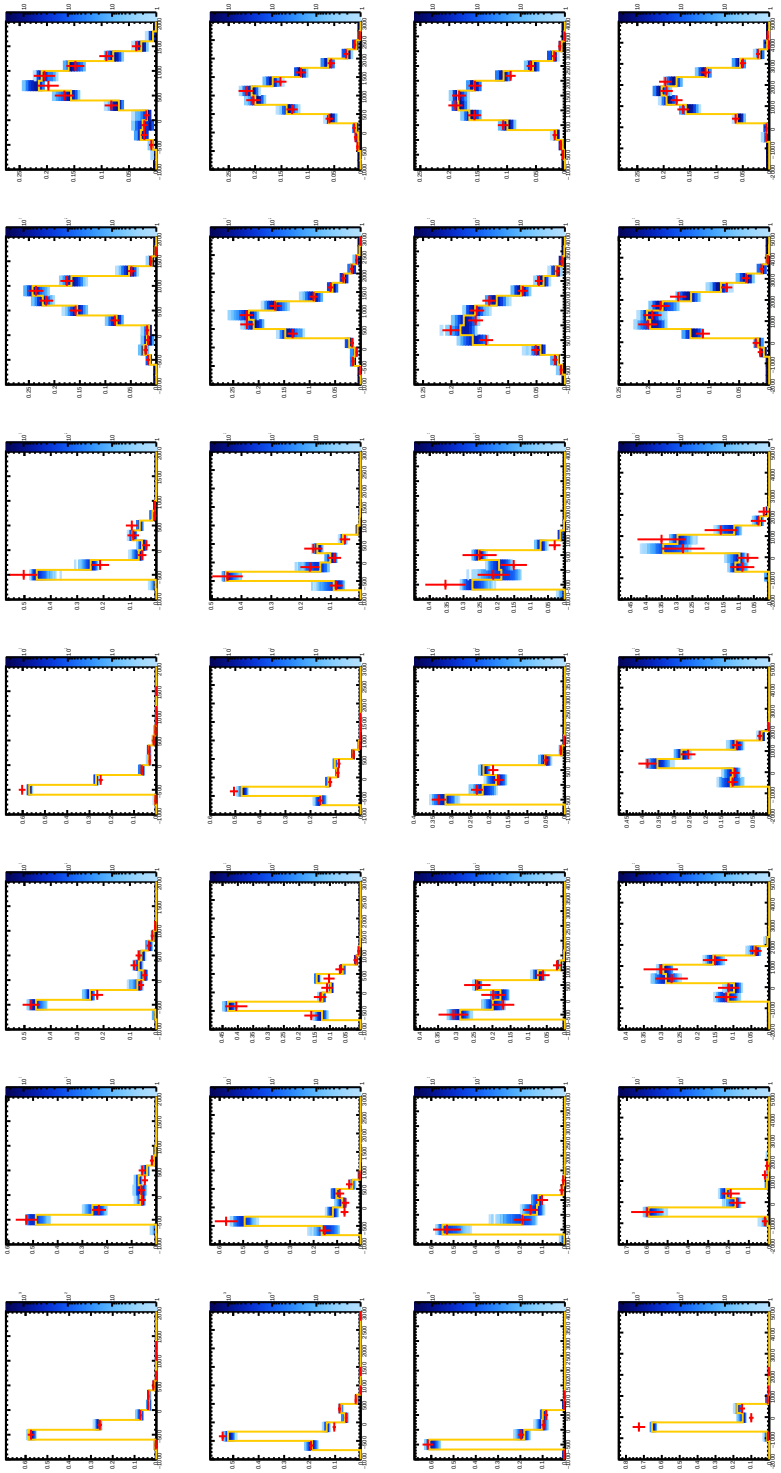

Figure A.10: The posterior predictive ring-counting parameter distributions of SK samples. The blue 2D histogram is made by sampling 2,500 steps from the fit posterior distribution without reactor constraint. Data is shown in red with statistical errors only. Orange shows the spectra made by setting all parameters at the mode of their respective 1D posterior distribution without reactor constraint.

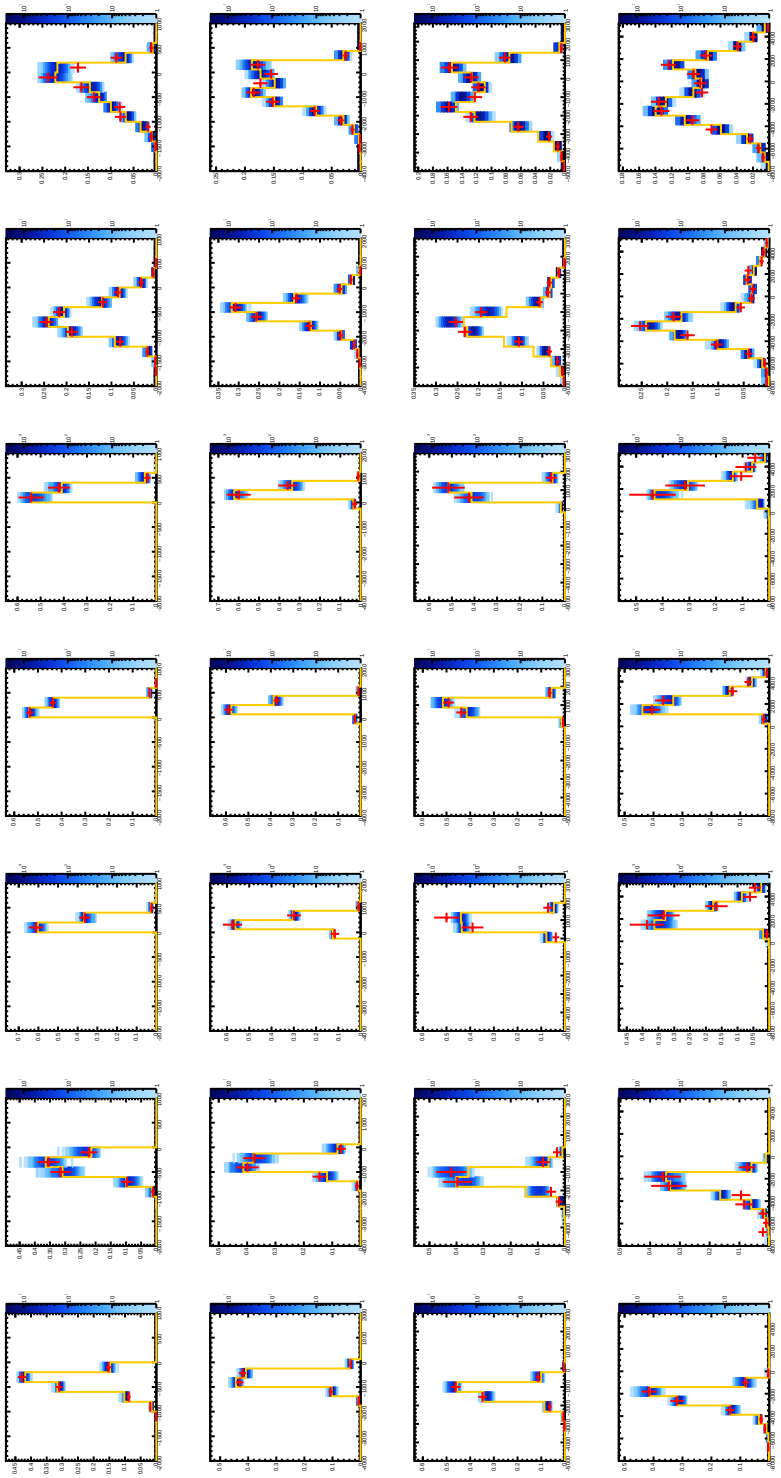

Figure A.11: The posterior predictive e/μ PID parameter distributions of SK samples. The blue 2D histogram is made by sampling 2,500 steps from the fit posterior distribution without reactor constraint. Data is shown in red with statistical errors only. Orange shows the spectra made by setting all parameters at the mode of their respective 1D posterior distribution without reactor constraint.

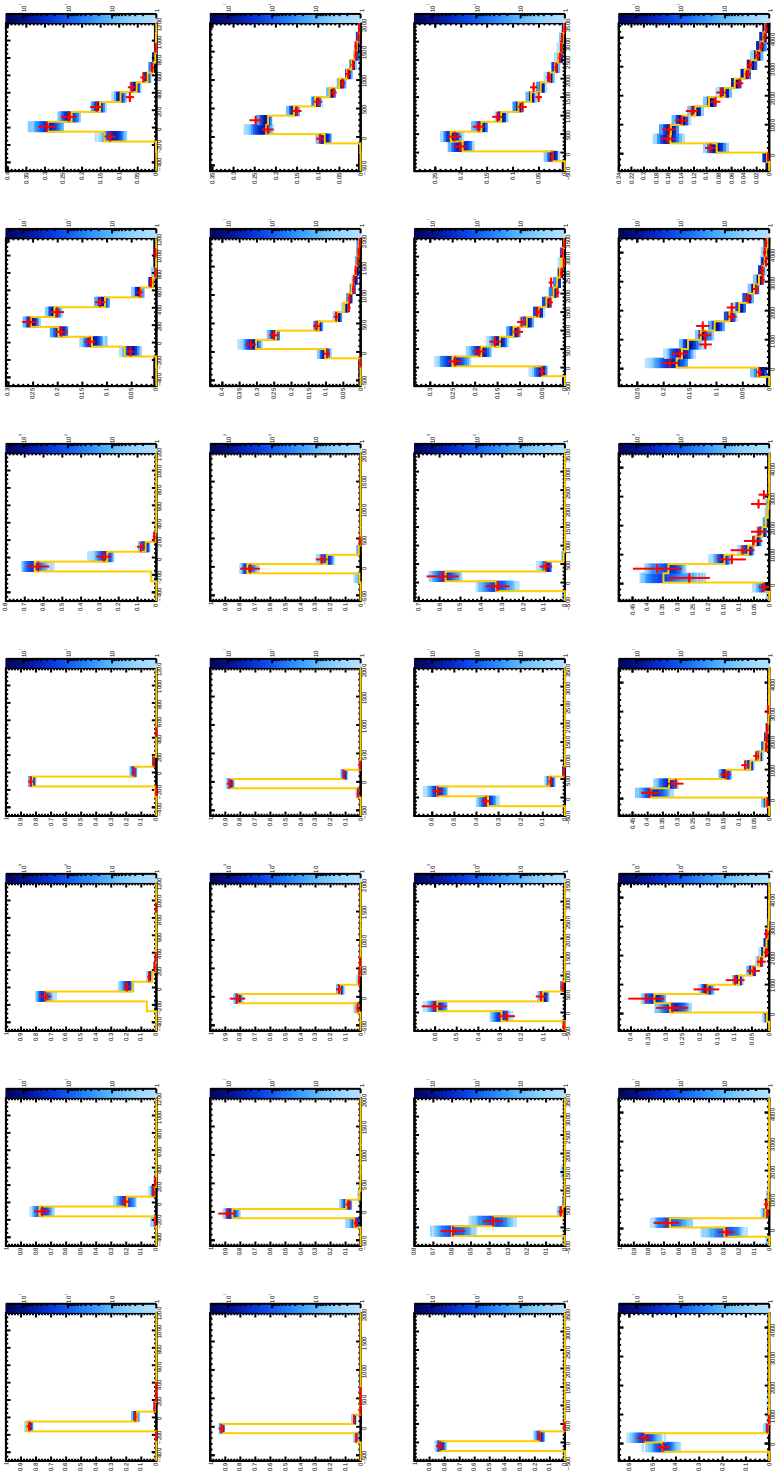

Figure A.12: The posterior predictive e/π^0 PID parameter distributions of SK samples. The blue 2D histogram is made by sampling 2,500 steps from the fit posterior distribution without reactor constraint. Data is shown in red with statistical errors only. Orange shows the spectra made by setting all parameters at the mode of their respective 1D posterior distribution without reactor constraint.

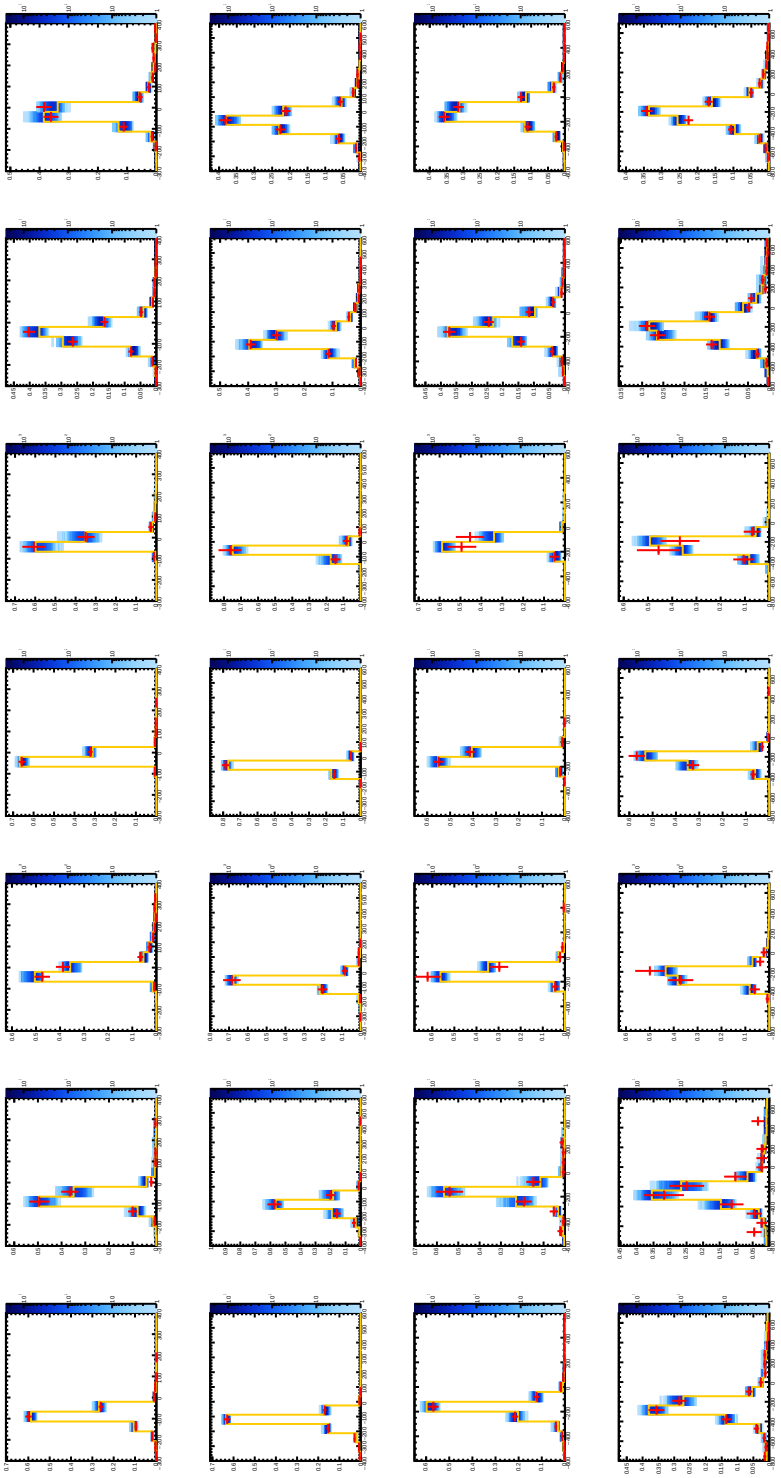

Figure A.13: The posterior predictive μ/π^+ PID parameter distributions of SK samples. The blue 2D histogram is made by sampling 2,500 steps from the fit posterior distribution without reactor constraint. Data is shown in red with statistical errors only. Orange shows the spectra made by setting all parameters at the mode of their respective 1D posterior distribution without reactor constraint.

Bibliography

[1] K. Abe et al. Combined Analysis of Neutrino and Antineutrino Oscillations at T2K. *Phys. Rev. Lett.*, 118(15):151801, 2017.

[2] Mark Hartz. T2k neutrino oscillation results with data up to 2017 summer. KEK Seminar, 2017.

[3] Carlos Giunti and Chung W. Kim. *Fundamentals of Neutrino Physics and Astrophysics*. Oxford University Press, Great Clarendon Stree, Oxford OX2 6DP, 2007.

[4] . `http://www.texample.net/tikz/examples/model-physics/`.

[5] C. L. Cowan, F. Reines, F. B. Harrison, H. W. Kruse, and A. D. McGuire. Detection of the free neutrino: a confirmation. *Science*, 124(3212):103–104, 1956.

[6] M. Goldhaber, L. Grodzins, and A. W. Sunyar. Helicity of neutrinos. *Phys. Rev.*, 109:1015–1017, Feb 1958.

[7] B. Pontecorvo. Electron and Muon Neutrinos. *Sov. Phys. JETP*, 10:1236–1240, 1960. [Zh. Eksp. Teor. Fiz.37,1751(1959)].

[8] G. Danby, J-M. Gaillard, K. Goulianos, L. M. Lederman, N. Mistry, M. Schwartz, and J. Steinberger. Observation of high-energy neutrino reactions and the existence of two kinds of neutrinos. *Phys. Rev. Lett.*, 9:36–44, Jul 1962.

[9] M. L. Perl et al. Evidence for anomalous lepton production in $e^+ - e^-$ annihilation. *Phys. Rev. Lett.*, 35:1489–1492, Dec 1975.

[10] K. Kodama et al. Observation of tau neutrino interactions. *Physics Letters B*, 504(3):218 – 224, 2001.

[11] S. W. Herb et al. Observation of a dimuon resonance at 9.5 gev in 400-gev proton-nucleus collisions. *Phys. Rev. Lett.*, 39:252–255, Aug 1977.

[12] F. Abe et al. Observation of top quark production in $\overline{p}p$ collisions with the collider detector at fermilab. *Phys. Rev. Lett.*, 74:2626–2631, Apr 1995.

[13] S. Abachi et al. Observation of the top quark. *Phys. Rev. Lett.*, 74:2632–2637, Apr 1995.

[14] D. DeCamp et al. Determination of the number of light neutrino species. *Physics Letters B*, 231(4):519 – 529, 1989.

[15] P. Aarnio et al. Measurement of the Mass and Width of the Z^0 Particle from Multi - Hadronic Final States Produced in e^+e^- Annihilations. *Phys. Lett.*, B231:539–547, 1989.

[16] B. Adeva et al. A Determination of the Properties of the Neutral Intermediate Vector Boson Z^0. *Phys. Lett.*, B231:509, 1989.

[17] Precision electroweak measurements on the z resonance. *Physics Reports*, 427(5):257 – 454, 2006.

[18] M. Tanabashi and others (Particle Data Group). Neutrino Masses, Mixing, and Oscillations. *Phys. Rev. D*, 98:030001, 2018.

[19] V. Castellani, S. Degl'Innocenti, G. Fiorentini, M. Lissia, and B. Ricci. Solar neutrinos: Beyond standard solar models. *Phys. Rept.*, 281:309–398, 1997.

[20] Raymond Davis, Don S. Harmer, and Kenneth C. Hoffman. Search for neutrinos from the sun. *Phys. Rev. Lett.*, 20:1205–1209, May 1968.

[21] K. S. Hirata et al. Observation of B-8 solar neutrinos in the Kamiokande-II detector. *Physical Review Letters*, 63:16–19, July 1989.

[22] W. Hampel et al. Gallex solar neutrino observations: Results for gallex iii. *Physics Letters B*, 388(2):384 – 396, 1996.

[23] J. N. Abdurashitov et al. Measurement of the solar neutrino capture rate with gallium metal. *Phys. Rev. C*, 60:055801, Oct 1999.

[24] Y. Fukuda et al. Measurements of the solar neutrino flux from super-kamiokande's first 300 days. *Phys. Rev. Lett.*, 81:1158–1162, Aug 1998.

[25] Q. R. Ahmad et al. Measurement of the rate of $\nu_e + d \rightarrow p + p + e^-$ interactions produced by ^8b solar neutrinos at the sudbury neutrino observatory. *Phys. Rev. Lett.*, 87:071301, Jul 2001.

[26] J. Boger et al. The Sudbury neutrino observatory. *Nucl. Instrum. Meth.*, A449:172–207, 2000.

[27] John N. Bahcall, M. H. Pinsonneault, and Sarbani Basu. Solar models: Current epoch and time dependences, neutrinos, and helioseismological properties. *Astrophys. J.*, 555:990–1012, 2001.

[28] F. Capozzi, G. L. Fogli, E. Lisi, A. Marrone, D. Montanino, and A. Palazzo. Status of three-neutrino oscillation parameters, circa 2013. *Phys. Rev.*, D89:093018, 2014.

[29] Y. Fukuda et al. Evidence for oscillation of atmospheric neutrinos. *Phys. Rev. Lett.*, 81:1562–1567, Aug 1998.

[30] K. Abe et al. Atmospheric neutrino oscillation analysis with external constraints in super-kamiokande i-iv. *Phys. Rev. D*, 97:072001, Apr 2018.

[31] R. Acciarri et al. Design and Construction of the MicroBooNE Detector. *JINST*, 12(02):P02017, 2017.

[32] K. Abe et al. Observation of electron neutrino appearance in a muon neutrino beam. *Phys. Rev. Lett.*, 112:061802, Feb 2014.

[33] P. Adamson et al. Constraints on Oscillation Parameters from ν_e Appearance and ν_μ Disappearance in NOvA. *Phys. Rev. Lett.*, 118(23):231801, 2017.

[34] R. Acciarri et al. Long-Baseline Neutrino Facility (LBNF) and Deep Underground Neutrino Experiment (DUNE). 2016.

[35] S. Abe et al. Precision measurement of neutrino oscillation parameters with kamland. *Phys. Rev. Lett.*, 100:221803, Jun 2008.

[36] F. P. An et al. Observation of electron-antineutrino disappearance at daya bay. *Phys. Rev. Lett.*, 108:171803, Apr 2012.

[37] J. K. Ahn et al. Observation of Reactor Electron Antineutrino Disappearance in the RENO Experiment. *Phys. Rev. Lett.*, 108:191802, 2012.

[38] Y. Abe et al. Indication of reactor $\overline{\nu}_e$ disappearance in the double chooz experiment. *Phys. Rev. Lett.*, 108:131801, Mar 2012.

[39] F. P. An et al. Measurement of electron antineutrino oscillation based on 1230 days of operation of the daya bay experiment. *Phys. Rev. D*, 95:072006, Apr 2017.

[40] M. Fukugita and T. Yanagida. Baryogenesis Without Grand Unification. *Phys. Lett.*, B174:45–47, 1986.

[41] K. Abe et al. Hyper-Kamiokande Design Report. 2018.

[42] Fengpeng An et al. Neutrino Physics with JUNO. *J. Phys.*, G43(3):030401, 2016.

[43] Ivan Esteban, M. C. Gonzalez-Garcia, Michele Maltoni, Ivan Martinez-Soler, and Thomas Schwetz. Updated fit to three neutrino mixing: exploring the accelerator-reactor complementarity. *JHEP*, 01:087, 2017.

[44] P. A. R. Ade et al. Planck 2015 results. XIII. Cosmological parameters. *Astron. Astrophys.*, 594:A13, 2016.

[45] V. N. Aseev et al. An upper limit on electron antineutrino mass from Troitsk experiment. *Phys. Rev.*, D84:112003, 2011.

[46] Ch. Kraus et al. Final results from phase II of the Mainz neutrino mass search in tritium beta decay. *Eur. Phys. J.*, C40:447–468, 2005.

[47] KATRIN Collaboration. Katrin design report 2004. Technical report, Forschungszentrum, Karlsruhe, 2005. 51.54.01; LK 01; Auch: NPI ASCR Rez EXP-01/2005; MS-KP-0501.

[48] A. Gando et al. Search for Majorana Neutrinos near the Inverted Mass Hierarchy Region with KamLAND-Zen. *Phys. Rev. Lett.*, 117(8):082503, 2016. [Addendum: Phys. Rev. Lett.117,no.10,109903(2016)].

[49] M. Agostini et al. Improved limit on neutrinoless double-β decay of ^{76}Ge from gerda phase ii. *Phys. Rev. Lett.*, 120:132503, Mar 2018.

[50] J. B. Albert et al. Search for Neutrinoless Double-Beta Decay with the Upgraded EXO-200 Detector. *Phys. Rev. Lett.*, 120(7):072701, 2018.

[51] The Super-Kamiokande Collaboration. The super-kamiokande detector. *Nuclear Instruments and Methods in Physics Research Section A: Accelerators, Spectrometers, Detectors and Associated Equipment*, 501(2):418 – 462, 2003.

[52] K. Abe et al. Calibration of the Super-Kamiokande Detector. *Nucl. Instrum. Meth.*, A737:253–272, 2014.

[53] K. Abe et al. The T2K Experiment. *Nucl. Instrum. Meth.*, A659:106–135, 2011.

[54] Letter of Intent Neutrino Oscillation Experiment at JHF. http://neutrino.kek.jp/jhfnu/loi/loi_JHFcor.pdf.

[55] K. Abe and others. Search for proton decay via $p \to e^+\pi^0$ and $p \to \mu^+\pi^0$ in 0.31 megaton·years exposure of the super-kamiokande water cherenkov detector. *Phys. Rev. D*, 95:012004, Jan 2017.

[56] T. Tanaka et al. An indirect search for weakly interacting massive particles in the sun using 3109.6 days of upward-going muons in super-kamiokande. *The Astrophysical Journal*, 742(2):78, 2011.

[57] Georges Charpak, J. Derre, Y. Giomataris, and P. Rebourgeard. MICROMEGAS, a multipurpose gaseous detector. *Nucl. Instrum. Meth.*, A478:26–36, 2002.

[58] A. Suzuki, M. Mori, K. Kaneyuki, T. Tanimori, J. Takeuchi, H. Kyushima, and Y. Ohashi. Improvement of 20 in. diameter photomultiplier tubes. *Nuclear Instruments and Methods in Physics Research Section A: Accelerators, Spectrometers, Detectors and Associated Equipment*, 329(1):299 – 313, 1993.

[59] H. Nishino, K. Awai, Y. Hayato, S. Nakayama, K. Okumura, M. Shiozawa, A. Takeda, K. Ishikawa, A. Minegishi, and Y. Arai. High-speed charge-to-time converter ASIC for the Super-Kamiokande detector. *Nucl. Instrum. Meth.*, A610:710–717, 2009.

[60] S. Nakayama K. Iyogi and Y. Obayashi. T2K data acquisition and FC event selection at Super-Kamiokande. T2K-TN-027 http://www.t2k.org/docs/technotes/027.

[61] G. Battistoni et al. The fluka code: description and benchmarking. *AIP Conference Proceedings*, 896(1):31–49, 2007.

[62] R. Brun, F. Bruyant, M. Maire, A. C. McPherson, and P. Zanarini. GEANT3. 1987.

[63] C. Zeitnitz and T. A. Gabriel. *The GEANT-CALOR Interface User's Guide*. ORNL, 1996.

[64] N. Abgrall et al. Measurements of cross sections and charged pion spectra in proton-carbon interactions at 31 gev/c. *Phys. Rev. C*, 84:034604, Sep 2011.

[65] N. Abgrall et al. Measurement of production properties of positively charged kaons in proton-carbon interactions at 31 gev/c. *Phys. Rev. C*, 85:035210, Mar 2012.

[66] T. Eichten et al. Particle production in proton interactions in nuclei at 24-GeV/c. *Nucl. Phys.*, B44:333–343, 1972.

[67] I. Chemakin et al. Pion production by protons on a thin beryllium target at 6.4, 12.3, and 17.5 gev/c incident proton momenta. *Phys. Rev. C*, 77:015209, Jan 2008.

[68] K. Abe et al. Measurements of neutrino oscillation in appearance and disappearance channels by the T2K experiment with 6.6×10^{20} protons on target. *Phys. Rev.*, D91(7):072010, 2015.

[69] M. Honda, T. Kajita, K. Kasahara, S. Midorikawa, and T. Sanuki. Calculation of atmospheric neutrino flux using the interaction model calibrated with atmospheric muon data. *Phys. Rev. D*, 75(4):043006, February 2007.

[70] M. Honda, T. Kajita, K. Kasahara, and S. Midorikawa. Improvement of low energy atmospheric neutrino flux calculation using the JAM nuclear interaction model. Phys. Rev. D, 83(12):123001, June 2011.

[71] B. Blau, S.M. Harrison, H. Hofer, S.R. Milward, J.S.H. Ross, S.C.C. Ting, J. Ulbricht, and G. Viertel. The superconducting magnet of ams-02. *Nuclear Physics B - Proceedings Supplements*, 113(1):125 – 132, 2002.

[72] Sadakazu Haino et al. Measurements of primary and atmospheric cosmic - ray spectra with the BESS-TeV spectrometer. *Phys. Lett.*, B594:35–46, 2004.

[73] . `https://www.ngdc.noaa.gov/IAGA/vmod/igrf.html`.

[74] US Standard Atmosphere. `https://ntrs.nasa.gov/archive/nasa/casi.ntrs.nasa.gov/19770009539.pdf`.

[75] Stefan Roesler, Ralph Engel, and Johannes Ranft. The Monte Carlo event generator DPMJET-III. In *Advanced Monte Carlo for radiation physics, particle transport simulation and applications. Proceedings, Conference, MC2000, Lisbon, Portugal, October 23-26, 2000*, pages 1033–1038, 2000.

[76] Koji Niita, Tatsuhiko Sato, Hiroshi Iwase, Hiroyuki Nose, Hiroshi Nakashima, and Lembit Sihver. Phits—a particle and heavy ion transport code system. *Radiation Measurements*, 41(9):1080 – 1090, 2006. Space Radiation Transport, Shielding, and Risk Assessment Models.

[77] T. Sanuki et al. Measurements of atmospheric muon spectra at mountain altitude. *Phys. Lett.*, B541:234–242, 2002. [Erratum: Phys. Lett.B581,272(2004)].

[78] P. Achard et al. Measurement of the atmospheric muon spectrum from 20-GeV to 3000-GeV. *Phys. Lett.*, B598:15–32, 2004.

[79] G. D. Barr, T. K. Gaisser, P. Lipari, S. Robbins, and T. Stanev. Three-dimensional calculation of atmospheric neutrinos. *Phys. Rev. D*, 70(2):023006, July 2004.

[80] G. Battistoni, A. Ferrari, T. Montaruli, and P. R. Sala. The FLUKA atmospheric neutrino flux calculation. *Astroparticle Physics*, 19:269–290, May 2003.

[81] S. Agostinelli et al. GEANT4: A Simulation toolkit. *Nucl. Instrum. Meth.*, A506:250–303, 2003.

[82] Yoshinari Hayato. A neutrino interaction simulation program library NEUT. *Acta Phys. Polon.*, B40:2477–2489, 2009.

[83] T. A. Gabriel, J. D. Amburgey, and B. L. Bishop. CALOR: A Monte Carlo Program Package for the Design and Analysis of Calorimeter Systems. 1977.

[84] M. Nakahata et al. Atmospheric Neutrino Background and Pion Nuclear Effect for KAMIOKA Nucleon Decay Experiment. *J. Phys. Soc. Jpn.*, 55:3786–3805, 1986.

[85] D. Casper. The Nuance neutrino physics simulation, and the future. *Nucl. Phys. Proc. Suppl.*, 112:161–170, 2002. [,161(2002)].

[86] J. A. Formaggio and G. P. Zeller. From eV to EeV: Neutrino Cross Sections Across Energy Scales. *Rev. Mod. Phys.*, 84:1307–1341, 2012.

[87] C.H. Llewellyn Smith. Neutrino reactions at accelerator energies. *Physics Reports*, 3(5):261 – 379, 1972.

[88] S. Bolognesi et al. NIWG model and uncertainties for 2017 oscillation analysis. T2K-TN-315 `http://www.t2k.org/docs/technotes/315`.

[89] K Nakamura and Particle Data Group. Review of particle physics. *Journal of Physics G: Nuclear and Particle Physics*, 37(7A):075021, 2010.

[90] Veronique Bernard, Latifa Elouadrhiri, and Ulf-G. Meissner. Axial structure of the nucleon: Topical Review. *J. Phys.*, G28:R1–R35, 2002.

[91] E. Pinzon et al. Tuning of the NEUT Cascade Model using $\pi^{\pm}$-A Scattering External Data to Improve Final State Interaction and Secondary Interaction Systematic Uncertainties. T2K-TN-325 `http://www.t2k.org/docs/technotes/325`.

[92] J. Nieves, I. Ruiz Simo, and M. J. Vicente Vacas. Inclusive charged-current neutrino-nucleus reactions. *Phys. Rev. C*, 83:045501, Apr 2011.

[93] A. A. Aguilar-Arevalo et al. First measurement of the muon neutrino charged current quasielastic double differential cross section. *Phys. Rev. D*, 81:092005, May 2010.

[94] Asmita Redij et al. Implementation of a multi-nucleon interaction model into NEUT. T2K-TN-170 `http://www.t2k.org/docs/technotes/170`.

[95] Dieter Rein and Lalit M Sehgal. Neutrino-excitation of baryon resonances and single pion production. *Annals of Physics*, 133(1):79 – 153, 1981.

[96] Krzysztof M. Graczyk and Jan T. Sobczyk. Form factors in the quark resonance model. *Phys. Rev. D*, 77:053001, Mar 2008.

[97] Ch. Berger and L. M. Sehgal. Lepton mass effects in single pion production by neutrinos. *Phys. Rev. D*, 76:113004, Dec 2007.

[98] G. M. Radecky et al. Study of single-pion production by weak charged currents in low-energy νd interactions. *Phys. Rev. D*, 25:1161–1173, Mar 1982.

[99] T. Kitagaki et al. Charged-current exclusive pion production in neutrino-deuterium interactions. *Phys. Rev. D*, 34:2554–2565, Nov 1986.

[100] M. Kabirnezhad. Single pion production in neutrino-nucleon interactions. *Phys. Rev. D*, 97:013002, Jan 2018.

[101] Dieter Rein and Lalit M. Sehgal. Coherent π^0 production in neutrino reactions. *Nuclear Physics B*, 223(1):29 – 44, 1983.

[102] A. Higuera et al. Measurement of coherent production of $\pi^{\pm}$ in neutrino and antineutrino beams on carbon from E_{ν} of 1.5 to 20 gev. *Phys. Rev. Lett.*, 113:261802, Dec 2014.

[103] Torbjörn Sjöstrand. High-energy-physics event generation with pythia 5.7 and jetset 7.4. *Computer Physics Communications*, 82(1):74 – 89, 1994.

[104] C.H. Albright and C. Jarlskog. Neutrino production of m+ and e+ heavy leptons (i). *Nuclear Physics B*, 84(2):467 – 492, 1975.

[105] M. Glück, E. Reya, and A. Vogt. Dynamical parton distributions revisited. *The European Physical Journal C - Particles and Fields*, 5(3):461–470, Sep 1998.

[106] A. Bodek and U. K. Yang. Modeling neutrino and electron scattering cross sections in the few gev region with effective lo pdfs. *AIP Conference Proceedings*, 670(1):110–117, 2003.

[107] Sowjanya Gollapinni. Neutrino Cross section Future. In *Proceedings, Prospects in Neutrino Physics (NuPhys2015): London, UK, December 16-18, 2015*, 2016.

[108] C.W. De Jager, H. De Vries, and C. De Vries. Nuclear charge- and magnetization-density-distribution parameters from elastic electron scattering. *Atomic Data and Nuclear Data Tables*, 14(5):479 – 508, 1974. Nuclear Charge and Moment Distributions.

[109] R. B. Patterson, E. M. Laird, Y. Liu, P. D. Meyers, I. Stancu, and H. A. Tanaka. The Extended-track reconstruction for MiniBooNE. *Nucl. Instrum. Meth.*, A608:206–224, 2009.

[110] S. Berkman et al. FiTQun: A New Reconstruction Algorithm for Super-K. T2K-TN-146 `http://www.t2k.org/docs/technotes/146`.

[111] Shimpei Tobayama. *An Analysis of the Oscillation of Atmospheric Neutrinos*. PhD thesis, THE UNIVERSITY OF BRITISH COLUMBIA, 2016.

[112] F. James and M. Winkler. MINUIT User's Guide. 2004.

[113] A. Himmel T. Wongjirad and A. Minamino. KDI Numu Disappearance Analysis with 6.57×10^{20} POT. T2K-TN-164 `http://www.t2k.org/docs/technotes/164`.

[114] Lee Ka Pik. *Study of the neutrino mass hierarchy with the atmospheric neutrino data observed in Super-Kamiokande*. PhD thesis, University of Tokyo, 2012.

[115] Jun Kameda. Updated study of the systematic error in numu disappearance analyses from Super-Kamiokande. T2K-TN-159 `http://www.t2k.org/docs/technotes/159`.

[116] Prob3++. `http://webhome.phy.duke.edu/~raw22/public/Prob3++/`.

[117] L. Haegel K. Duffy, A. Kaboth and P. Dunne. MaCh3 Run 1-7 Joint Analysis. T2K-TN-269 `http://www.t2k.org/docs/technotes/269`.

[118] James Imber. Ptheta Run1-6 Joint Fit Analysis. T2K-TN-267 `http://www.t2k.org/docs/technotes/267`.

[119] M. Hartz et al. ND280 Flux and Cross Section Constraint (BANFF) for 2015/16. T2K-TN-230 `http://www.t2k.org/docs/technotes/230`.

[120] P. dePerio et al. NEUT Systematic Studies for 2010a Analysis. T2K-TN-032 `http://www.t2k.org/docs/technotes/032`.

[121] P. de Perio and J. Imber. Super-K Systematic Uncertainties for RUN1-4 Joint Nue+Numu Analyses. T2K-TN-186 `http://www.t2k.org/docs/technotes/186`.

[122] Andrew Missert. SK Atmospheric Neutrino Fit and Fiducial Volume Optimization. T2K-TN-318 `http://www.t2k.org/docs/technotes/318`.

[123] K. Abe et al. Atmospheric neutrino oscillation analysis with external constraints in super-kamiokande i-iv. *Phys. Rev. D*, 97:072001, Apr 2018.

[124] J. Imber et al. T2K-SK Systematic Error Summary for the 2017 Oscillation Analysis. T2K-TN-326 `http://www.t2k.org/docs/technotes/326`.

[125] P. Adamson et al. Combined analysis of ν_μ disappearance and $\nu_\mu \to \nu_e$ appearance in minos using accelerator and atmospheric neutrinos. *Phys. Rev. Lett.*, 112:191801, May 2014.

[126] James Imber. T2K-Super-Kamiokande Combined Fit Study. T2K-TN-169 `http://www.t2k.org/docs/technotes/169`.

[127] R. Barlow et al. *Data Analysis in High Energy Physics*. Wiley-VCH Verlag GmbH & Co., KGaA, Boschstr, 12, 69469 Weinheim, Germany, 2013.

[128] Radford M Neal. Probabilistic Inference Using Markov Chain Monte Carlo Methods. http://www.cs.toronto.edu/ radford/ftp/review.pdf, 1993.

[129] N. Metropolis et al. Equation of state calculations by fast computing machines. *The Journal of Chemical Physics*, 21:1087–1092, 1953.

[130] W. K. Hastings. Monte carlo sampling methods using markov chains and their applications. *Biometrika*, 57:97–109, 1970.

[131] C. Patrignani and others (Particle Data Group). 2016 review of particle physics. *Chin. Phys. C*, 40:100001, 2016.

[132] C. Wilkinson et al. Testing charged current quasi-elastic and multinucleon interaction models in the neut neutrino interaction generator with published datasets from the miniboone and minerνa experiments. *Phys. Rev. D*, 93:072010, Apr 2016.

[133] P. Stowell, C. Wret, C. Wilkinson, L. Pickering, S. Cartwright, Y. Hayato, K. Mahn, K. S. McFarland, J. Sobczyk, R. Terri, L. Thompson, M. O. Wascko, and Y. Uchida. NUISANCE: a neutrino cross-section generator tuning and comparison framework. *JINST*, 12:P01016, January 2017.

[134] S. Bienstock et al. Constraining the Flux and Cross Section Models with Data from the ND280 Detector using FGD1 and FGD2 for the 2017 Joint Oscillation Analysis. T2K-TN-324 http://www.t2k.org/docs/technotes/324.

[135] C. Colle et al. Extracting the mass dependence and quantum numbers of short-range correlated pairs from $a(e, e'p)$ and $a(e, e'pp)$ scattering. *Phys. Rev. C*, 92:024604, Aug 2015.

[136] Melanie Day and Kevin S. McFarland. Differences in quasielastic cross sections of muon and electron neutrinos. *Phys. Rev. D*, 86:053003, Sep 2012.

[137] M. Dunkman et al. Updated Recommendation of the 2014-5 Oscillation Parameters. T2K-TN-265 http://www.t2k.org/docs/technotes/265.

[138] P. Adamson et al. Neutrino and antineutrino inclusive charged-current cross section measurements with the minos near detector. *Phys. Rev. D*, 81:072002, Apr 2010.

[139] Y. Kurimoto et al. Improved measurement of neutral current coherent π^0 production on carbon in a few-gev neutrino beam. *Phys. Rev. D*, 81:111102, Jun 2010.

[140] Sayipjamal Dulat, Tie-Jiun Hou, Jun Gao, Marco Guzzi, Joey Huston, Pavel Nadolsky, Jon Pumplin, Carl Schmidt, Daniel Stump, and C.-P. Yuan. New parton distribution functions from a global analysis of quantum chromodynamics. *Phys. Rev. D*, 93:033006, Feb 2016.

[141] M. Martini, M. Ericson, G. Chanfray, and J. Marteau. Unified approach for nucleon knock-out and coherent and incoherent pion production in neutrino interactions with nuclei. *Phys. Rev. C*, 80:065501, Dec 2009.

[142] P. de Perio et al. NEUT Nuclear Effects (FSI). T2K-TN-033 http://www.t2k.org/docs/technotes/033.

[143] SPY Collaboration. K/π production ratios from 450 GeV/c protons on beryllium. *Phys. Lett. B*, 420:225–232, February 1998.

[144] A. E. Hedin. Extension of the MSIS Thermosphere Model into the middle and lower atmosphere. *J. Geophys. Res.*, 96:1159–1172, February 1991.

[145] The T2K beam group. Flux releases summary. T2K-TN-264 http://www.t2k.org/docs/technotes/264.

[146] K. Abe et al. Evidence for the appearance of atmospheric tau neutrinos in super-kamiokande. *Phys. Rev. Lett.*, 110:181802, May 2013.

[147] K. Duffy et al. A Joint ND280-SK $1R_\mu$-SK $1R_e$ fit of neutrino and antineutrino-mode data using MCMC. T2K-TN-320 `http://www.t2k.org/docs/technotes/320`.

[148] X. L. Meng A. Gelman and H. Stern. Posterior predictive assessment of model fitness via realized discrepancies. *Statistica Sinica*, 6:733–759, 2016.